Octupole deformation in ^{221}Ac and development of the SEASON detector

Emmanuel Rey-Herme

université PARIS-SACLAY

Octupole deformation in ^{221}Ac and development of the SEASON detector

Déformation octupolaire dans le noyau de ^{221}Ac et développement du détecteur SEASON

Thèse de doctorat de l'université Paris-Saclay

École doctorale n°576 Particules, hadrons, énergie et noyau : instrumentation, imagerie, cosmos et simulation (PHENIICS)
Spécialité de doctorat : Physique Nucléaire
Graduate School : Physique, Référent : Faculté des sciences d'Orsay

Thèse préparée au **Département de Physique Nucléaire** (Université Paris-Saclay, CEA), sous la direction de **Marine VANDEBROUCK**, Ingénieure-chercheure

Thèse soutenue à Paris-Saclay, le 26 juin 2023, par

Emmanuel REY-HERME

Composition du jury

Membres du jury avec voix délibérative

Araceli LOPEZ-MARTENS Directrice de Recherche, CNRS, IJCLab, Orsay	Présidente
Olivier DORVAUX Professeur, IPHC, Université de Strasbourg	Rapporteur & Examinateur
Jérôme GIOVINAZZO Directeur de Recherche, CNRS, LP2I, Bordeaux	Rapporteur & Examinateur
Michael BENDER Directeur de Recherche, CNRS, IP2I, Lyon	Examinateur
Michael BLOCK Professeur, University of Mainz	Examinateur

THESE DE DOCTORAT
NNT : 2023UPASP064

université PARIS-SACLAY

ÉCOLE DOCTORALE
Particules, hadrons, énergie et noyau : instrumentation, imagerie, cosmos et simulation (PHENIICS)

Titre : Déformation octupolaire dans le noyau de ^{221}Ac et développement du détecteur SEASON
Mots clés : Noyaux lourds, Structure nucléaire, Déformation octupolaire, Spectroscopie de décroissance, Spectroscopie laser

Résumé : L'étude des déformations octupolaires est un sujet important en physique nucléaire. Elles sont attendues dans différentes régions de la carte des noyaux et notamment dans les actinides déficients en neutrons où de fortes déformations sont prédites. Toutefois ces déformations n'ont pu être mesurées que dans un nombre limité de cas. Cette thèse se concentre sur l'étude du ^{221}Ac par la spectroscopie de décroissance α du ^{225}Pa à IGISOL (Ion Guide Isotope Separation On-Line), Université de Jyväskylä. Le schéma de niveau du ^{221}Ac a été reconstruit et interprété comme correspondant à des bandes de doublets de parités provenants d'une déformation octupolaire statique. Des indices de la présence d'une transition vers des vibrations octupolaires, pour les isotopes de l'actinium encore plus déficients en neutrons, ont été trouvés.

De plus, un travail a également été effectué pour le développement du détecteur SEASON (Spectroscopy Electron Alpha in Silicon bOx couNter). Ce détecteur a été conçu pour effectuer la spectroscopie de décroissance des noyaux lourds et super-lourds. Il fera partie du dispositif S^3-LEB, où il servira également de compteur d'ions, afin de permettre la combinaison de la spectroscopie de décroissance avec la spectroscopie laser. Parmi les études possibles, SEASON va ouvrir de nouvelles opportunités pour l'étude des déformations octupolaires dans les actinides déficients en neutrons. Dans cette thèse, les simulations GEANT4 du détecteur ont été améliorées pour obtenir une bonne description des efficacités de détection et des résolutions en énergie attendues. De plus, une étude des feuilles d'implantation du détecteur a été réalisée. Des feuilles de carbone et de SiN ont été comparées afin de déterminer le meilleur choix pour le détecteur.

Title: Octupole deformation in ^{221}Ac and development of the SEASON detector
Keywords: Heavy nuclei, Nuclear structure, Octupole deformation, Decay spectroscopy, Laser spectroscopy

Abstract: Octupole deformation is a hot topic of nuclear physics. They are expected in several regions of the nuclear chart and notably in the neutron-deficient actinides where strong deformations are predicted. However those deformations are measured only in a limited number of cases. This thesis focuses on the study of ^{221}Ac through the α-decay spectroscopy of ^{225}Pa at the IGISOL (Ion Guide Isotope Separation On-Line) facility, University of Jyväskylä. The level scheme of ^{221}Ac was reconstructed and interpreted as parity-doublet bands arising from a static octupole deformations. Hints of a transition towards octupole vibration for more neutron-deficient actinium isotopes were found.

In addition, work was also done for the development of the SEASON (Spectroscopy Electron Alpha in Silicon bOx couNter) detector. This detector is designed to perform decay spectroscopy of heavy and super-heavy nuclei and will be part of the S^3-LEB setup where it will act as an ion counter, thus enabling the combination of decay spectroscopy with laser spectroscopy. Among the possible studies, SEASON will open opportunities in the study of octupole deformation in the neutron-deficient actinides. In this thesis the GEANT4 simulations of the detector were improved to have a good description of the expected detection efficiency and energy resolution. In addition a study of the detector implantation foils was performed, comparing carbon foils with SiN foils, to determine the best choice for the detector.

Acknowledgments

First I would like to thanks the members of my jury: Araceli Lopez-Martens, Olivier Dorvaux, Jérôme Giovinazzo, Michael Bender and Michael Block, for reading this work. Their questions, remarks and comments pushed me further in my understanding of nuclear physics and gave me new insights. In particular I would like to thank the referees, Olivier Dorvaux and Jérôme Giovinazzo for their thorough reading of this work and all their precious comments which helped improve it.

Of course I would like to thank Marine Vandebrouck, my PhD supervisor, for her guidance during those three years. She worked hard to help me grow as a physicist and pushed me to give my best in this work, with a lot of patience. She ensured that this thesis took place in the best possible condition knowing the circonstances and her door was always open for my scientific or personal questions. In addition she offered me the opportunity to see more than just my PhD subject, to discover other experiments, questions and subjects. I will always be grateful for those three years.

I would also like to express my gratitude to Iain Moore for patiently answering my countless questions about laser spectroscopy, the IGISOL facility and many other subjects. First from far away, during COVID, through numerous visio-conferences, and finally in person, especially during my stay at Jyväskylä. I also want to thank all the team at Jyväskylä and in particular Andrea and Ilkka. I really enjoyed working with you during those years !

I am grateful to Michael Block and Sebastian Raeder, as well as the whole RADRIS team, for welcoming me twice at GSI and teaching me so much about laser spectroscopy and RADRIS experiments. A special thank you for Jessica, working with you and Andrea, both at GSI and Jyväskylä was amazing !

A special thank you also to Diane for her presence and invaluable advice and to Christophe and Barbara. I would also like to express my gratitude to the direction of the DPhN, Franck Sabatié and Hervé Moutarde, for welcoming me for this thesis and for their implication for the PhD students of the department.

I also had the chance to meet an amazing group of PhD students and Postdocs. Thank you to Aude, André, Rudolphe, Borana, Pierre, Desi, Michael, Andrea, Andrii and Kevin. It was great to work in that atmosphere and I wish you the best. Thanks to Damien for always agreeing to immerse himself with me in the physical (and sometimes meta-physical) questions that arose throughout my thesis. I will miss crossing the corridor, the Bohr and Mottelson book in hand, eyebrows furrowed as I fail to graps some concept, and knocking at your door to debate, discuss, exchange and finally understand. Thanks also to Perine, Jonathan, Guillem and Louis for all the moments we shared.

Those three years would have been very hard without my friends outside of CEA, for all the fun evenings, playing role play games and killing monsters, having a drink, laughing to bad puns and so on. Thank you to Alexandre, Mathilde, Théophile, Théo Ash, Ludovic, Amélie, Jean-Baptiste and Aymeric. I am lucky to have so many amazing friends.

Un grand merci à ma famille pour leur soutien et leur amour. J'ai beaucoup de chance d'avoir une telle famille. En particulier, merci Maman. Merci de m'avoir transmis tes valeurs, de m'avoir toujours encouragé à donner le meilleur de moi-même et d'avoir toujours cru en moi.

Enfin ces dernière lignes sont dédiées à ma chère et tendre Emeline. Merci. Merci d'avoir été là pendant ces trois années, de m'avoir soutenu, d'avoir cru en moi, d'avoir été le roc sur lequel m'appuyer dans la tempête. Merci d'avoir accepté de me voir partir, parfois longtemps, dans d'autres

villes ou même d'autres pays, pour participer à des expériences et découvrir plus de cette physique qui me passionne. Merci pour tout, et merci d'avoir dit oui.

Résumé

0.1 . Introduction

La physique nucléaire est un sujet d'étude depuis plus d'un siècle et de nombreuses questions demeurent. Une de ces questions est celle de la déformation du noyau. Il est aujourd'hui bien établi que le noyau peut se déformer. La déformation la mieux connue est la déformation quadrupolaire où le noyau s'allonge pour prendre une forme de ballon de rugby, ou bien s'applatit pour prendre une forme de disque. Ces déformations sont étroitement liées aux effets de structure, on peut par exemple noter qu'au niveau des fermetures de couches les noyaux tendent à redevenir sphériques. Ainsi, étudier l'évolution des déformations d'un noyau à l'autre peut nous renseigner sur la structure de ces noyaux (de même que l'étude de la structure des noyaux renseigne sur la déformation).

Si la déformation quadrupolaire reste un sujet d'étude actif, elle est aujourd'hui bien connue. Toutefois d'autres déformations, plus exotiques, peuvent être définies. Parmi ces déformations plus exotiques se trouve la déformation octupolaire pour laquelle le noyau prend une forme de poire. L'inclusion de la possibilité d'une déformation octupolaire est essentielle dans la description du processus de fission afin d'expliquer le caractère asymétrique de la fission des actinides. Toutefois il s'agit là d'une déformation dynamique et l'on peut se demander si une telle déformation peut exister dans l'état fondamental du noyau.

Cette question a été étudiée, à la fois par la théorie et par l'expérience, et deux régions de déformation octupolaire ont été établies, l'une autour du noyau ^{222}Ra ($Z = 88$, $N = 134$) et l'autre autour du noyau ^{144}Ba ($Z = 56$, $N = 88$). Toutefois l'étendue de ces régions, ainsi que l'intensité des déformations dans ces régions, ne sont pas encore pleinement caractérisées.

Afin de mieux caractériser ces régions, plusieurs outils ont été utilisés tel que l'excitation Coulombienne, l'étude des schémas de niveaux, l'étude des décroissances radioactives ou encore la spectroscopie laser.

Cette thèse se place dans le contexte de l'étude des actinides déficients en neutrons pour lesquels de fortes déformations octupolaires sont prédites, et, pour certains noyaux, mesurées. Elle s'est concentrée sur deux points : l'étude du noyau de ^{221}Ac au travers d'une expérience de spectroscopie de décroissance du ^{225}Pa ayant eu lieu en juillet 2020 à IGISOL, Université de Jyväskylä, et le développement du détecteur SEASON (Spectroscopie Electron Alpha in Silicon bOx couNter) avec notamment un travail sur les simulations du détecteur et un travail sur l'étude de ses feuilles d'implantation.

0.2 . Décroissance nucléaire : Un outil pour étudier la forme du noyau

Un noyau peut se stabiliser au travers de l'émission de particules, soit afin de diminuer son énergie d'excitation, soit en se transformant en un autre noyau. L'un de ces modes de décroissance est la décroissance α où le noyau radioactif émet un noyau d'hélium. Cette décroissance α peut être décrite par un modèle de pénétration par effet tunnel, toutefois ce modèle ne prend pas en compte les effets de structure. Ainsi, en divisant la demi-vie mesurée pour une transition par la demi-vie calculée avec le modèle de pénétration par effet tunnel, il est possible de calculer un *facteur d'empêchement* (Hindrance Factor en anglais) qui donne des informations empiriques sur la similarité ou non entre l'état initial et l'état final (entre 1 et 4 pour un état initial et un état final identiques, plus de 1000 pour

des états radicalement différents). Le facteur d'empêchement peut notamment être un indicateur de la présence de déformation octupolaire. En effet, les transitions α entre deux états de parités différentes vont typiquement avoir un facteur d'empêchement supérieur à 100, toutefois cela n'est plus le cas en présence de déformation octupolaire. Le facteur d'empêchement pour ce genre de transitions est alors de l'ordre de 10.

Une autre signature de déformation octupolaire, dans les noyaux de masse impaire, est la présence de doublets de parités : deux états de même spin et de parité opposée provenant de la même orbitale. La différence en énergie entre les deux états du doublet de parité donne une indication sur la nature du comportement octupolaire : une faible différence (quelques dizaines de keV) indique une déformation de l'état fondamental, tandis qu'une plus grande différence (quelques centaines de keV) indique plutôt un comportement vibratoire.

0.3 . L'expérience I262 a IGISOL, Jyväskylä

L'expérience I262 visait à étudier la production des actinides déficients en neutron au travers d'une réaction de fusion évaporation induite par proton sur une cible de ^{232}Th. L'expérience a eu lieu en juillet 2020 à IGISOL (Ion Guide Isotope Separation On-Line) à l'université de Jyväskylä, en Finlande. Un faisceau de protons de 65 MeV (1-3 µA) est envoyé sur une cible fine (2.2 mg/cm^2) de ^{232}Th. Les produits de réaction sont arrêtés dans une cellule gazeuse ($\sim$ 1 cm^3) puis extraits, séparés en masse et envoyés dans un dispositif de spectroscopie de décroissance (figure 1).

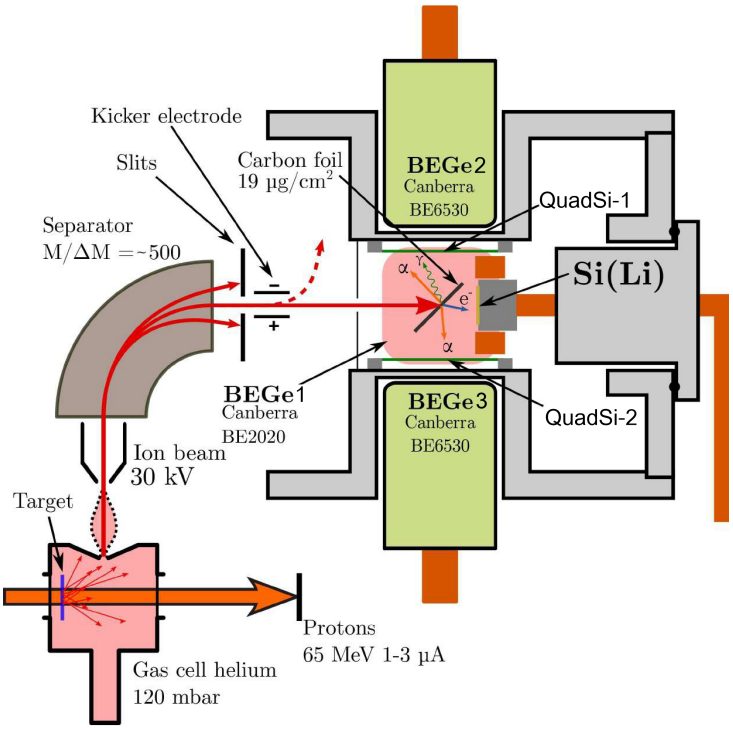

FIGURE 1 : Vue schématique du dispositif expérimental.

Les ions sont implantés dans une feuille d'implantation de carbone entourée de détecteurs silicium et germanium pour mesurer les particules émises lors de la décroissance (α, γ, électrons de conversion).

0.4 . Analyse

Après des calibrations en énergie et en efficacité pour tous les détecteurs, un ajustement est effectué sur le spectre en énergie des particules α afin de mesurer l'énergie et l'intensité des différentes transitions α observées. Ensuite, l'analyse se concentre sur l'étude des données pour la masse 225 et notamment sur la décroissance α du ^{225}Pa ($Z = 91$, $N = 134$). Elle se base sur l'utilisation de coïncidences α-γ vérifiants $Q_\alpha + E_\gamma = Q_\alpha$(g.s.-to-g.s.) (avec Q_α l'énergie libérée lors de la transition α, E_γ l'énergie du gamma et Q_α(g.s.-to-g.s.) l'énergie libérée lors de la transition vers l'état fondamental) pour identifier les niveaux d'énergie du ^{221}Ac ($Z = 89$, $N = 132$). Une fois les niveaux d'énergie identifiés, les transitions entre les différents états excités sont placées dans le schéma de niveau et l'étude des coefficients de conversion (rapport entre le nombre d'électrons de conversion et le nombre de γ émis pour une transition donnée) permet de déterminer les multipolarités des transitions. A partir de ces multipolarités, des facteurs d'empêchement et des règles de sélections les spins et parités des différents états sont reconstruits.

0.5 . Résultats et interprétation

Le schéma de décroissance reconstruit pour le ^{225}Pa est présenté figure 2.

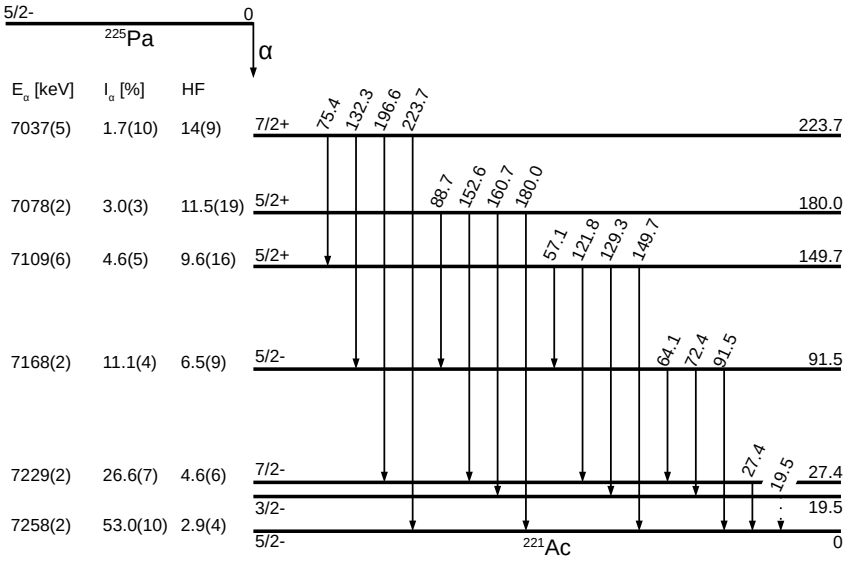

FIGURE 2 : Schéma de niveaux reconstruit pour la décroissance ^{225}Pa $\rightarrow$ ^{221}Ac. Les énergies des transitions α E_α, leurs intensités I_α et leurs facteurs d'empêchement HF (Hindrance Factor) sont représentés, ainsi que l'énergie des niveaux et des transitions γ. Les attributions proposées de spin et de parité sont également indiquées.

Ce schéma de niveaux peut être comparé au schéma de niveaux du ^{223}Ac obtenu par spectroscopie de décroissance du ^{227}Pa (figure 3). Des similarités sont observées entre les deux schémas de niveaux, avec notamment le facteur d'empêchement le plus faible pour la transition α vers l'état fondamental du noyau fils, la présence de doublets de parité et la présence de facteur d'empêchement de l'ordre de 10 pour des transitions changeant la parité. Ainsi le noyau ^{221}Ac est interprété comme présentant une déformation octupolaire dans son état fondamental. Toutefois la différence en énergie entre les

doublets de parité est plutôt élevée ($\sim$ 150 keV) par rapport à ce qui est typiquement attendu pour une déformation statique (quelques dizaines de keV). Ainsi le noyau ^{221}Ac est également interprété comme étant à la transition entre la région de déformation octupolaire statique (pour les noyaux d'actinium plus riches en neutrons) et la région de vibration octupolaire (pour les noyaux d'actinium plus déficients en neutrons). Cette interprétation est cohérente avec des résultats récents présentés par E. Verstraelen.

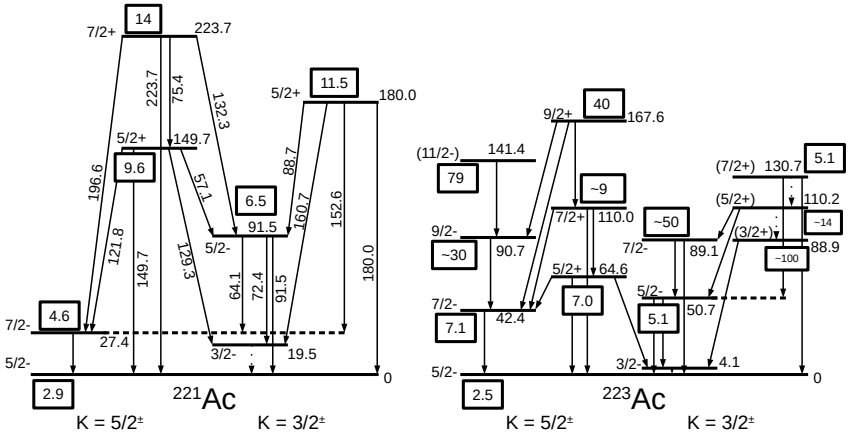

FIGURE 3 : Comparaison entre le schéma de niveaux proposé pour le noyau ^{221}Ac et le schéma de niveaux du noyau ^{223}Ac. Les facteurs d'empêchement sont indiqués dans les boites en gras.

0.6 . SEASON

SEASON (Spectroscopie Electron Alpha in Silicon bOx couNter) est un détecteur en cours de développement qui est destiné à être installé auprès de la branche basse énergie (LEB, Low Energy Branch) à S^3 (Super Separateur Spectromètre). SEASON est destiné à effectuer des mesures de spectroscopie de décroissance, tout en étant un détecteur de comptage pour la spectroscopie laser effectuée par S^3-LEB, le tout afin d'étudier les noyaux lourds et super-lourds. Un schéma du détecteur est présenté figure 4.

Le détecteur est constitué d'une station principale dans laquelle sont envoyés les atomes ionisés par laser provenant de la LEB. Cette station principale est un ensemble de 5 détecteurs silicium DSSD (Double-sided Silicon Strip Detector) afin de mesurer les particules α et les électrons de conversion. Ces 5 détecteurs sont placés dans une configuration de boite (avec un côté ouvert afin de laisser passer le faisceau d'ions) autour d'une feuille d'implantation en carbone dans laquelle sont arrêtés les ions. Cette feuille d'implantation est montée sur une roue possédant un total de 11 feuilles d'implantation. Ainsi lorsque la fréquence laser est changée, la roue tourne de 4/11$^{\text{ème}}$ de tour, ce qui déplace la feuille initialement dans la station principale vers une station secondaire (faite de deux DSSD pour poursuivre la spectroscopie pour les noyaux ayant une longue demi-vie) et ce qui amène une autre feuille, vierge de toute contamination radioactive provenant de la fréquence laser précédente, dans la station principale. Enfin deux détecteurs germanium sont placés, un à chaque station, afin de mesurer les γ émis.

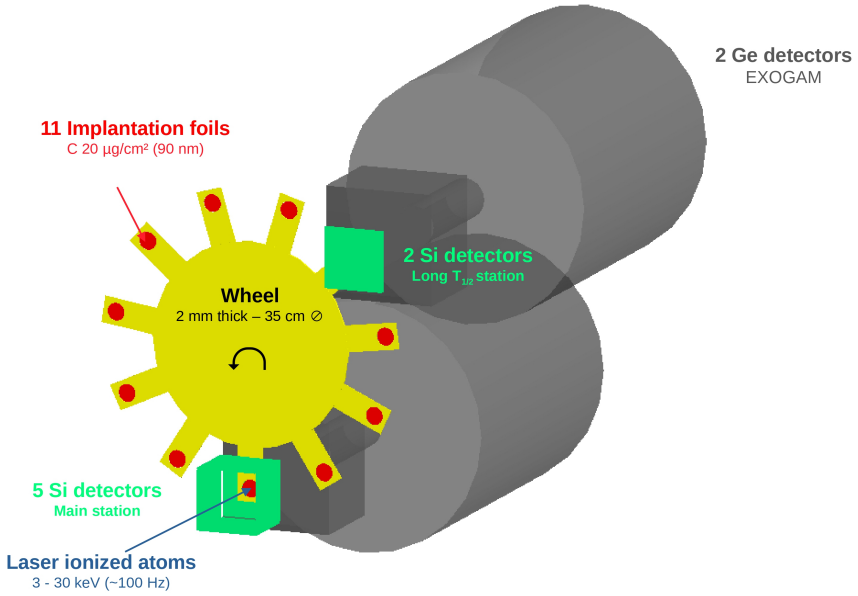

FIGURE 4 : Visualisation du détecteur SEASON dans les simulations GEANT4. Les DSSDs sont représentés en vert, les feuilles d'implantation en rouge, la roue en jaune et les détecteurs germanium en gris.

0.7 . Simulations

Des simulations du dispositif ont été effectuées en utilisant NPTool, une librairie GEANT4 pour la simulation des détecteurs de physique nucléaire. Les simulations étudient notamment les efficacités de détection pour les particules α et pour les électrons de conversion. Les simulations sont progressivement améliorées afin de prendre en compte des détails de plus en plus fins et donc d'obtenir une description la plus précise possible de l'efficacité de détection. Pour les particules α, l'impact sur la résolution en énergie des différents matériaux que la particule traverse avant d'arriver dans les détecteurs est étudié. Pour les électrons de conversion, les effets de rétro-diffusion sont étudiés afin de vérifier leur bonne reproduction dans les simulations. De plus, l'impact d'effets de sommation sur l'efficacité de détection électron est également étudié.

Dans la configuration finale, une efficacité de détection de 83,3 % est obtenue pour les particules α et de 56.2 % pour les électrons de conversion (sans tenir compte des effets de sommation). Ces valeurs peuvent être comparées aux efficacités de détection mesurées pendant l'expérience I262 (∼30 % pour les particules α et ∼ 1 % pour les électrons) ce qui met en évidence l'amélioration importante des performances que représente SEASON.

0.8 . Feuilles d'implantation

Les feuilles d'implantation sont un élément crucial de SEASON. En effet, le dispositif vise à atteindre une résolution en énergie de l'ordre de 15 keV (largeur à mi-hauteur) pour les particules α, or la feuille d'implantation peut dégrader significativement cette résolution à cause des pertes d'énergie des particules α dans la feuille. Ainsi, pour SEASON, deux matériaux ont été considérés pour les feuilles : le carbone (avec une épaisseur de 20 µg/cm^2, soit environ 90 nm) ou le nitrure de

silicium (SiN, avec une épaisseur de 9 ou de 15 µg/cm^2, soit environ 30 ou 50 nm). Les feuilles de carbone sont déjà utilisées dans de nombreux dispositifs de physique nucléaire et leur propriétés sont bien connues. De plus, elle sont peu chères et faciles d'utilisation pour SEASON. Le SiN n'est pas un matériau usuel en physique nucléaire, toutefois il est plus résistant que le carbone, il est donc possible de faire des feuilles nettement plus fines, ce qui réduit la dégradation de la résolution causée par la feuille. En revanche elles sont plus coûteuses et plus compliquées à intégrer dans SEASON.

Une étude comparative des feuilles de carbone et de SiN a été effectuée à l'aide d'un banc de test permettant la mesure de la perte d'énergie de particules α lorsqu'elles traversent la feuille. Trois types de feuilles ont été envisagées : des feuilles de carbone fabriquées au GANIL, des feuilles de carbone fournies par une entreprise (ACF Metal) et des feuilles de SiN fournies par une autre entreprise (SILSON). L'étude avec le banc de test montre un manque de reproductibilité dans les feuilles de carbone produites au GANIL. Pour les feuilles de carbone fournies par ACF Metal, elles semblent bien conformes à ce qui est annoncé par le fournisseur. Enfin, un écart est trouvé entre les épaisseurs des feuilles de SiN mesurées avec le banc de test, et les épaisseurs annoncées par le constructeur. Pour comprendre l'origine de cet écart, une étude a également été effectuée par microscopie électronique en transmission auprès de la plateforme JANNuS à IJCLab. Cette étude a permis de confirmer différentes propriétés des feuilles de SiN (nature amorphe de la feuille, stoechiométrie 1 :1), de confirmer la mesure d'épaisseur effectuée avec le banc de test, mais aussi de mettre en évidence la porosité de ces feuilles.

Cette étude conclut à l'usage des feuilles de carbone fournie par ACF Metal pour SEASON.

0.9 . Conclusion et perspectives

Dans ce travail, la chaîne de décroissance ^{225}Pa $\rightarrow$ ^{221}Ac $\rightarrow$ ^{217}Fr a été étudiée à IGISOL, permettant notamment la reconstruction du schéma de niveaux de ^{221}Ac. Dans ce schéma de niveaux, des signatures de déformation octupolaire sont trouvées, notamment la présence de doublets de parité et des facteurs d'empêchement bas pour des transitions changeant la parité.

De plus, des simulations NPTool (GEANT4) ont été effectuées pour le détecteur SEASON, permettant notamment d'estimer les efficacités de détection attendues. Pour les feuilles d'implantation de SEASON, une étude comparative de différents matériaux a été effectuée et conclut à l'utilisation de feuilles de carbone.

Le commissioning de SEASON est prévu à IGISOL en utilisant la même réaction que celle utilisée pour l'expérience I262 analysée dans cette thèse : ^{232}Th(p,xn)$^{233-x}$Pa. Les améliorations importantes en terme d'efficacité de détection et de résolution en énergie devraient permettre de considérablement améliorer les mesures. De plus, d'autres expériences devraient être proposées utilisant différentes combinaisons faisceau-cible (^{232}Th(α,xn)$^{236-x}$U, ^{233}U(p,xn)$^{234-x}$Np, ^{233}U(α,xn)$^{237-x}$Pu, etc.) pour produire d'autres actinides déficients en neutrons. Après cette campagne, SEASON sera installé auprès de S^3-LEB pour étudier les noyaux lourds et super-lourds.

Enfin, dans ce travail l'intérêt des facteurs d'empêchement pour caractériser l'étendue de la région de déformation octupolaire dans les actinides est mis en évidence. Ces facteurs d'empêchement étaient déjà utilisés dans les années 1980 et 1990, mais les progrès des différentes installations ouvrent de nouvelles opportunités.

Contents

1 - Introduction

Since Rutherford's famous experiment in 1909, and the first hints of an atomic nucleus, the properties of the nucleus have been the subject of many studies. Today, more than 100 years later, the nucleus is still a subject of interest as many questions remain and new questions appeared. For example, the characteristics of nuclear matter and its equation of state, the nucleosynthesis process and the origin of the elements, the properties of exotic nuclei, or the nature of the nuclear interaction are still active subjects under study.

Among those questions, the subject of nuclear deformation and its evolution throughout the nuclear chart is a hot topic and has been so for decades. In 1939 the first evidence of nuclear fission was found. It was not predicted by the nuclear physics theory existing at the time and almost immediately the supposition of a deformation of the nucleus was made by Lise Meitner and Otto Robert Frisch to explain this fission using the liquid-drop model [1].

Today nuclear deformation is a well established topic and most of the nuclei, apart from those near shell closures, are known to have a non-zero deformation. Several parameterisations exist to describe those deformations, but when an axial symmetry is assumed the first order of deformation, called quadrupole deformation, is usually parametrised using the β parameter, with prolate shapes (rugby-ball-like) for $\beta > 0$ and oblate shapes (disc-like) for $\beta < 0$. Figure 1.1 present theoretical calculations of this β parameter, showing that deformation is present across the whole nuclear chart, but also that the nucleus regains its spherical shape ($\beta = 0$) around some specific proton and neutron numbers (grey areas).

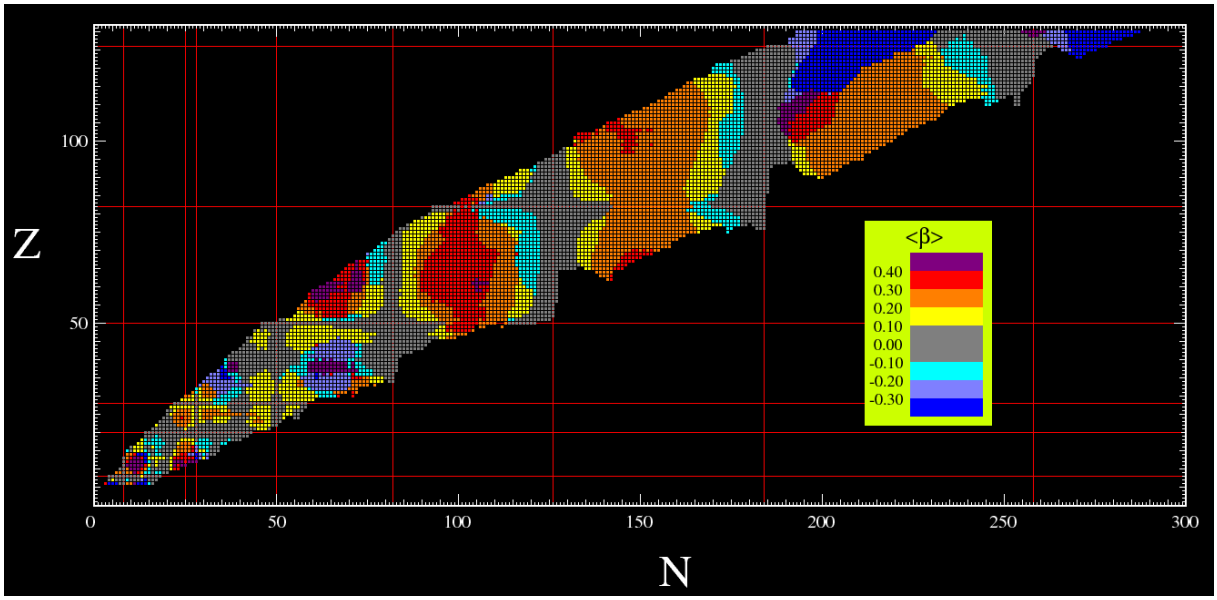

Figure 1.1: Chart of nuclei taken from reference [2]. See text for details.

In a similar way, the evolution of the mean-squared charge radii, another tool to look at changes in the nuclear structure, exhibit changes of trends for some specific numbers, for example around

$N = 50$ in figure 1.2. Those two effects, and many other similar observations, are evidences that nuclear deformation is tighly linked with the underlying structure of the nucleus and thus can be used as a tool to study this structure. Indeed, the regain of sphericity around specific proton and neutron numbers is an indicator of the presence of shell closures, and the change of trend in the evolution of the mean-squared charge radii at $N = 50$, a known shell closure, is linked to this effect.

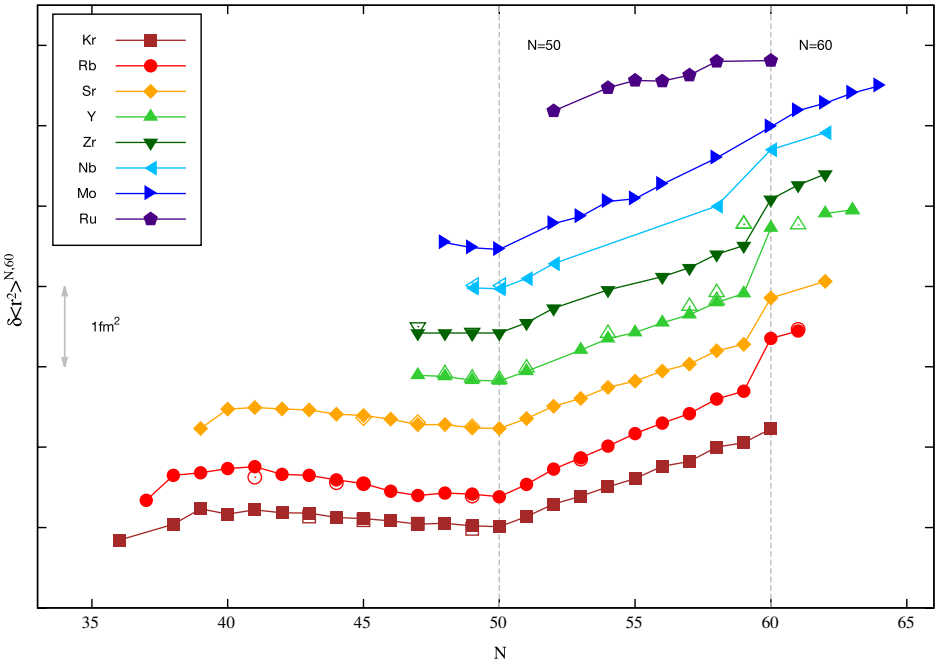

Figure 1.2: Changes in nuclear mean-square charge radii as a function of neutron number in the Kr to Ru region. The $N = 50$ shell gap, corresponding to spherical shapes, is denoted with a dotted line and can be seen in the variation of the mean-square charge radii. A shape change to prolate deformation can also be seen at $N = 60$ and is denoted by another dotted line. Figure taken from reference [3].

The connection between deformation and shell effects goes further as the presence of deformation in a nucleus affect the orbitals predicted by the shell model, removing some degeneracy and thus splitting some orbitals, but also pushing them higher or lower in energy. This leads to Nilsson diagrams [4] showing the evolution of the orbitals as a function of the quadrupole deformation. In these Nilsson diagrams, new gaps appears for both specific deformation and proton or neutron numbers, hence the apparition of deformed shell closures which can play a major role in the stability of heavy and super-heavy nuclei. Indeed, for the super-heavy nuclei ($Z \geq 104$), a pure liquid drop model predicts that they should not be bound at all due to the Coulomb repulsion. The existence of those nuclei is purely due to the presence of shell effects stabilizing the nucleus. Notably areas of enhanced stability due to deformed shell closure appear in the region.

In addition, and as stated before, nuclear deformation is also tightly linked with the fission process. Indeed, one can intuitively understand that, before splitting, a nucleus must go through intermediate deformed shapes and thus the fission process can be impacted by the presence of deformations in the ground state of a nucleus. However this goes further than the quadrupole deformation mentioned

earlier as the experimental observation is that fission of actinide isotopes is almost always asymmetric, with one of the fission fragment being heavier than the other. This means that, right before fission occurs, the nucleus must pass through reflection asymmetric shapes and thus more complex deformations. The next order of deformation, after quadrupole deformation, is the octupole deformation (see section 2.2.2), where the axial symmetry is preserved but reflection symmetry is broken, leading to "pear shape" nuclei. Thanks to fission processes, those octupole deformations are known to occur somewhere on the fission path, but a question remain: does octupole deformations exist in the ground state ?

This question has been answered through the years thanks to both experimental measurements and theory predictions and several regions of static octupole deformations have been identified. One of those regions is the neutron-deficient actinides where theoretical calculations predicts such deformations to occur around ^{222}Ra ($Z = 88,\ N = 134$) [5, 6, 7, 8]. Those predictions are confirmed by experimental evidences [9, 10, 11], however the measurement of such deformations is not an easy task and a lot of experimental work is still needed to characterise both the extent of the region and the magnitude of those deformations.

Several tools exist for the study of nuclear deformation. One of the most precise ones uses the measurement of E2 (E3) transition strength to access the quadrupole (octupole) moment, and thus to determine the shape of the nucleus. Those transitions strength are usually obtained through Coulomb excitation measurements or through lifetime measurements, however those are not always possible, especially for radioactive nuclei. Thus other signatures are needed.

Signatures of those deformations have been found in the level schemes and the decay properties of nuclei and, although it usually does not enable a quantitative measurement, it allows for a characterisation of the extent of deformation regions, especially in the case of octupole deformation [9], paving the way for further studies.

Another tool should be mentioned here: laser spectroscopy. It is initially an atomic physics tool based on the use of lasers to study the electronic structure of the atoms. However, for the past decades, it has been used in the nuclear physics community, exploiting the coupling between the atomic electrons and the nucleus to extract information about the properties of said nucleus. Indeed, the atomic hyperfine structure arises from coupling between the nucleus and the atomic electrons and thus hold information about the ground state properties of the nucleus. In laser spectroscopy measurements, a laser is used to scan the atomic hyperfine structure and then, using experimental measurements or theoretical calculations to determine the atomic part, one can extract information such as the change in charge radii along an isotopic line, the spin of the ground state, as well as the magnetic dipole moment and electric quadrupole moment. The electric quadrupole moment is linked to quadrupole deformation and thus enable its measurement. However for octupole deformation, the situation in more complicated. In principle octupole deformations will have an impact on the hyperfine structure. However, as the next order effect, it is far beyond the reach of current facilities and such direct measurements are not foreseeable. Nevertheless there are on-going experimental and theoretical works to link laser spectroscopy observables with octupole deformation, with some recent successes such as reference [11] where experimental laser spectroscopy measurements were compared to theoretical calculations to infer evidences of octupole deformation in actinium isotopes.

This thesis work is framed in the context of the study of the neutron-deficient actinides where

strong octupole deformations are predicted [5, 8, 6, 7] and, for some nuclei, measured [9, 10, 11]. It focused on two main axis:

Firstly the analysis of an experiment performed in July 2020 at IGISOL, University of Jyväskylä, where the neutron-deficient actinides were produced through a proton-induced fusion-evaporation reaction on a ^{232}Th target and studied by decay spectrocopy. This analysis focused mainly on the α-decay of ^{225}Pa towards ^{221}Ac, nuclei where octupole deformation was expected. A signature of octupole deformation is seen in ^{221}Ac through the study of the decay properties of ^{225}Pa and the reconstruction of ^{221}Ac level scheme, and an interpretation of this level scheme as parity doublet bands is proposed.

Secondly, the development of the SEASON (Spectroscopy Electron Alpha in Silicon bOx couNter) detector is discussed. It is designed to perfom α, γ and conversion-electron spectrocopy of heavy and super-heavy nuclei. It will be part of the S^3-LEB installation to combine decay spectrocopy measurements with the laser spectrocopy measurements performed there. I performed simulations of the detector, to better characterise the detection efficiency and the expected energy resolution, and I studied two possible materials for the detector's implantation foils.

This thesis is presented as follows: after a first chapter presenting decay spectroscopy as a tool to study the shape of the nucleus, the thesis will be split in two parts. First the decay spectroscopy of ^{225}Pa ($Z = 91$, $N = 134$) at IGISOL to study the properties of its daughter ^{221}Ac will be presented in three chapters including the experimental setup, the analysis and the interpretation. Second, the SEASON detector, with a first chapter presenting the detector and the S^3-LEB installation and then two chapters presenting my work on this detector, with one dedicated to the simulations of the detector, and the other to its implantation foils.

2 - Nuclear decay: A tool to study the shape of the nucleus

Radioactivity was first observed as early as 1857, althought it was not understood as radioactivity at the time, and became a subject of study at the end of the XIXth century, a decade before the discovery of the atomic nucleus. Very soon it was discovered that the radiation emitted by uranium ore was splitted in three when exposed to an electric or a magnetic field and the three radiations were named α , β and γ. This phenomenon was later understood, for α and β radioactivity, as the transformation of a nucleus into another nucleus, thus changing the number of protons and/or neutrons, by the emission of one or more particles, and for γ radioactivity as the de-excitation of a nucleus through the emission of a very energetic photon. Today, more than a century later, those decay modes are well understood and new decay modes have been discovered, such as the 1p and 2p radioactivity [12], where protons are emitted, or the cluster emission, where a light nucleus (e.g. a carbon nucleus) is emitted. However, even today, radioactive decay remains a subject of study and some exotic decay modes are predicted by theories but are yet to be measured, such as the 2-α decay [13] or the $0\nu2\beta$ decay [14].

The common point for all those decays, in addition to the transformation of a nucleus into another nucleus, is that they all carry information about the underlying structure of the nucleus. Indeed, through those decays, one can partially reconstruct the level scheme of the daughter nucleus and use it to extract information on the nuclear structure. In addition, the properties of the decay itself can provide structure information, for example through *ft* measurements for β-decay (also called "comparative half-life" and used to compare β-decay probabilities in different nuclei) or hindrance factors for α decay (see section 2.1.1.2). In this work, hindrance factors were used to obtain information about the deformation of ^{221}Ac ($Z = 89$, $N = 132$) and, combined with other properties, indicate the presence of octupole deformation (see section 5.3).

In this chapter, the tools for the study of α-decay will be presented, as well as octupole deformations and its signatures relevant for this work.

2.1 . Decay and de-excitation

This work will focus on the properties of α-decay, which occurs mostly for heavy nuclei and is the main decay mode for the majority of the neutron-deficient actinides. In particular it is the decay mode for ^{225}Pa and ^{221}Ac studied in this work.

2.1.1 . Alpha-decay and hindrance factors

Alpha-decay was already known before the discovery of the atomic nucleus and played a major role in the early nuclear physics, notably as a tool for nuclear reactions before particle accelerators were developped. The process of α-decay can be written as:

$$ {}^{A}_{Z}X_N \rightarrow {}^{A-4}_{Z-2}Y_{N-2} + {}^{4}_{2}He_2 + Q_\alpha \tag{2.1} $$

with X a given element with Z protons, N neutrons and $A = Z + N$ nucleons, decaying to another element Y and emitting a helium nucleus ${}^{4}_{2}He_2$ called an α-particle, while releasing energy Q_α. For

nuclei above $A \sim 150$ this process stabilises the nucleus by reducing its mass. Indeed the binding energy per nucleon has its maximum value around $A \sim 56$ and decreases for heavier nuclei, leading to positive Q_α values for nuclei with $A > 150$. It becomes the dominant decay in the case of heavy and super-heavy nuclei ($A > 210$), as well as for some nuclei close to the proton drip line, with typical Q_α values between 4 and 9 MeV.

Knowing the masses of the parent (M_X) and daughter (M_Y) nuclei, as well as the mass of an helium nucleus (M_{He}), one can compute the energy released:

$$Q_\alpha = M_X c^2 - M_Y c^2 - M_{He} c^2 \tag{2.2}$$

As this is a two-body decay the kinematics of the reaction is totally defined. The available energy Q_α will be divided between the α-particle and the recoiling daughter nucleus following energy and momentum conservation rules. This leads to a kinetic energy for the emitted α-particle defined as:

$$E_\alpha = \frac{M_Y}{M_Y + M_\alpha} Q_\alpha \tag{2.3}$$

with M_Y (resp. M_α) the mass of the daughter nucleus (resp. α-particle) and Q_α the energy difference between the initial state (usually the ground state of the parent nucleus) and the final state. The kinetic energy of the recoiling daughter nucleus is:

$$E_Y = \frac{M_\alpha}{M_Y + M_\alpha} Q_\alpha \tag{2.4}$$

As this decay occurs mostly for heavy nuclei with typical masses $A > 200$, the recoiling daughter nucleus typically takes less than $\sim \frac{4}{200} = 2\,\%$ of the available energy. In the example of ^{238}U α-decay, the energy released is $Q_\alpha = 4.270$ MeV, giving a kinetic energy for the α-particle $E_\alpha = \frac{234}{238} Q_\alpha = 4.198$ MeV and for the recoiling daughter nucleus $E_Y = \frac{4}{238} Q_\alpha = 0.072$ MeV. Due to the considerable mass difference between the heavy recoiling daughter nucleus and the light α-particle, the kinetic energy of the α-particle is very close to the Q_α value. However the kinetic energy of the recoiling daughter nucleus is of the order of 100 keV which is not negligeable. In particular, if the parent nucleus in shallowly implanted in a material, the recoil energy can be enough to push the daughter nucleus out of the material. This has to be taken into account for radioactive sources, where the deposit of radioactive material is coated to prevent such effects, but also in some experimental cases (see section 4.1.2).

In addition, α-decay can also occur towards an excited state of the daughter nucleus. In this case part of the available energy is kept as excitation energy of the daughter nucleus and the energy released Q_α will be decreased accordingly, an effect that can be used experimentally (see section 4.3.2).

2.1.1.1 . Modeling α-decay

Very early in the study of α-decay, it was realised that there was a strong correlation between the released energy Q_α and the half-life of α-decaying nuclei. This lead to the empirical Geiger-Nuttall law of α-decay [15]:

$$\log_{10} T_{1/2} = C_1 + \frac{C_2}{\sqrt{Q_\alpha}} \tag{2.5}$$

with $T_{1/2}$ the half-life of the parent nucleus, Q_α the released energy and C_1 and C_2 two constants for a given Z. This law reproduces correctly the trend of the data for α-decay half-life, spanning over 20

orders of magnitude and an improved version of this law, including an explicit Z and A dependence, is still used today to estimate the half-lives of unknown nuclei [16].

The effectiveness of the Geiger-Nuttall law, formulated as early as 1911, was understood later with a model proposed by Gamow in 1928 [17]. In this model, it is assumed that the α-particle is preformed in the parent nucleus before decay and is trapped within a potential well formed by the strong nuclear force and the Coulomb barrier. Figure 2.1 presents a schematic representation of the potential seen by the α-particle. For a distance $r < R$, with R the radius of the potential well, the depth of the potential well V_0 is defined by the strong nuclear force (typically $V_0 \sim 30$ MeV). For a distance $r \geq R$ the height of the potential barrier is defined by the Coulomb interaction:

$$V(r) = \frac{Z_\alpha Z_Y e^2}{4\pi\epsilon_0 r} \tag{2.6}$$

with $Z_Y = Z - 2$ ($Z_\alpha = 2$) the number of proton in the daughter nucleus (α-particle), e the elementary charge and ϵ_0 the electric permittivity. R can be approximated to $1.2(A^{1/3} + 4^{1/3})$ fm, A beeing the mass of the daughter nucleus. In the case of ^{238}U, taking $\frac{e^2}{4\pi\epsilon_0} = 1.440$ MeV.fm and $R \approx 1.2(234^{1/3} + 4^{1/3}) \approx 9.3$ fm, we obtain $V(R) \approx 28$ MeV.

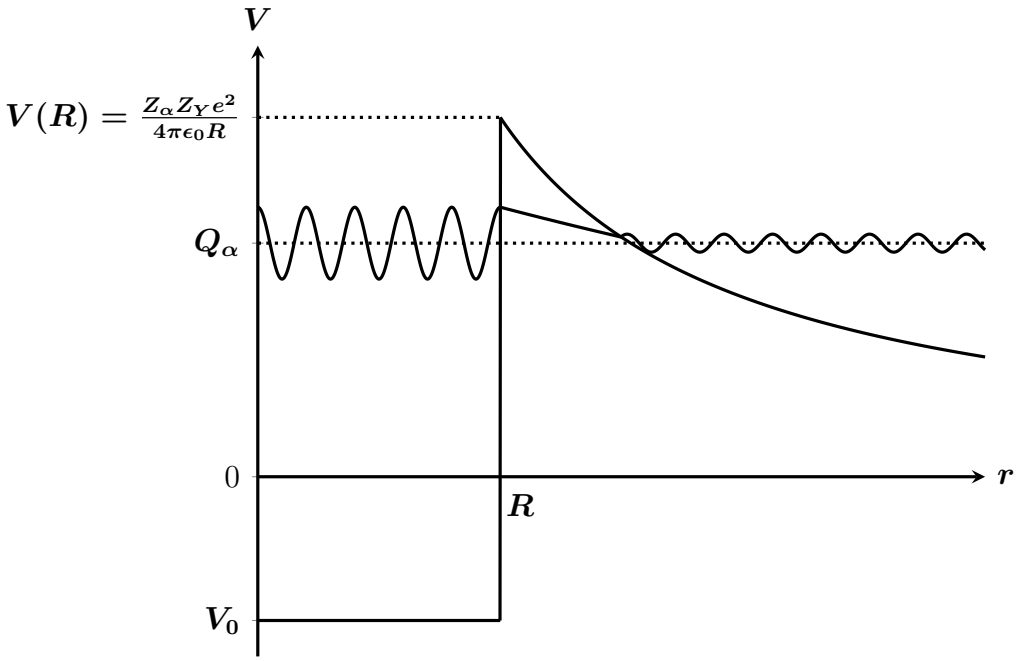

Figure 2.1: Visualisation of α-decay described as a preformed α-particle tunneling through the potential barrier. See text for details.

The wave function of the preformed α-particule is trapped in the potential well and oscillates, bouncing off the potential barrier at a rate f. This rate can be estimated as:

$$f = \frac{v_\alpha}{2R} = \frac{\sqrt{2\frac{V_0+Q_\alpha}{\mu}}}{2R} \tag{2.7}$$

with $v_\alpha = \sqrt{2\frac{V_0+Q_\alpha}{\mu}}$ the velocity of the α-particle when trapped inside the nucleus and $\mu = \frac{M_Y M_\alpha}{M_Y + M_\alpha}$

the reduced mass of the system. Using $V_0 = 30$ MeV and $Q_\alpha = 4.2$ MeV (for ^{238}U), one obtains $f = 2.3 \times 10^{21}$ s^{-1}.

Each time the α-particle bounces off the barrier, it has a finite probability of transmission T due to the tunneling effect as the potential barrier is not infinite, thus becoming a propagating wave outside of the barrier potential. Computing the transmission factor T, one obtains $T = e^{-2G}$ with $2G$ the Gamow factor. The Gamow factor can be defined as [16]:

$$2G = \frac{2}{\hbar}\int_R^b [2\mu(\frac{Z_\alpha Z_Y e^2}{4\pi\epsilon_0 r} - Q_\alpha)]^{1/2} dr \tag{2.8}$$

with $b = \frac{Z_\alpha Z_Y e^2}{4\pi\epsilon_0 Q_\alpha}$ the classical distance of closest approach (for ^{238}U we have $b \approx 62$ fm). Solving the integral, one get:

$$2G = \frac{2b}{\hbar}\sqrt{2\mu Q_\alpha}(\cos^{-1}(\sqrt{\frac{R}{b}}) - \sqrt{\frac{R}{b}(1-\frac{R}{b})}) \tag{2.9}$$

or, assuming $R \ll b$:

$$2G = \frac{\pi}{2}\frac{e^2}{4\pi\epsilon_0\hbar} Z_\alpha Z_Y \sqrt{\frac{2\mu}{Q_\alpha}} \tag{2.10}$$

Using this, one can compute the probability of transmission for ^{238}U: $T = 3.7 \times 10^{-38}$.

The decay rate λ_α can then be understood as the product of those two factors:

$$\lambda_\alpha = fT \tag{2.11}$$

Computing it in the case of ^{238}U, one get $\lambda_\alpha = 8.4 \times 10^{-17}$ s^{-1}, corresponding to $T_{1/2} = \frac{\ln(2)}{\lambda_\alpha} = 0.26$ Gy. The actual half-life for ^{238}U is $T_{1/2} = 4.5$ Gy, roughly 1 order of magnitude larger. In fact, the half-lives calculated with this method are typically one or two orders of magnitudes lower than the measured ones. This is understood as arising from the assumption of an already preformed α-particle appearing within the nucleus with probability one.

2.1.1.2 . Hindrance factors

Alpha-decay has been described as a preformed α-particle tunneling through the potential barrier formed by the Coulomb repulsion. However this model assumes that the α-particle is already preformed in the nucleus and does not take into account the preformation probability P_α of the α-particle in the parent nucleus. This preformation probability is linked to structure effects: the more similar the initial and the final wave functions are, the higher the probability to preform an α-particle [16]. Thus the effective partial half-life of the α-decay transition will be larger than the one computed with the Gamow model and their ratio, called the hindrance factor, is an indication of the impact of structure effects on the α-decay, i.e. how similar the initial and final wave functions of the parent and daughter nuclei are.

The hindrance factor HF is defined as:

$$\mathrm{HF} = \frac{T_{1/2,exp}}{T_{1/2,th}} \tag{2.12}$$

with $T_{1/2,exp}$ the experimentally measured partial half-life for the transition and $T_{1/2,th}$ the one computed using a barrier tunneling model. In this work, the hindrance factors are computed using the ALPHAD code [18]. This code computes the theoretical half-lives with Preston's spin-independent prescription [19], an improved version of the Gamow model, using the Q_α of the transition and an effective radius for the daughter nucleus r_0 (corresponding to the R parameter in section 2.1.1.1). It also computes the experimental partial half-life using the total half-life of the parent nucleus and the branching ratio of the transitions. It then outputs the hindrance factors for each transition. For even-even nuclei the effective radius r_0 is defined so that the hindrance factor for the ground-state to ground-state α-decay is 1 [20]. For odd-mass and odd-odd nuclei, it is interpolated (or, when interpolation is not possible, extrapolated) from neighbouring even-even nuclei [21].

Once the hindrance factors are calculated, they can be used to extract information on the initial and final state properties. Indeed, if the hindrance factor is low, it indicates similar initial and final states. Higher hindrance factors indicates more profound changes. Empirically, one can say [16]:

- HF $\sim$ 1-4: "Favored transition", identical initial and final single-particle states.
- HF $\sim$ 4-10: Initial and final single-particle states are mixed or have a favorable overlap.
- HF $\sim$ 10-100: Initial and final single-particle states do not have a favorable overlap, but parity and spin projection are the same.
- HF $\sim$ 100-1000: Initial and final single-particle states do not have a favorable overlap, parity changes but spin projection is the same.
- HF $>$ 1000: Initial and final single-particle states do not have a favorable overlap, parity changes and spin flips.

Thus, if the hindrance factor is low (1-4), and if one knows the spin and parity of the initial (final) state, one can deduce the spin and parity of the final (initial) state. Higher hindrance factors indicates that initial and final states should be different.

2.1.2 . Electromagnetic transitions

After the α-decay, the daughter nucleus can be left in an excited state and, in the energy range relevant here (<1 MeV), can release its excess energy through electromagnetic transitions. Those electromagnetic transitions can occur through photon emission and internal conversion.

2.1.2.1 . Photon emission

A nuclear electromagnetic transition can occur through the emission of a photon, called a γ-ray, from an excited nucleus to release the excess energy. During a γ-ray emission there is no change in Z or in A, it is only a transition in-between two states of the same nucleus.

Those γ-ray transitions can occur between two excited states or between an excited state and the ground state. In both cases three conservation rules apply:

- Energy conservation $E_\gamma = E_i - E_f$
- Parity conservation $\pi_\gamma = \pi_i \times \pi_f$
- Angular momentum conservation $\overrightarrow{I_i} = \overrightarrow{I_f} + \overrightarrow{L}$

with E_γ, $\overrightarrow{L}$ and π_γ the energy, total angular momentum and parity of the emitted γ-ray and E_i, $\overrightarrow{I_i}$ and π_i (E_f, $\overrightarrow{I_f}$ and π_f) the energy, total angular momentum and parity of the initial (final) state. For historical reasons, the angular momentum of the emitted γ-ray $\overrightarrow{L}$ is usually called "multipolarity".

For the energy conservation, it should be noted that the rule written above is not exact. Indeed in reality momentum conservation leads to a recoil of the nucleus. However this recoil is of the order of a few eV to a few dozens of eV, much lower than the typical energy resolution of high-resolution γ-ray detectors (~ 1 keV). Thus the recoil energy is almost always considered as negligeable.

The angular momentum conservation leads to the following composition rule:

$$|I_i - L| \leq I_f \leq |I_i + L| \tag{2.13}$$

or:

$$|I_i - I_f| \leq L \leq |I_i + I_f| \tag{2.14}$$

Finally two types of transitions, called "Electric" (noted E) and "Magnetic" (noted M), exist. The parity of the emitted photon depends both on the type of the transition and on its multipolarity. Noting σ the type of the transition and taking $\sigma = 0$ for electric transitions and $\sigma = 1$ for magnetic transitions, the photon parity can be defined as $\pi_\gamma = (-1)^{L+\sigma}$. Transitions are often denoted using their type and multipolarity as "EL" and "ML".

As photon always carries at least 1 unit of angular momentum, $\Delta I = 0$ transitions are forbidden via electromagnetic decay. E0 transitions have been observed as they proceed through internal conversion (addressed in section 2.1.2.2). M0 transitions are not observed and, as of today, there are no experimental evidences for the existence of magnetic monopoles.

In addition, the lower the multipolarity L of the transition, the higher the transition probability, and for the same multipolarity, electric transitions are more likely than magnetic transitions. Thus, when allowed by selection rules, the E1 transition is usually the dominant one. As E1 transition changes parity, for transitions between states with the same parity, the M1 and E2 transitions are dominant and compete between each other. Transitions of higher order (M2, E3 etc.) are rarely observed.

When two multipolarities are in competition (usually M1 and E2), a mixing coefficient can be defined as:

$$\delta = \sqrt{\frac{P_{E2}}{P_{M1}}} \tag{2.15}$$

with P_{E2} (P_{M1}) the E2 (M1) transition probability.

2.1.2.2 . Internal conversion

Additionally to γ-ray emission, the nucleus can also transmit its energy excess to one of the atomic electrons. In this case, as the typical energy of an nuclear transition is of the order of a few hundred keV to a few MeV and as the typical binding energy of the atomic electrons is at most of the order of 100 keV (115.6 keV for K-shell electrons in Uranium), the electron is ejected from the atom. This process is known as internal conversion and the emitted electron is called a conversion electron.

The conversion electron will have a kinetic energy smaller than the energy of the transition as it initially is in an atomic bound state. Its exact energy will depend on the atomic shell S it was extracted from:

$$E_e = (E_i - E_f) - B_S \tag{2.16}$$

with E_e the kinetic energy of the conversion electron, $E_i - E_f$ the energy of the transition and B_S the binding energy of the electronic shell S.

The internal conversion probability is lower for higher shells as there is a lower overlap between the electron wave function and the nuclear wave function. Thus, when allowed energetically, the dominant conversion electrons are usually the ones coming from the K shell, then L, M, N etc. The probability of internal conversion is related to the probability of γ-ray emission by the conversion coefficient α_e:

$$\alpha_e = \frac{N_e}{N_\gamma} \tag{2.17}$$

with N_e (N_γ) the number of electrons (γ-rays) emitted for the given transition.

Conversion coefficient can also be defined for a specific shell:

$$\alpha_{e,S} = \frac{N_{e,S}}{N_\gamma} \tag{2.18}$$

with N_γ the same as previously and $N_{e,S}$ the number of electrons emitted from the S shell. The total conversion coefficient is simply the sum of conversion coefficients for each shell.

The total conversion coefficient, as well as its distribution on the different shells, changes depending on the type, multipolarity and energy of the transition. As a rule of thumb, and at a given energy, magnetic transitions are more converted than electric transitions and higher multipolarity transitions are more converted than lower ones. In addition, the lower the transition energy, the more converted the transition is. Thus E1 transition have usually very low conversion coefficient (< 1), wheras M1 and E2 transitions can be highly converted with conversion coefficients of the order of a few dozens to a few thousands.

In the case of mixed transition, the conversion coefficient is a mixture of the conversion coefficients for each multipolarity [22]:

$$\alpha_e, mixed = \frac{\alpha_e(\sigma L) + \delta^2 \alpha_e(\sigma' L')}{1 + \delta^2} \tag{2.19}$$

with δ the same mixing ratio as the one defined for electromagnetic transitions in equation 2.15 and $\alpha_e(\sigma L)$ ($\alpha_e(\sigma' L')$) the conversion coefficient for a transition of type and multipolarity σL ($\sigma' L'$). By convention, this formula is defined with $L' > L$. It should be noted that when one want to obtain the mixing ratio from the measured conversion coefficients, a graphical method can be more precise than equation 2.19 [23].

All conversion coefficients can be computed using the BrIcc code [22] using as an input Z the proton number of the nucleus, the transition energy $E_i - E_f$ and the type and multipolarity of the transition, as well as the mixing ratio for mixed transitions. The code outputs the conversion electron energy and conversion coefficient for each shell or, if required, for each subshell. The code is based on tables computed using a atomic physics theoretical model (self consistent Dirac-Fock method with the "Frozen Orbital" approximation). Between the calculated points the code uses a spline interpolation. The theoretical uncertainty is estimated through comparison with experimental measurements and is of the order of 1 %. The error due to the interpolation is also estimated and incorporated in the uncertainty on the theoretical conversion coefficient in the code output. Some parameters can have an

impact in the conversion coefficient and are not taken into account by the BrIcc code (for example the change of nuclear mass from one isotope to another). Those effects are typically of the order of 1 % or below. However, it should be noted that anomalous $E1$ conversion coefficients have been reported for some nuclei in the heavy and super-heavy nuclei, with experimental conversion coefficients larger than the theoretical ones (typically a factor 2 or 3). All those effects should be kept in mind for the interpretation of the results.

By comparing measured coefficients with computed ones, one can determine the type and multipolarity of a transition.

2.2 . Deformation and pear-shape nuclei

If the question of the deformation of the nucleus is more than 70 years old, it is still a very hot topic, for the study of quadrupole deformation and their impact on nuclear structure, with all the linked questions, but also for the study of more exotic deformations, among which the octupole deformation is of particular interest in this work.

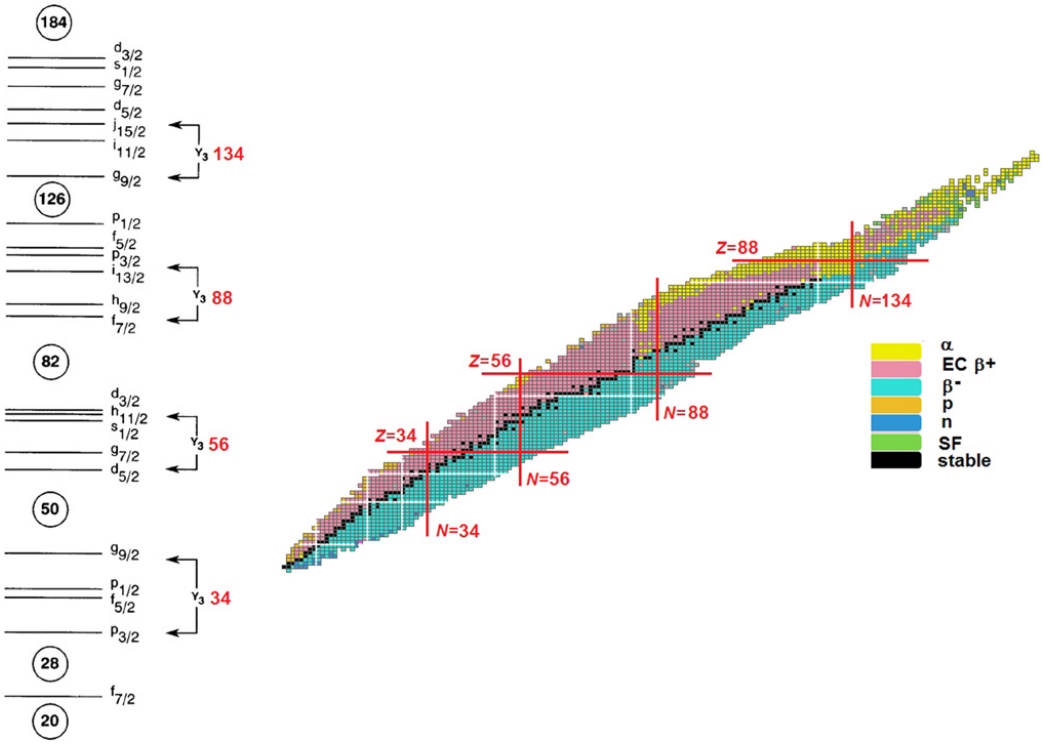

Figure 2.2: Left: Nuclear single-particle orbitals for spherical nuclei. The strongest octupole couplings are indicated (see text for details).
Right: Chart of nuclei with decay mode indicated. The particles numbers corresponding to the regions of octupole correlations are indicated with red lines and the shell closures are indicated with white lines.
Figure taken from reference [24].

Octupole deformation is a macroscopic property of the nucleus, but it is also tightly linked to the

underlying microscopic structure. Indeed octupole deformation arises from the presence of octupole correlations in the internal structure, i.e. close $\Delta l = \Delta j = 3$ single-particle states affecting each other, with j (l) the total (orbital) angular momentum. This tends to appear naturally just above closed shells (see figure 2.2).

The particle numbers corresponding to these regions of octupole correlations are $\approx$ 34, 56, 88, 134 [24] and the largest ones occur around ^{144}Ba (Z=56, N=88) and ^{222}Ra (Z=88, N=134).

2.2.1 . The interest of octupole deformation

Beyond its intrinsic interest for our understanding of the nucleus and its internal structure, octupole deformation is related to other important questions. Indeed, octupole deformation is closely linked to the stability of heavy and super-heavy nuclei as they can considerably decrease the fission barrier [25, 26], changing the fission cross section and thus changing the half-lives. They also play a major role in the description of cluster emission [27, 28]. Moreover, the collective behaviour arising from octupole correlations results in a large enhancement of symmetry-violating nuclear properties, such as the Schiff moment [29, 30]. A measurement of this property would help to constrain a possible source of charge-parity (CP) violation, proposed as a necessary ingredient in our understanding of the observed matter-antimatter asymmetry in the universe. Further sensitivity may be gained through the study of radioactive molecules incorporating heavy, octupole-deformed nuclei, highlighting a renewed interest in the underlying structure of such nuclei [31]. For all those reasons, octupole deformation has been a hot topic for the past decades [32, 33, 24, 34] and is still under scrutiny.

2.2.2 . Macroscopic description

The macroscopic deformation of the nucleus can be described using the generalised Rayleigh shape. It allows for the description of the surface of a nucleus by expressing its radius $R(\theta, \phi)$ in terms of spherical harmonics $Y_{\lambda\mu}(\theta, \phi)$:

$$R(\Omega) = c(\alpha) \left[1 + \sum_{\lambda=1}^{\infty} \sum_{\mu=-\lambda}^{+\lambda} \alpha_{\lambda\mu} Y_{\lambda\mu}(\Omega) \right] \tag{2.20}$$

with $\alpha_{\lambda\mu}$ the deformation parameters and $c(\alpha)$ a factor, function of the $\alpha_{\lambda\mu}$ parameters, determined from the spherical radius $R_0 = r_0 A^{1/3}$ to ensure the volume conservation. In this description the orientation of the axes is arbitrary, the only constraint being that the origin is placed at the nucleus center of mass. Each λ term is called the 2^λ-pole, so $\lambda = 1$ is the dipole term, $\lambda = 2$ is the quadrupole term and so on.

The first order of the development, the dipole term $\alpha_{1\mu}$ only describes a shift of the center of mass and thus is generaly ignored so that the development starts at the quadrupole term.

In the quadrupole term two of the parameters, α_{21} and α_{2-1}, are zero in the nucleus intrinsic frame and two other parameters, $\alpha_{2,2}$ and α_{2-2}, are equal. Thus only 2 parameters are required to describe quadrupole deformation: α_{20} and α_{22}. In practice another convention, based on two parameters β and γ, is often used. In this convention β describes the elongation of the nucleus and γ describes the deviation from axial symmetry, with $\alpha_{20} = \beta \cos(\gamma)$ and $\alpha_{22} = \frac{\beta \sin(\gamma)}{\sqrt{2}}$.

When axial symmetry is assumed all $\mu \neq 0$ vanish and only $\alpha_{\lambda 0}$ parameters remains. Those parameters are usually renamed as β_λ and the quadrupole (octupole) deformation of the nucleus can thus be described with β_2 (β_3).

This allows the description of several kinds of behaviour. First the nucleus can vibrate around a

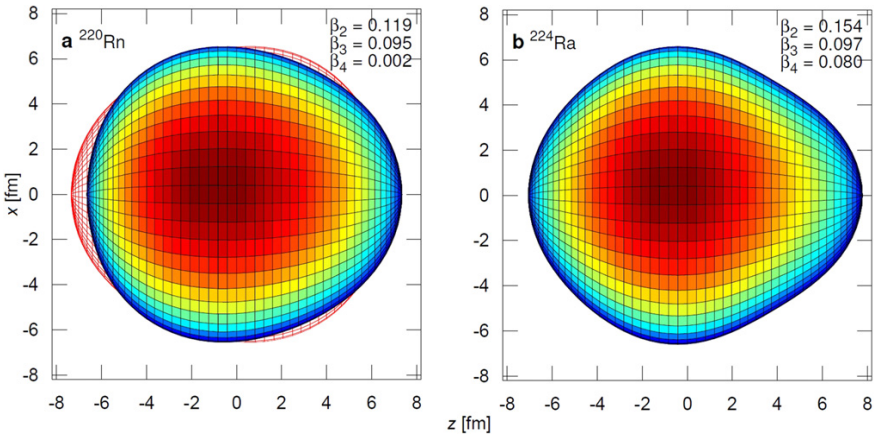

Figure 2.3: Graphical representation of the shapes of ^{220}Rn and ^{224}Ra.
Panel **a**: Vibrational motion around a plane of symmetry for ^{220}Ra.
Panel **b**: Static octupole deformation in the intrinsic frame for ^{224}Ra.
Figure taken from reference [10].

given shape, for example a quadrupole vibration around a spherical shape or octupole vibration around a quadrupole shape. Panel **a** of figure 2.3 depicts such an octupole vibration around a quadrupole deformation in the case of ^{220}Ra. The nucleus can also assume a static deformation in the intrinsic frame such as in ^{224}Ra shown in panel **b** of figure 2.3. In addition, when the nucleus has a static deformation it can rotate around an axis different from its symmetry axis.

2.2.3 . Microscopic description

As stated earlier, the macroscopic deformation is linked to the microscopic properties of the nucleus. For example, in the case of quadrupole deformation, the appearance of regularly spaced energy levels called rotational bands.

The presence of octupole vibrations and of static octupole deformations in nuclei leads to the appearance of low-lying negative parity states in the level scheme of the deformed nuclei. This effect is presented, both for even-even and for odd-A nuclei, in figure 2.4 for three different cases: octupole vibration on panel (a), rigid octupole deformation on panel (c) and soft octupole deformation on panel (b).

Octupole vibration occurs when the potential energy minimum is reached for $\beta_3 = 0$ and corresponds to a vibration around a static quadrupole deformation. For the ground state band of even-even nuclei, this leads to the appearance of a band of negative parity states $I^\pi = 1^-, 3^-, 5^-, \ldots$ with the $I^\pi = 1^-$ band-head quite high above the first $I^\pi = 2^+$ state. For odd-A nuclei, this leads to the appearance of a parity doublet band with the parity doublets having quite large energy differences.

Rigid octupole deformation is the ideal case where the potential barrier between the degenerate octupole deformed minima is infinite. In this case, for even-even nuclei, the positive and negative parity bands alternates. For odd-A nuclei, the parity doublets are fully degenerate.

Finally, soft octupole deformation is the realistic case of static octupole deformation. Two deformed minima are separated by a finite potential barrier (usually relatively small). For even-even nuclei this leads to a $I^\pi = 1^-$ band-head very close in energy to the first $I^\pi = 2^+$ state. For odd-A nuclei, the parity doublets becomes closer in energy.

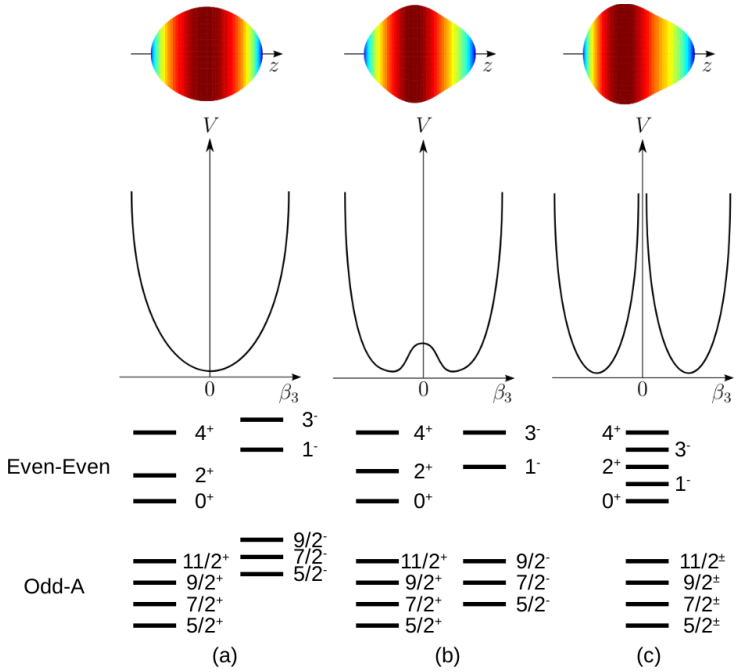

Figure 2.4: Deformation plots, potential energy versus β_3 and energy level spectra for (a) octupole vibration, (c) rigid octupole deformation and (b) soft octupole deformation (see text for details). Adapted from reference [33] and [35].

2.2.4 . α-decay signature

Static octupole deformations can be probed through the study of α-decay. Indeed, as stated in section 2.1.1.2, α-transitions between states of similar configurations are favored. In even-even nuclei, the α-decay from the ground-state of the parent nucleus to the ground-state of the daughter nucleus is typically dominant. To the contrary, in odd-A nuclei, the dominant α-decay is usually towards an excited state of the daughter nucleus which arises from the same single-particle state as the ground-state of the parent nuclei. In addition, α-decay tends to conserve parity (see 2.1.1.2). Hence the transition probability for parity-changing α-decay tends to be lower than for parity-preserving α-decay. However, octupole deformation breaks P-invariance and parity doublets arise from the same orbital. This leads to enhanced transition probabilities, and thus reduced hindrance factors towards the low-lying opposite parity states, thus making α-decay transition probabilities a signature for octupole deformation [9]. Indeed, when octupole deformation is present, transitions towards the parity doublet states can have hindrance factors of the order of 10 or lower, whereas the hindrance factor for similar transitions in reflection symmetric nuclei would typically be higher than 100.

2.2.5 . Other signatures and measurements

The α hindrance factors and the parity doublets are not the only possible signatures for octupole deformation. The use of Coulomb excitation measurements to study the E3 transition strength [10] is currently the most precise measurement for octupole deformation. The idea is to use the Coulomb force to excite the nucleus. If the beam energy is low enough with respect to the Coulomb barrier, this will be a purely electromagnetic process. By measuring the probability of each excitation, one can obtain sets of matrix elements linking the states without resorting to nuclear physics models. Then

those matrix elements can be used to compute the deformation through nuclear physics models.

However Coulomb excitation measurements are not easy to perform on radioactive isotopes as it requires either a target or a beam made of the isotope of interest. Targets of radioactive isotopes are only possible for isotopes available in macroscopic quantities, whereas beams of radioactive elements are produced by a primary reaction and then used for Coulomb excitation as a secondary reaction, thus requires facilities enabling the use of secondary beams.

But other observables can also be linked to octupole deformation. The inclusion of octupole degree of freedom to properly reproduce the masses of the actinides have been one of the first indications of the presence of octupole collectivity in this region [36, 37, 38, 39]. Octupole collectivity have also been studied through the measurement of dipole moment (E1 strenght) [37, 40, 41], however recent results (such as references [42, 43]) tends to indicates that other parameters play a role in E1 strenght and thus nucleus with an important octupole collectivity can have a low E1 strength. The inverted odd-even staggering appearing both the in the ^{144}Ba region and in the ^{222}Ra region is thought to be caused by the presence of octupole deformation [44], however this has yet to be definitly established. The presence of identical magnetic moments between parity-doublets in odd-mass nuclei [45, 46], as well as the presence of opposite decoupling parameters [45, 47] is understood as a confirmation of the parity-doublet nature of the states and thus of the presence of octupole deformation.

In addition, as mentioned in the introduction, there are on-going works to find ways of probing octupole deformation through laser spectrocopy measurements. For example, reference [11] discusses the possible impact of octupole deformation on the trends in mean-squared charge radii.

Part I

Decay spectroscopy of ^{225}Pa

In the Accelerator Laboratory of the University of Jyväskylä, an on-going program aims at the study of the neutron-deficient actinides through proton-induced fusion-evaporation reactions. In 2019, a collaboration started between CEA and the University of Jyväskylä dedicated to this study, aiming to perform decay spectroscopy of those neutron-deficient actinides and, in the future, their laser spectroscopy, both at Jyväskylä and at the S^3-LEB facility at GANIL-SPIRAL2, France (see part II).

In this context, the I262 experiment took place from the 15^{th} to the 21^{st} of July 2020 at IGISOL (Ion Guide Isotope Separator On-line) at the Accelerator Laboratory. This experiment used a proton-induced fusion-evaporation reaction on a ^{232}Th target, thus producing the neutron-deficient actinides in the vicinity of ^{232}Th. During my PhD thesis, I worked on the data analysis of this experiment, and, in particular, on the ^{225}Pa decay chain.

In this part, a first chapter will present the Accelerator Laboratory, the IGISOL facility and the I262 experiment. A second chapter will detail the analysis methodology and the tools used. Finally, a third chapter will present the results from the experiment and the associated interpretation.

3 - The I262 experiment at IGISOL, Jyväskylä

3.1 . The Accelerator Laboratory

The Accelerator Laboratory is a part of the Department of Physics at the University of Jyväskylä. Accelerator-based research at Jyväskylä started in the mid 1970s with a first cyclotron accelerating hydrogen and helium beams. This cyclotron was decommissioned in 1991 and a new K-130 cyclotron was installed in the Accelerator Laboratory, with its first beams delivered in 1992 and the first nuclear physics experiment in 1993.

This K-130 cyclotron is designed to provide up to 130 MeV/nucleon heavy ion beams, however it can also provide light ion beams. For proton beams, its focusing power limits the accessible energy to a theoretical maximum of 90 MeV and in practice the maximum energy for proton beams is ∼70 MeV. The proton beam can reach up to 20 µA at 30 MeV, but the intensity decreases with higher energy, with a typical intensity at 60 Mev of a few µA. This cyclotron has been used in the past 30 years for a wide range of experiment and the measurement areas have been constantly upgraded to maintain the Accelerator Laboratory as a state-of-the-art facility.

More recently, in 2010, the installation of a MCC30/15 cyclotron has started and, in the future, it will be used to provide proton and deuteron beams to IGISOL, with up to 30 MeV energy and up to 20 µA intensity.

These cyclotrons deliver beams to several experimental areas, the main ones for nuclear physics being RITU, MARA and IGISOL. RITU and MARA will be presented here and IGISOL will be detailed in section 3.2.

A portrait of the laboratory is available in reference [48].

3.1.1 . RITU

RITU (Recoil Ion Transport Unit) is a gas-filled recoil separator [49], initially designed for the study of the decay properties of heavy ions. It enables the separation between the beam and the reaction products using electric quadrupoles and a magnetic dipole to simultaneously filter and focus the fusion-evaporation products. It is coupled with detection arrays both at the target position (JUROGAM 3, SAGE and LISA) and at the final focal plane (GREAT) (see section 3.1.3).

The RITU installation and all its detection arrays, combined with the triggerless Total Data Readout (TDR) acquisition, provided countless successful experiments for nuclear physics in the last decades.

3.1.2 . MARA

MARA (Mass Analysing Recoil Apparatus) is a vacuum mode mass spectrometer [50], using a quadrupole triplet, an electrostatic deflector and a magnetic dipole. It enables a better separation in symmetric or inverse kinematics reactions compared to RITU and thus is a complementary apparatus. MARA's detection arrays are the same as RITU's as those arrays are designed to be movable from one separator to the other (see section 3.1.3).

In addition a Low Energy Branch (MARA-LEB) [51] is under development for MARA to study exotic nuclei through laser spectroscopy and mass measurement. It will mainly be dedicated to the study of nuclei close to the proton drip line, taking advantage the high resolving power of MARA and

stopping the ions in a small-volume buffer gas cell.

3.1.3 . Associated detectors

Several detectors can be associated to both RITU and MARA:

- JUROGAM 3 is a germanium array for γ-ray measurements at the target position, enabling the in-beam study of the nuclei [52].
- SAGE (Silicon And GErmanium) is designed for the simultaneous in-beam study of internal conversion electrons and of γ-rays at the target position, using JUROGAM 3 to detect the γ-rays and a segmented silicon detector for the conversion electrons [53].
- LISA (Light Ion Spectrometer array) is an array of silicon detectors dedicated to the measurement of charged particles emitted in the decay of short lived (ns) states at the target position.
- GREAT (Gamma Recoil Electron-Alpha Tagging) is an array of detectors, combining a multi-wire proportional chamber for time-of-flight measurements, a Double-sided Silicon Strip Detector (DSSD) to measure ion-recoils and α or β decay products, a pin diode tunnel for conversion electron measurement, as well as germanium detectors for γ-ray measurement [54]. This enables the use of the Recoil-Decay Tagging technique for in-beam studies, as well as the delayed spectroscopy of the reaction products.

3.2 . IGISOL

IGISOL (Ion Guide Isotope Separator On-Line) is both the name of an experimental technique, consisting in the stopping of ions in a gas cell, followed by a quick extraction to produce an ion beam, and of the facility implementing this technique at the University of Jyväskylä. This facility aim at the production of low-energy beams (30 keV), both stable and radioactive and is equipped with a large variety of experimental setups to take advantage of those low-energy beams to study the atomic nucleus and its properties. A full portrait of IGISOL at Jyväskylä up to 2012 is available in reference [55] and a description of the IGISOL-4 upgrade is available in reference [56]. In the following, a quick overview of the facility will be provided and a scheme of its layout, from the accelerator to the detection setups, is shown in figure 3.1.

The heart of the IGISOL facility is the ion-guide placed in the target chamber. It is composed of a thin target (typically a few mg/cm^2) followed by a small ($\sim$1 cm^3) gas-filled chamber (typically $\sim$100 mbar helium) with a hole enabling the gas extraction. The beams incoming from the K-130 and the MCC30/15 accelerators (on the top-left side of figure 3.1) are delivered to the target and the reaction products are extracted from the target thanks to the reaction kinematics. They are then stopped by the gas where they go through charge exchange, with a significant fraction reaching a singly-charged state, and extracted using electric fields and a helium gas jet via a sextupole ion guide (SPIG) [58].

Several gas cells are available depending on the reaction used to produce the nuclei of interest (fusion-evaporation, fission, multi-nucleon transfer, etc.). In the I262 experiment, the gas-cell used was the fusion-evaporation fast gas cell for which the extraction process is optimised in order to obtain a fast extraction (< 1 ms), thus enabling the study of short lived isotopes.

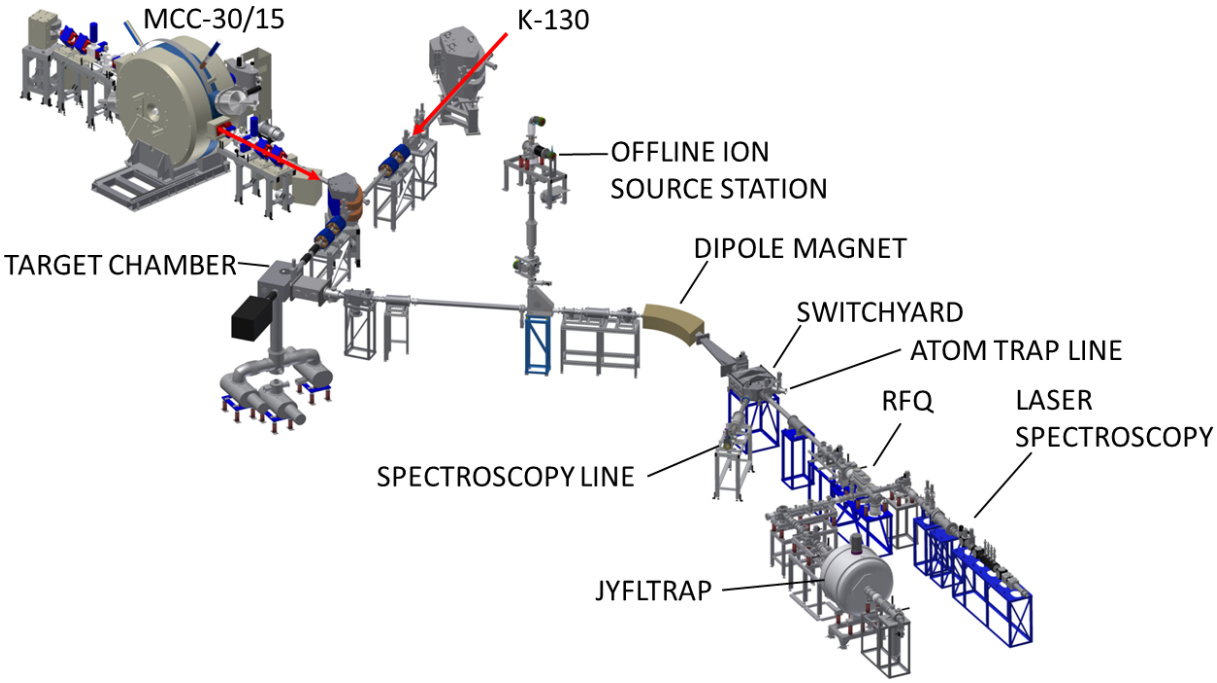

7777777

Figure 3.1: Layout of the IGISOL facility [57]. The MORA experiment mentioned in the text is not shown here. It is located on the 90° bender connecting the RFQ transfer line to the JYFLTRAP beam line.

After extraction, the ions are electrostatically accelerated to ∼30 keV (for singly-charged ions) and guided, using ion optics, towards the dipole magnet for a mass separation with a typical mass resolving power (M/ΔM) between 250 and 500. In the case of the I262 experiment, the mass resolving power was M/ΔM ∼ 350.

Directly after the dipole magnet is the "switchyard" which can be activated to bend the beam towards various experimental devices. On one side is the decay spectroscopy line, on the other side is the atom trap line and straight ahead is a RFQ (Radio-Frequency Quadrupole) cooler-buncher followed by the laser spectroscopy line and by the JYFLTRAP device, as well as the MORA experiment.

This ion-guide technique is not limited by the chemical and physical properties of the elements of interest and thus enable their fast extraction, even in the case of refractory element, a considerable advantage compared to the traditional ISOL technique. On the other hand this method produces a beam with a relatively large energy spread (10-150 eV) mainly due to collisions in the gas.

3.2.1 . The decay spectroscopy line

The decay spectroscopy line is placed after the switchyard and consist in a series of ion optics leading to a decay station. The decay station is modular and can be adapted for each experiment. A complete description of the decay station used for the I262 experiment can be found in section 3.3.2.

3.2.2 . The atom trap line

The atom trap line is part of a recent project set up by the University College London (UCL) aiming at the first experimental demonstration of a Bose-Einstein condensate of caesium isomers using

a magneto-optical trap [59, 60, 61]. This Bose-Einstein condensate could be the first step towards the coherent emission of γ-rays.

3.2.3 . The RFQ cooler-buncher

As mentioned above, one of the major drawbacks of the ion-guide technique is the relatively large energy spread of the resulting beam. For laser spectroscopy and for mass measurement, a lower energy spread means more reliability and more precise measurements. In addition, for mass measurements it is critical to have ion bunches. Thus a radio-frequency quadrupole (RFQ) cooler-buncher was placed in between the switchyard and the mass measurement and laser spectroscopy setups [**nieminen2001a**]. The ion beam is decelerated from 30 keV to $\sim$100 eV. The decelerated beam is then trapped inside a quadrupole rod structure filled with a low pressure ($\sim$1 mbar) helium buffer gas to cool it down through collisions with the buffer gas atoms. The ions are then periodically released as short bunches to the laser spectroscopy line or to JYFLTRAP.

3.2.4 . The laser spectroscopy line

A collinear laser spectroscopy line [62, 63, 64] is installed after the RFQ cooler-buncher to perform high-resolution laser spectroscopy both through fluorescence detection and through resonance ionisation spectroscopy.

3.2.5 . JYFLTRAP

JYFLTRAP [65] is a double Penning-trap designed to perform high resolution beam purification and mass measurements. It uses the first trap, filled with helium gas, to make an isobaric purification of the ion beam and the second trap to make high-precision atomic mass measurements.

It can also be coupled with a decay spectroscopy station to make trap-assisted decay spectroscopy.

3.2.6 . MORA

The MORA (Matter's Origin from the RadioActivity of trapped and oriented ions) project aims at the study of nuclear β decay to contribute to the search of CP violation [66].

3.3 . The I262 experiment

3.3.1 . Nuclei production and mass separation

The neutron-deficient actinides were produced through proton-induced fusion-evaporation reaction using a 65 MeV primary proton beam from the K130 accelerator, with an intensity between 1 and 3 µA, on a ^{232}Th target of 2.2 mg/cm^2 thickness. The reaction products are stopped in the ion-guide, guided towards the dipole magnet, mass selected and sent towards the decay spectroscopy line where a dedicated decay setup was build.

3.3.2 . Decay spectroscopy setup

The experimental setup used is shown in figure 3.2. The isobarically selected nuclei are implanted into a 19 µg/cm^2 thick carbon foil, tilted 45° with respect to the beam axis and surrounded by silicon and germanium detectors.

Two 1 mm-thick quadrant silicon detectors, composed of 4 pads of 24.75 mm width each, are placed on the sides of the foil ($\sim$2450 mm^2 total active area for each detector), one at 30.2 mm (later referred as QuadSi-1) of the foil and the other at 26.7 mm (later referred as QuadSi-2). The

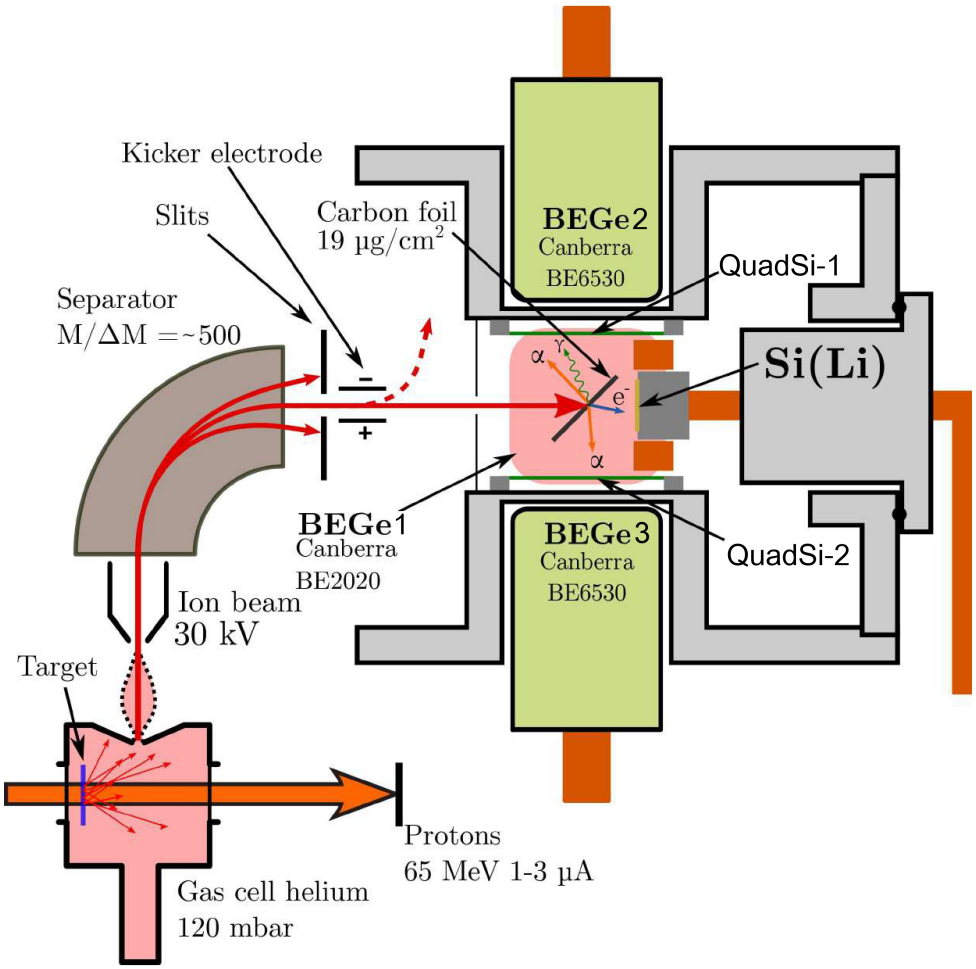

Figure 3.2: Schematic view of the experimental setup. The circular Si (CircSi) detector placed beneath the carbon foil and the BEGe detector placed above the setup (BEGe4) are not represented.

wire bonding of one of the pads of QuadSi-2 was broken before the start of the experiment, possibly while manipulating the detectors to put them in the chamber. Both QuadSi detectors have an energy resolution between 30 and 40 keV (FWHM) at 7 MeV. One 1 mm-thick circular silicon detector ($\sim$300 mm^2 active area, 40 keV energy resolution at 7 MeV, later referred to as CircSi) is placed beneath the foil at 30.2 mm and a 4 mm-thick liquid nitrogen cooled Si(Li) detector ($\sim$300 mm^2 of active area) is placed at 20.6 mm behind the foil on the beam axis. The Si(Li) detector allowed the measurement of both α-particles ($\sim$25 keV FWHM energy resolution at 7 MeV) and conversion electrons ($\sim$2 keV FWHM energy resolution at 100 keV).

For γ-ray measurements, four Broad Energy Germanium (BEGe) detectors [67] were placed in a compact geometry around the chamber ($\sim$1 keV FWHM energy resolution at 300 keV). One of those detectors, placed $\sim$10 cm above the implantation foil and later refered to as BEGe1, was the BE2020 model with a surface area of 20 cm^2 and a thickness of 20 mm. The other three detectors were the BE6530 model with a surface area of 65 cm^2 and a thickness of 30 mm. Two of them were placed on each side of the setup, behind the QuadSi detectors, at $\sim$4.5 cm from the implantation foil, and are

refered to as BEGe2 and BEGe3. Finally, the last one, refered to as BEGe4, was placed ∼11.5 cm underneath the implantation foil.

One of the main advantage of those BEGe detectors is that they are optimized to be sensitive at low energies (down to ∼10 keV) with the front of the BEGe detectors covered by a 0.6 mm thick carbon window instead of the usual aluminium window. To take full advantage of this capability for BEGe1, BEGe2 and BEGe3, holes were drilled in the detection chamber and then covered by a 0.1 mm thick kapton foil to reduce low energy photon absorbtion and thus enhance the detection efficiency at low energy. It was not possible to do the same for BEGe4.

3.3.3 . Data acquisition

After a pre-amplification by a Mesytec MPR 16 card for the QuadSi detectors, and by the internal preamp for the Si(Li) and for the BEGe, the signals coming from the different detectors were recorded by mean of a trigger-less data acquisition system composed of two NUTAQ VHS-ADC V4 14bit 100 MHz cards, synchronised by an externally provided clock. Each signal is processed by the board's internal FPGA using a moving window deconvolution filter to extract energy information and to timestamp (100 MHz) the events that are then sent to the acquisition computer where they are time sorted and written to disk.

During the experiment, the dipole magnet was set to a given mass and data were accumulated for a few hours for each mass of interest. In total, runs were taken from mass A=219 to mass A=227, with several isotopes produced for each mass. The masses, data acquisition duration and produced isotopes are summarised in table 3.1. The produced isotopes were identified using their α-decay energies.

Mass	Run duration	Produced isotopes
219	∼2.5 h	^{219}Fr
220	∼4 h	^{220}Ra
221	∼2.5 h	^{221}Ra, ^{221}Ac
222	∼7 h	^{222}Ra, ^{222}Ac
223	∼7.5 h	^{223}Ac
224	∼8.5 h	^{224}Ra, ^{224}Ac, ^{224}Th
225	∼12 h	^{225}Pa, ^{225}Th
226	∼24 h	^{226}Pa, ^{226}Th
227	∼6 h	^{227}Pa, ^{227}Th

Table 3.1: Summary of the main produced isotopes and the duration of data taken for each one.

The beam was periodically stopped during the acquisition to measure the decay and thus check the half-lives of the produced elements.

3.3.4 . Event reconstruction

The data acquisition is triggerless, thus all detector hits are saved on disc un-grouped. The event reconstruction is done afterwards using a code written for the experiment by A. Raggio, a PhD student from the University of Jyväskylä. This code reads the data files written is a format specific to this acquisition setup and convert the raw data files into grouped events written in a root TTree. In

addition to the data files, it takes as input three configuration files:

- Calibration file, containing, for each detector, calibration coefficients for a polynomial function up to order 3 (4 calibration parameters in total). Only linear calibrations were required in this work.

- Event builder file, containing the channels on which the code should trigger, as well as the time windows to use before and after the trigger.

- Tree configuration file, indicating the format of the ouput tree.

Several configurations were tested for the event builder, changing the trigger detectors as well as the time window to reach an optimal configuration. In chapter 4 the trigger was performed on Si detectors with a 4 µs time window (2 µs before and after the trigger) to group events. Attemps were also made to use a trigger on germanium detectors to perform γ -γcoincidences, however the statistic was too low and this did not yield satisfactory results.

In this event structure, an α-particle and a γ-ray are considered in coincidence if the γ-ray is detected in a 1 µs time window after the α-particle. The same coincidence window is used for the conversion electrons.

3.4 . Experimental context

This experiment is part of an exploratory program started at the University of Jyväskylä a few years ago. The goal of the program is to study the production of actinides isotopes through proton-induced fusion-evaporation reactions, in order to, in the future, perform the laser spectroscopy of such isotopes. A first experiment, the I245 experiment, was performed in 2018 with a similar setup as the one presented above, however the nuclei were implanted directly in a silicon detector. The analysis of this experiment is still on-going.

The I262 experiment main goal was to further characterise the production rate, using on-shelf detectors assembled in the setup presented in section 3.3.2.

Most of the produced isotopes that α-decay are well known with typical Q_α value uncertainties of a few keV and precise measurements of emitted γ-rays and conversion electrons. However, two protactinium isotopes (^{225}Pa, $Z = 91$, $N = 134$ and ^{226}Pa, $Z = 91$, $N = 135$) had less existing literature, and notably no γ-rays and conversion electrons measured in coincidence with the α-decays. My work focused on the ^{225}Pa α-decay chain.

An addendum to the I262 proposal was submitted and accepted, requesting more beamtime to study the production of longer lived (closer to stability) isotopes through mass measurement with JYFLTRAP.

Another experiment, the I263 experiment, took place in October 2022 to continue the study. The goal was to use a ^{233}U target to study neutron-deficient actinides further away from stability. The ^{233}U targets did not perform as expected and nothing could be seen on the experimental setup. However, this experimental setup was an improved version of the I262 experimental setup and this experiment served as a commissioning of the VADER (Versatile Actines DEcay spectRoscopy) setup [68].

3.4.1 . Implantation summary

During the run for mass 225, five decay chains were identified in the data and explained all peaks observed. The nuclei directly implanted in the foil, as well as the number of decay occuring during the run for those nuclei, are listed in table 3.2. The two main decay chains are the decay chains for ^{225}Th and ^{225}Pa. ^{226}Th and ^{226}Pa are also observed as they partly pass through the mass selection. Finally, ^{224}Ra is also observed as it was produced in a previous run from mass 224 and is long-lived ($T_{1/2} = 3.6$ d).

Parent nuclei	N_{decay}	R_{decay} (Hz)
^{224}Ra	87000 ± 7000	2.0 (2)
^{226}Th	278000 ± 15000	6.4 (3)
^{225}Th	896000 ± 72000	20.7 (17)
^{226}Pa	140000 ± 20000	3.2 (5)
^{225}Pa	1170000 ± 90000	27.1 (21)

Table 3.2: Decay chains identified in the run for mass 225, and their estimated number of decay occuring during the run N_{decay}, as well as the associated estimated decay rate R_{decay} in Hz. The number of decay is estimated using the number of detected α-decay and the known branching ratios.

3.4.2 . Previous results on ^{225}Pa decay chain

Parent nuclei	E_α (keV)	I_α (%)	HF	E_{pop} (keV)
^{225}Pa ($5/2^-$)	7264(3)	61(6)	2.6(3)	0
	7234(4)	15(4)	8.1(19)	30(5)
	[7205(8)]	9(3)	11(5)	60(8)
	7182(8)	5(2)	16(7)	88.2(15)
	7135(8)	1.8(6)	32(11)	124.9(12)
	7112(8)	3.7(13)	12(5)	152.2(15)
	7084(8)	4.0(12)	9(3)	179.8(15)
^{221}Ac ($5/2^-$)	7642(3)	71(4)	5.3(5)	0
	7440(3)	20(2)	4.1(5)	208.7(11)
	7364(5)	9(2)	5.2(12)	276.0(10)

Table 3.3: α-decay energies E_α, branching ratios I_α, hindrance factors HF and excitation energy of the populated states E_{pop} for ^{225}Pa $\rightarrow$ ^{221}Ac and for ^{221}Ac $\rightarrow$ ^{217}Fr taken from reference [69]. Those shown in square brackets are tentative.

The α-decay of ^{225}Pa has previously been reported in a few references [69, 70, 71, 72, 73, 74], with the most extensive study [69] published in March 2022 by E. Parr and collaborators. This study, performed with the RITU separator (see section 3.1.1), reported seven α-decay branches for ^{225}Pa (see table 3.3). In addition they observed for the first time γ-rays in coincidence with the α-decay of ^{225}Pa and they suggested a $I^\pi = 5/2^-$ assignment for the ground state of both ^{225}Pa and ^{221}Ac. The resulting decay scheme is shown in figure 3.3. They could not measure conversion electrons

in coincidence as the nuclei of interest were directly implanted in a DSSD, leading to a difficult assignment of multipolarities for the transitions.

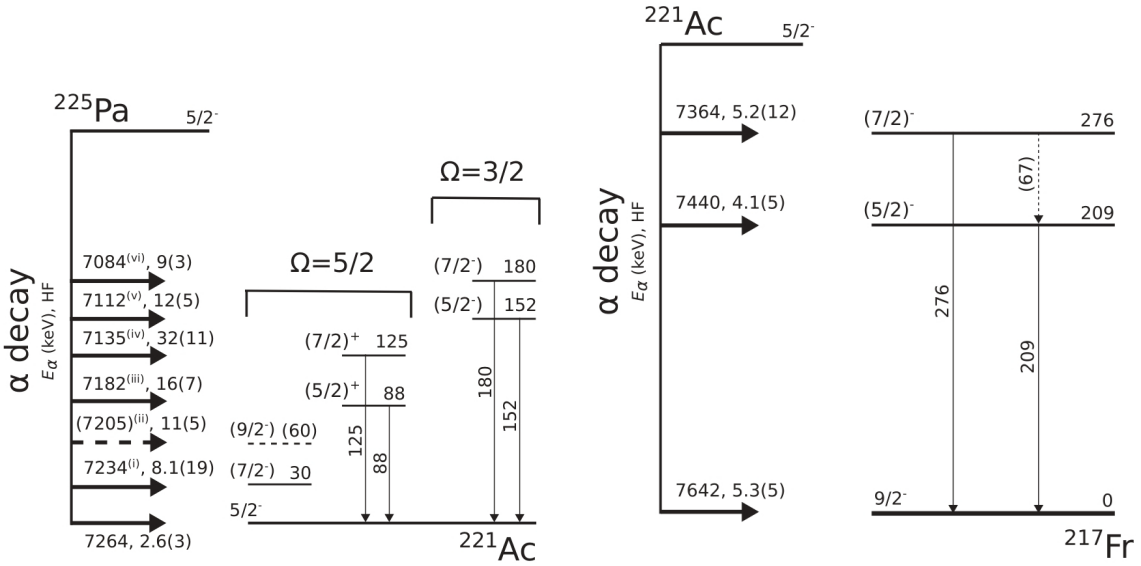

Figure 3.3: Decay scheme for the ^{225}Pa α-decay (left) and for the ^{221}Ac α-decay (right). Figures taken from [69].

Before this recent study, the most extensive study for ^{225}Pa α-decay was the one of M. Huyse and collaborators [74], performed in 1988 at IGISOL (see section 3.2), with the measurement of three α-decay branches with energies and branching ratios [7261(5) keV, 53(2)%], [7235(5) keV, 30(2)%] and [7170(5) keV, 17(1)%].

In addition to the α-decay studies, an in-beam spectroscopy of ^{221}Ac using the ^{209}Bi(^{14}C,2n)^{221}Ac reaction has been performed, and a level scheme based on two alternating parity bands has been reported [75]. A tentative $I^\pi = (3/2)^-$ ground state has been assigned, in disagreement with the $I^\pi = 5/2^-$ assigned in decay spectroscopy experiments. The excited states obtained during this study do not match the ones populated through α-decay studies.

For ^{221}Ac, as mentioned above, there is a disagreement on the spin assignment of the ground state between the in-beam [75] and α-decay [69] studies. In addition, the α-decay of ^{221}Ac was studied several times in the past [72, 73, 74, 70, 69] with the most recent one being the work of E. Parr and collaborators [69], reporting three α-decay branches (see table 3.3) consistent with the previously measured ones. They also measured γ-rays in coincidence for the first time. It should be noted that in reference [73], an additional α-decay branch was reported with energy and intensity [7170(10) keV, $\sim 2\%$].

The ground state of ^{217}Fr, ^{221}Ac's daughter nucleus, was determined without ambiguity to be $I^\pi = 9/2^-$ due to a dominant unhindered α-decay towards the $I^\pi = 9/2^-$ ground state of ^{213}At. A tentative spin assignment $I^\pi = (5/2)^-$ for the first excited state and $I^\pi = (7/2)^-$ for the second excited state have also been proposed by E. Parr and collaborators [69]. Their reconstructed decay scheme for ^{221}Ac is shown in figure 3.3.

4 - Analysis

In this chapter data analysis will be detailed, starting with a presentation of the energy and efficiency calibrations and then the general methodology used for the analysis, as well as the tools developped for the purpose of this analysis.

4.1 . Energy calibrations

4.1.1 . BEGe energy calibration

The BEGe energy calibration was performed in two steps: first all the detectors were aligned to one of the BEGe using online data. In a second step, this detector was calibrated using a linear function and peaks from ^{152}Eu and ^{133}Ba sources.

For each detector, each peak of interest was fitted using the "radware" fit function for γ-peaks. This function fit each peak using the sum of three components [76]:

- A Gaussian function:

$$G = p \times C \times \exp(-\frac{(x-\mu)^2}{2\sigma^2}) \tag{4.1}$$

- A skewed gaussian function which arises from incomplete charge collection:

$$SG = (1-p) \times C \times \exp(\frac{x-\mu}{\beta}) \times erfc(\frac{x-\mu}{\sqrt{2}\sigma} + \frac{\sigma}{\sqrt{2}\beta}) \tag{4.2}$$

- A smoothed step function to describe the higher background on the low-energy side of a peak:

$$Bckg = step \times C \times erfc(\frac{x-\mu}{\sqrt{2}\sigma}) \tag{4.3}$$

Where erfc is the complementary error function. The parameters are the same for each component of the fit function and are defined as:

- the centroid of the gaussian μ
- the standard deviation of the gaussian σ
- the amplitude C
- the proportion of events in the gaussian p
- a deformation parameter for the skewed gaussian β
- a proportion of the amplitude C used to define the height of the background on the low-energy side $step$.

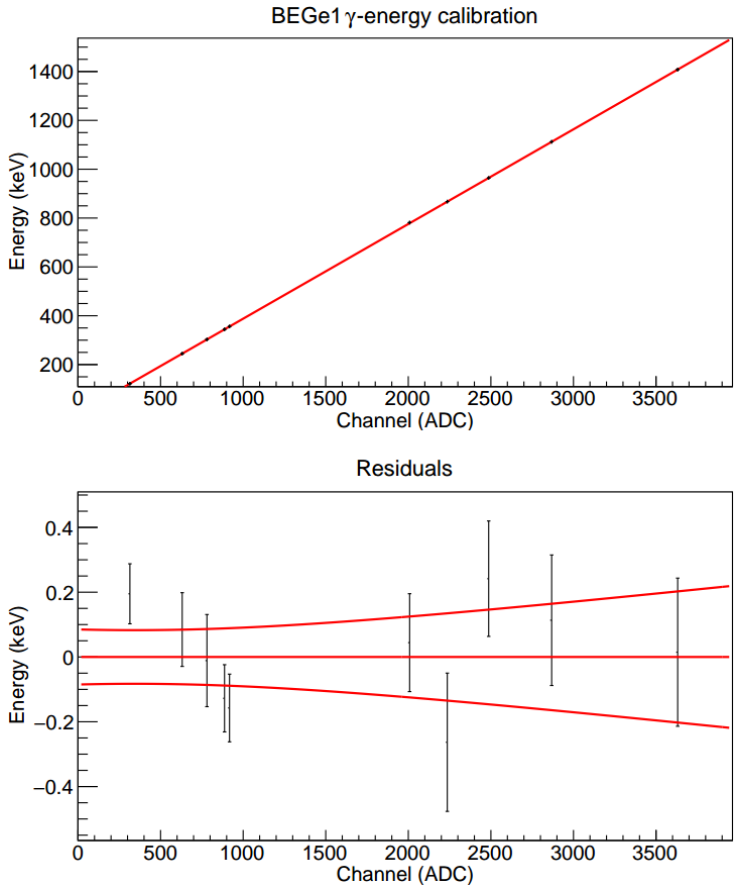

Figure 4.1: BEGe1 γ-energy calibration. Top: Linear regression. Bottom: Fit residuals. The 1-σ error bars ar shown on the residual plot.

All parameters (6 per peak) are let free with only initial guesses. The p parameter is constrained to be between 0 and 1. When possible, several peaks are fitted at the same time with a linear or quadratic background added.

Subsequently, this same function was systematically used to extract the energies and intensities of the γ-peaks.

An example calibration fit for BEGe1 is given in figure 4.1. The calibration is performed with a linear fit function and the residuals, defined as the difference between the calculated energy and the reference energy, are plotted below. A good agreement is obtained between the fit and the data, with the residuals typically below 0.2 keV. The same results are obtained for the other detectors.

4.1.2 . α-energy calibration

Alpha energy calibrations were performed on the experimental data, using known α-decays for each mass. Indeed, if the energy calibration were performed with sources, the energy loss in the implantation foil would not be taken into account, which would lead to systematic errors on the energies. The α-peaks are fitted using a skewed gaussian function. This function is the sum of two terms: a gaussian function and a deformed gaussian. The deformed gaussian term is the convolution of the gaussian resolution of the detector with an exponential tail arising from energy losses of α-particles in the materials it passes through before depositing its energy within the silicon detector.

The fit function is taken from reference [77] and can be defined as:

$$S(E) = I \times \left[\frac{p}{\sqrt{2\pi}\sigma} \exp\left(\frac{-(E-\mu)^2}{2\sigma^2}\right) + \frac{(1-p)\alpha}{2\sigma} \exp\left(\frac{-\alpha^2}{4} + \alpha\frac{E-\mu}{\sigma}\right)\left(1 + erf\left(\frac{-(E-\mu)}{\sigma}\right)\right)\right] \tag{4.4}$$

where:

- I is the integral of the gaussian
- μ is the mean of the gaussian
- σ is the standard deviation of the gaussian
- p is a weight parameter
- α is a deformation parameter

For the Si(Li), it was noted that the gain was slightly drifting during the experiment. To take this into account, several calibrations had to be performed on separate runs and the closest calibration from the run analysed was used.

In addition, during the α-decay, the recoil energy of daughter nuclei is enough for them to come out of the implantation foil with a ~ 50 % probability. Indeed, the kinetic energy of the incoming ions is ~ 30 keV, whereas the recoil energy is of the order of 100 keV. Thus α-particle energy calibrations need to be adjusted for the daughter nuclei to take into account the different energy losses of the α-particle before reaching the detectors, leading to separate calibrations. This is only true for the α-particle energy calibrations as the electrons and γ-rays are less affected by the materials they pass through. This effect also have important consequences on the efficiencies, discussed in more details in section 4.2.4.

Parent nucleus	E_α (keV)	I_α (%)
^{226}Th	6336.8 (10)	75.5 (3)
^{225}Th	6441 (3)	13.5 (16)
	6478 (4)	39 (4)
	6501 (3)	12.6 (15)
^{226}Pa	6824 (10)	34
	6864 (10)	38
^{221}Ac	7374 (4)	7.0 (10)
	7437 (4)	20.0 (20)
	7642 (4)	72 (3)

Table 4.1: α-decay used for the Si(Li) energy calibration.

The calibration fit for the Si(Li) for mass 225 is given in figure 4.2. The α-decay used in this calibration are given in table 4.1. The calibration is performed with a linear fit function and the residuals are plotted below. A good agreement is obtained between the fit and the data, with the

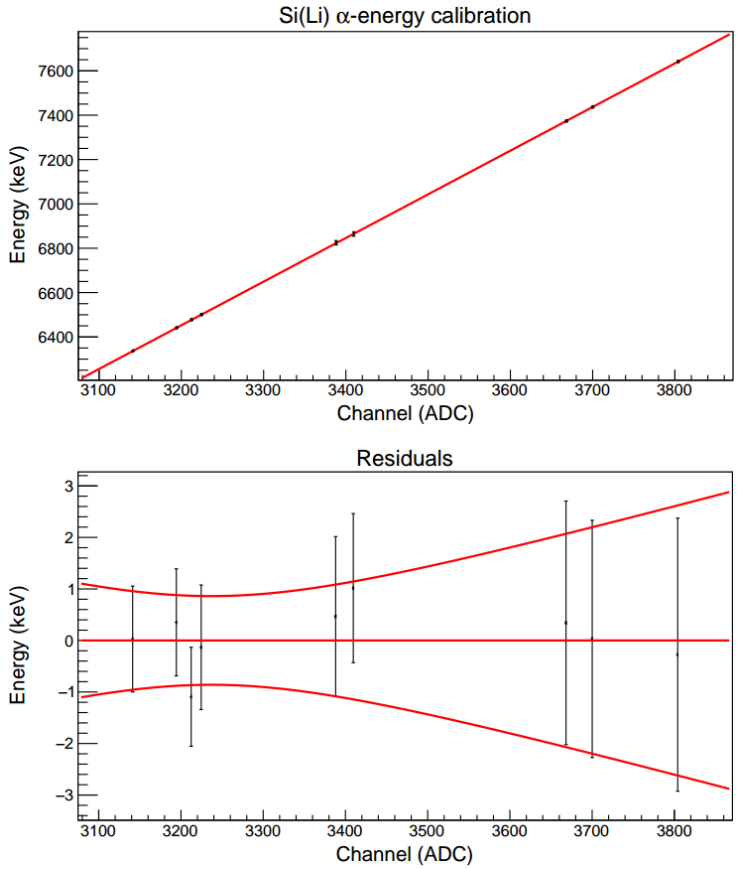

Figure 4.2: Si(Li) α-energy calibration. Top: Linear regression. Bottom: Fit residuals. The 1-σ error bars ar shown on the residual plot.

residuals typically below 1 keV. However, one can notice that the 1-σ error bars plotted on the residuals are not linear ones but curved ones. This comes from the covariance of the parameters of the linear regression. Indeed, the slope and the y-intercept are strongly correlated and as the energy range of the calibration does not cover the whole energy range measured, it can have a considerable impact on the uncertainties for peaks far away, thus this covariance is crucial to properly compute the uncertainties. However, the peaks of interest in this study are between 7 and 7.6 MeV, perfectly within the range of the calibration, and thus have relatively low uncertainties. This covariance was also studied for the other energy calibrations, however it is not detailed as it only had a significant effect in the case of the α-energy calibrations. The same results are obtained for the other detectors.

4.1.3 . Electron energy calibration

The only detector able to detect electrons with enough precision is the Si(Li). The electron energy calibration was thus only performed for the Si(Li) using α-electron coincidences to clearly identify the conversion electrons emitted during the α-decay of ^{225}Th and ^{226}Th (see table 4.2).

The electron peaks were fitted with a gaussian function and a linear background.

The calibration fit for the electron detection in the Si(Li) is given in figure 4.3. The calibration is performed with a linear fit function and the residuals are plotted below. A good agreement is obtained between the fit and the data, with the residuals typically below 1 keV. One can notice that the two

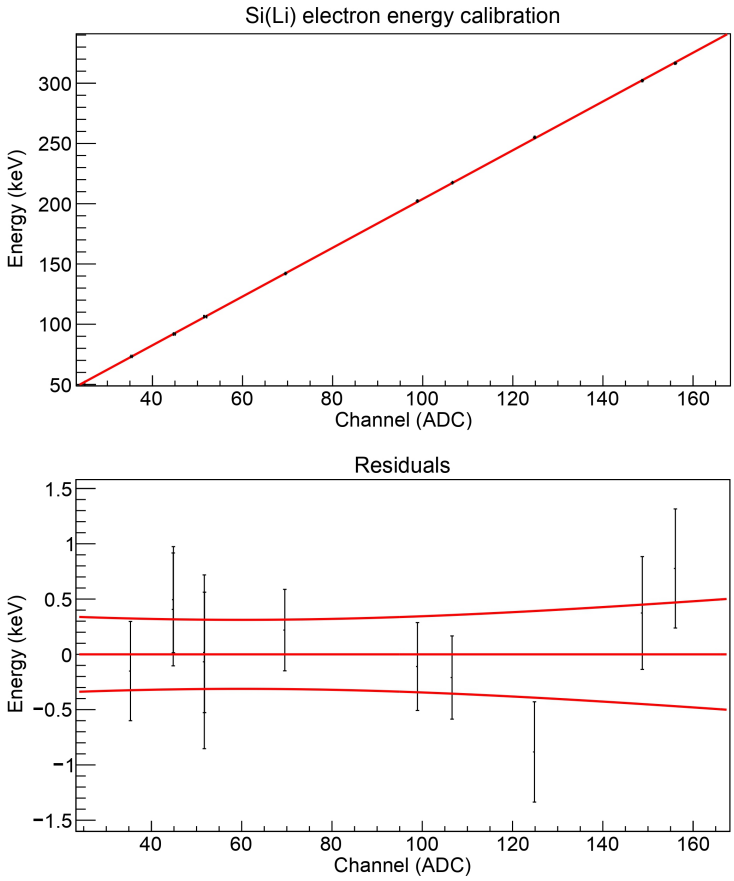

Figure 4.3: Si(Li) electron energy calibration. Top: Linear regression. Bottom: Fit residuals. The 1-σ error bars ar shown on the residual plot.

peaks around channel 50 of the ADC are included twice. Those peaks are seen in two different runs, one at the begining of the experiment and one at the end, and thus were measured twice and included twice in the calibration. They were also used as a check that, even if the Si(Li) gain drifted during the experiment and thus that the α-energy calibration had to be adjusted accordingly, it was not the case for the electrons and the same calibration remained valid during the whole experiment. Indeed, the calibration does not need to be adjusted for those two peaks between the two runs, whereas the α-energy calibration changed considerably between those two runs.

Parent nucleus	E_{e^-} (keV)	I_{e^-} (%)
^{225}Th	73.28 (10)	2.5 (3)
	142.08 (10)	5.3 (5)
	201.98 (10)	2.3 (3)
	217.48 (10)	11.21 (1)
	255.08 (10)	1.49 (22)
	302.16 (10)	2.059 (1)
	316.58 (10)	0.49 (1)
^{226}Th	91.88 (3)	14.3 (9)
	106.30 (3)	3.88 (24)

Table 4.2: Conversion electrons used for the Si(Li) electron energy calibration.

4.2 . Efficiency calibrations

4.2.1 . BEGe efficiency calibration

BEGe efficiency calibrations were computed using ^{152}Eu and ^{133}Ba sources. Additional data from a 3-α source and from a ^{223}Ra α-recoil source (^{223}Ra deposited on the tip of a needle) were used to fill the gaps and increase the precision of the calibration (see table 4.3 for the γ-rays used in the calibration).

The peaks are fitted using the function described in section 4.1.1. Once the number of events is obtained for each peak and each detector, the efficiency corresponding to each peak, as well as the associated error, was extracted with the formula:

$$\epsilon = \frac{N}{A_s \times T_{acq} \times I_g} \tag{4.5}$$

where ϵ is the absolute efficiency (the product of the intrinsic and geometric efficiencies), N is the number of events in the peak, A_s is the activity of the source in becquerel at the time of the measurement, T_{acq} is the duration of the acquisition in seconds and I_g is the literature intensity of the peak (number of emitted γ-rays for 100 decays).

Once the efficiencies are extracted for each peak, a fit was done to obtain the efficiency as a function of the energy. The fit function used was the "radware" one [76]:

$$\epsilon = K \times exp(((A + Bx + Cx^2)^{-G} + (D + Ey + Fy^2)^{-G})^{-\frac{1}{G}}) \tag{4.6}$$

where ϵ is the efficiency at a given energy, K is a constant factor fixed to have the correct order of magnitude (here K was fixed to $\frac{1}{100000}$), A, B, C, D, E, F, G are the parameters of the fit, $x = log(\frac{E}{E_1})$ with $E_1 = 100\,keV$ and $y = log(\frac{E}{E_2})$ with $E_2 = 1\,MeV$. The values E_1 and E_2 are fixed following the recommendations from reference [76]. In practice C is fixed to 0 and for one detector (BEGe4) it was necessary to fix G. G was fixed to 30. The fit results and residue are presented in figure 4.4.

The detection efficiencies are significantly higher for BEGe2 and BEGe3 as they are the closest ones for the implantation foil (they are put in sockets to be as close as possible). BEGe4 is slightly further away from the implantation foil than BEGe1, however it has a larger surface area and it is thicker, hence a higher efficiency at high energy for BEGe4. However, at low energy, the γ-rays are

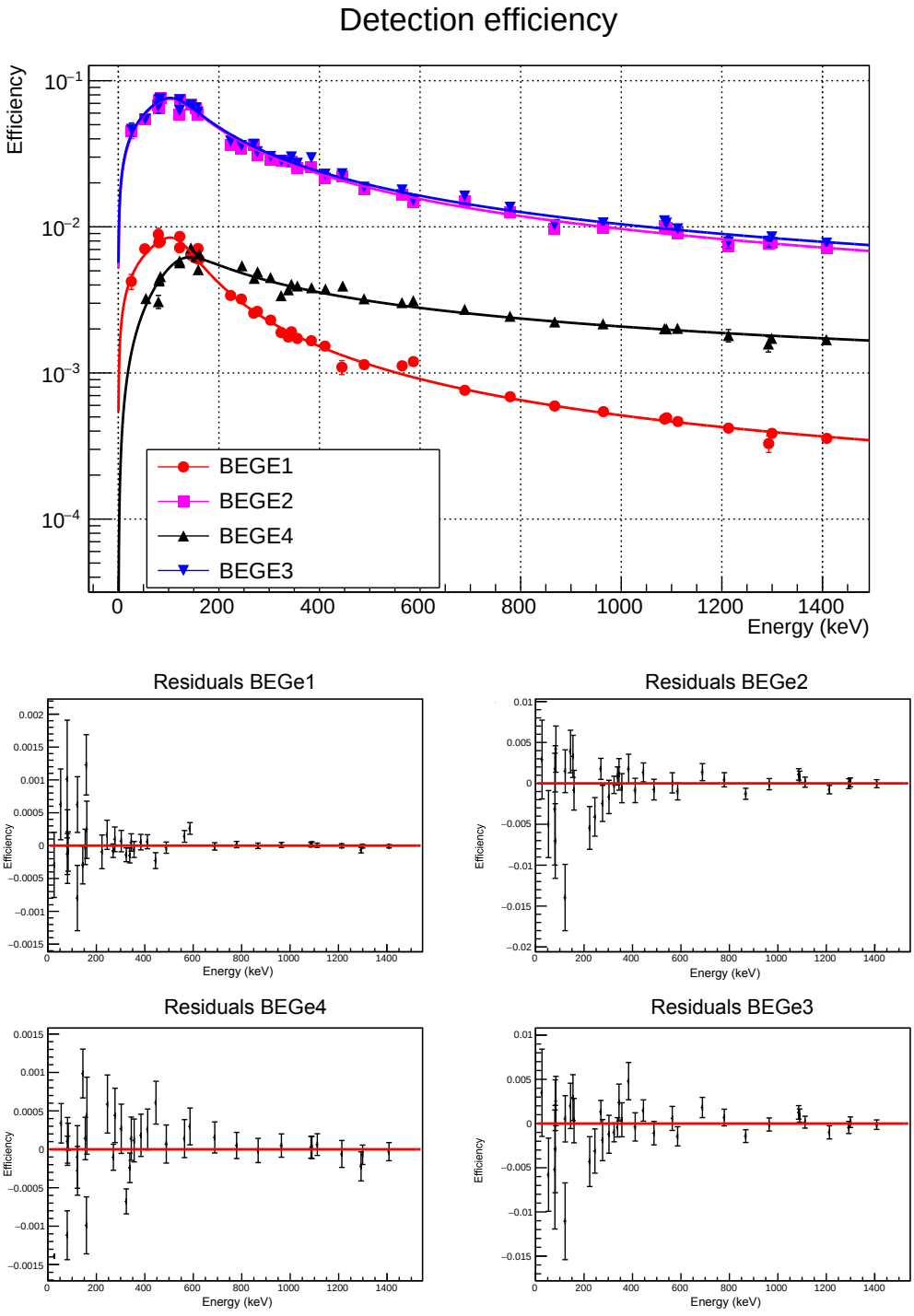

Figure 4.4: Gamma-ray detection efficiency calibration. BEGe 1 and 2 are the detectors placed on the sides. BEGe 3 and 4 are the ones placed above and below the setup.
Top: Gamma detection efficiency as a function of the energy for each detector and the associated fit. For most points the error bars are not shown as they are to small.
Bottom: Fit residuals.

Source	E_γ (keV)	I_γ (%)
^{152}Eu	121.7817 (3)	28.41 (13)
	244.6974 (8)	7.55 (4)
	344.2785 (12)	26.59 (12)
	411.1165 (12)	2.238 (1)
	488.6792 (2)	0.4139 (24)
	563.990 (7)	0.457 (13)
	586.265 (3)	0.462 (4)
	688.670 (5)	0.841 (6)
	778.9045 (24)	12.97 (6)
	867.380 (3)	4.243 (23)
	964.079 (18)	14.5 (6)
	1085.837 (10)	10.13 (6)
	1089.737 (5)	1.73 (1)
	1112.076 (3)	13.41 (6)
	1212.948 (11)	1.416 (9)
	1292.778 (19)	0.104 (3)
	1299.142 (8)	1.633 (9)
	1408.013 (3)	20.85 (8)
^{133}Ba	53.1622 (18)	2.14 (6)
	79.6142 (19)	2.63 (19)
	80.9979 (11)	33.31 (3)
	160.6121 (16)	0.638 (6)
	223.2368 (13)	0.45 (5)
	276.3989 (12)	7.13 (6)
	302.8508 (5)	18.31 (11)
	356.0129 (7)	62.05 (19)
	383.8485 (12)	8.94 (6)
^{241}Am	26.3446 (2)	2.31 (8)
^{223}Ra	81.069 (1)	14.86 (23)
	83.787 (1)	24.5 (4)
	122.319 (10)	1.238 (19)
	144.27 (2)	3.36 (8)
	154.208 (10)	5.84 (13)
	158.635 (10)	0.713 (16)
	269.463 (10)	14.23 (32)
	323.871 (10)	4.06 (8)
	338.282 (10)	2.85 (6)
	445.033 (12)	1.28 (4)

Table 4.3: γ-rays used for the BEGe detection efficiency calibration. Data taken from reference [78, 79, 80, 81]

partially stopped by the aluminium chamber for BEGe4, whereas they can pass through the kapton foil for BEGe1, hence the higher efficiency for BEGe1 at lower energy.

4.2.2 . α-efficiency calibration

The α-particle detection efficiency was obtained with the α-recoil source. The needle was placed in the chamber with the tip at the position of the centre of the implantation foil. The efficiencies were extracted by fitting the peaks from the ^{223}Ra α-decay with the deformed gaussian presented in section 4.1.2 and computing the efficiency with the formula:

$$\epsilon = \frac{N}{A_s \times T_{acq} \times I_\alpha} \tag{4.7}$$

where ϵ is the absolute efficiency (the product of the intrinsic and geometric efficiencies), N is the number of events in the peak, A_s is the activity of the source in becquerel at the time of the measurement, T_{acq} is the duration of the acquisition in seconds and I_α is the intensity of the peak taken from the literature.

Only the α-decay of ^{223}Ra was used and not the one of its daughter nuclei. Indeed, as with the implantation foil, the recoil energy is large enough to eject the daughter nuclei from the tip of the needle ∼50 % of the time, leading to an unknown distribution of the daughter nuclei inside the chamber. Thus the detection efficiency could only be extracted at a given energy (5.7 MeV). The assumption was made that the α-particle detection efficiency is independent from the α-particle energy, which is expected to be true for the typical energy range of α-decay that we studied (between 5 and 10 MeV).

One of the detectors (QuadSi-1) was disabled during the run performed with the α-source. In-beam data were used to compute its efficiency relative to the other detector, inducing larger uncertainties for this detector.

In addition, one of the pads of QuadSi-2 (QuadSi-2-1) had its wire bonding broken during the whole experiment and thus could not be used.

It is expected that the detection efficiency for α-particles is almost purely geometric since the detectors intrinsic detection efficiency is expected to be close to 100%. Thus the measured efficiencies were compared with simulations made with NPTool [82] (based on GEANT4 [83]) giving an estimate of the geometrical efficiencies (see table 4.4), as well as actual geometric computations of the solid angle covered by the detectors.

Several discrepancies between measured and calculated/simulated efficiencies can be observed. The main discrepancy appear for the Si(Li) detector. Indeed, there is almost a factor three between the measured detection efficiency and the calculated/simulated ones. This discrepancy is also seen in the α-particles counting rate in the detectors. Indeed, the Si(Li) is expected to have a higher efficiency than any single pad of a QuadSi. In practice it has a lower counting rate in the α-particles energy ranges. After some checks it was found that the surface of the Si(Li) was damaged and that a large scratch was visible. The lower than expected efficiency is thus understood as a consequence of those damages and it was assumed that only part of the detector was working, the actual active area being lower than the initial one (roughly 1/3).

For all the other detectors, the measured efficiency is slightly higher than expected from simulations and calculations. This most likely comes from the uncertainties on the source and detector positions, as well as the fact that the shape of the beam is not known and thus the simulations are made with a point-like source. When simulations are performed with a source with a reasonable (few mm) spatial

Detector	Measured (%)	Simulated (%)	Calculated (%)
QuadSi-2-2	4.18 (38)	∼3.8	∼3.8
QuadSi-2-3	3.60 (27)	∼3.9	∼3.8
QuadSi-2-4	4.52 (66)	∼3.8	∼3.8
QuadSi-1-1	4.00 (22)	∼3.2	∼3.3
QuadSi-1-2	3.72 (20)	∼3.3	∼3.3
QuadSi-1-3	3.39 (19)	∼3.3	∼3.3
QuadSi-1-4	3.51 (29)	∼3.2	∼3.3
Si(Li)	1.85 (13)	∼4.9	∼4.9
CircSi	1.97 (25)	∼1.9	∼2.0
Total	30.7 (9)	∼31.3	∼31.5

Table 4.4: α-particles detection efficiencies for each silicon detector. The simulated and geometrically calculated efficiencies are also reported, see text for details.

extent, the change in efficiency is typically lower (∼ 0.1 %) than the experimental uncertainties (∼ 0.2 %). The discrepancy is thus considered as acceptable and the measured efficiencies are used.

4.2.3 . Electron efficiency calibration

The electron detection efficiency could not be computed using the raw electron spectra. It was instead computed through two different methods using α-electron and α-γ coincidences. Let us consider a given transition between an initial state i and a final state f and write N the number of transitions between those states. The transitions can occur either through the emission of a γ-ray or through the emission of a conversion electron. We have:

$$N = N_\gamma + N_e \tag{4.8}$$

with N_γ (N_e) the number of γ-rays (conversion electrons) emitted for this transition. In addition, one can define the total conversion coefficient for the transition:

$$\alpha_e = \frac{N_e}{N_\gamma} \tag{4.9}$$

One can thus write equation 4.8 as:

$$N = N_e(\frac{1+\alpha_e}{\alpha_e}) \tag{4.10}$$

The number of electrons emitted from a given atomic shell S (and thus the number of electrons emitted at a given energy) relates to the total number of emitted electrons through:

$$N_e(S) = N_e\frac{\alpha_e(S)}{\alpha_e} \tag{4.11}$$

with $\alpha_e(S)$ the conversion coefficient for this specific shell. This leads to:

$$N_e(S) = \frac{N\alpha_e(S)}{1+\alpha_e} \tag{4.12}$$

In addition, considering N_α α-decays towards this initial state, one can write:

$$N = IN_\alpha \tag{4.13}$$

with I the probability that the de-excitation occurs through the studied transition. I can be computed from the knowledge of the relative γ-ray intensities $I_{\gamma,k}$ and their associated conversion coefficients $\alpha_{e,k}$. Thus one can relate the number of emitted electrons from a given state at a given energy to the number of emitted α-particles towards this state through:

$$N_e(S) = \frac{IN_\alpha \alpha_e(S)}{1+\alpha_e} \tag{4.14}$$

or through:

$$N_e(S) = \frac{I\hat{N}_\alpha \alpha_e(S)}{\epsilon_\alpha(1+\alpha_e)} \tag{4.15}$$

with $\hat{N}_\alpha$ the number of detected α-particles and ϵ_α the α-particles detection efficiency. Finally, one can write:

$$\epsilon_e = \frac{\hat{N}_e(S)}{N_e(S)} = \frac{\hat{N_e}(S)\epsilon_\alpha(1+\alpha_e)}{I\hat{N}_\alpha \alpha_e(S)} \tag{4.16}$$

with $\hat{N_e}(S)$ the number of detected electrons for the transition and ϵ_e the electron detection efficiency. In practice one can access the number of electrons detected in coincidence with an α-particle $\hat{N_{e,\alpha}}(S) = \epsilon_\alpha \hat{N}_e(S)$ and thus one can measure the electron detection efficiency independently from the α-particle detection efficiency with:

$$\epsilon_e = \frac{\hat{N_{e,\alpha}}(S)(1+\alpha_e)}{I\hat{N}_\alpha \alpha_e(S)} \tag{4.17}$$

The second method is based on the comparison between the number of detected electrons and the number of detected γ-rays for a given transition. One can write:

$$\epsilon_e = \frac{\hat{N_e}(S)}{N_e(S)} = \frac{\hat{N_e}(S)}{\alpha_e(S)N_\gamma} = \frac{\hat{N_e}(S)\epsilon_\gamma}{\alpha_e(S)\hat{N}_\gamma} \tag{4.18}$$

with ϵ_e the electron detection efficiency, $N_e(S)$ the number of conversion electrons emitted for a given shell S, $\hat{N_e}(S)$ the number of electrons detected, $\alpha_e(S)$ the conversion coefficient for this transition and the shell S, N_γ the number of γ-rays emitted for this transition, $\hat{N}_\gamma$ the number of detected γ-rays and ϵ_γ the γ-rays detection efficiency at this energy. This method is less dependent on the previous knowledge of the transition as only the conversion coefficient is needed and not the γ-ray intensities, but depends on the γ-ray detection efficiency.

The two methods were applied for 4 known K-electrons transitions from the α-decay of ^{225}Th. Table 4.5 gives a summary of the electron energies and the measured efficiencies ϵ_e with both methods.

In the simulations the electron detection efficiency is observed to be independent from the electron energy in the relevant energy range (40-300 keV). Indeed, the detection efficiency is the geometrical efficiency minus the electron backscattering coefficient and, if the backscattering coefficient is assumed to be independent of the electron energy below 300 keV, so is the detection efficiency. In reality the backscattering rate is not independent of the electron energy, however, in the considered energy range

Electron energy (keV)	$\alpha_e(K)$	ϵ_e (%)	
		Method 1	Method 2
142.08	0.987 (14)	0.93 (17)	1.02 (14)
201.98	0.541 (8)	1.13 (30)	1.42 (30)
217.48	0.473 (7)	1.07 (16)	1.11 (10)
255.08	0.350 (5)	1.06 (40)	1.23 (41)

Table 4.5: Measured electron detection efficiencies for four different transitions in ^{225}Th. Method 1 uses the number of α-particles detected and method 2 uses the number of γ-rays detected.

(40-300 keV) it is almost the case. For example, for electrons at a normal incidence, the backscattering coefficient on aluminium goes from ∼13 % at 40 keV to ∼12 % at 300 keV [84]. Thus a weighted average of all the measured efficiencies is used and yield a detection efficiency $\epsilon_e = 1.08 \pm 0.06$ %. This efficiency is lower than the α-particles detection efficiency in the Si(Li) ($\epsilon_\alpha = 1.85 \pm 0.13$ %). This is due to the backscattering of electrons on the detector surface and corresponds to a probability of backscattering $p_{backscattering} = 42 \pm 10$ % similar to what can be expected in a close-up geometry (roughly 40 % to 50 % [85]) and to what is obtained in GEANT4 simulations of the setup (35 %).

4.2.4 . Validity of the efficiency calibrations

As explained in section 4.1.2, the recoil energy during the α-decay is enough to extract daughter nuclei from the implantation foil with a ∼50 % probability. This leads to an unknown distribution of the daughter nuclei inside the chamber. The detection efficiencies are obtained in the case of nuclei directly implanted in the foil and thus cannot be applied to the daughter nuclei.

It might have been technically possible to extract efficiencies for the daughter nuclei by comparing the number of α-particles detected for a directly implanted nucleus and for its daughter nucleus. However this would have added a considerable uncertainty to the efficiencies. Since the main nuclei of interest are nuclei directly implanted in the foil, we made the choice to work with efficiencies extracted only for directly implanted nuclei. Thus, for the other nuclei, the intensities are not computed in this work.

4.3 . Analysis methodology

This section will present the general methodology for the data analysis, with the concrete example of the mass A=225 data analysis. The results for the masses A=225 and A=221 will be detailed later.

4.3.1 . Alpha-energy spectrum fit procedure

To extract peaks energies and integrals, a fit of the whole α-spectrum is performed using a sum of the skewed gaussian function presented in section 4.1.2. No background was used in the fit as the background purely arises from the low energy tail of the α-peaks and the skewed gaussian is able to take those tails into account. Initially one could expect the shape of all peaks to be similar and thus try to force the fit to use the same shape parameters for all peaks. However, as explained in section 4.2.4, the daughter nuclei do not have the same distribution in the chamber as their parent nuclei. As a consequence, the α-particles emitted by the daughter nuclei will, in average, not pass

through the same type and thicknesses of materials as the α-particles emitted by their parent nuclei. As deformation of the peaks with respect to a gaussian peak is understood as a consequence of energy losses in the materials the α-particle pass through, it is expected that the shape of the peaks will depend on the distribution of the nuclei inside the chamber. Thus, the spectrum was fitted using the same shape parameters for a given "generation" of nuclei, but different parameters from one generation to the other. For the α-decay chain of ^{225}Pa, a total of four generations of α-decay coexist ($^{225}\mathrm{Pa} \rightarrow {}^{221}\mathrm{Ac}$, $^{221}\mathrm{Ac} \rightarrow {}^{217}\mathrm{Fr}$, $^{217}\mathrm{Fr} \rightarrow {}^{213}\mathrm{At}$, $^{213}\mathrm{At} \rightarrow {}^{209}\mathrm{Bi}$) and thus four peak shapes were needed.

In practice a fifth one was added to fit properly the peaks coming from the ^{221}Ac α-decay. Indeed, the fit function used worked perfectly fine at relatively low statistics, but shows its limits at higher statistics. The higher the statistic, the more complex fit functions are required, often using a sum of several deformed gaussians (from 3 deformed gaussians for "simple" models up to 14 in reference [86] to fit peaks with millions of events per bin). In our case, for most of the peaks, the statistic is not high enough for the deviation to be relevant, however, for the α-decay of ^{221}Ac, the deviation starts to be significant for one of the peaks and as there are several other peaks in the same generation, the model does not have enough freedom to adapt. Rather than using a more complex model for this peak only, it was chosen to use a separate shape of parameters for all α-peaks arising from this specific decay. This led to the 5 sets of shape parameters presented in table 4.6.

Generation	α	p	σ(keV)
0	0.063 (3)	0.639 (6)	10.7 (1)
1	0.80 (10)	0.159 (20)	14.7 (6)
2	0.072 (4)	0.680 (6)	11.9 (1)
3	0.148 (4)	0.543 (7)	12.3 (2)
^{221}Ac	0.185 (13)	0.717 (9)	10.7 (2)

Table 4.6: Shape parameters used to fit the whole α-spectrum. Generation 0 corresponds to the α-decay of nuclei directly implanted in the foil. The parameters are the ones defined in section 4.1.2. See text for more details.

A comparison of the shapes of the first two generations is shown in figure 4.5 and the resulting fit of the whole α-spectrum as well as the corresponding residuals are shown in figure 4.6.

A reduced χ^2 of 1.69 is obtained when fitting the whole α-spectrum with a total of 34 α-peaks from 6.15 MeV to 9.1 MeV, thus fitting 1475 points with $2 \times 34 + 3 \times 5 = 83$ free parameters (2 for each of the 34 peak, plus 3 for each of the 5 sets of shape parameters). The reduced χ^2 deviation from unity is understood, as explained above, as reaching the limits of the fit function used in the case of the high statistic peaks. This can be seen in the residuals of the fit in figure 4.6. The 1σ (2σ) deviation is plotted as a yellow (green) area. Thus, if the model was perfectly adapted, one would expect to have ∼95 % of the residuals within the green area, and the fact that it is not the case is an indication that we are reaching the limits of the model. The highest residuals are reached in the tails of the highest peaks (7.65 MeV, 8.3 MeV and 9.05 MeV peaks, corresponding respectively to ^{221}Ac, ^{217}Fr and ^{213}At decays), where the limits of the peak's tail model can clearly be seen as there are no or almost no other peaks to help compensate. However it was considered that the impact of this deviation remained negligible with respect to other sources of errors, therefore this fit was kept.

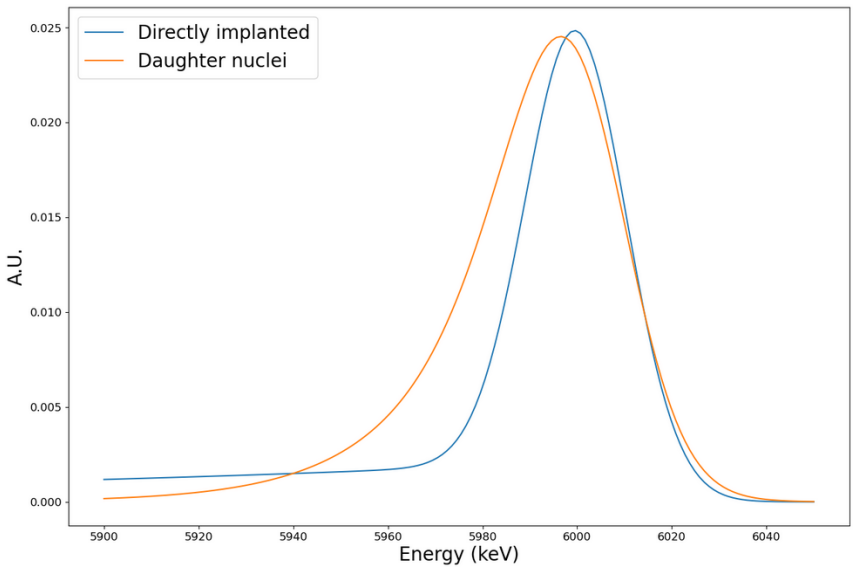

Figure 4.5: Comparison of peaks shape for a directly implanted nucleus and for its daughter nucleus. Both have a centroid fixed at 6000 keV and both have an integral of 1.

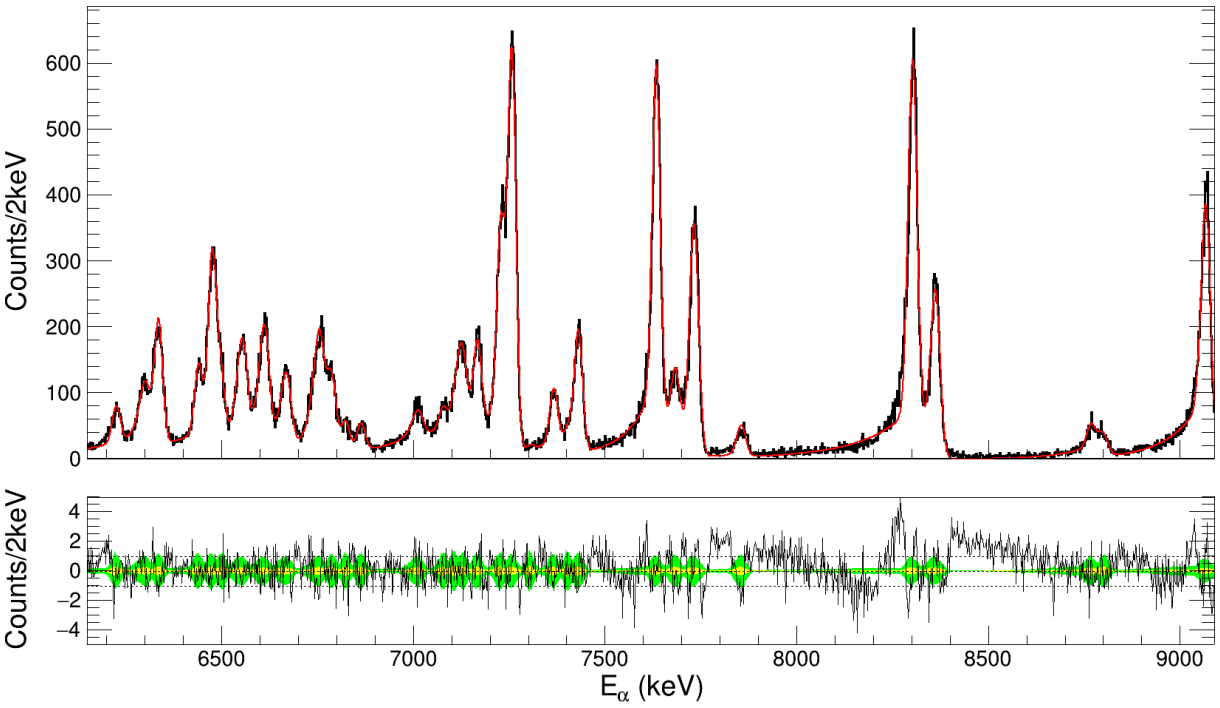

Figure 4.6: Top: Alpha-energy scpectrum for mass A=225 and the associated fit. Bottom: Residual of the above fit. The yellow (green) area is the 1σ (2σ) deviation of the fit, see text for details.

4.3.2 . Energy levels identification

The identification of α-particles emitted by a given nucleus is performed through α-γ coincidences, measuring the sum $Q_\alpha + E_\gamma$ and comparing it with the ground-state to ground-state energy Q_α(g.s.-to-g.s.) (within ± 3 keV). E_γ is the measured γ-ray energy and Q_α values are calculated using the α-particle energy E_α and the equation $Q_\alpha = \frac{m_d + m_\alpha}{m_d} \times E_\alpha$ with m_α the mass of the α-particle and m_d the mass of the daughter nucleus.

In practice the α-γ coincidence 2D energy spectrum is plotted, the $Q_\alpha + E_\gamma = Q_\alpha$(g.s.-to-g.s.) line is added on it and the peaks falling on the line are denoted as shown in figure 4.7. This enables the identification of all γ-rays feeding directly the ground-state, and of the energy levels.

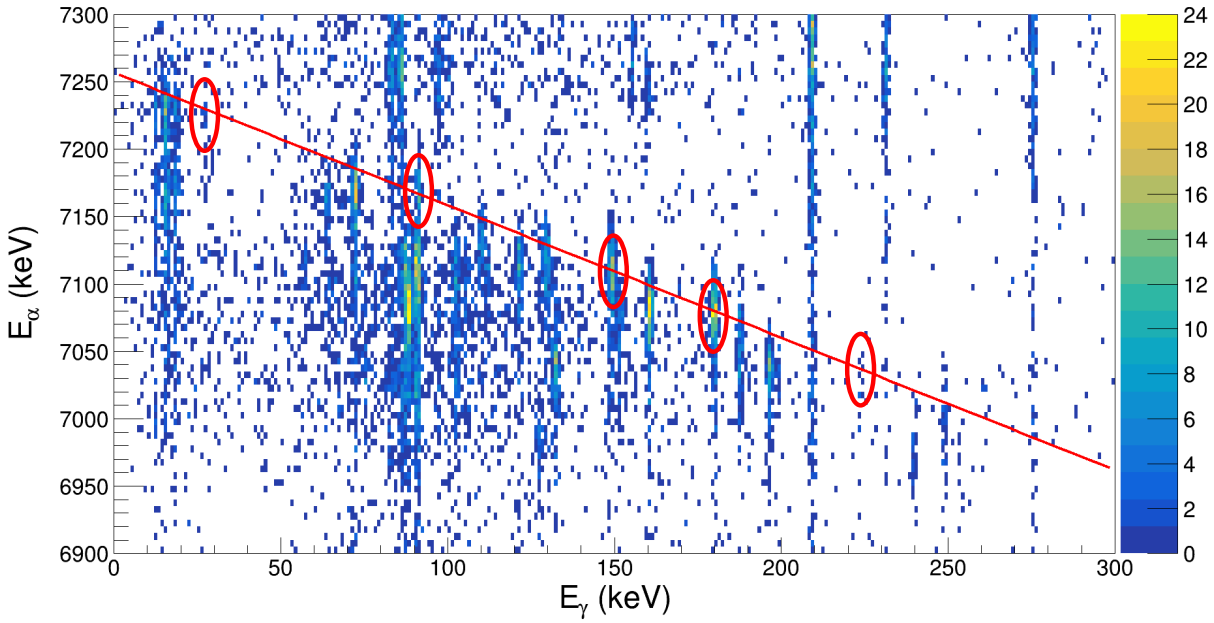

Figure 4.7: α-γ coincidence 2D energy spectrum. The red line is the $Q_\alpha + E_\gamma = Q_\alpha$(g.s.-to-g.s.) line for ^{225}Pa. The peaks highlighted with red circles are the α-γ coincidence peaks falling on this line. The bins are 1 keV large on the E_γ axis and 5 keV large on the E_α axis.

The α-γ coincidence peaks highlighted in figure 4.7 extend above the red line, but this is purely an energy resolution effect. Indeed, the energy resolution of the sum of all detectors is ∼40 keV (FWHM). This effect can be seen in figure 4.8

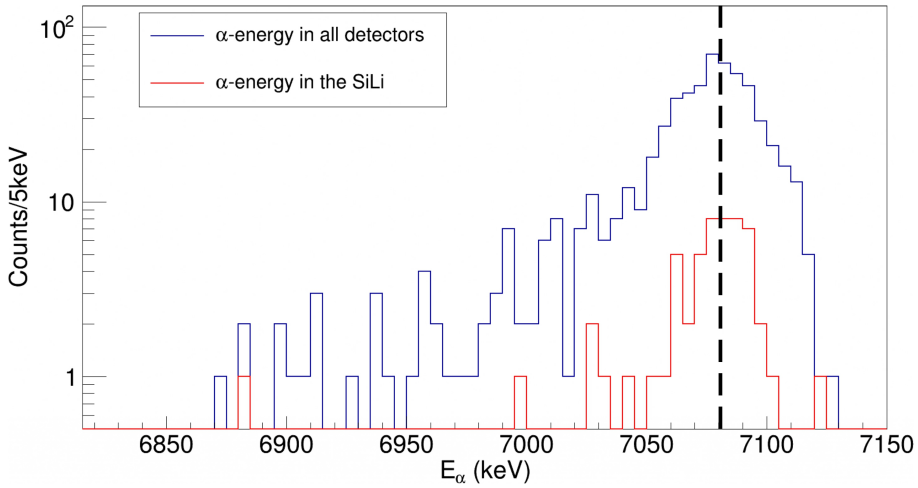

Figure 4.8: α-energy spectrum for α-particles detected in any Si detector (blue) or exclusively in the Si(Li) (red) in coincidence with a γ-ray with 179 keV< E_γ <181 keV.

4.3.3 . γ-transitions identification

Once the identification of energy levels is done, the γ-transitions from an exited state towards another exited state are identified by checking the energy of the α-particles detected in coincidences to ensure the initial level, as well as the fact that the γ-ray energy matches the energy difference between exited states.

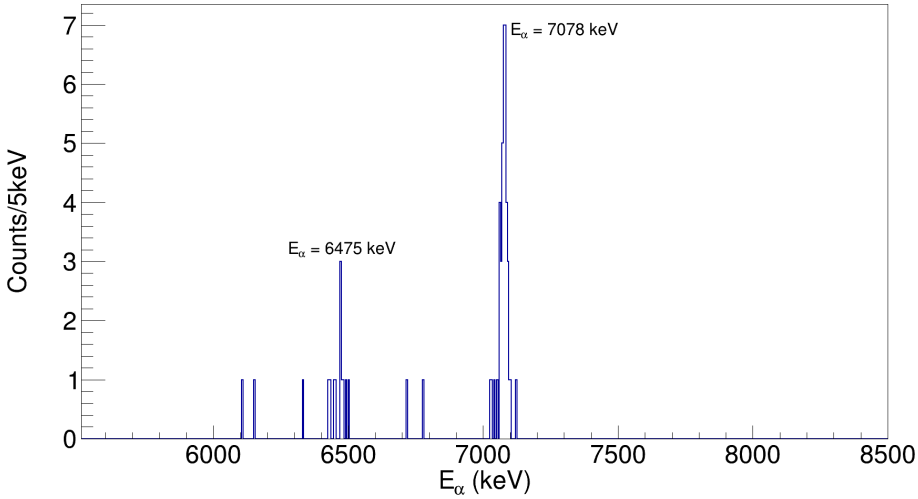

Figure 4.9: Projection of figure 4.7 on the y-axis (E_α) for 178 keV< E_γ <182 keV. The measured centroid of the peaks are indicated. The $E_\alpha = 6475$ keV peak corresponds to the α-decay of ^{225}Th (emitting a γ-ray at 177.2 keV) and the $E_\alpha = 7078$ keV peak corresponds to the α-decay of ^{225}Pa (see figure 5.6 for the decay scheme of ^{225}Pa).

This process corresponds to projections of the figure 4.7 on the E_α and E_γ axes. First a cut is done on the E_γ energy of one peak corresponding to a transition to the ground state to make a projection on the E_α axis. This projection is shown in figure 4.9 and the α-peak corresponding can clearly be identified. This peak is fitted to extract its energy as cleanly as possible and this is used to

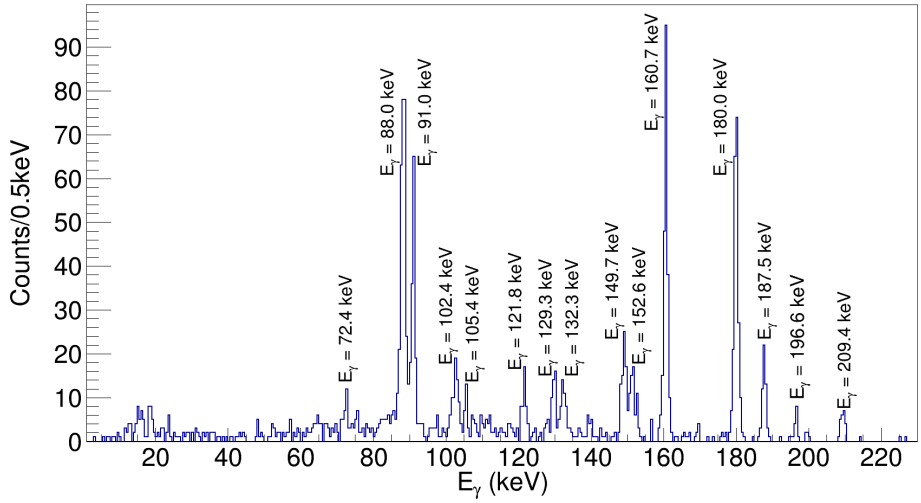

Figure 4.10: Projection of figure 4.7 on the x-axis (E_γ) for 7050 keV$< E_\alpha <$7100 keV. The measured centroid of the peaks are indicated. Most peaks comes from the de-exitation of ^{221}Ac, with a few also coming from the de-excitation of ^{217}Fr. The $E_\gamma = 88.0$ keV and $E_\gamma = 91.0$ keV peaks are both a mixture of a γ-ray coming from the de-excitation of ^{221}Ac and a X-ray coming from the de-excitation of the atomic electrons of ^{221}Ac (see Appendix A for a table of X-rays).

make a cut on the E_α energy to obtain the γ-rays in coincidence with this α-decay (see figure 4.10). For each peak in this projected spectrum a gate is set again on the E_γ energy, without any condition on the E_α energy, to verify that the α-decay in coincidence is the proper one and thus to identify without ambiguity the initial level. The γ-ray is then placed in the level scheme if its energy matches the energy difference between the initial level and another level.

4.3.4 . Conversion coefficients and multipolarities

Once transitions are identified, the BrIcc (Band-Raman Internal Conversion Coefficients) code [22] is used to compute expected conversion electron energies and conversion coefficients for each transition. The conversion coefficients obtained for each multipolarity are then compared with the measured ones. As the γ-ray and conversion electron peaks are not seen without α-γ and α-electron coincidences, the conversion coefficients are extracted by selecting a given α-energy gate and looking at the number of γ-rays ($\hat{N}_\gamma$) and conversion electrons ($\hat{N}_e$) detected at the proper energy and in coincidence with an α-particle within the energy gate. An example of conversion electrons energy spectrum is given in figure 4.11. This spectrum is obtained by selecting conversion electrons in coincidence with an α-particle with 7140 keV$< E_\alpha <$7200 keV, selecting α-particle feeding the 91.5 keV state of ^{221}Ac (see figure 5.6 in section 5.1.1). The expected L, M and N conversion electrons from the three transitions possible for this state are denoted on the spectrum. As the electrons are detected only in the Si(Li), it is not possible to make α-electron coincidences with the α-particle detected in the Si(Li). Thus, in order to be independent from the α-particle detection efficiency, the α-particles measured in the Si(Li) are not considered. The conversion coefficient is thus computed with the formula:

$$\alpha_e = \frac{\hat{N}_e \times \epsilon_\gamma}{\hat{N}_\gamma \times \epsilon_e} \tag{4.19}$$

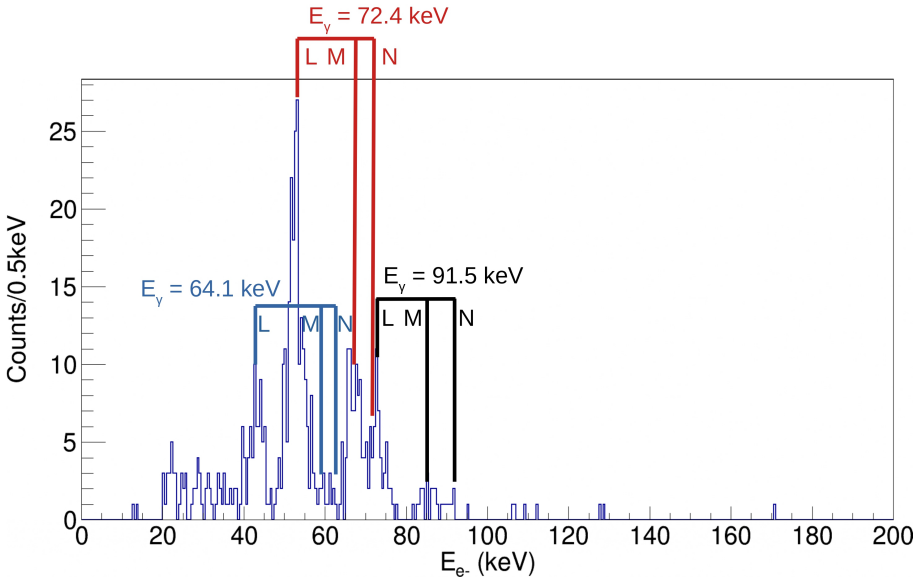

Figure 4.11: Electron energy spectrum measured in the Si(Li) in coincidence with an α-particle with 7140 keV$<E_\alpha<$7200 keV. The expected energies for the L, M and N shells electrons are indicated on the spectrum for the transitions at $E_\gamma = 91.5$ keV, $E_\gamma = 72.4$ keV and $E_\gamma = 64.1$ keV.

with ϵ_γ (resp. ϵ_e) the γ-rays (resp. electrons) detection efficiency.

Due to a very low electron detection efficiency ($\epsilon_e = 1.08 \pm 0.6$ %), in most cases no electrons, or very few electrons ($\hat{N_e} \leq 10$), are detected in coincidence at the expected energy. Figure 4.12 shows such an example for the 149.7 keV transition. In this spectrum, the conversion electrons are selected in coincidence with a α-particle with 7100 keV$<E_\alpha<$7140 keV, selecting the α-particles feeding the 149.7 keV state of ^{221}Ac (see figure 5.6 in section 5.1.1). The K, L and M conversion electrons for this transition are denoted on the spectrum, as well and the conversion electrons emitted from the 91.5 keV state. Indeed, there is a transition feeding the 91.5 keV state from the 149.7 keV state. The K shell electrons for the 149.7 keV transition are mixed with the L shell electrons for the 64.1 keV transition. For the L and M shell electrons for the 149.7 keV transition, only a few electrons are detected in the proper energy region (respectively 4 and 1).

In such cases, a upper limit is set on the number of emitted electrons and thus on the conversion coefficient with a confidence interval of 95 %. This higher limit is set as follows:

Given that N_e electrons were emitted and with a probability ϵ_e to detect an emitted electron, the probability to detect k electrons follows a binomial law:

$$P(X = k) = \binom{N_e}{k} {\epsilon_e}^k (1 - \epsilon_e)^{N_e - k} \tag{4.20}$$

thus the probability to detect 0 electrons given that N_e electrons were emitted is:

$$P(X = 0) = (1 - \epsilon_e)^{N_e} \tag{4.21}$$

and thus, the probability to detect at least 1 electron given that N_e electrons were emitted is:

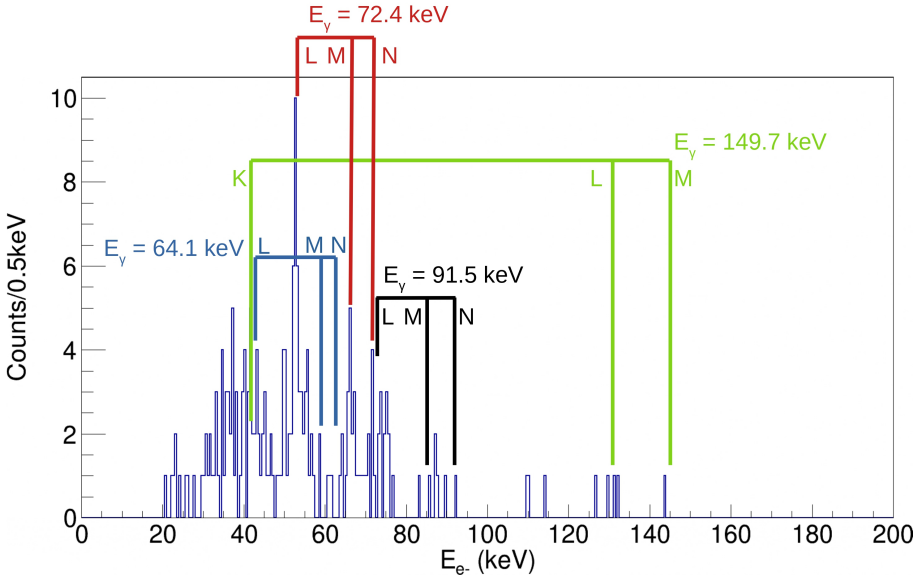

Figure 4.12: Electron energy spectrum measured in the Si(Li) in coincidence with an α-particle with 7100 keV< E_α <7140 keV. The expected energies for the L, M and N shells electrons are indicated on the spectrum for the transitions at $E_\gamma = 91.5$ keV, $E_\gamma = 72.4$ keV and $E_\gamma = 64.1$ keV, as well as for the $E_\gamma = 149.7$ keV transition. For this $E_\gamma = 149.7$ keV transition, the conversion electrons for the K shell, expected at $E_e = 43$ keV, are mixed with the conversion electrons from the $E_\gamma = 64.1$ keV L shell, expected at $E_e = 44$ keV. For the L (resp. M) shell electrons for the $E_\gamma = 149.7$ keV transition, 4 (resp 1) electrons are detected in a ±3 keV energy region, and thus only upper limits on the number of emitted electrons are extracted.

$$P(X > 0) = 1 - P(X = 0) = 1 - (1 - \epsilon_e)^{N_e} \tag{4.22}$$

We search N_{min} such as $P(X > 0) = P_{min}$ with P_{min} the confidence interval chosen, in our case $P_{min} = 95$ %. One can write :

$$P(X > 0) = P_{min} = 1 - (1 - \epsilon_e)^{N_{min}} \tag{4.23}$$

thus:

$$N_{min} = \frac{\ln(1 - P_{min})}{\ln(1 - \epsilon_e)} \tag{4.24}$$

For a $P_{min} = 95$ % confidence interval, and assuming a detection efficiency for the electrons $\epsilon_e = 1.08$ %, one have $N_{min} = 275$. Thus, when no electrons were detected at the expected energy, it was assumed that $N_e \leq N_{min}$ and thus:

$$\alpha_e \leq \frac{N_{min} \times \epsilon_\gamma}{\hat{N}_\gamma} \tag{4.25}$$

In the case of very low numbers of detected electrons ($\hat{N}_e \leq 10$), the same work can be done to

compute a upper limit on the number of emitted electrons, changing equation 4.22 to:

$$P(X > \hat{N}_e) = 1 - \sum_{i=0}^{\hat{N}_e} P(X = i) \tag{4.26}$$

Finding an analytical solution in the case $\hat{N}_e \leq 1$ is not trivial, however the problem can be easily solved numerically to obtain N_{min} in each case.

The higher limit extracted, combined with parity-based considerations, allows to define the multipolarity of the transition in almost all cases.

5 - Results and interpretation

In this chapter, the results obtained for masses $A = 225$ and $A = 221$ are presented, as well as the interpretation of ^{221}Ac as an octupole deformed nucleus.

5.1 . Results

5.1.1 . Mass $A = 225$

As shown in table 3.1, approximately 12 h of data acquisition was obtained for mass $A = 225$. The α energy spectrum is composed of several contributions. The two main contributions are ^{225}Th and ^{225}Pa, and their respective α-decay chains. In addition, there is a contribution from the α-decay chains of ^{226}Th and ^{226}Pa as both are partly passing through the mass selection. Finally the implantation foil has a remaining contamination of long lived ^{224}Ra ($T_{1/2} \sim 3.6$ d) coming from a previous run on mass A = 224. Figure 5.1 shows the α-energy spectrum and the attribution of each peak to a given decay chain.

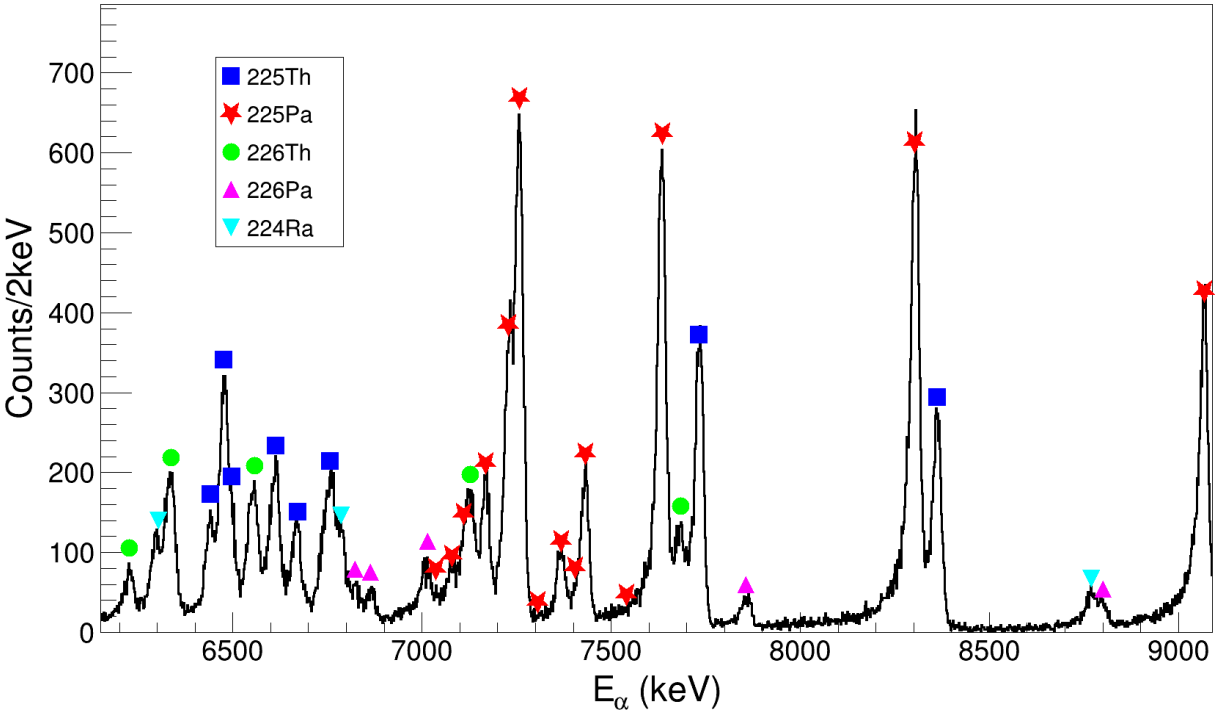

Figure 5.1: α energy spectrum. All identified peaks used for the fit are indicated with a symbol. Different colored symbols denote the different implanted nucleus, as well as their decay chains.

As detailed in section 4.3.1, a fit of the whole α-energy spectrum is performed using a sum of deformed gaussian functions (a zoom on the ^{225}Pa α-energy region is presented in figure 5.2). This enables a precise extraction of the peaks centroid and intensity, except for the 7037 keV α-decay. Indeed, this transition is at the limit of our detection capabilities and thus its intensity cannot be

determined directly from the α-energy spectrum. It was determined using α-γ coincidences enabling the precise selection of this α-decay. However it comes at the cost of a larger uncertainty as the detection efficiencies are used in the process.

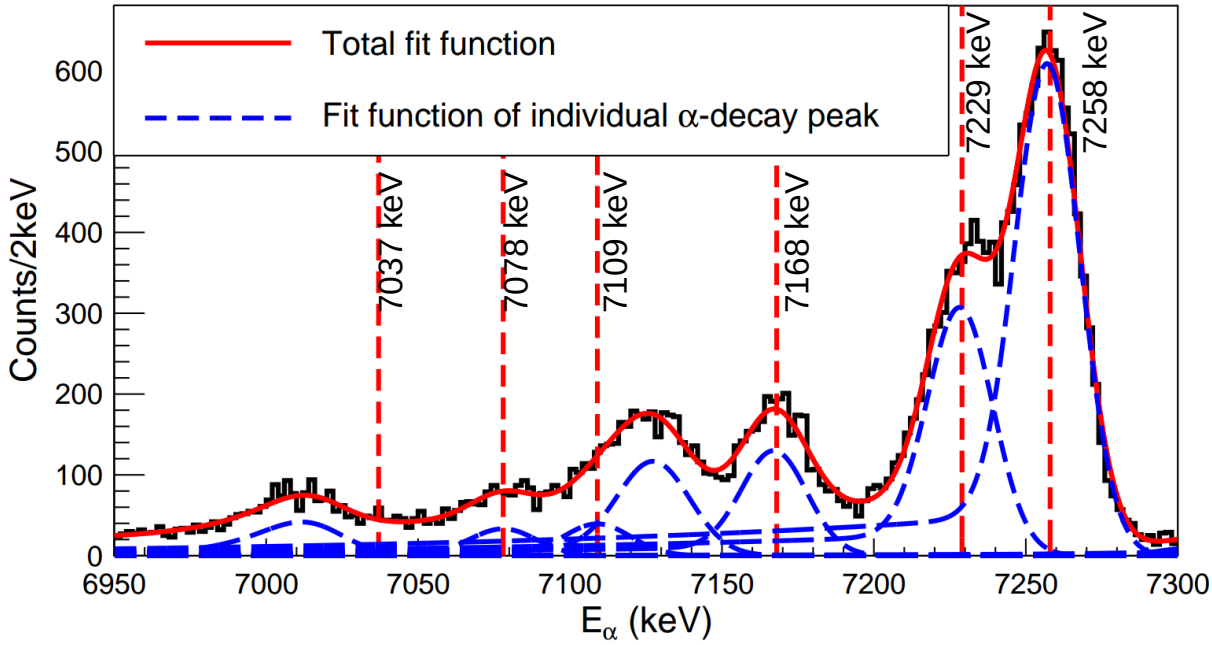

Figure 5.2: α energy spectrum (E_α) measured in the Si(Li) between 6.95 MeV and 7.3 MeV, corresponding to the α-decay energy region of ^{225}Pa. The total fit can be seen as a solid red line and each peak contribution can be seen as blue dashed lines. Vertical dashed lines indicates ^{225}Pa α-decay with the extracted E_α. The peak at 7037 keV is not seen in plot as the peak intensity is to low. The peak was found through α-γ coincidences. The two α-peaks that are not denoted with the vertical lines are contamination from ^{222}Ac (7008.6 keV, ^{226}Pa decay chain) and ^{218}Rn (7129.1 keV, ^{226}Th decay chain).

The α-γ coincidence 2D energy spectrum and its projection on the x-axis (E_γ) is shown figure 5.3. On this coincidence spectrum, three very clear peaks fall on the $Q_\alpha + E_\gamma = Q_\alpha$(g.s.-to-g.s.) line at $E_\gamma = 91.5$ keV, $E_\gamma = 149.7$ keV and $E_\gamma = 180.0$ keV. In addition, two other smaller peaks are seen on the line, one at $E_\gamma = 27.4$ keV and one at $E_\gamma = 223.7$ keV. The $Q_\alpha + E_\gamma$ for each peak are summarised in table 5.1. All $Q_\alpha + E_\gamma$ fall within 2 keV from each other and a weighted average of all measured values leads to a measured Q_α(g.s.-to-g.s.) $= 7388 \pm 1$ keV, thus improving the uncertainty compared to the previous value (Q_α(g.s.-to-g.s.) $= 7380 \pm 50$ keV [87]).

From there, the hindrance factors are extracted from the energies and intensities using Preston's spin-independent equations [19] (see section 2.1.1.2), with $r_0 = 1.5475$ fm interpolated from neighbouring even-even nuclei [21, 20], and $T_{1/2} = 1.95(10)$ s the half-life measured in reference [69].

All γ-transitions measured in coincidence with ^{225}Pa α-decay are reported in table 5.2. Several transitions ([$E_i = 91.5$ keV, $E_\gamma = 72.4$ keV], [$E_i = 149.7$ keV, $E_\gamma = 129.3$ keV], [$E_i = 180.0$ keV, $E_\gamma = 160.7$ keV]) are clearly seen in coincidence with α-particles feeding a known level, but do not match the energy difference with any other excited state. However, the three of them are consistent

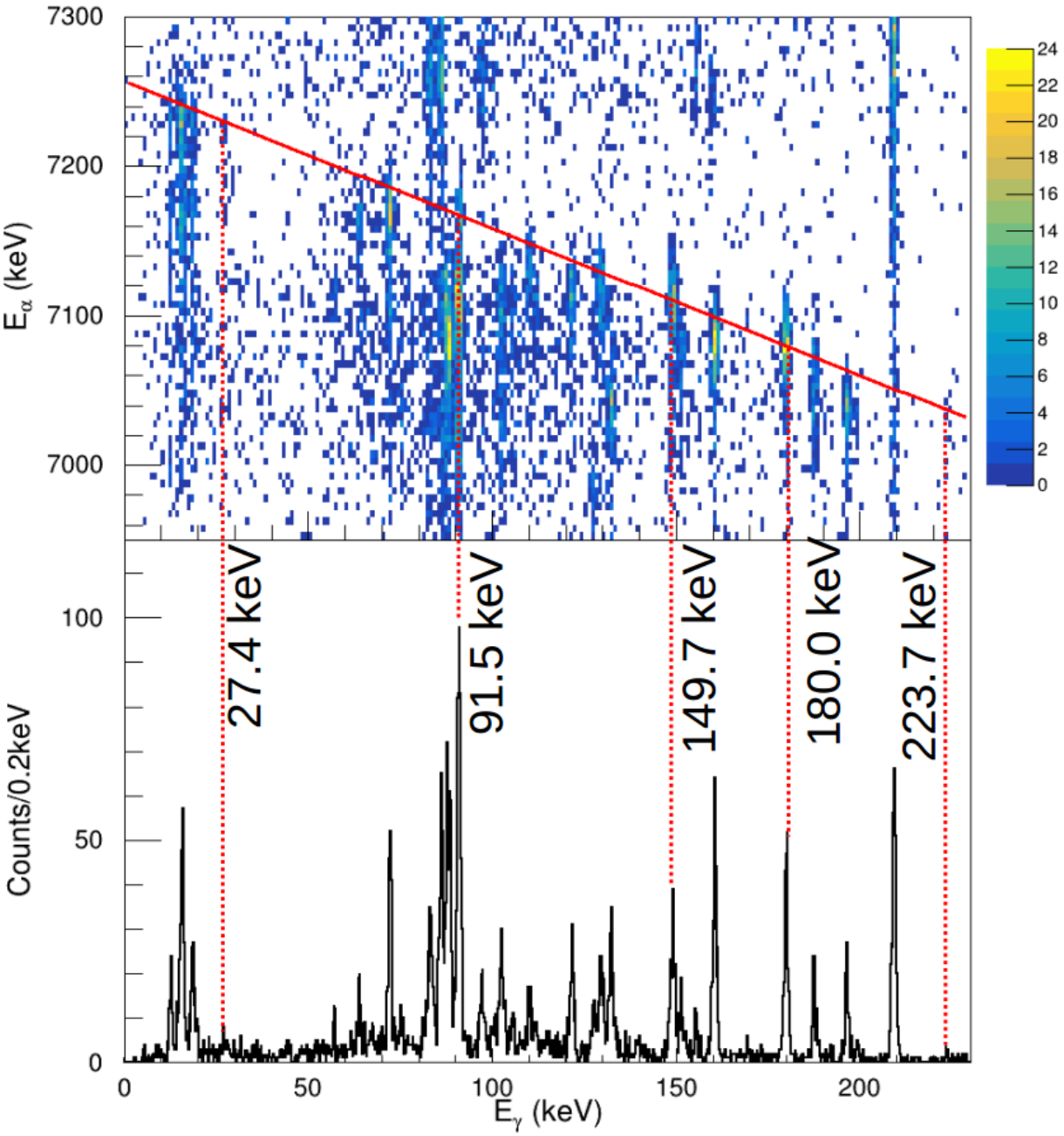

Figure 5.3: Top: α energy (E_α) vs γ energy (E_γ) for ^{225}Pa → ^{221}Ac. The solid red line denotes the $Q_\alpha + E_\gamma = Q_\alpha$(g.s.-to-g.s.) line where the coincidences with γ-rays feeding directly the ground state are expected.
Bottom: projection of the top view on the x-axis (E_γ). The dashed red lines denotes α-γ coincidences for which $Q_\alpha + E_\gamma$ is close to Q_α(g.s.-to-g.s.) and link them to the corresponding peak on the γ-energy spectrum. The associated γ-ray energy is indicated. Some peaks fall close to the line (e.g. $E_\gamma = 72.4$ keV, $E_\gamma = 160.7$ keV or $E_\gamma = 209.4$ keV), but do not correspond to transitions towards the ground state. For $E_\gamma = 72.4$ keV and $E_\gamma = 160.7$ keV the $Q_\alpha + E_\gamma$ do not match the Q_α(g.s.-to-g.s.) and those are transitions towards excited states. For the $E_\gamma = 209.4$ keV peak, it comes from the α-decay of ^{221}Ac.

E_α (keV)	E_γ (keV)	Q_α (keV)	$Q_\alpha + E_\gamma$ (keV)
7258 (2)	0	7389 (2)	7389 (2)
7229 (2)	27.4 (1)	7360 (2)	7387 (2)
7168 (2)	91.5 (2)	7297 (2)	7389 (2)
7109 (6)	149.7 (3)	7238 (6)	7388 (6)
7078 (2)	180.0 (1)	7207 (2)	7387 (2)
7037 (3)	223.7 (5)	7165 (3)	7389 (3)

Table 5.1: Summary of E_α, E_γ, Q_α and $Q_\alpha + E_\gamma$ for all α-decay peaks measured in this experiment for ^{225}Pa.

with the presence of a level around 19.5 keV. The γ-ray transition from this level to the ground state of ^{221}Ac is not clearly observed as it is mixed with X-rays close in energy, and no α-decay towards this level is observed (see Appendix A for a table of X-rays). Appendix B shows the α and γ energy spectra measured in coincidence with each transition α or γ attributed to the decay scheme of ^{225}Pa.

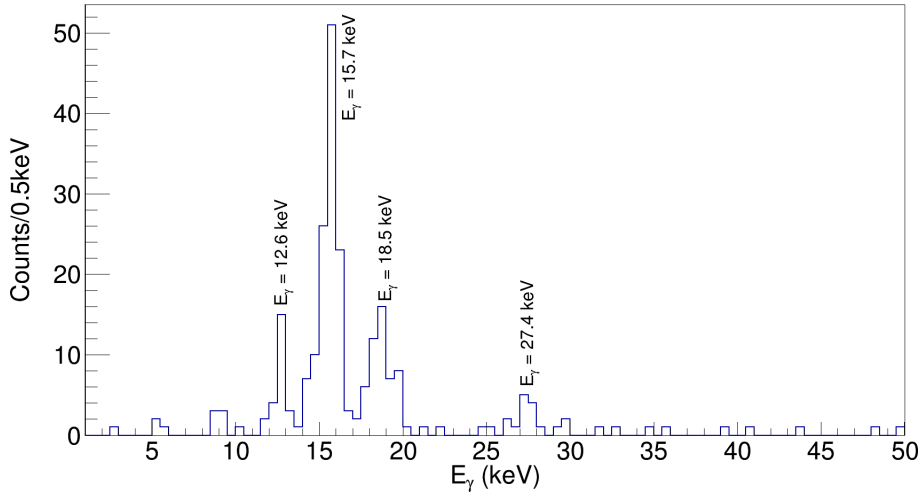

Figure 5.4: Gamma-ray energy spectrum in coincidence with an α-particle between 7185 and 7235 keV. The measured centroid of the peaks are indicated. The three lower energy peaks are X-rays (see Appendix A for a table of X-rays). A structure comes out of the background at 27.4 keV.

The transitions from the 27.4 keV and 223.7 keV levels to the ground state are very weak and thus do not appear clearly on figure 5.3. However, when looking at the γ-energy spectrum properly cleaned using α-γ coincidences, a structure comes out of the background in both cases (see figures 5.4 and 5.5). In addition several transitions are observed feeding the 27.4-keV level, as well as several transitions emitted from the 223.7 keV level in coincidence with the α-decay towards this level.

Spin-parity assignments are made on the basis of the multipolarities defined using the conversion coefficients calculated as detailed in section 4.3.4. For each transition where a conversion coefficient could be extracted or where a higher limit could be set, the deduced multipolarities are presented in table 5.3. However, for some transitions it was not possible to extract any number for the conversion coefficients, neither a value, nor a upper limit. This is the case, for example, for the 57.1 keV transition

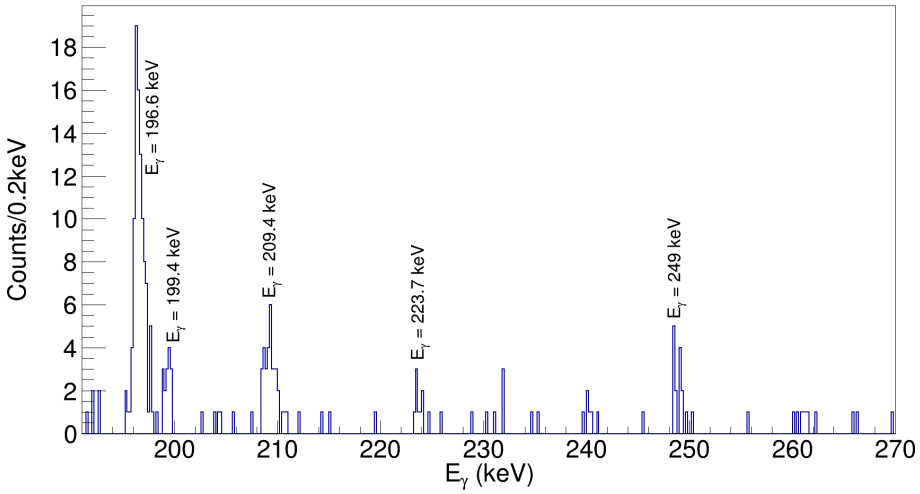

Figure 5.5: Gamma-ray energy spectrum in coincidence with an α-particle between 7000 and 7050 keV. The measured centroid of the peaks are indicated. A structure comes out of the background at 223.7 keV.

E_i (keV)	E_γ (keV)	I_γ	MP
223.7	223.7(5)	0.044(13)	?
	196.6(1)	0.34(5)	E1*
	132.3(3)	0.37(5)	E1
	75.4(2)	0.048(16)	M1*
180.0	180.0(1)	0.74(10)	E1
	160.7(1)	0.72(9)	E1
	152.6(2)	0.21(4)	E1*
	88.7(3)	0.43(6)	E1
149.7	149.7(3)	0.52(7)	E1*
	129.3(3)	0.34(5)	E1
	121.8(1)	0.31(4)	E1
	57.1(1)	0.066(23)	E1*
91.5	91.5(2)	0.43(10)	M1+E2 or E2
	72.4(1)	0.48(6)	M1+E2
	64.1(1)	0.148(25)	M1+E2 or M1
27.4	27.4(1)	0.032(16)	M1+E2 or M1

Table 5.2: Measured initial level energies E_i, energies E_γ and intensities I_γ (number of γ emitted for 100 α-decays) of the γ-rays and multipolarity assignments for ^{221}Ac. Multipolarities deduced using parity arguments are denoted with a star.

where the conversion electrons are emitted at similar energies (37-41 keV for the L shells electrons, 52-54 keV for the M shells electrons and 56-57 keV for the N shells electrons) as the 72.4 keV (52-56 keV for the L shells electrons, 67-69 keV for the M shells electrons and 71-72 keV for the N shells electrons) and 64.1 keV (44-48 keV for the L shells electrons, 59-61 keV for the M shells electrons and 63-64 keV for the N shells electrons) transition's conversion electrons. If the transition was highly converted a clear electron peak would come out of the background created by the other transition and a number of emitted electrons could be extracted. However no clear peak is seen and, as the energy region is not background free, it is hard to extract a upper limit on the number of emitted conversion electrons. Thus the conversion coefficient could not be measured. The same happened for the 75.4 keV transition. For the 223.7 keV transition, the upper limit is too high to make any kind of conclusion as it would be compatible with any multipolarity from E1 to E3.

The 27.4 keV transition is tentatively assigned as M1+E2 on the basis of the ratio between the number of emitted γ-rays and α-particles (assuming no transition from this level to the 19.5 keV level). Indeed this ratio indicates a conversion coefficient $\alpha_e \approx 1000$ that lies between the predictions for M1 ($\alpha_e = 152.8$) and E2 ($\alpha_e = 5380$) transitions. However the large uncertainty on the BEGe detection efficiency at this energy, as well as the assumption that there is no competing transition, could reduce considerably this conversion coefficient, making it potentially consistent with a pure M1 transition.

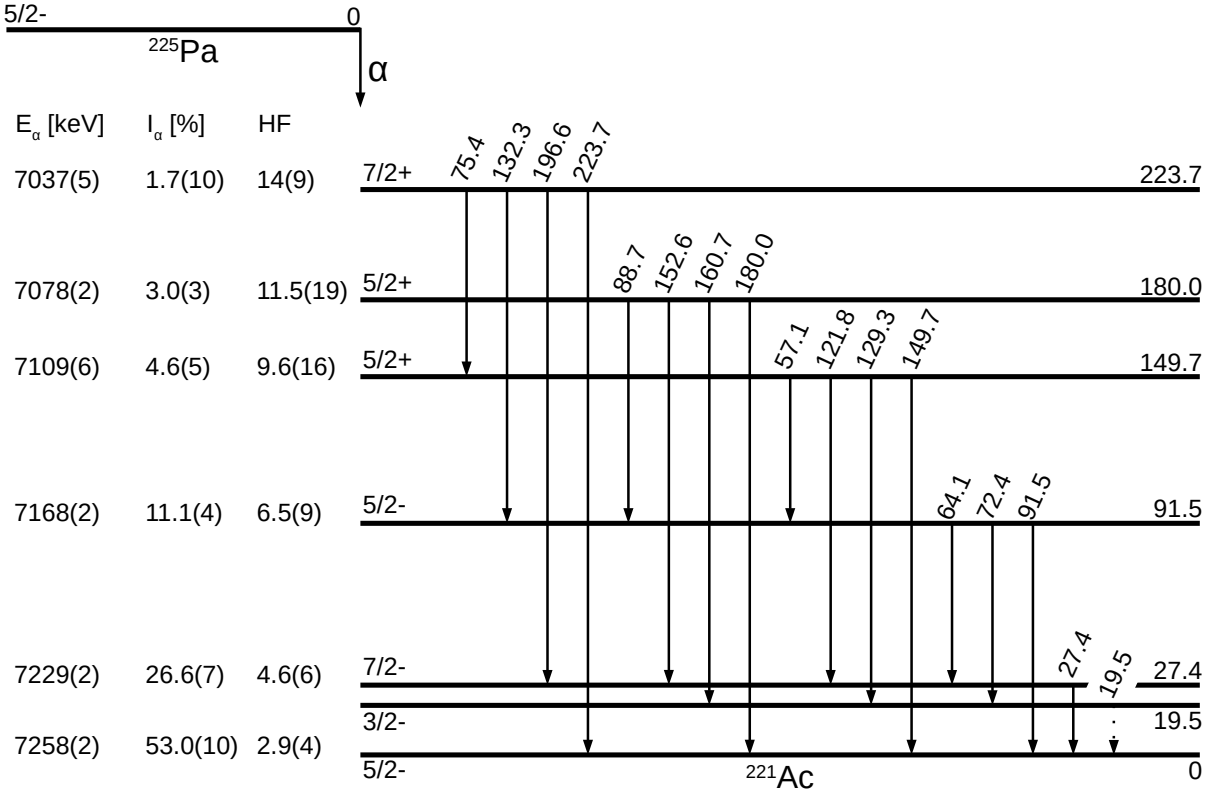

Figure 5.6: Measured decay scheme for ^{225}Pa $\rightarrow$ ^{221}Ac decay. The α-particle energies E_α, intensities I_α and hindrance factors HF are represented, as well as the levels and γ-transition energies and the proposed spin-parity assignment.

For several transitions, the measurement of conversion coefficients is not enough to define the

Transition energy (keV)	Measurement	BrIcc			Assignment
		E1	M1	E2	
27.4	$\alpha_{tot} \sim 1000$	3.53	152.8	5380	M1+E2 or M1
64.1	$\alpha_L = 30.2 \pm 7.3$ $\alpha_M = 3.8 \pm 1.6$	0.3 0.07	9.5 2.27	62.6 17.1	M1+E2 or M1 $\delta = 0.5 \pm 0.1$
72.4	$\alpha_L = 11.8 \pm 1.9$ $\alpha_M = 7.0 \pm 1.7$	0.2 0.05	6.6 1.6	34.9 9.6	M1+E2 $\delta = 0.4 \pm 0.1$
88.7	$\alpha_M < 0.73$	0.03	0.9	3.7	E1
91.5	$\alpha_L = 13.6 \pm 3.6$ $\alpha_M = 1.9 \pm 1.1$	0.1 0.03	3.3 0.8	11.5 3.15	M1+E2 or E2 $\delta = 1.3 \pm 0.2$
121.8	$\alpha_L < 0.86$	0.05	1.5	3.1	E1
129.3	$\alpha_L < 0.72$	0.04	1.2	2.4	E1
132.3	$\alpha_L < 0.47$ $\alpha_M < 0.47$	0.04 0.01	1.2 0.3	2.1 0.6	E1
149.7	$\alpha_L < 1$	0.03	0.8	1.2	E1*
160.7	$\alpha_L < 0.27$ $\alpha_M < 0.17$	0.03 0.006	0.7 0.2	0.9 0.2	E1
180.0	$\alpha_L < 0.16$	0.02	0.5	0.5	E1
196.6	$\alpha_K < 0.69$	0.08	2	0.2	E1*
223.7	$\alpha_K < 5.6$ $\alpha_L < 3.6$ $\alpha_M < 3.6$	0.057 0.011 0.003	1.4 0.26 0.06	0.13 0.21 0.06	?

Table 5.3: For each γ-ray transition seen in ^{221}Ac, this table gives the measured conversion coefficients α_K, α_L and/or α_M, as well as the ones computed with BrIcc and the deduced multipolarity assignments. When only a higher limit is given, this higher limit is computed with a 95 % confidence interval. For mixed transitions (M1+E2), the measured mixing ratio δ is indicated. Assignments denoted with a star (*) are deduced partially using parity arguments.

multipolarity, however in all cases but one (the 223.7 keV transition) the ambiguity on the multipolarity can be resolved on the basis of the initial and final states parity determined using the transitions with a known multipolarity.

The resulting decay scheme is shown figure 5.6, with the α-decay energies, intensities and hindrance factors, as well as the spin-parity assignment for each level.

An important discrepancy is noticed between the intensity feeding the 149.7 keV state ($I_\alpha = 4.6 \pm 0.5$ %) and the sum of all de-excitation observed from this state ($I_{de-excitation} = 1.55 \pm 0.12$ %). This discrepancy could be partially explained by anomalous E1 conversion coefficients [88], but also through the presence of unseen transitions towards states expected in ^{221}Ac and not seen in this work (see section 5.3).

5.1.2 . Mass $A = 221$

As shown in table 3.1, approximately 2 h of data acquisition was made for mass $A = 221$. This short run duration leads to a very low statistic for this run. Due to this low statistic, some interesting

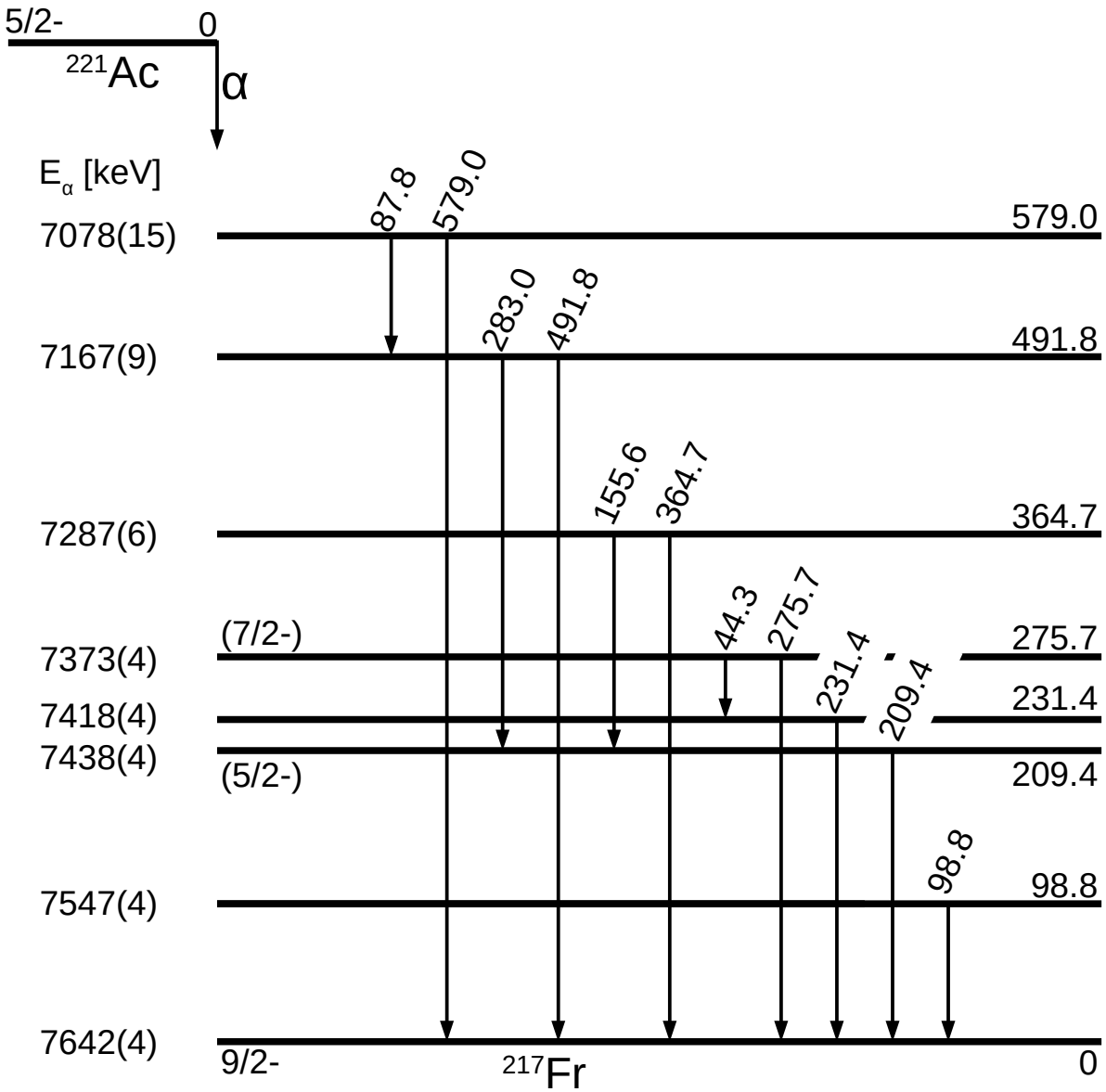

Figure 5.7: Measured decay scheme for ^{221}Ac $\rightarrow$ ^{217}Fr α-decay. The α-particle energies E_α, the γ-transition energies E_γ, as well as the proposed spin-parity assignment and energies of the levels are represented.

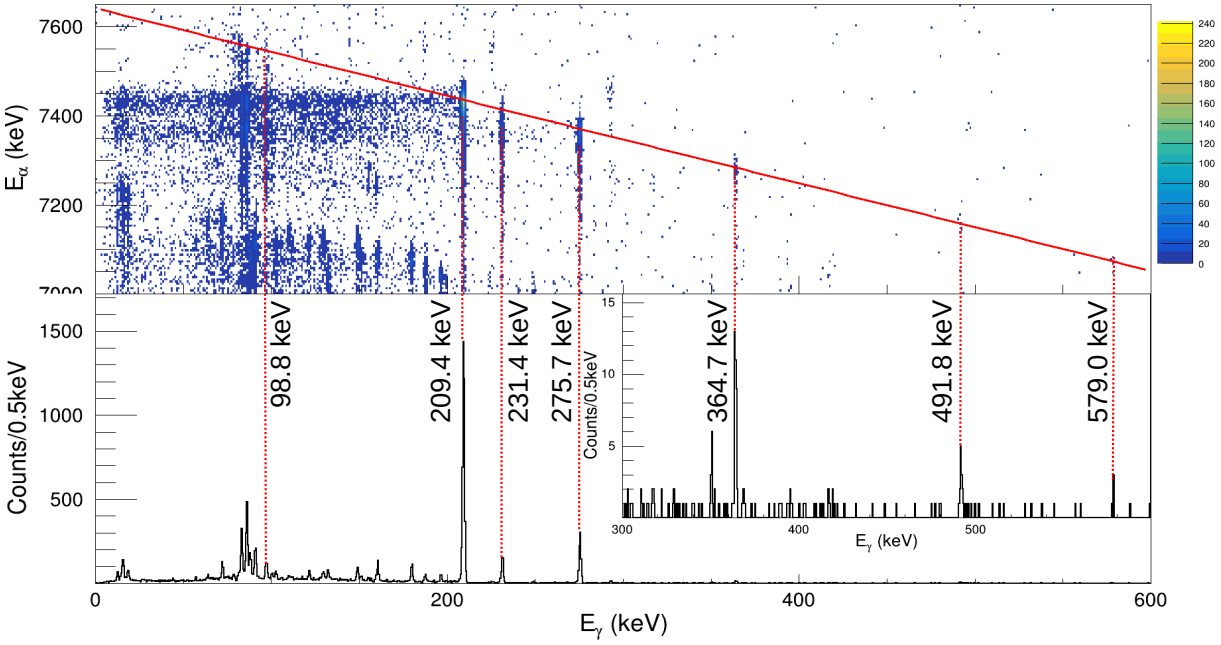

Figure 5.8: Top : α energy (E_α) vs γ-ray energy (E_γ) for ^{221}Ac → ^{217}Fr. The solid red line denotes the $Q_\alpha + E_\gamma = Q_\alpha$(g.s.-to-g.s.) line where the coincidences with γ-ray feeding directly the ground state are expected. Bottom : projection of the top view on the x-axis (E_γ), as well as a zoom for the 300-600 keV energy region in the inset. The dashed red lines denotes α-γ coincidences for which $Q_\alpha + E_\gamma$ is close to Q_α(g.s.-to-g.s.) and link them to the corresponding peak on the γ-energy spectrum. The associated γ-ray energy is indicated.

E_i (keV)	E_γ (keV)
579.0	579.0(10)
	87.8(2)
491.8	491.8(1)
	283.0(10)
364.7	364.7(1)
	155.6(1)
275.7	275.7(1)
	44.3(1)
231.4	231.4(1)
209.4	209.4(1)
98.8	98.8(14)

Table 5.4: Measured initial level energies E_i and γ-ray energies E_γ for ^{217}Fr.

coincidences for ^{221}Ac α-decay seemed to appear on the $A = 225$ run and not on the $A = 221$ run. Thus the analysis presented here was made on the $A = 225$ run. As a consequence, since the efficiencies are not known for the daughter nuclei (see section 4.2.4), no intensities could be extracted and a specific energy calibrations had to be used (see section 4.1.2). In addition, no conversion electron peak could be clearly attributed to the ^{221}Ac decay. In this work only the observed α-decay and γ-rays energies are reported.

The measured α-decay energies are reported in figure 5.7, the measured γ-rays are reported in table 5.4 and the α-γ coincidence 2D energy spectrum, as well as its projection of the x-axis (E_γ), are presented in figure 5.8. On this coincidence spectrum, three very clear peaks fall on the $Q_\alpha + E_\gamma = Q_\alpha$(g.s.-to-g.s.) line at $E_\gamma = 209.4$ keV, $E_\gamma = 231.4$ keV and $E_\gamma = 275.7$ keV. In addition, four other smaller peaks are seen on the line, one at $E_\gamma = 98.8$ keV, $E_\gamma = 364.7$ keV, $E_\gamma = 491.8$ keV and $E_\gamma = 579.0$ keV. The $Q_\alpha + E_\gamma$ for each peak are summarised in table 5.5. All $Q_\alpha + E_\gamma$ fall within error bars from each other and most of them fall within 3 keV. A weighted average of all measured values leads to a measured Q_α(g.s.-to-g.s.) $= 7785 \pm 2$ keV, thus improving the uncertainty compared to the previous value (Q_α(g.s.-to-g.s.) $= 7780 \pm 50$ keV [89]).

E_α (keV)	E_γ (keV)	Q_α (keV)	$Q_\alpha + E_\gamma$ (keV)
7642 (4)	0	7783 (4)	7783 (4)
7547 (4)	98.8 (14)	7686 (4)	7785 (4)
7438 (4)	209.4 (1)	7575 (4)	7784 (4)
7418 (4)	231.4 (1)	7555 (4)	7786 (4)
7373 (4)	275.7 (1)	7509 (4)	7785 (4)
7287 (6)	364.7 (1)	7421 (6)	7786 (6)
7167 (9)	491.8 (1)	7299 (9)	7791 (9)
7078 (15)	579.0 (10)	7209 (15)	7788 (15)

Table 5.5: Summary of E_α, E_γ, Q_α and $Q_\alpha + E_\gamma$ for all α-decay peaks measured for ^{221}Ac.

5.2 . Discussion

5.2.1 . Mass $A = 225$

The α-γ coincidences seen in this study are not fully in agreement with the results presented in E. Parr's paper [69] (cf table 5.6, see figure 3.3 for the associated decay scheme). Notably, two α-branches, $E_\alpha = 7205$ keV and $E_\alpha = 7135$ keV, seen by E. Parr are not seen in this work. The $E_\alpha = 7205$ keV α-transition is only proposed tentatively by E. Parr and no traces of it appear, neither in the raw α-spectrum, nor in the α-γ coincidence 2D spectrum obtained in our measurement.

The $E_\alpha = 7135$ keV α-transition is seen by E. Parr in coincidence with γ-ray with an energy $E_\gamma = 125$ keV with a total of 3 α-γ coincidences after all selections. In this work no γ-rays peak is seen coming out of the background in-between the $E_\gamma = 121.8$ keV and the $E_\gamma = 129.3$ keV peaks whereas the $E_\gamma = 125$ keV is the strongest transition seen by E. Parr. If the relative ratio between the $E_\gamma = 125$ keV and the other peaks in E. Parr's paper was even roughly preserved in our set of data, the peak at $E_\gamma = 125$ keV would be the most intense one. In addition, although an α-decay is seen around $E_\alpha = 7135$ keV, in this work it is clearly identified as a contamination from the α-decay

Ref [69]				This work			
E_α (keV)	I_α (%)	HF	E_{pop} (keV)	E_α (keV)	I_α (%)	HF	E_{pop} (keV)
7264(3)	61(6)	2.6(3)	0	7258(2)	53.0(10)	2.9(4)	0
7234(4)	15(4)	8.1(19)	30(5)	7229(2)	26.6(7)	4.6(6)	27.4(1)
[7205(8)]	9(3)	11(5)	60(8)				
7182(8)	5(2)	16(7)	88.2(15)	7168(2)	11.1(4)	6.5(9)	91.5(2)
7135(8)	1.8(6)	32(11)	124.9(12)				
7112(8)	3.7(13)	12(5)	152.2(15)	7109(6)	4.6(5)	9.6(16)	149.7(3)
7084(8)	4.0(12)	9(3)	179.8(15)	7078(2)	3.0(3)	11.5(19)	180.0(1)
				7037(5)	1.7(10)	14(9)	223.7(5)

Table 5.6: Comparison between reference [69] and this work for α-decay energies E_α, branching ratios I_α, hindrance factors HF and excitation energy of the populated states E_{pop} for ^{225}Pa $\rightarrow$ ^{221}Ac. Those shown in square brackets are tentative.

of ^{218}Rn coming from ^{226}Th decay chain. This α-decay is going directly to the ground state of ^{214}Po and thus totally disappears when making α-γ coincidences. Those two peaks are thus rejected in this work.

In addition, the $E_\alpha = 7037$ keV α-transition seen in this work is not reported in E. Parr's article. This α-branch is very weak compared to the other branches and the γ-ray going directly to the ground state has a low branching ratio, making the transition hard to identify. Considering the very selective conditions applied in E. Parr's work, as well as the lower statistic with respect to this experiment, this difference is not surprising.

As mentionned in section 5.1.1, it should also be noted that, for the 149.7 keV level, the total de-excitation intensity ($I_{tot} = 1.55(12)$ %) is significantly lower than the α branching ratio feeding this state ($I_\alpha = 4.6(5)$ %). A possible explanation for this discrepancy is proposed in section 5.3.

5.2.2 . Mass $A = 221$

Ref [69]		This work	
E_α (keV)	E_{pop} (keV)	E_α (keV)	E_{pop} (keV)
7642(3)	0	7642(4)	0
		7547(4)	98.8(14)
7440(3)	208.7(11)	7438(4)	209.4(1)
		7418(4)	231.4(1)
7364(5)	276.0(10)	7373(4)	275.7(1)
		7287(6)	364.7(1)
		7167(9)	491.8(1)
		7078(15)	579.0(10)

Table 5.7: Comparison between reference [69] and this work for α-decay energies E_α and excitation energy of the populated states E_{pop} for ^{221}Ac $\rightarrow$ ^{217}Fr.

The α-γ coincidences seen in this study are consistent with E. Parr's results (cf table 5.7, see figure 3.3 for the associated decay scheme), however several new α-decays are measured in coincidence

with γ-rays. Two of them at $E_\alpha = 7078$ keV and $E_\alpha = 7167$ keV for ^{221}Ac ($E_\alpha = 7168$ keV for ^{225}Pa) are observed in coincidence with several γ-rays, several of them being consistent with an assignment to the α-decay from ^{225}Pa to ^{221}Ac and others with an assignment to the α-decay from ^{221}Ac to ^{217}Fr. Everything in the data seems to point to the fact that both ^{225}Pa and ^{221}Ac emit α-particles at approximately the same energy, however further experiments are needed to confirm this.

It should also be noted that the transition $E_\gamma = 364.7$ keV matches one of the transitions ($E_\gamma = 364$ keV) seen through in-beam spectroscopy of ^{217}Fr using the ^{210}Pb(^{11}B,4n)^{217}Fr reaction [90].

5.3 . Interpretation

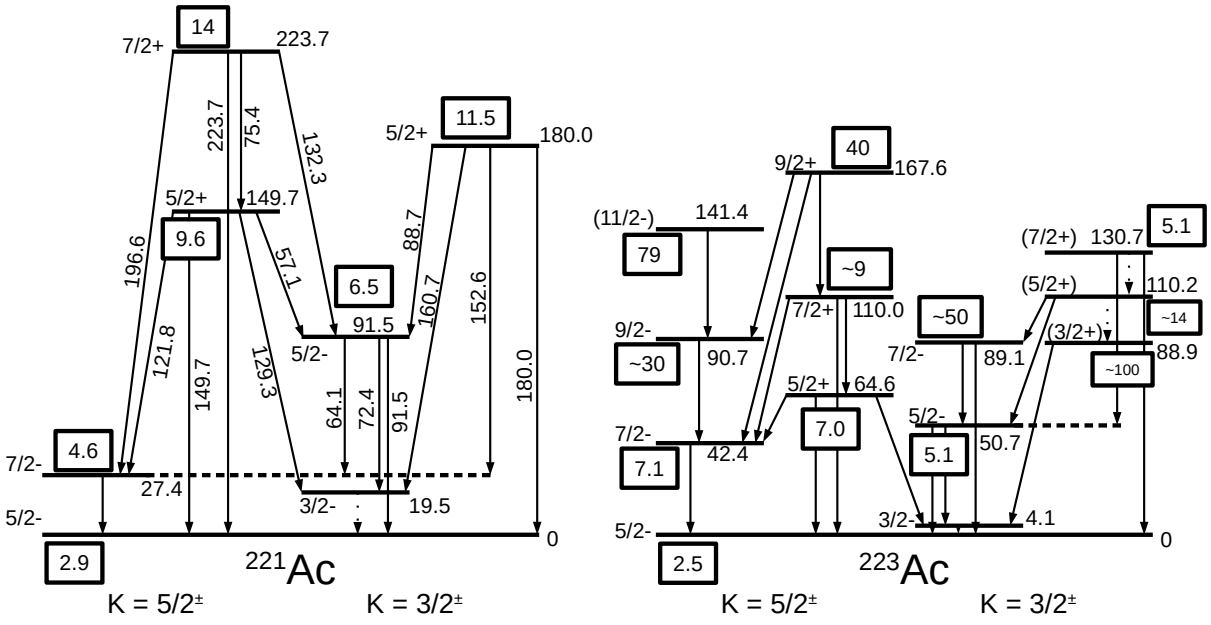

Figure 5.9: Comparison between the proposed level scheme interpretation for ^{221}Ac and the level scheme of ^{223}Ac. Hindrance factors are noted in bold boxes. Data for ^{223}Ac are taken from reference [91].

An extensive discussion of the ground state configurations of odd-A actinium and protactinium isotopes is given in reference [69], leading to a $I^\pi = 5/2^-$ assignment for both ^{225}Pa and ^{221}Ac. Our results are consistent with this assignment and are summarised hereafter.

A similarity is observed between the α-decay of ^{227}Pa reported in reference [91] and the α-decay of ^{225}Pa reported here (see figure 5.9). Indeed, both nucleus have a $I^\pi = 5/2^-$ ground state with similar hindrance factors towards this state. The $I^\pi = 7/2^-$ state at 27.4 keV in ^{221}Ac can be put in parallel with the $I^\pi = 7/2^-$ state at 42.4 keV in ^{223}Ac. Similarly, the $I^\pi = 5/2^+$ and $I^\pi = 7/2^+$ states at 149.7 and 223.7 keV can be put in parallel with the levels at 64.6 and 110.0 keV states in ^{223}Ac. The 19.5 keV state can be associated with the 4.1 keV state, the 91.5 kev state with the 50.7 keV and the 180.0 keV with the 110.2 keV. In all cases the hindrance factors towards the states are similar. Some states observed in ^{223}Ac are not seen in ^{221}Ac in this work, however all those states

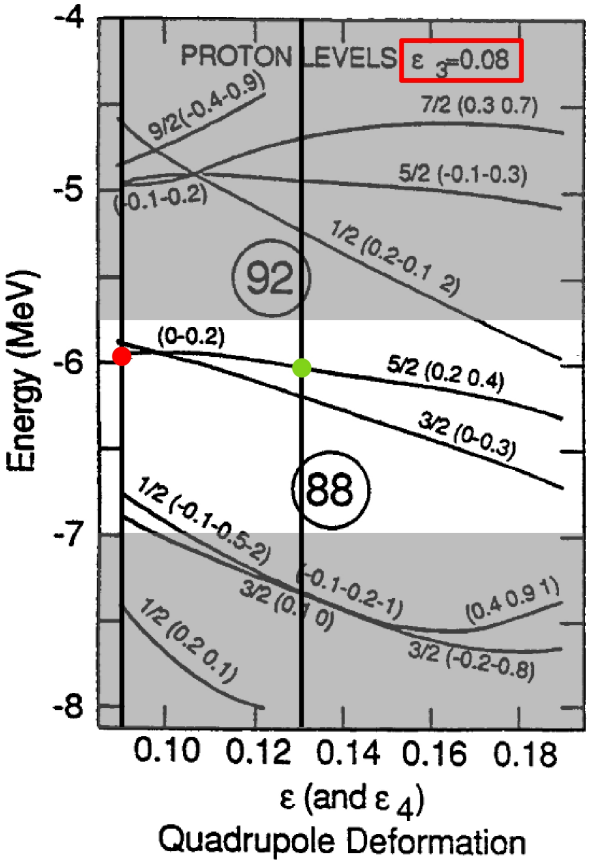

Figure 5.10: Single proton orbitals in an axially symmetric but reflection asymmetric folded Yukawa potential, with $\epsilon_3 = 0.08$, plotted against the quadrupole deformation (ϵ). The values showed on the orbitals corresponds to the quantum numbers Ω, $\langle \hat{s_z} \rangle$ and $\langle \hat{\pi} \rangle$. See text for details. The grey area denotes the non-relevant orbitals. The expected deformations of ^{225}Pa and ^{221}Ac are denoted with vertical lines around $\epsilon = 0.13$ and $\epsilon = 0.9$ respectively. A green (red) dot is indicated where the ^{225}Pa (^{221}Ac) single proton is expected to be. Figure adapted from reference [91].

have large hindrance factors and thus would be beyond the sensitivity of this work.

In both cases, the lowest hindrance factor is observed for the decay towards the ground state with very similar hindrance factors ($HF = 2.5$ for ^{227}Pa and $HF = 2.9$ for ^{225}Pa). This result is consistent with microscopic-macroscopic calculations breaking the reflection symmetry [47]. Indeed, those calculations predict two orbitals ($\Omega = 3/2$ and $\Omega = 5/2$) to be present at the proton Fermi level for both Ac (89 protons) and Pa (91 protons) isotopes with $N \sim 130 - 140$ [47, 92, 93]. Figure 5.10 present the Nilsson diagram resulting from those calculations and showing the evolution of the proton single-particle orbitals as a function of the quadrupole deformation, for a fixed octupole deformation ($\epsilon_3 = 0.08$). When the nucleus present an octupole deformation, the orbitals of same Ω (projection of the total angular momentum on the symmetry axis) and opposite parity lying close in energy from each other tends to mix, and the resulting orbitals are labeled by Ω, by $\langle \hat{s_z} \rangle$, related to the magnetic moment, and by $\langle \hat{\pi} \rangle$, measuring the mixing between positive and negative parity ($\langle \hat{\pi} \rangle = -1$ indicate a purely negative parity, $\langle \hat{\pi} \rangle = +1$ a purely positive parity and $\langle \hat{\pi} \rangle = 0$ a perfectly mixed parity).

For quadrupole deformation above $\epsilon \sim 0.1$, the $\Omega = 3/2$ orbital is the lowest energy orbital and should correspond to the ground state of Ac isotopes while the $\Omega = 5/2$ orbitals should correspond to the ground state of Pa isotopes. However, as the quadrupole deformation decreases, the two orbitals cross and the $\Omega = 5/2$ becomes the lowest energy one. The ^{227}Pa and ^{225}Pa are expected to have larger quadrupole deformations than their daughter Ac isotopes. For example, in reference [37], where theoretical calculation of the potential energy surfaces are performed to find the minimum for even-even nuclei, ^{224}Th and ^{226}U (the two even-even nuclei with 1 less and 1 more protons than ^{225}Pa) have a minimum found for $\epsilon = 0.13$ and for $\epsilon = 0.143$ respectively. Whereas, for ^{220}Ra and ^{222}Th (the two even-even nuclei with 1 less and 1 more protons than ^{221}Ac) the minima are found for $\epsilon = 0.091$ and for $\epsilon = 0.075$ respectively. Therefore the $\Omega = 5/2$ orbital would be the ground state of all four nuclei (^{227}Pa, ^{223}Ac, ^{225}Pa and ^{221}Ac) explaining the very low hindrance factor towards the ground state in both cases.

In addition, similar hindrance factors are also observed towards the excited states, with notably low hindrance factors ($HF \sim 10$) towards opposite parity states. This kind of behaviour has been interpreted several times as a sign of octupole deformation where opposite parity states mix and lead to low hindrance factors towards opposite parity states [94, 95, 91, 96].

Moreover the $I^\pi = 5/2^-$ and $I^\pi = 5/2^+$ levels could be interpreted as a parity doublet arising from octupole deformation. The splitting of 149.7 keV for the doublet seems higher than the splitting usually reported in the literature [91, 97, 96, 98, 99, 100]. However, it is also smaller than the one reported for ^{219}Fr, which is considered as transitional between static octupole deformation and octupole vibration with a splitting of 191.4 keV for the ground state band [101]. Thus ^{221}Ac could be interpreted as the beginning of the transitional region between static octupole deformation and octupole vibration for the Ac isotopes.

This interpretation is consistent with the results presented in reference [11]. In this study, laser spectroscopy of the isotopes $^{225-229}$Ac was performed, leading to new measurements of magnetic dipole moments and changes in mean-square charge radii. The changes in mean-square charge radii were compared with self-consistent blocked Hartree Fock Bogoliubov calculations using several energy density functionals and the SLy5s1 functional provides the best agreement with the data, but only when octupole deformation is included. This functional predicts octupole deformation to occur above $N = 130$ for the actinium isotopes, with a plateau of deformation from $N = 133$ to $N = 139$ and decreasing deformation on both sides (see figure 5.11). This would be consistent with our interpretation of ^{221}Ac, which has $N = 132$ neutrons, as a transitional nucleus between the static deformation for higher N nuclei and the vibrations for lower N nuclei. It would be interesting, in future experiments, to study ^{219}Ac to see if this static octupole deformation does indeed disappear, or if it remains, indicating a larger than expected static deformation region.

Finally, it should be noted that, considering the similarity between the ^{221}Ac and ^{223}Ac level schemes, the $I^\pi = 3/2^+$ state at 88.9 keV in ^{223}Ac, the parity doublet of the $I^\pi = 3/2^-$ state at 4.1 keV, is also expected in ^{221}Ac as the parity doublet of the $I^\pi = 3/2^-$ state at 19.5 keV. Following the trend of the states from ^{223}Ac to ^{221}Ac, it seems reasonable to expect this state, in ^{221}Ac, somewhere between the $I^\pi = 5/2^-$ state at 91.5 keV and the $I^\pi = 5/2^+$ state at 149.7 keV. If this $I^\pi = 3/2^+$ un-observed state does exist in-between those two states, a transition from the $I^\pi = 5/2^+$ state at 149.7 keV to this hypothetical $I^\pi = 3/2^+$ state could occur. However, this transition would be an M1 transition and would have a low energy (a few tens of keV), thus it would be a highly converted transition, with the emitted conversion electrons having an energy likely below

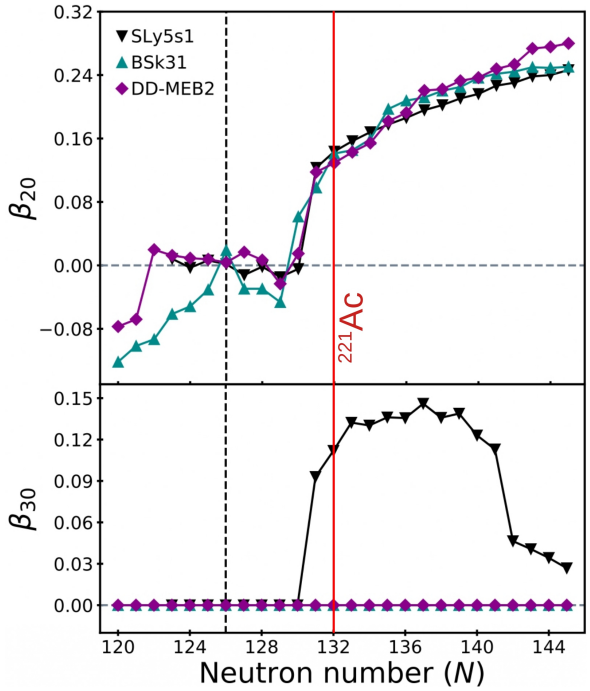

Figure 5.11: Comparison of the β_{20} and β_{30} values, for the Ac isotopic chain, for the SLy5s1, BSK31, and DD-MEB2 interactions. In the calculations with BSK31 and DD-MEB2 β_{30} is restricted to 0 by the imposed reflection symmetry. Triangles: nonrelativistic EDF values. Squares: relativistic EDF values. Dashed line: $N = 126$ shell closure. Red line: ^{221}Ac. Figure and caption adapted from reference [11].

our detection threshold. This would make this transition hard to detect, both in the γ-ray spectrum and in the conversion electron spectrum. Thus the presence of this un-observed state could explain the missing intensity from the 149.7-keV state in ^{221}Ac. With a hindrance factor of ∼100 for this $3/2^+$ state in ^{223}Ac, this state would likely not be seen directly through α-decay feeding this level and thus there would not be α-γ coincidences falling on the $Q_\alpha + E_\gamma = Q_\alpha$(g.s.-to-g.s.) line. As those α-γ coincidences are the basis of our methodology for the reconstruction of the level scheme, this level would be hard to identify in our experiment.

To summarise, the decay spectroscopy of ^{225}Pa was performed with a precision never reached before. The level scheme of ^{221}Ac was reconstructed with spin and parity assignements obtained thanks to the transitions multipolarities. These multipolarities were deduced from the measurement of the individual conversion electron energies and intensities. In addition, the hindrance factors of the different α-decay branches were measured. The combination of the hindrance factors measurement and the spin/parity assignements enabled the interpretation of ^{221}Ac level scheme in terms of parity doublet bands arising from a static octupole deformation. The splitting between the parity doublets indicates that ^{221}Ac is likely at the transition between static octupole deformation and octupole vibration. This study has been published in PRC [102].

However, the low electron detection efficiency was a limiting factor, with only upper limits obtained for most conversion coefficients. Moreover, some highly converted transitions might have been missed.

Another experiment performed in October 2022 solved part of the problems, using a more compact setup to slightly increase the α-particle detection efficiency and considerably increase the conversion electrons detection efficiency (factor 10) [68]. However, technical issues with the targets, as well as a considerable drift in the gain of the Si(Li) detector, limited the results obtained from this experiment. The SEASON detector, currently under development at CEA, will represent another considerable improvement and will be presented in the second part of this thesis.

Part II
The SEASON detector

The new GANIL-SPIRAL2 facility, located at Caen in France, opens up new opportunities due to very high intensity beams produced by the SPIRAL2 (Système de Production d'Ions RAdioactifs en Ligne 2) accelerator, coupled with the high selectivity of the Super Separator Spectrometer (S^3). This facility aims to study mainly two areas of the nuclear chart: the N=Z region near the proton drip line, and the heavy and super-heavy nuclei. In particular the characteristics of the installation will enable the production of neutron-deficient actinides even further from the stability than available at IGISOL. With this perspective, the program for the study of the neutron-deficient actinides started at IGISOL will carry on at GANIL-SPIRAL2.

In particular, a Low Energy Branch (LEB) will be installed at S^3 to perform laser spectroscopy. In this context, a decay spectroscopy station has been planned for this Low Energy Branch: the SEASON (Spectroscopy Electron Alpha in Silicon bOx couNter) detector. This detector is designed to combine decay spectroscopy (α, γ and conversion electrons) and laser ionisation spectroscopy to study heavy and super heavy nuclei.

The second half of my PhD thesis was focused on the development of this detector, with two main points:

- the GEANT4 simulations of the detector,
- the study of the detector implantation foils.

In this part, I will first present the GANIL-SPIRAL2 facility and the SEASON detector. I will then detail my work on this detector, with a first chapter dedicated to the detector simulations and a second chapter dedicated to the study of its implantation foils.

6 - SEASON

As mentioned before, the SEASON detector is designed to be placed at the S^3-LEB facility in the new GANIL-SPIRAL2 installation. In this chapter I will present the installation and the different rooms and setup planned, with a particular focus on the SEASON detector.

6.1 . SPIRAL2

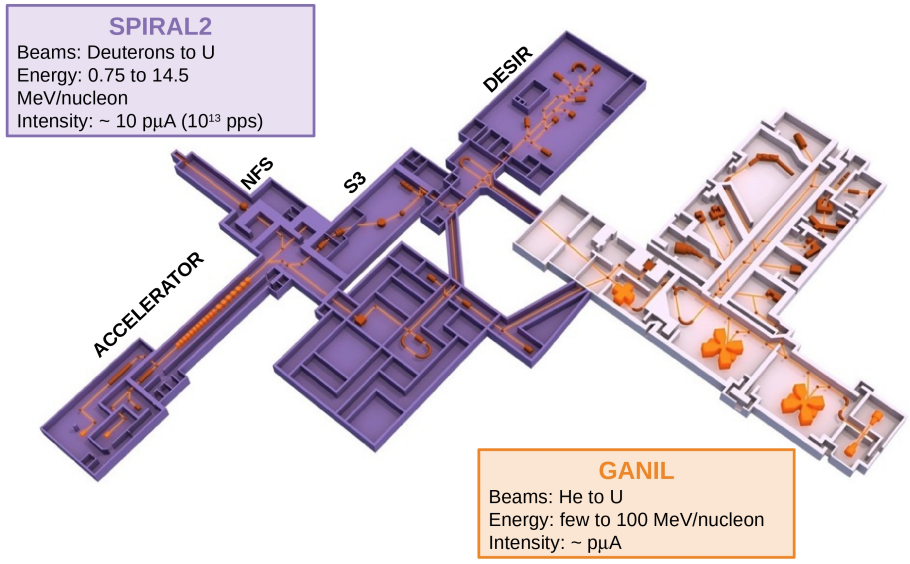

Figure 6.1: Visualisation of the GANIL facility. On the right side, in orange, is the original GANIL facility. On the left side, in purple, is the new SPIRAL2 facility.

The SPIRAL2 facility [103] is a new installation at the GANIL (Grand Accélerateur National d'Ions Lourds) facility, aiming at the production of new high intensity RIB (Radioactive Ion Beam). It consists of a linear particle accelerator coupled with two different ion sources in order to provide a large variety of beams (from protons up to the heaviest stable nuclei such as uranium) with beam energy ranging from 0.75 MeV/nucleon up to 14.5 MeV/nucleon and a high beam intensities (around 10 pμA). Three separate experimental areas are planned for the SPIRAL2 facility:

- NFS (Neutron For Science) [104],
- S^3 (Super Séparateur Spectromètre) [105, 106],
- DESIR (Décroissance, Excitation et Stockage des Ions Radioactifs) [107, 108]

NFS saw its fist experiments in 2021, S^3 is still under construction and its commissioning should start in 2024 and the DESIR experimental hall construction should start soon. A scheme of the GANIL-SPIRAL2 facility is shown in figure 6.1.

6.1.1 . NFS

The NFS facility provides high intensity neutron beams for nuclear physics measurements. Two neutron production modes are available: deuteron break-up reactions with a beryllium converter and proton charge exchange reactions on a lithium target. The first reaction generates a white neutron spectrum between 1 and 40 MeV and the second one provides quasi mono-energetic neutron beams up to ~ 30 MeV. This facility is delivering unprecedented intensities for neutron beams at this energy.

6.1.2 . S^3

S^3 is a spectrometer optimised to use the high intensity beams delivered by SPIRAL2 for the study of heavy and super heavy elements (HE/SHE) as well as the N=Z nuclei near the proton drip line. Both have in common exotic nuclei with a low production cross sections. S^3 will thus offer new opportunities to study nuclear matter in exotic systems.

As it aims to study nuclei with very low cross sections, it is crucial to reach a very good rejection of the primary beam to separate rare events from a high intensity background. In addition, a very good transmission of the nuclei of interest is required. Finally, a mass resolution $M/\Delta M > 300$ is required to be able to separate super-heavy nuclei.

To reach those specifications, S^3 consists of two stages: a momentum achromat separator and a mass spectrometer, with an intermediate focal plane in-between. The momentum achromat separator is designed to combine both a large acceptance with a rejection of more than 99.9 % of the primary beam. The second part will perform the physical mass separation with the desired resolution $M/\Delta M > 300$ before delivering the beam to a final focal plane where the experiments will be placed.

Two modes are foreseen: a high mass resolution mode reaching the desired $M/\Delta M > 300$ and a high convergence mode in which the mass resolution is sacrificed to gain in transmission efficiency.

Two main experimental setups are planned at the final focal plane: SIRIUS (Spectroscopy and Identification of Rare Isotopes Using S^3), a state-of-the-art focal plane detection system for decay spectroscopy [109, 110], and the S^3-LEB (S^3 Low Energy Branch), a laser ionisation spectroscopy setup [111], coupled with PILGRIM (Piège à Ions Linéaire du GANIL pour la Résolution des Isobares et la mesure de Masse), a mass measurement device (MR-ToF-MS [112]) and a decay station: SEASON. In the future, the S^3-LEB will also provide beams for the DESIR facility.

6.1.3 . DESIR

The DESIR facility is an experimental hall that will receive beams both from S^3-LEB and from the SPIRAL1 installation. In this experimental hall, several detection setups will be installed in order to perform laser spectroscopy, decay spectroscopy, mass measurement, as well as trap-assisted spectroscopy.

6.2 . The SEASON detector

SEASON (Spectroscopy Electron Alpha in Silicon bOx couNter) is a detector designed to combine decay spectroscopy (α, γ and conversion electrons) and laser ionisation spectroscopy for heavy and super-heavy nuclei as a counting detector for the S^3-LEB setup.

6.2.1 . S^3-LEB

The S^3-LEB setup will perform in-gas cell and in-gas jet laser spectroscopy of the exotic nuclei produced and selected by S^3. On the scheme shown in figure 6.2, the evaporation residue arrives

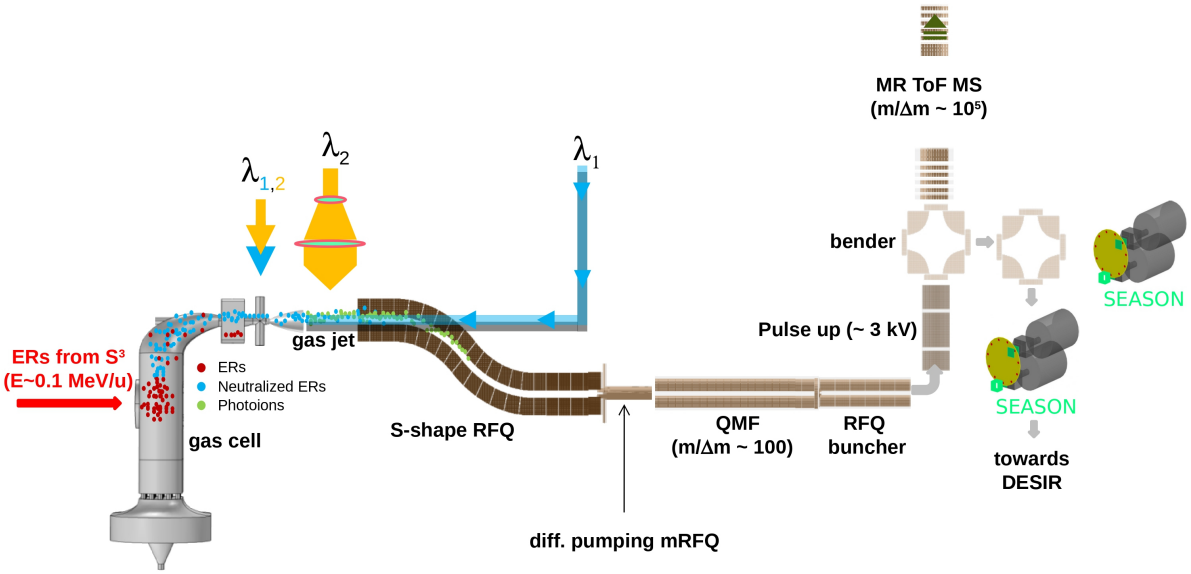

Figure 6.2: Schematic view of the S^3-LEB setup. See text for more details.

from S^3 on the left side. They are stopped in a gas cell where they will be neutralised and extracted through a de Laval nozzle to form a supersonic gas jet [113, 114, 115]. An electrode is placed before the nozzle to stop the remaining ions before the extraction from the gas cell. Laser ionisation spectroscopy will be performed either in the gas cell, right before extraction, or in the gas jet [114, 113]. The ions produced by the laser ionisation are then guided through a S-shaped RFQ (Radio-Frequency Quadrupole) towards the counting system, which can be either the MR-ToF-MS setup or, after a bender, SEASON which will count the ions through the measurement of their decay products.

The first offline comissioning of the S^3-LEB setup is presented in reference [116].

6.2.2 . SEASON's design

As mentioned before, as a counting detector for S^3-LEB SEASON is designed to combine decay spectroscopy and laser ionisation spectroscopy for heavy and super-heavy nuclei. The nuclei selected by laser spectroscopy will be detected through their decay products (mainly α-particle emission). As the goal of SEASON is to study heavy nuclei with low production rate, it is crucial to reach a high detection efficiency, and, for the decay spectroscopy, one need a good energy resolution, but also a good granularity to be able to measure individual conversion electron energies. Indeed, in this region of mass, some nuclei de-excite via a series of highly converted transitions and thus via the quasi-simultaneous emission of several conversion electrons that must be detected individually. This is achieved by combining a high granularity with the use of an implantation foil instead of implanting the ions directly into the detector as will be done for the SIRIUS setup. Finally, in order to avoid long-lived contamination of the implantation foil, one need to be able to change it when the laser frequency changes or, in the case of pure decay spectroscopy, when another nucleus is send to the setup.

To answer to all those constraints, SEASON was designed with a box of five Si detectors around an implantation foil (on the bottom of figure 6.3), one of them behind the foil with respect to the beam axis, and four of them in a tunnel configuration in front of the foil. This implantation foil is mounted on a wheel containing a total of eleven foils to be able to change foils by rotating the wheel.

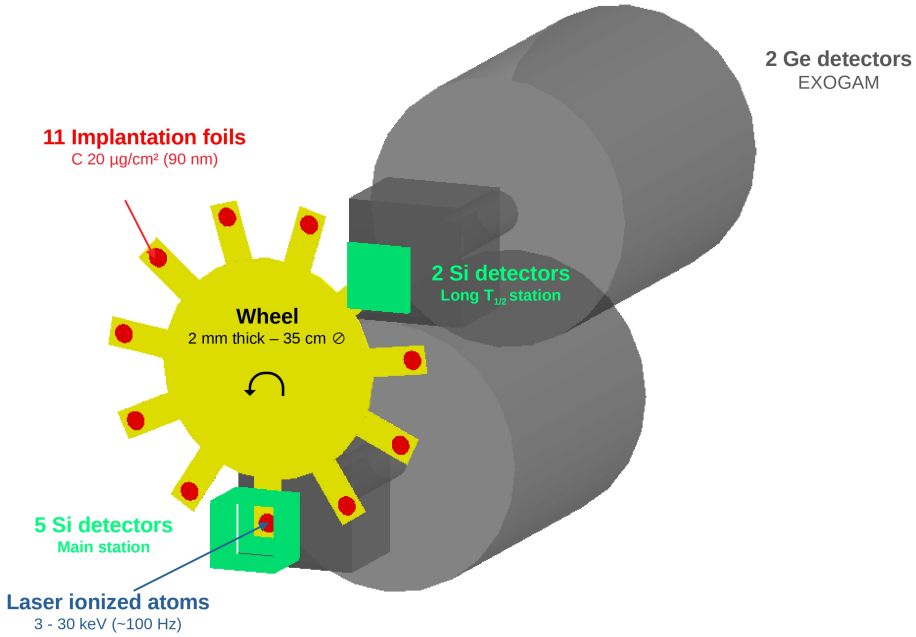

Figure 6.3: Representation of the SEASON detector in GEANT4 simulations [83]. The DSSDs are represented in green, the implantation foils in red, the wheel in yellow and the germanium detectors in grey. See text for more details.

A secondary decay station consisting of two Si detectors in a sandwich configuration is placed around the fourth foil (on the top-right side of the wheel on figure 6.3). Thus, when the laser frequency is changed, the wheel is also rotated 4/11th of a turn and thus the foil initially placed at the main station is moved to the secondary decay station, which continue the measurement for longer half-life isotopes. In addition, a germanium detector (EXOGAM [117]) is placed behind each station in order to measure γ-rays emitted in coincidence with the α-decay. Striped detectors are needed in order to reach the required granularity to limit summing effects (see section 7.2.3.2). Finally, the detectors are mounted on a motorised support to be able to change the distance between the detectors and the implantation foil to avoid summing in high count rate cases. EXOGAM detectors are also mounted on a mobile support so that they can be moved with the silicon detectors.

6.2.3 . SEASON's DSSDs

As mentionned before, to limit summing effects, stripped detectors are required. Double-sided Silicon Strip Detectors (DSSDs) where choosen for SEASON.

6.2.3.1 . DSSDs working principle

Double-sided silicon strip detectors are semiconductor detectors. The working principle of a semiconductor is to create a p-n junction to obtain a "depletion zone" devoid of mobile charge carrier. An electric field appears in this depletion zone and thus the charge carrier created (or entering) in the depletion zone will exit the area under the effect of this electric field. When a charged particle enters in this area it will deposit its energy through the creation of electron-hole pairs. Those electron-holes pairs are carried by the electric field and can be collected, electrons on one side of the junction and holes on the other side. The number of electron-hole pairs produced is proportional to the deposited

energy and thus the induced signal amplitude and integrated charge are proportional to the particle energy.

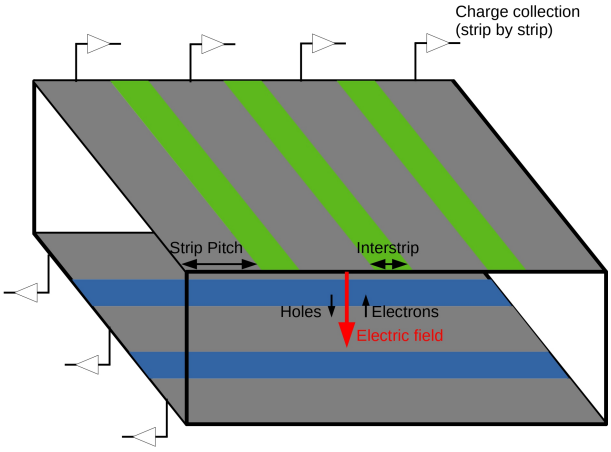

Figure 6.4: Principle of operation of a DSSD.

DSSDs work under the same principle, however, instead of using a single electrode to collect the charge on a given side of the detector, several electrodes, called strips, are used (see figure 6.4) and each strip is read individually. Thus the charge carriers will be collected in the strip closest to their creation point, giving an indication of the interaction position. In addition, if two particles interact at the same time at two different points corresponding to two different strips, as both strips are read independantly, both energies will be detected properly, whereas, in a detector without strips, only the sum energy would have been measured. The strips on one side are perpendicular to the strips on the other side, thus creating pixel areas for the detection. Finally, the strips are separated by interstrip areas. When a particle deposit its energy in an interstrip area, the charge carriers created will be splitted between both neighbouring strips, each one seeing only part of the deposited energy.

6.2.3.2 . BB7 DSSD

Initial simulations testing the impact of some parameters (see section 7.1), showed that:

- for the detector placed behind the implantation foil, a strip width of 3 mm or lower was required to limit summing effects;
- for the tunnel detectors, larger strips could be used as the summing effect was less important.

Using a larger detector behind the implantation foil than for the tunnel was considered, however the final choice was to use the same model for all detectors as this presented several advantages. First, this means that a spare detector can replace easily any disfunctionning detector. Second, and most important, it simplified significantly the front-end electronics. Indeed, SEASON's front end electronics, FEANICS (Front-End Adaptative gaiN Integrated Circuits), is internally developed at CEA Irfu and is designed to be placed under vacuum, as close as possible from the detectors. In fact the ASIC (Application-Specific Integrated Circuit) electronic chips will be placed on cards plugged directly on the detectors without any intermediate cables. Using the same model for all detectors means that only one design of front-end cards can be made and used for all detectors. Thus a detector model was fixed: the BB7 detector [118] from Micron Semiconductor Ltd.

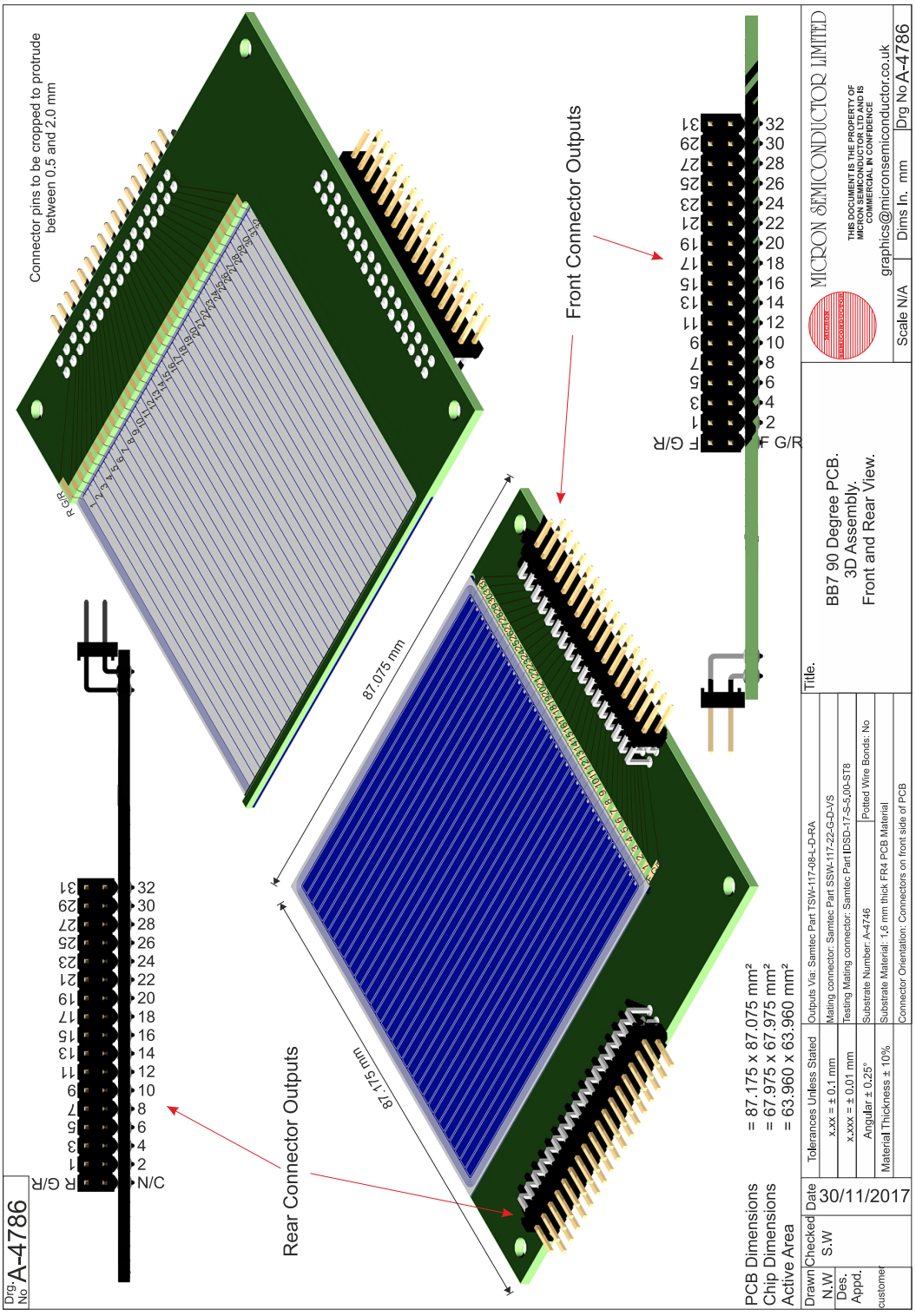

Figure 6.5: View of BB7 detectors on their PCB. Scheme is the courtesy of Micron Semiconductor Ltd.

This detector has a $68 \times 68\,mm^2$ chip area and a $64 \times 64\,mm^2$ active area with 32×32 strips (2 mm width), is 1 mm thick to enable the detection of conversion electrons up to 600 keV and a high resistivity ($> 10\,k\Omega.cm$) was requested to enhance the energy resolution. In addition, several dead-layer thicknesses are available, ranging from 50 nm to 500 nm, as well as several PCB configurations. The configuration used is showed in figure 6.5. The PCB is only on two sides of the detector to enable a very compact configuration of the tunnel and the FEANICS electronic cards will be plugged directly on the connectors. On this figure, the detector guard ring can be seen surrounding the detector chip. The interstrip area present in-between the strips is also visible on the scheme. This interstrip area is 75 µm large on the front side and 40 µm large on the rear side. The active part of the strips is, in reality, 1.925 mm large on the front side and 1.960 mm large on the rear side. The depletion voltage given by Micron Semiconductor Ltd is 70 V and for operation a negative voltage (-100 V, defined as the end of the plateau on Current-Voltage curves) is applied to the front side of the detector and the rear side is at mass.

A view of the detectors design with its chamber, wheel, electronics etc. is shown in figure 6.6.

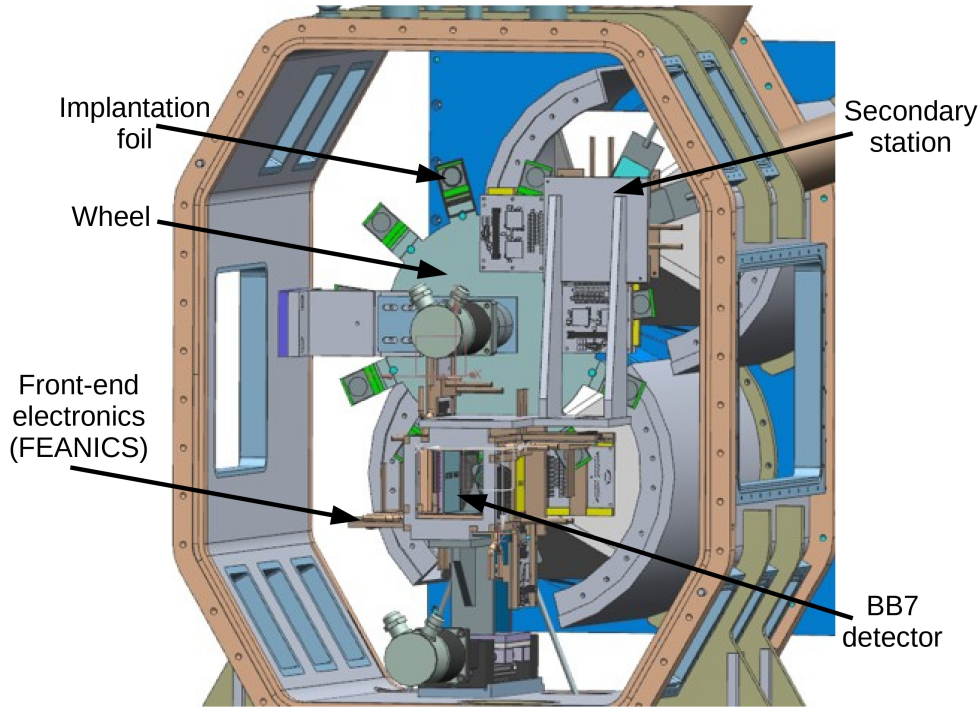

Figure 6.6: View of the SEASON detector with its mechanical design.

The goal for SEASON is to reach a detection efficiency as high as possible as it will be used in low count rate experiments (∼10-100 Hz), but also to have good energy resolution for both α-particles (aiming for 15 keV FWHM at 7 Mev) and conversion electrons (aiming for 7 keV FWHM at 200 keV). For this to be possible, the front-end cards will have an automatic gain switch, enabling a default high gain, optimised for the conversion electrons energy range, and switching to a low gain, optimised for α-particle energy range, when the signal reaches a certain threshold.

A first test detector have been received and energy resolution below 20 keV for α-particles and around 10 keV for conversion electrons are reached. This results should still be improved as some sources of noise have been identified (a noisy component in the FEANICS chips, as well as the

material choice for the PCB) and will be solved for the final version.

My work on the SEASON detector focused mainly on two points: the use and improvement of the detector simulations, and the study of its implantation foils. The following chapters will present those two points.

7 - Simulations

As mentioned before, preliminary simulations were already performed by T. Goigoux [119] for the SEASON detector. Those simulations enabled a first design for the detector as well as the study of the impact of some parameters on the measurements and thus lead to the choice of the BB7 detector model [118]. During my PhD, I took in hand the simulations performed by T. Goigoux, implemented in the simulations the new detector configuration based on the detector choice and improved the simulations to take into account several points that were not considered before. This enabled a better estimate of the detection efficiency and of the energy resolution of the detector. I will first present the status of the simulations when I arrived, and then detail my contribution.

7.1 . Previous simulations

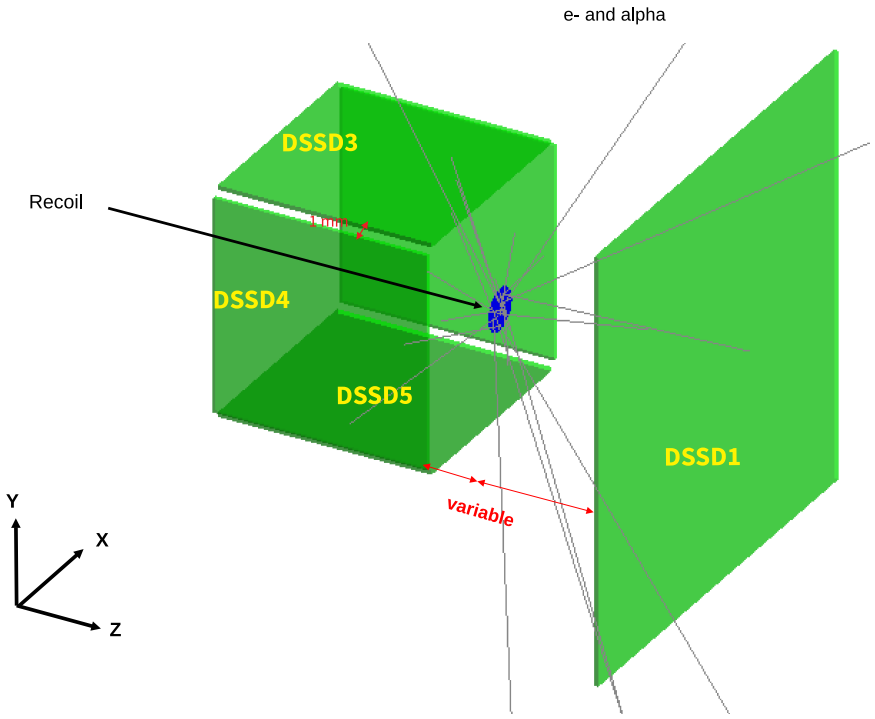

Figure 7.1: Visualisation of SEASON's initial design in NPtool.

The SEASON detector was simulated with NPtool (Nuclear Physics Tool) [82] a GEANT4 [83] library for the simulation of nuclear physics detectors. In the simulations, several parameters were optimised to maximise detection efficiency and minimise the summing effect (i.e. the simultaneous detection of several particles in a given pixel). The initial version of the detector looked like figure 7.1 with one large DSSD behind the implantation foil (DSSD1) and four smaller DSSDs in a tunnel configuration to let the beam pass through. The impact of detector sizes and distances between the

implantation foil and the detectors on the detection efficiency was studied, as well as their influence, combined with the size of the strips, on the summing effect. The backscattering of electrons was also studied.

The final configuration was:

- carbon foil, 1 cm diameter, 20 µg/cm^2 thickness;
- DSSD1 of 10 x 10 cm, 33 x 33 strips, 1 mm thickness,
- tunnel with 4 DSSDs of 5 x 5 cm, 5 x 5 strips, 1 mm thickness,
- tunnel-foil and foil-DSSD1 distances of 2 mm by default, adjustable as a function of the detectors' count rates,
- 2 mm distances between tunnel DSSDs.

With this configuration, a detection efficiency of 87.6 % was reached for α-particles in simulations. At this stage, several parameters were not taken into account:

- the detectors guard ring;
- the interstrip;
- the dead layer at the surface of the detector;
- the aluminium grid enabling the charge collection.

7.2 . New simulations

On the basis of the initial simulations, a detector model was chosen : the BB7 detector from Micron Semiconductor Ltd (see section 6.2.3).

The first step was to reproduce previous simulations to ensure that the simulation code was working as expected. Two points were checked: the α-particle detection efficiency as a function of detector-foil distances and the electron backscattering as a function of the incidence angle.

7.2.1 . α-particles detection efficiencies

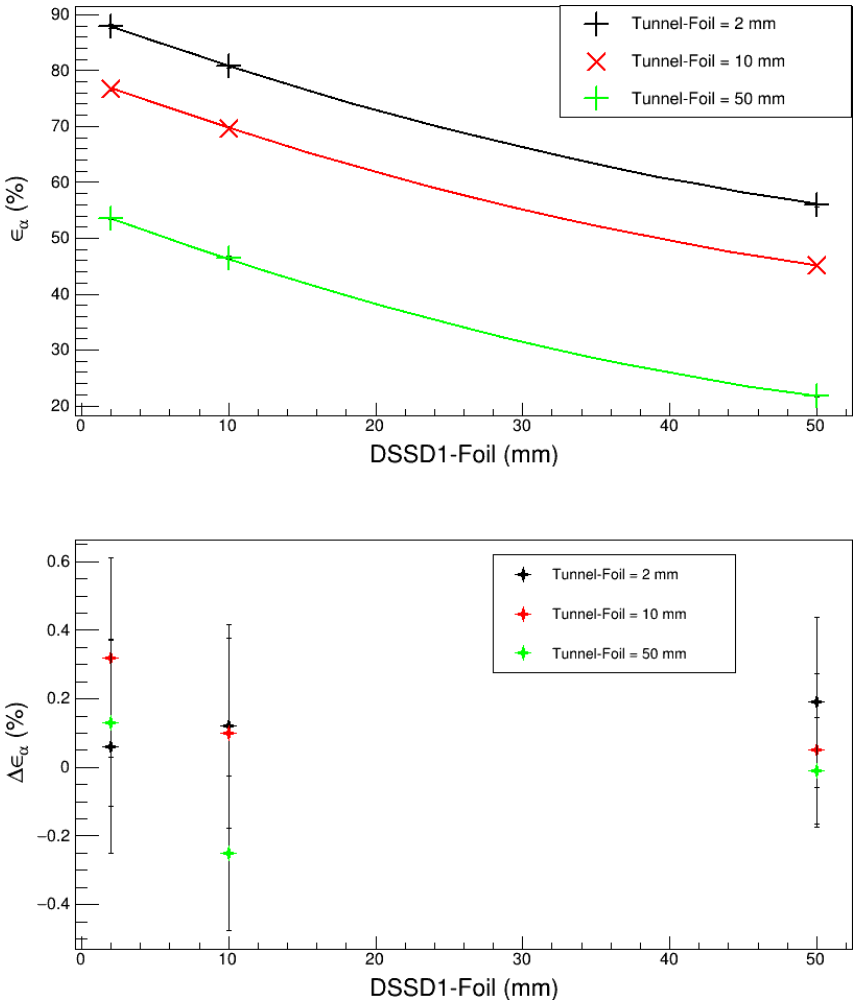

Figure 7.2: Top: Comparison between T. Goigoux simulated detection efficiencies (full lines) and this work simulated detection efficiencies (markers).
Bottom: Point-by-point difference between T. Goigoux simulated detection efficiencies and this work simulated detection efficiencies.

For the α-particle detection efficiencies as a function of detector-foil distances, the results were in perfect agreement (see figure 7.2) with an average absolute deviation between T. Goigoux results and this work $\Delta\bar{\epsilon}_\alpha = 0.14\,\%$ (with 100 000 events per point for the simulations in this work, leading to a typical statistical uncertainty between 0.1 and 0.3 %).

7.2.2 . Electron backscattering

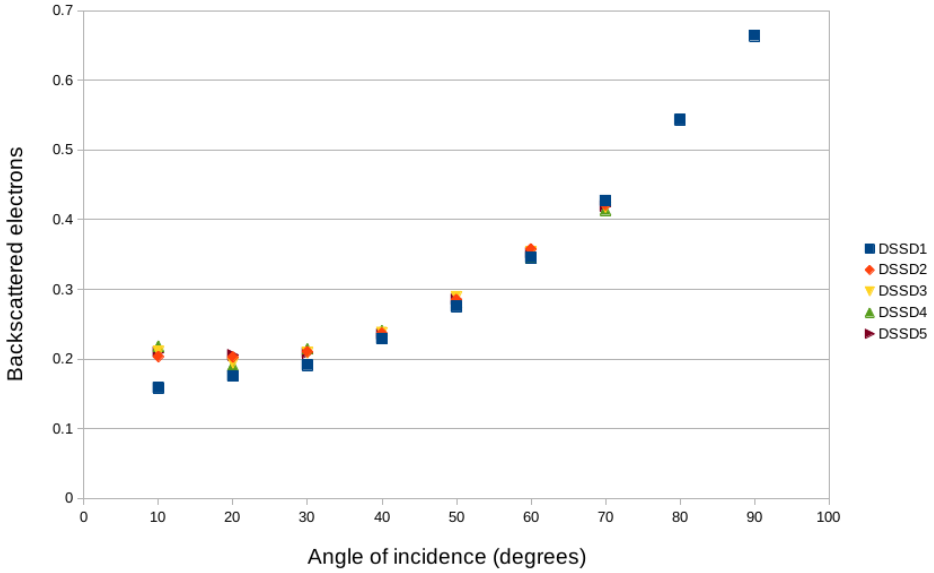

Figure 7.3: 100 keV electron backscattering ratio as a function of incidence angle on the different DSSDs in T. Goigoux simulations. A 0° incidence angle corresponds to a normal incidence. Each point represents a 10° range, with the value shown being the maximum value of the range. The first point is for electrons with 0-10° incidence angle etc.

For the electron backscattering, T. Goigoux's results are shown in figure 7.3. The backscattering ratio (number of backscattered electrons divided by number of electrons arriving on the detector at a given incidence) on DSSD1 matches the literature [85] (see figure 7.4), however a deviation is observed at low incidence angle (normal incidence) for the tunnel DSSDs. In his report, this deviation was attributed to a low number of counts at normal incidences in the tunnel. However, the fact that all tunnel DSSDs had very similar backscattering coefficients at normal incidence was strange. After reproducing those results, the deviation at low incidence angles was studied. A possible explanation for this was a bad determination of the incidence angle. In NPTool, the momentum of the emitted particles is saved in the output tree and this momentum was used to compute the incidence angle. However, the electrons were emitted from the implantation foil and interaction within the foil could change their momentum. To verify this, simulations were performed with and without the implantation foil. With the implantation foil, T. Goigoux results were perfectly reproduced. Without the foil, the deviation a low incidence angles disappeared and the simulations were in agreement with the literature (see figure 7.5). For the tunnel, there are not points for 80 and 90° as those incidences are not possible for particles emitted from the center of the implantation foil. In fact the maximal incidence angle for the tunnel detectors is ∼66°. This maximal incidence angle also explain the deviation for the point at 70° for the tunnel detectors: this point actually correponds only to the 60-66° range and not to the 60-70° range for the tunnel detectors.

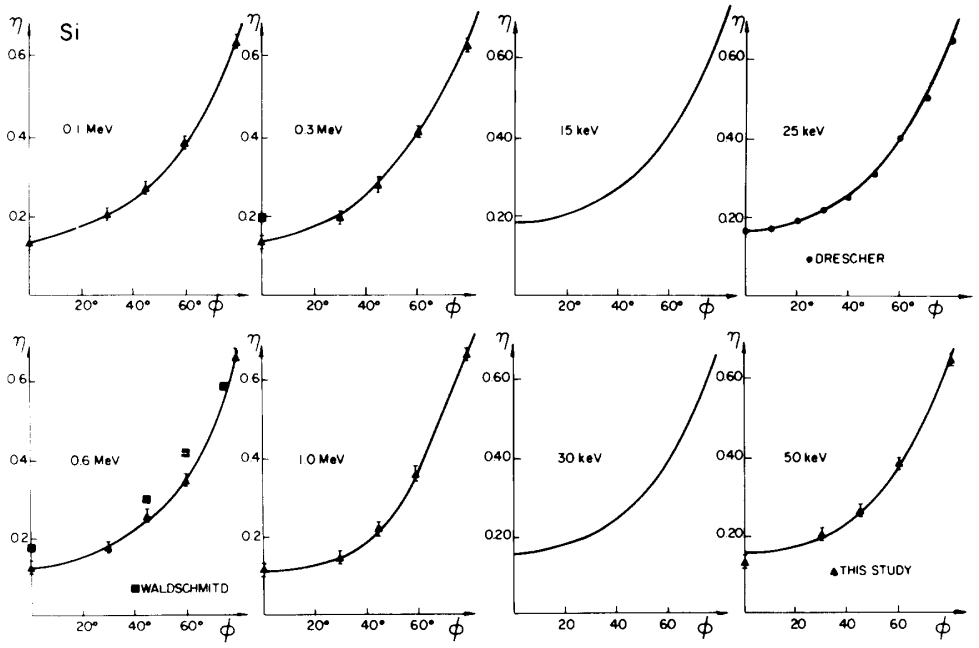

Figure 7.4: Dependence of the backscattering ratio on angle of incidence for silicon at 15, 25, 30, 50, 100, 300, 600 and 1000 keV. Figure and caption taken from reference [85].

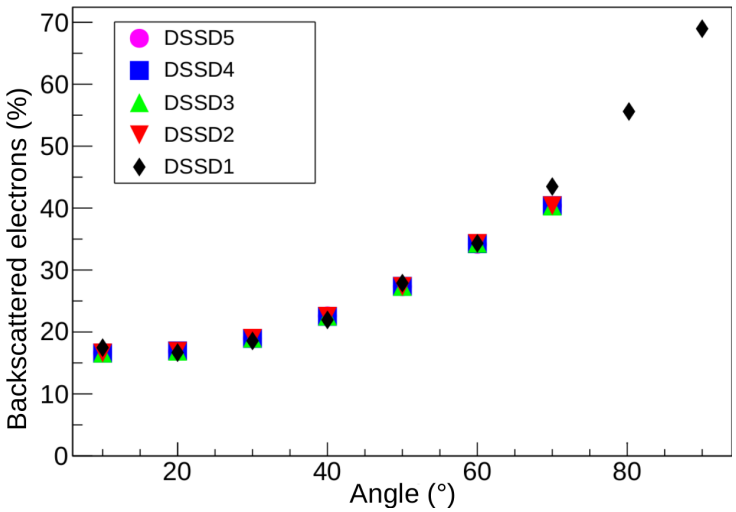

Figure 7.5: 100 keV electron backscattering ratio as a function of incidence angle on the different DSSDs in this work. Each point represents a 10° range, with the value shown being the maximum value of the range. The first point is electrons with 0-10° incidence angle etc.

7.2.3 . Simulations with BB7

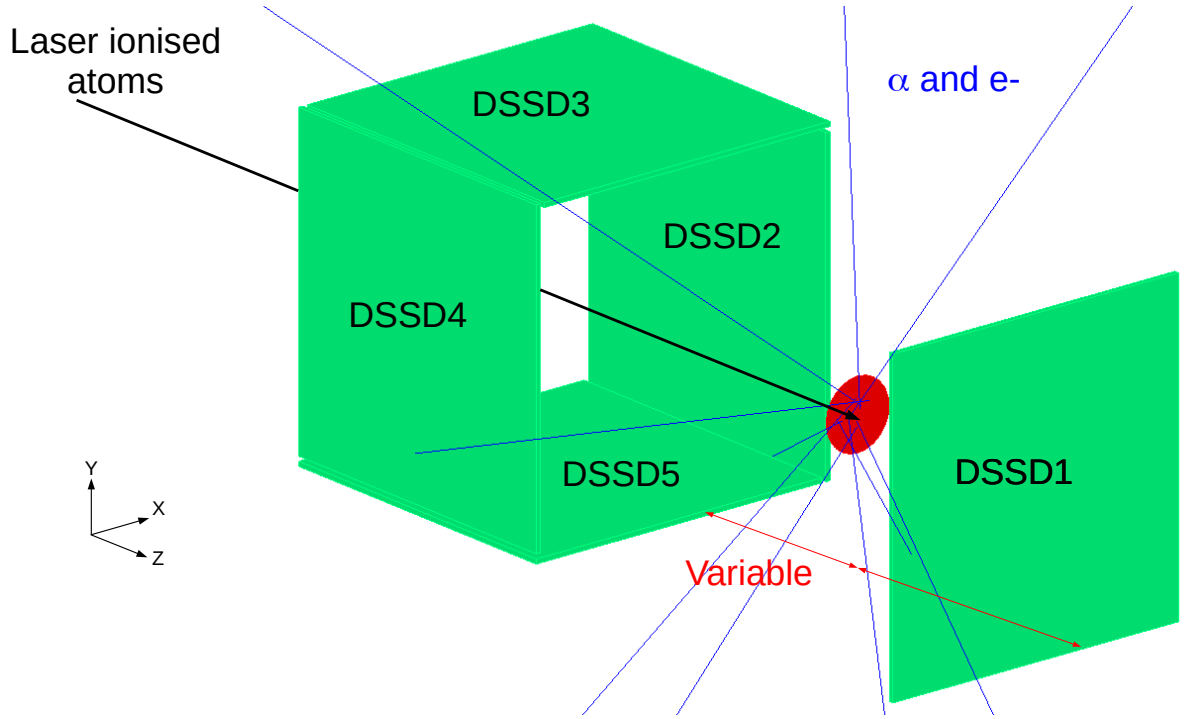

Figure 7.6: Visualisation of SEASON's main station design with BB7 detectors in NPtool.

Once the previous simulations were properly reproduced, the new detector design was implemented in the simulations (see fig. 7.6) and the detection efficiency, as well as the summing effect, were checked. Then the simulations were improved in order to take into account additional details:

- detector's guard ring,
- interstrip,
- surface dead layer,
- aluminium grid collecting the charges.

7.2.3.1 . α-particle detection efficiency

With the BB7 configuration added in the simulations, the impact of detector-foils distances was studied again (see figure 7.7 for a comparison between the previous configuration and BB7) and an α-particle detection efficiency of 87.5 % (60.0 % for the electrons) is reached in the compact configuration (2 mm distances for both tunnel-foil and DSSD1-foil distances), against 87.6 % (59 % for the electrons) with the previous compact configuration. The total efficiency is almost the same as in the previous configuration, however the distribution between detectors is slightly different. Indeed, looking into the detail for each detector, the DSSD1 efficiency is slightly lower (~ 0.5 % loss, due to a smaller detector) but the tunnel efficiency is slightly higher (~ 0.4 % gain, due to a slightly longer tunnel) such that both effects compensate.

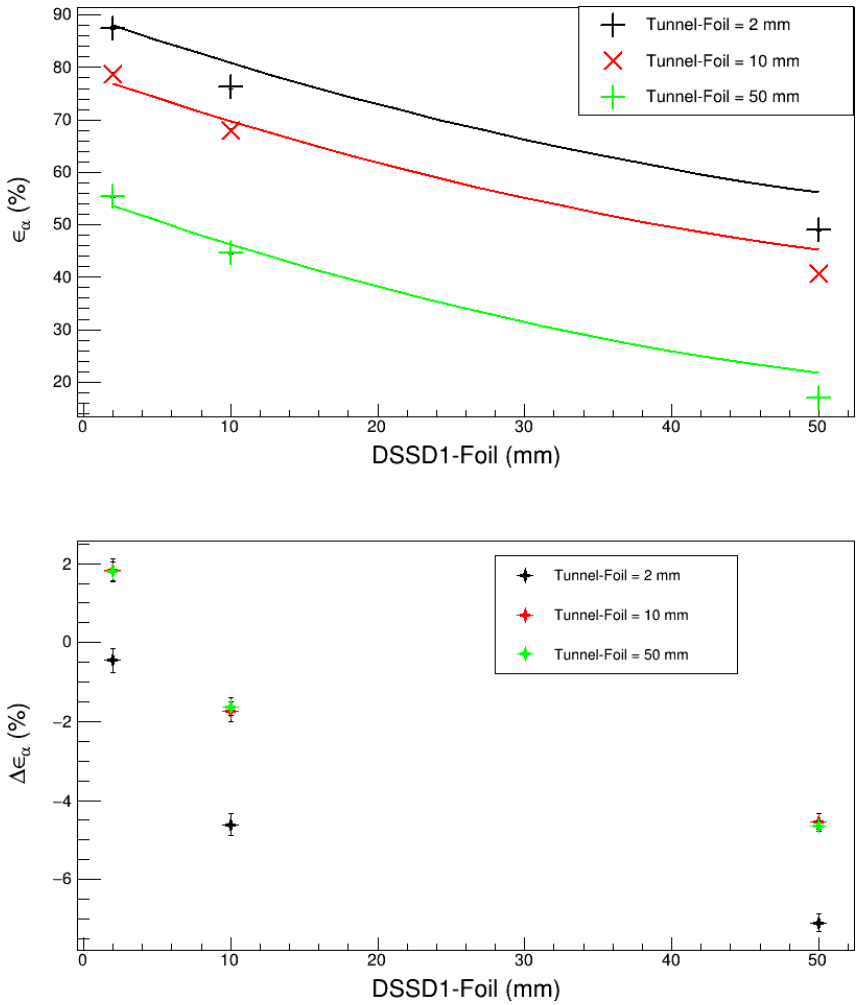

Figure 7.7: Top: Comparison between simulated detection efficiencies with the previous configuration (full lines) and BB7 simulated detection efficiencies (markers).
Bottom: Point-by-point difference between BB7 simulated detection efficiencies simulated detection efficiency with the previous configuration.

When looking at the evolution as a function of both distances, one can notice that there is a more important efficiency loss at large distances for BB7 with respect to the previous configuration. This is easily explained by the smaller detector size. As the compact configuration should be the principal one and even in high-rate experiments it is not expected to require distances larger than 10-20 mm, this was not considered as an issue.

These results confirm the choice to use the same model for all SEASON detectors as the efficiency loss induced is very low in the most compact configurations.

7.2.3.2 . Summing

The summing effect (detecting two particles at the same time in the same pixel of the detector and thus measuring their sum energy instead of the individual energy of each particle) was also studied. Indeed, during a decay, the α-particle and the conversion electrons are emitted simultaneously (except in the case of α-decay feeding an isomeric state) and one of the goals of SEASON is to be able to

access individual conversion electron energy. In addition, random summing (two uncorrelated decay at the same time with the emitted particle detected in the same pixel) can also occur, however the expected count rates for SEASON are quite low (typically a few dozens of implantations per second), thus this effect will be negligeable and was not taken into account in the simulations.

For this purpose it is necessary to verify that several simultaneously emitted particles have a sufficiently low probability of being detected in the same pixel. Two simulations were performed: one with α-particles to check each pixel counting rate and one with the simultaneous emission of several electrons.

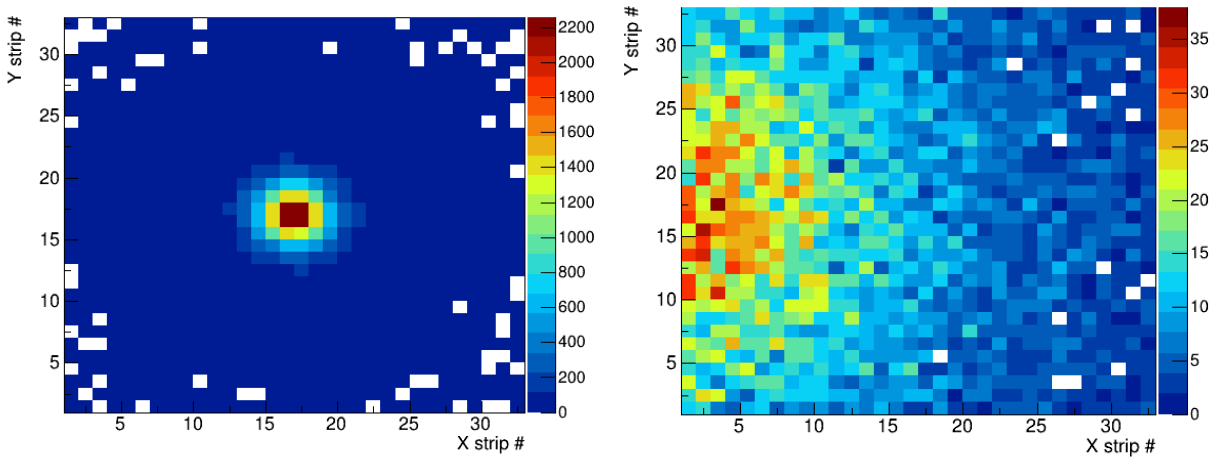

Figure 7.8: Number of counts per pixel for the isotropic emission of 100 000 α-particles. The picture on the left is the DSSD1, the picture on the right is the DSSD2 (one of the tunnel detector).

α-particles and pixel count rate A simulation was performed with 100 000 α-particles emitted isotropically from the centre of the implantation foil. The results are shown in fig. 7.8. First, one can notice that the number of counts in any single pixel in the tunnel detectors is very low. Indeed, the pixel with the highest number of counts has ∼35 counts, which corresponds to a detection efficiency of any given pixel lower than 0.035 %. Thus the summing effect will likely be negligible in the tunnel, which was expected as previous simulations showed that 1 cm strips were sufficient for the tunnel, whereas BB7 strips are 2 mm large. For this reason the tunnel channels will probably be coupled 4 by 4 in order to reduce the number of required acquisition channels. For the DSSD1 the counts are mostly concentrated in the 4 central pixels and decrease quickly when going away from the centre. The central pixels reach a detection efficiency of ∼2.2 %. The summing effect in those pixels needs to be checked with the simultaneous emission of several particles.

Simultaneous emission of several electrons To check the summing effect, simulations were performed with the simultaneous emission of an α-particle and several electrons. An α-particle and from 1 to 5 electrons were emitted simultaneously from the implantation foil. This high number of emitted conversion electrons can appear in the de-excitation of isomeric states passing through series of highly converted M1 transitions (for example in the case of ^{254}No [120]). A simulation was also performed with the emission of only 1 electron and no α-particle to use as a reference. For each number of emitted particles several detector-foil distances were considered (2, 3, 4, 5, 7, 10 and

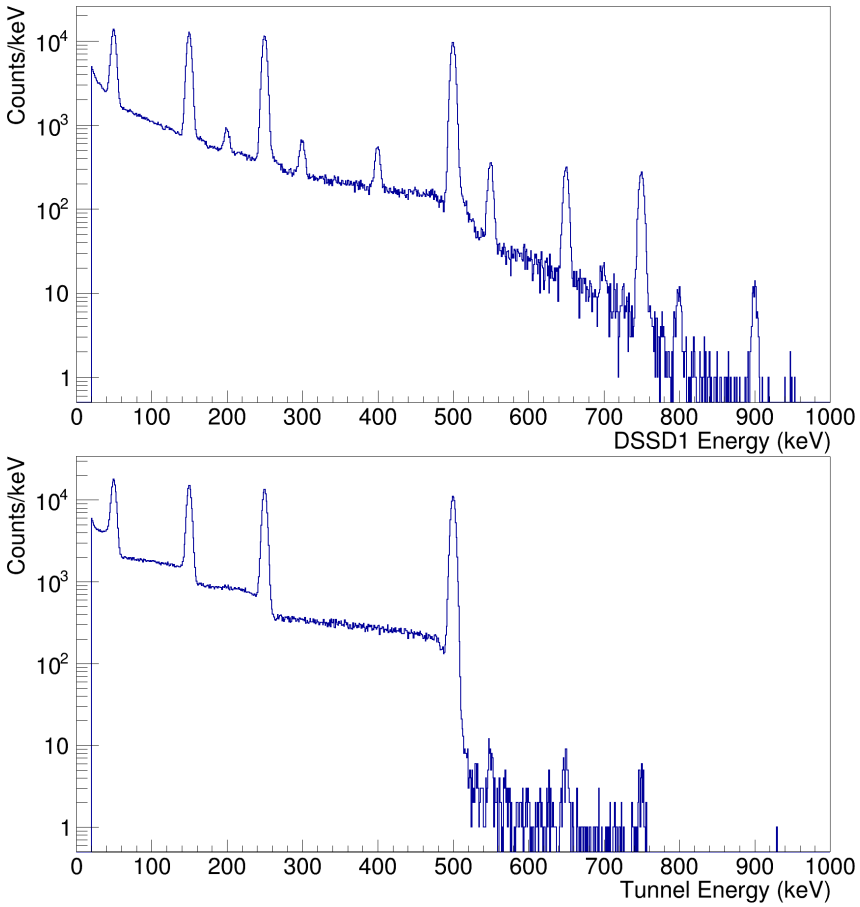

Figure 7.9: Energy spectrum for DSSD1 (top) and all tunnel detectors (bottom) taken from a simulation with the simultaneous emission of 1 α-particle and 4 electrons (50, 150, 250 and 500 keV) in compact configuration. Clear summing peaks appear on DSSD1 and small summing peaks appear on tunnel detectors.

15 mm). For the sake of simplicity the tunnel-foil distance was always the same as the DSSD1-foil distance in order to reduce the amount of simulations needed. For each number of emitted particles and, for each detector-foil distance, 400 000 events were simulated, with one event corresponding to the emission of 1 to 6 particles depending on the simulation. The simulations were performed assuming an 7 keV intrinsic energy resolution (FWHM) for the detector as this is the energy resolution SEASON should achieve for conversion electrons.

The spectra in the case of the emission of an α-particle and 4 electrons, with energies 50, 150, 250 and 500 keV, are shown in figure 7.9. When less than 4 electrons are emitted, only the lower energy peaks are used (thus, in the case of 1 electron emitted, its energy is 50 keV, in the case of 2 electrons it is 50 and 100 keV etc.). In the case of the emission of 5 conversion electrons, an electron is added with 125 keV energy. Those energies are choosen so that summing peaks cannot fall at the same energy as individual conversion electron peaks. The summing peaks are almost non-existent from the tunnel detectors spectrum. This is consistent with the observation of section 7.2.3.2.

For the DSSD1, summing peaks clearly appear. The four main peaks correspond to the detection of a single electron. Then there are six peaks of similar intensities at 200, 300, 400, 550, 650 and

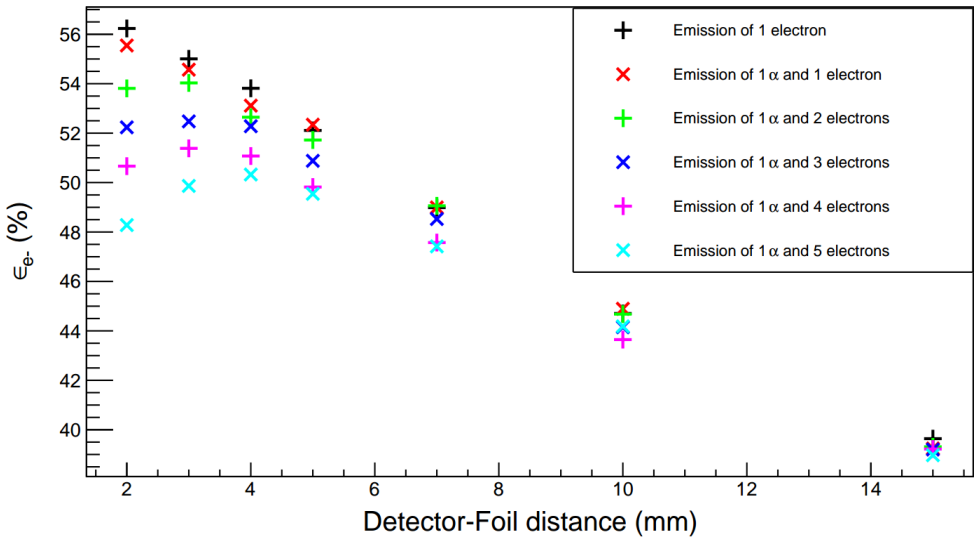

Figure 7.10: Electron single detection efficiency, for all detectors combined, as a function of detector-foil distance for several numbers of emitted particles. The efficiency is measured for the 50 keV electron peak. Statistical uncertainties are not shown as their size is typically of the order of the marker size.

750 keV that correspond to the simultaneous detection of two electrons. Four peaks of even smaller intensities also appear at 450, 700, 800 and 900 keV corresponding to the simultaneous detection of three electrons. Finally the smallest peak at 950 keV corresponds to the simultaneous detection of all four electrons. In addition, similar peaks, resulting from the summing of a conversion electron and the α-particle, appear near the peak corresponding to the detection of the α-particle (not shown here).

By extracting the single detection efficiency (i.e. the probability to detect a conversion electron at the right energy) for a given peak in each simulation, the impact of the number of emitted particles on the single detection efficiency can be checked as a function of the detector-foil distances. The single detection efficiency is computed by fitting the peaks with a gaussian function and a background in order to extract the integral of the peak. This integral is then divided by the number of electrons emitted at this energy. The simulations were performed with the effects detailed in section 7.2.4, 7.2.5 and 7.2.6 taken into account to be as close as possible to the final setup, hence a lower single detection efficiency than before in the case of the emission of 1 electron. The results for the 50 keV peak are shown in figure 7.10. On this figure, for three or more emitted particles, the electron single detection efficiency clearly starts by increasing when the detector-foil distance increases, before decreasing at higher distances. This effect is due to a competition between the increase in efficiency coming from the reduction of the summing effect and the decrease in geometrical efficiency.

When plotting the single detection efficiency separately for the DSSD1 and for the tunnel detectors (see figure 7.11) it appears clearly that this summing effect is only present in the DSSD1 and not in the tunnel detectors, even for a large number of emitted particles. This is one more confirmation that the summing effect in the tunnel is negligible.

Table 7.1 gives the optimal distances for DSSD1 for each number of emitted particles, as well as the associated total single detection efficiency. The total single detection efficiency is calculated with the tunnel detectors placed in the compact configuration. In the case where 5 conversion electrons

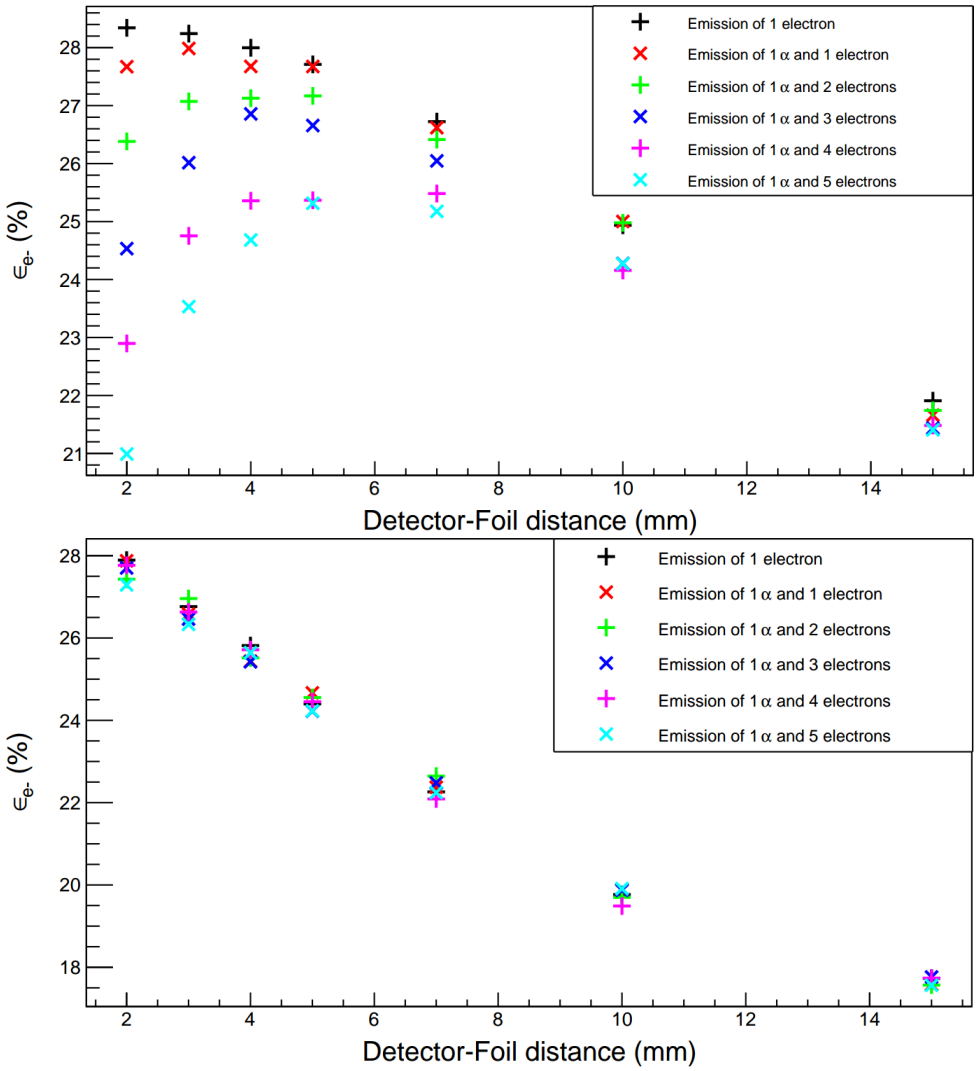

Figure 7.11: Electron single detection efficiency in DSSD1 (top) and in the tunnel detectors (bottom) as a function of the detector-foil distances for several numbers of emitted particles. The efficiency is measured for the 50 keV electron peak. Statistical uncertainties are not shown as their size is typically of the order of the marker size.

$N_{emitted}$	D_{opt} (mm)	ϵ_{tot} (%)
1	2	56.2
2	3	55.9
3	4	55.0
4	4	54.7
5	5	53.3
6	5	53.2

Table 7.1: Single detections efficiencies ϵ_{tot} with the DSSD1 placed at the optimal distance D_{opt} for each number of emitted particles $N_{emitted}$.

are expected to be emitted in coincidence with an α-particle the loss of single detection efficiency is only of ∼3 %.

In some cases several conversion electrons might be emitted simultaneously while only one was expected. In such cases the setup would be in its compact configuration instead of the optimal one for conversion electron detection. This would lead to a single detection efficiency lower than what is given in table 7.1. Considering the case where 5 conversion electrons are emitted simultaneously with the setup in its compact configuration, leading to the simultaneous emission of 6 particles, the single detection efficiency loss is ∼8 %, reducing the electron detection efficiency to 48.3 %. This correspond to the difference between the black (emission of 1 electron) and light blue (emission of 1α and 5 electrons) curves for a 2 mm detector-foil distance in figure 7.10.

7.2.4 . Guard Ring

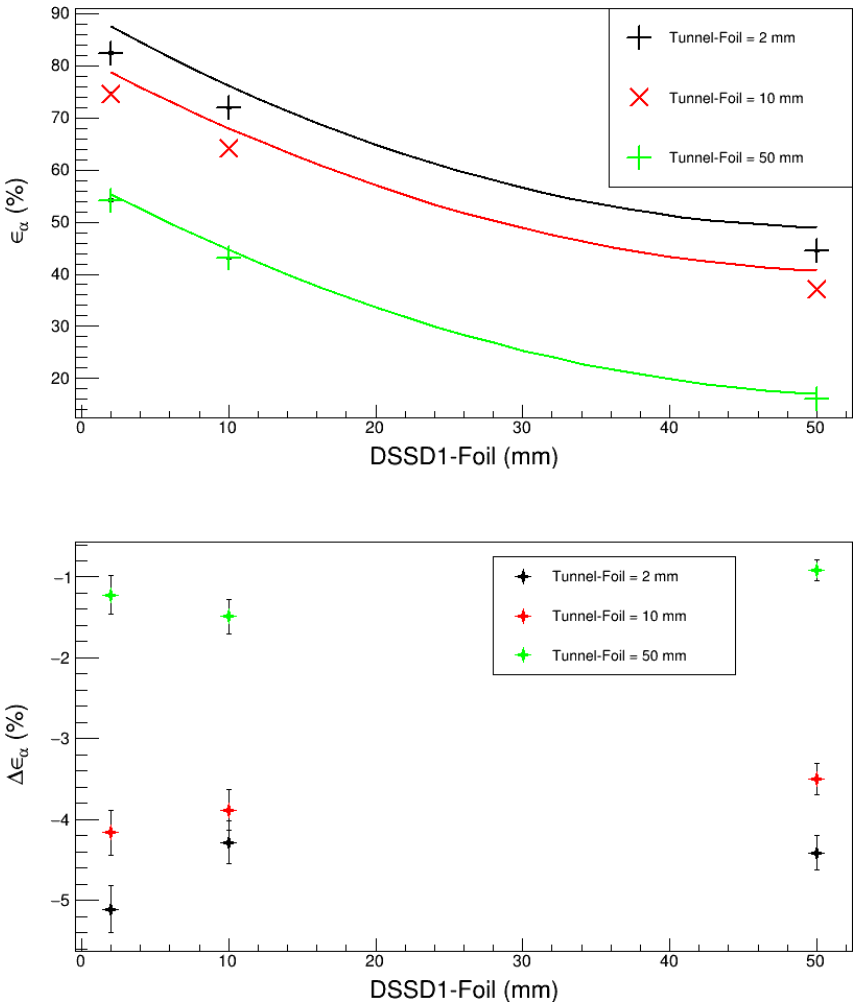

Figure 7.12: Top: Comparison between SEASON α-particles simulated detection efficiencies without (full lines) and with (markers) the guard ring.
Bottom: Point-by-point difference between SEASON α-particles simulated detection efficiencies with and without the guard ring.

Up to this point, simulations were performed assuming that the detector only consisted of it's

active area. To improve the simulation, the guard ring of the detector were taken into account. Indeed, if the detector's support was chosen so that the active area of the detector could be placed as close as possible from the implantation foil, the detector itself has a thin (2 mm) inactive area on the whole border due to the presence of the guard ring. This effectively increases by 2 mm the distance between the active part of the tunnel detectors and the wheel. This also increases the distance between the active part of the different tunnel detectors. Hence this will reduce the detection efficiency.

A comparison with what was obtained without the guard ring is shown in figure 7.12. With the guard ring, the detection efficiency is globally lower. This efficiency loss is more or less constant when DSSD1-foil distance increases, but decreases with larger tunnel-foil distances.

In compact configuration the α-particle detection efficiency decreases from 87.5 % to 82.4 % and the electron detection efficiency decreases from 60.0 % to 55.5 % (without taking into account summing effects).

7.2.5 . Interstrip

In a DSSD, the strips are separated by a small interstrip area (see section 6.2.3). Events occurring in this interstrip area can be reconstructed as the charges are collected by the neighbouring strips, however this is a difficult process. This interstrip was including in the NPTool simulations, reproducing the charge deposition within the detector and thus, when a charge particle interact in the interstrip area, the energy deposition is properly splitted between the two strips. The choice was made to assume that we will not be able to reconstruct properly the interstip event. Thus the interstrip had to be taken into account to have an accurate detection efficiency. The possibility to handle interstrip this way was already implemented in NPTool but was not used in the SEASON simulations before and thus was added at this stage. The total strip width and the active width are given in reference [118] under the names of "Strip Pitch" and "Strip Width". The strips are 2 mm width and, for the front side of the detector, the active width is 1.925 mm, with a 75 µm large interstrip. For the back side the active width is 1.960 mm, with a 40 µm large interstrip (see section 6.2.3).

This was included in the simulations and a comparison with what was obtained considering only the guard ring is shown in figure 7.13. As could be expected, the detection efficiency is once again globally lower than before, with a larger absolute loss at small detector-foil distances.

In the compact configuration, the α-particle detection efficiency decreases from 82.4 % to 79.2 % and the electron detection efficiency decreases from 55.5 % to 52.2 % (without taking into account summing effects).

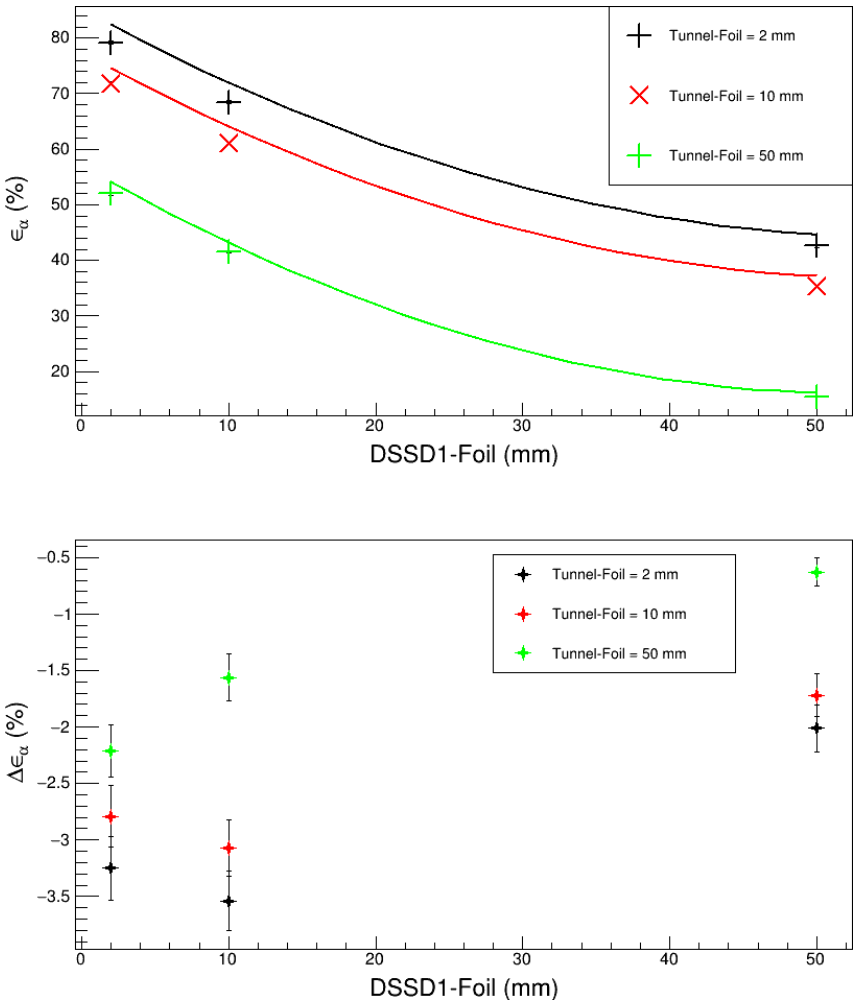

Figure 7.13: Top: Comparison between SEASON α-particles simulated detection efficiencies with the interstrips and guard ring (markers) and with only the guard ring (full lines). Bottom: Point-by-point difference between SEASON α-particles simulated detection efficiencies with and without the interstrips.

7.2.6 . A more compact tunnel

In the initial configuration, the tunnel detectors were separated from each other by 2 mm horizontally and 2 mm vertically (see left side of figure 7.14). However, after discussion with the team designing the mechanical structure, this distance could be reduced to 1 mm either vertically or horizontally (see right side of figure 7.14). This change leads to a considerably more compact tunnel and thus a higher detection efficiency.

The resulting efficiencies as a function of both detector foil distances are shown in figure 7.15. In the compact configuration, the α-particle detection efficiency increases from 79.2 % to 83.3 % and the electron detection efficiency increases from 52.2 % to 56.2 % (without taking into account summing effects).

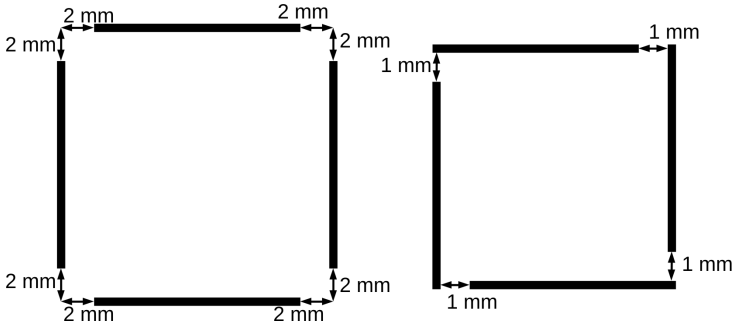

Figure 7.14: Left: Initial configuration for the tunnel detectors, viewed from the implantation foil.
Right: Final configuration for the tunnel detectors, viewed from the implantation foil.

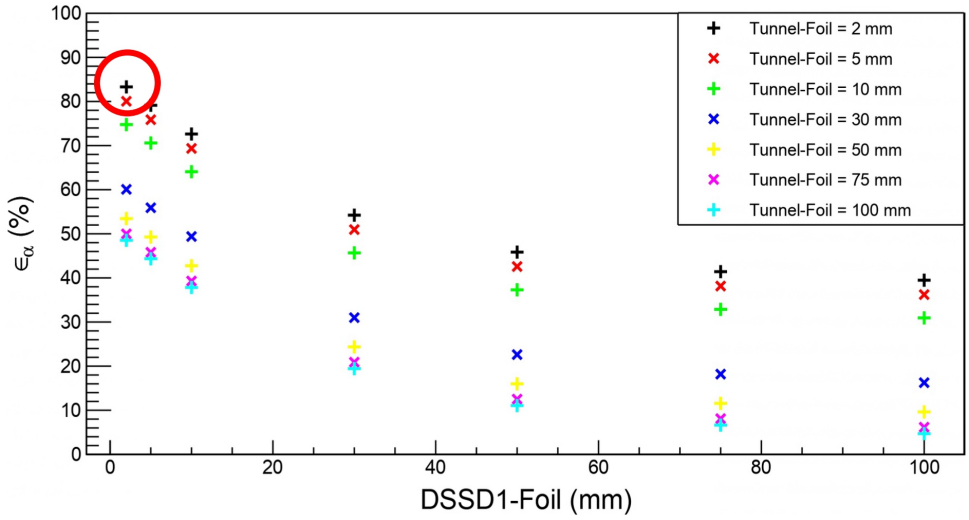

Figure 7.15: Final α-particle detection efficiencies as a function of both detector foil distances. The red circle denotes the expected configuration for SEASON.

7.2.7 . Dead layer and aluminium grid

Up to now, only the detection efficiency was studied in the simulations. However, the energy resolution of the detector is also a critical point and the materials seen by the particles before interacting in the detector can have a important impact on this energy resolution.

In this context, an extensive study of the implantation foils was performed and is detailed in chapter 8, but the dead layer of the detectors is also a critical point and, contrary to the implantation foil, this could not be studied experimentally.

Indeed, before entering the active area of the detector, the particle passes through the electrode collecting the charges. Typically a metallic electrode covers the whole active area, but Micron offers an option (called "P metallisation type") where the metallic electrode only covers the periphery of the active area. In front of the active area, only a dead layer remains, made of a thin layer of doped silicon. Several thicknesses are available for this dead layer, going from 50 nm to 500 nm. The goal of the energy loss simulations was to verify the impact of this dead layer and determine what was its appropriate thickness to maintain a good energy resolution.

The simulations were performed with a spatially extended α-source emitting 8 MeV α-particles isotropically. Implantation simulations performed by T. Goigoux gave an implantation depth of 6 nm for 3 keV ions (the expected kinetic energy of ions arriving from the LEB) in a 20 µg/cm^2 carbon implantation foil. Thus the α-source was placed in the simulations in a plan at 6 nm depth (corresponding to the implantation depth obtained in SRIM simulations for carbon foils) in the implantation foil, with a spatial extent in the foil's plane of 5 mm FWHM (gaussian distribution) matching the expected width of the ion beam. Several dead layer thicknesses were simulated (0 nm, 10 nm, 50 nm, 100 nm, 300 nm and 500 nm), both with and without an implantation foil. The energy loss and the straggling produced by those thicknesses were studied. SEASON aims at a final energy resolution between 15 and 20 keV FWHM for the α-particles and 7 keV FWHM energy resolution for the electrons. To reach those resolutions the straggling created by the dead layer and the implantation foil have to be reduced as much as possible.

Simulations were performed assuming a 16.5 keV FWHM detector intrinsic resolution for the detection of α-particles, similar to the intrinsic energy resolution observed currently in the detector tests. The effective energy resolution and the energy loss were then deduced from the simulations for both DSSD1 and DSSD2 and used to compute the straggling induced by the dead layer and the implantation foil with the formula $\Delta_{stragg} = \sqrt{\Delta_{sim}^2 - \Delta_{int}^2}$ with Δ_{sim} the simulated energy resolution (FWHM) and Δ_{int} the intrinsic energy resolution (FWHM). The results are reported in table 7.2.

Dead layer	Without implantation foil (keV)						With implantation foil (keV)					
	DSSD1			DSSD2			DSSD1			DSSD2		
	Δ_{sim}	Δ_{stragg}	E_{loss}	Δ_{sim}	Δ_{stragg}	E_{loss}	Δ_{sim}	Δ_{stragg}	E_{loss}	Δ_{sim}	Δ_{stragg}	E_{loss}
0 nm	16.5	0.0	0.0	16.5	0.0	0.0	20.9	12.8	16.1	17.2	4.8	1.9
10 nm	17.2	5.0	2.7	16.7	2.5	1.5	21.0	13.0	17.4	17.2	4.8	3.5
50 nm	19.1	9.6	9.4	17.6	6.2	7.2	22.1	14.7	22.6	17.5	5.8	9.3
100 nm	20.9	12.9	16.6	18.8	9.0	14.0	23.1	16.2	28.8	19.1	9.7	16.4
300 nm	25.0	18.8	40.9	24.6	18.2	40.3	27.7	22.3	53.1	24.7	18.4	42.7
500 nm	29.2	24.1	64.8	27.9	22.5	64.4	31.1	26.4	76.2	26.2	20.4	66.2

Table 7.2: Simulated energy resolution Δ_{sim} (keV), straggling induced by the foil and the dead layer Δ_{stragg} (keV) and energy loss E_{loss} (keV) for DSSD1 and for a tunnel detector (DSSD2), for different dead layer thicknesses and both with and without the implantation foil (20 µg/cm ^{2}).

The results shows that the implantation foil and the dead layer can have an important impact on the energy resolution, inducing up to 26 keV straggling, much more than the expected intrinsic energy resolution of the detector. Notably, considering the implantation foil and a 100 nm dead layer, the straggling induced by the materials is already at 16 keV in DSSD1. Thus, to ensure energy resolutions below 20 keV, the choice was made to use a 50 nm dead layer.

One can also notice that the straggling induced by the materials is globally lower in the tunnel detectors than in the DSSD1. This is due to the geometric configuration of the setup: the α-particles arrive in the tunnel detectors with an incident angle in average closer to the normal incidence than for the DSSD1. This leads to a lower effective thickness seen by the particles and thus a lower straggling. In addition, the implantation in the foil is very shallow. Hence the implantation foil produces almost no straggling for the tunnel detectors whereas it produces an important straggling for the DSSD1.

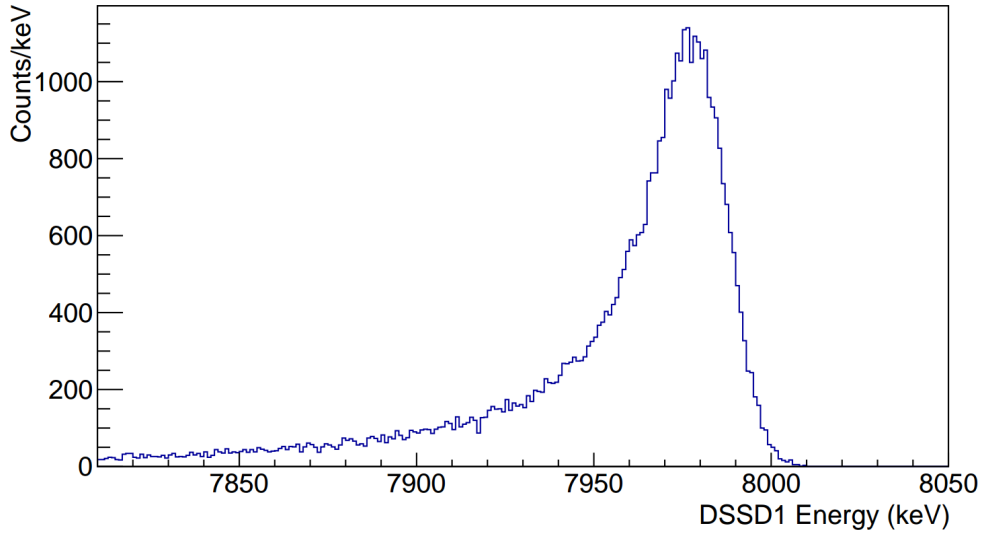

Figure 7.16: Energy spectrum for DSSD1 taken from simulations with the emission of 100 000 α-particles isotropically at 8 MeV. The low-energy tail is due to the difference in dead layer thickness seen by α-particles arriving in different pixels.

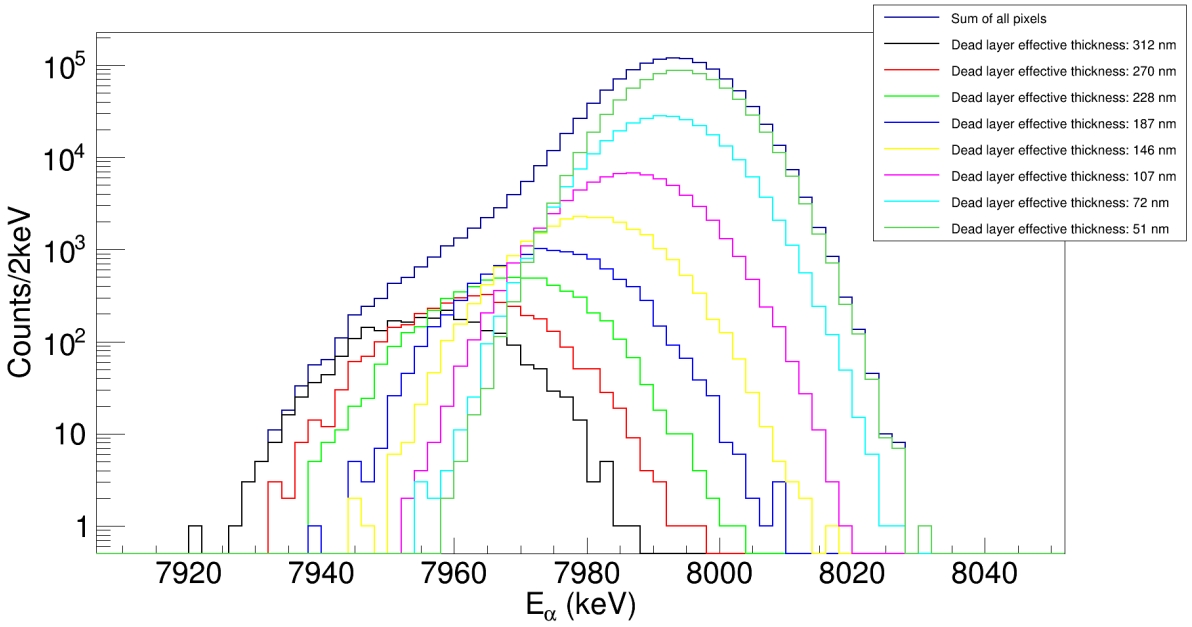

Figure 7.17: Energy spectra for pixels along the DSSD1 diagonal from simulations with the emission of 100 000 000 α-particles isotropically at 8 MeV. The source is placed 5 mm away from the detector. Each spectrum correspond to a given pixel along the diagonal and is labeled by the thickness of dead layer seen by an α-particle arriving at the middle of the pixel. The sum energy spectrum is also represented.

In addition to this straggling, it was noticed that a important tail appear on the low-energy side of the α-peaks in DSSD1 (see fig. 7.16). This arises from the fact that from one strip to another the incidence angle changes and thus the effective thickness seen by the α-particle changes. For two neighbouring strips the change is small, but between a central and peripheral strip in DSSD1 the difference can be important. For example, an α-particle arriving in one corner of the detector has an incidence angle of 87.5°. This means that with a dead layer of 50 nm, the thickness seen by the α-particle arriving in this pixel is roughly 1.1 µm. However, this tailing effect is expected to be reduced by a proper strip-by-strip (or even pixel-by-pixel) calibration. This can be seen in figure 7.17 where the α-energy spectra are plotted for several pixels along the diagonal for the DSSD1. The tail appearing on the sum spectrum arises mainly from the increase of average energy loss from one pixel to the other and thus a proper alignement of all pixels will significantly reduce the tail of the peak.

For the electrons, the transport through materials has a much smaller effect and simulations showed that it was small with respect to electronic noise. Indeed, even with a 500 nm dead layer and the implantation foil, the straggling is only 2.5 keV. With the chosen 50 nm dead layer and the implantation foil, this straggling is reduced to 1.2 keV, thus the electron energy resolution will be dominated by the electronic noise and the detector intrinsic resolution, and not by the straggling induced by the materials.

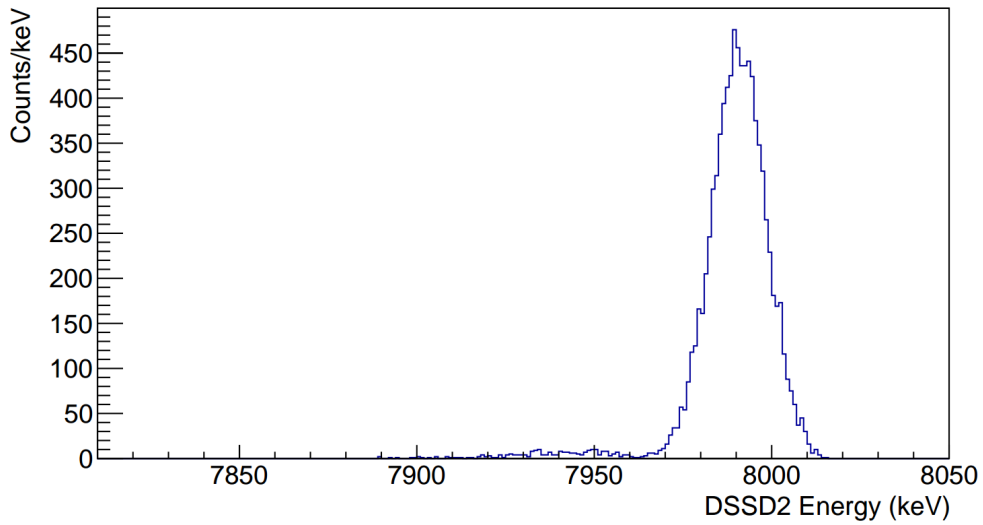

Figure 7.18: Energy spectrum for DSSD2 taken from simulations with the emission of 100 000 α-particles isotropically at 8 MeV. A structure appears around 7940 keV due to the aluminium grid.

In addition to the dead layer, there is an aluminium grid (30 µm large and 300 nm thick) around each strip to collect the charges. This grid does not lead to a significant change in the energy resolution or in detection efficiency. However it create a small lower-energy duplicate of the α-peak in the tunnel detectors (see fig. 7.18). This is understood as α-particles passing through the grid and arriving in a strip. This effect might also be present in the DSSD1, however it is hidden by the tailing effect of the dead layer. This needs to be taken into account in the future, especially for experimental data analysis.

7.3 . Summary

The simulations of SEASON's main station were performed with GEANT4 and NPTool. Previous simulations were reproduced and improved, and a good understanding of the expected behaviour of the detector was reached. The expected detection efficiency was characterised and a final value of 83.3 % (56.2 %) was reached for the α-particles (electrons) detection efficiency. This high efficiency will be important for the study of low production rate isotopes. In addition, the effect of the detector's dead layer on the energy resolution was studied, as well as the effect of the implantation foil, and enabled a decision on the dead layer thickness to be used for the detectors: 50 nm. For the implantation foil, a detailed study will be presented in the next chapter.

In addition, a unexpected effect of the aluminium grid surrounding the strip was noticed: it deforms the α-particles energy spectra in the tunnel, creating a small lower energy duplicate of the peaks.

8 - Implantation Foils

As noted in the previous chapter, the materials seen by the α-particles before detection have an important effect on the energy resolution. The implantation foil has a large contribution to this effect, especially for the DSSD1. Having a thinner implantation foil can thus improve significantly the final energy resolution. Carbon foils are typically used for this kind of setup (for example for the Windmill setup at ISOLDE [121]) and thus ∼20 µg/cm^2 carbon foils was the easiest solution for SEASON. However, using another, more robust, material could help to make thinner foils and thus reduce the straggling induced by them. Silicon Nitride (SiN) is known to be robust and thus could be a good option. However, SiN foils are not commonly used in nuclear physics and thus their behaviour in our experimental conditions must be checked. In addition, the SiN foils are much more expensive than the carbon foils (∼10 times more) and thus a significant gain with respect to carbon foils is needed for them to be worthwhile.

A comparative study of thin carbon and SiN foils was performed to characterise their performances for the SEASON detector and is presented in this chapter. The main goal is to minimise energy losses and straggling of α-particles going through the foil. The ease of use of the foils, as well as their cost, should also be considered.

Simulations showed the potential impact of the foils choice on the energy resolution. Then a study was performed with a test bench at DEDIP (Département d'Electronique des Détecteurs et d'Informatique pour la Physique), CEA. Additional measurements by Transmission Electron Microscopy (TEM) was performed for SiN foils using the JANNuS facility at IJCLab.

Three suppliers of foils were considered :

1. carbon foils produced at GANIL by G. Frémont;
2. SiN foils supplied by SILSON [122];
3. carbon foils supplied by ACF Metal [123].

8.1 . Simulations

Before testing the foils with a test bench, GEANT4 simulations were performed as a preliminary study. The simulation was performed with an α-source placed in front of a silicon detector. A foil could be placed in the simulations in-between the source and the detector (see figure 8.1), and the foil material and thickness were adjustable. This was set to reproduce the test bench presented in section 8.2 and the distances are the same as the ones presented in figure 8.3: 16 mm between the α source and the sample foil and 55 mm between the sample foil and the detector.

The detector was set with an intrinsic energy resolution of 11 keV FWHM, matching the expected energy resolution of the detector used in the test bench detailed in section 8.2. For each combination of foil material and thickness, 100 000 α-particles were emitted isotropically with a 5 MeV kinetic energy. The simulation results are shown in figure 8.2 and in table 8.1. One can see that the 20 µg/cm^2 carbon foil already contributes around 8 keV to the straggling, and that it creates an important energy loss. This effect will be amplified for SEASON, as the particles will be emitted directly from the foil and the detectors are very close, especially the DSSD1, the effective thickness seen by the α-particles can

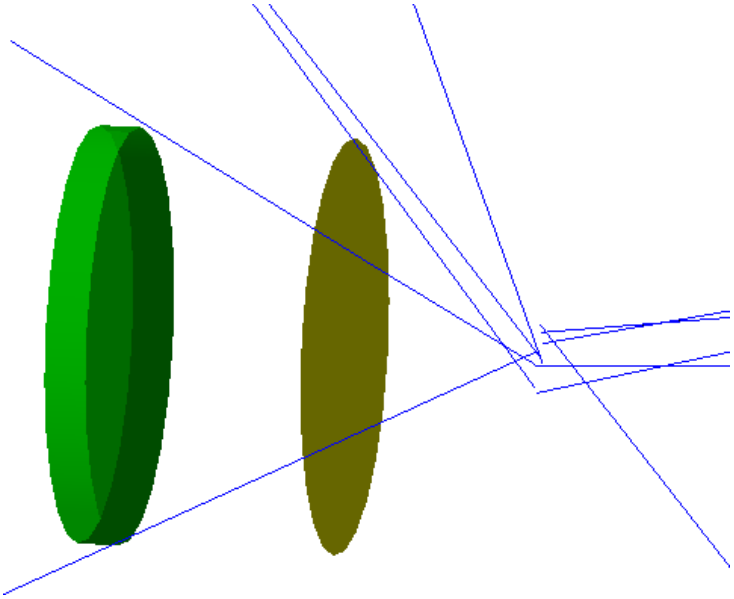

Figure 8.1: Visualisation of the test bench simulations in NPTool.

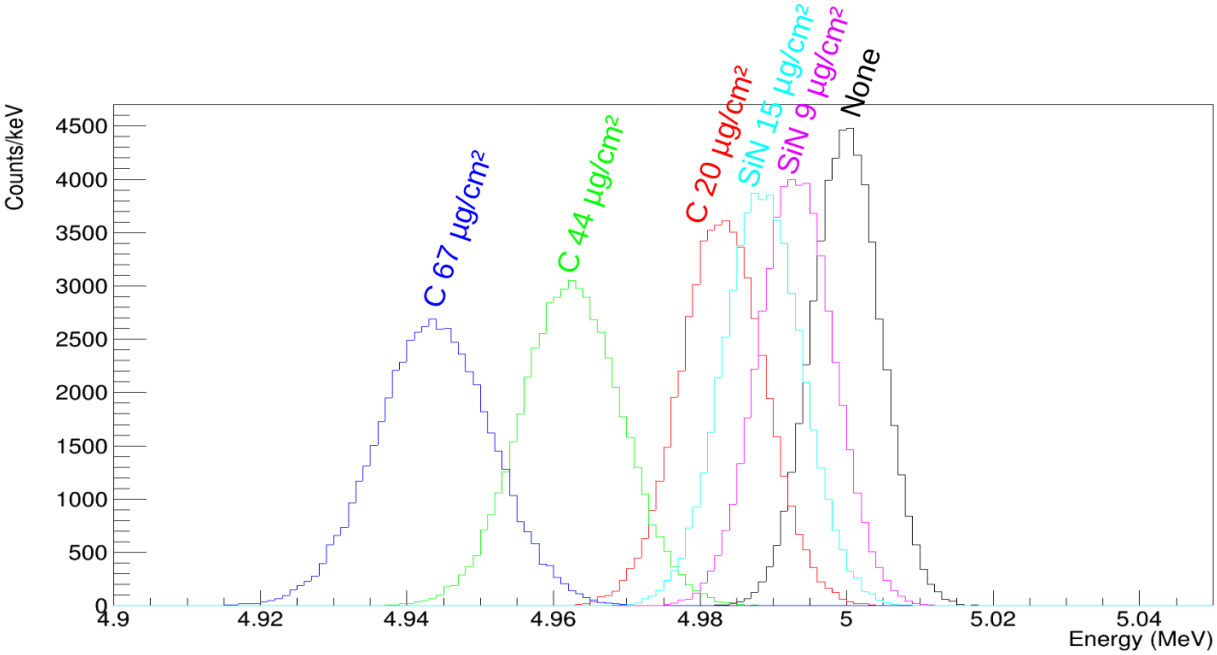

Figure 8.2: α energy spectra in the silicon detector for each foil material and thickness. In each case, 100 000 α-particles with a 5 MeV kinetic energy were emitted isotropically.

Material	Foil Thickness		E_{loss}	Δ_{meas}	Δ_{stragg}
	($\mu g/cm^2$)	(nm)	(keV)	(keV FWHM)	(keV FWHM)
None	0	0	0	11	0
C	20	90	17	13.5	7.9
	44	200	38	16.2	11.9
	70	300	56	18.4	14.8
SiN	9	30	7	12.1	5.0
	15	50	11	12.8	6.5

Table 8.1: Simulated energy resolution Δ_{meas} (keV FWHM), straggling induced by the foil Δ_{stragg} (keV FWHM) and energy loss E_{loss} (keV) for different implantation foil materials and thicknesses.

be much larger. The thicker carbon foils degrades things even more. For the SiN foils, the straggling and the energy loss are reduced with respect to the 20 $\mu g/cm^2$ carbon foil. An experimental study is needed to verify this and determine whether it is worthwhile to use those SiN foils or not.

8.2 . Test bench

For the experimental study, a test bench was already developed for similar studies for the FAL-STAFF emissive foils [124] and thus was easily available for our study.

8.2.1 . Setup

In a vacuum chamber, an α-particle source and a silicon detector are placed face to face. The sample foil is placed on a motorised support in-between the source and the detector. Then one can study the α-spectrum in the silicon detector with and without the sample foil in-between and measure the energy loss in the sample foil and the associated degradation of the energy resolution (straggling).

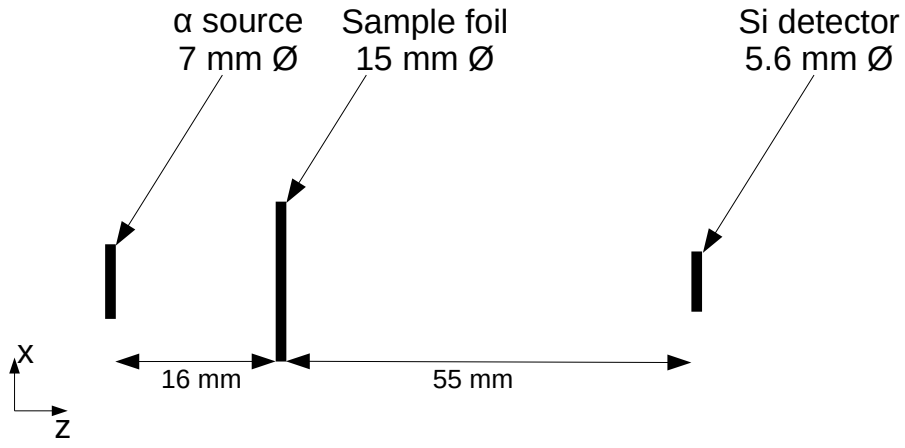

Figure 8.3: Schematic view (from above) of the test bench. The sample foil can move along the x-axis and rotate around the y-axis (vertical axis).

A schematic view of the setup can be seen in fig. 8.3.

Emitter	E_α (keV)	I_α (%)
^{239}Pu	5105.5 (8)	11.94 (7)
	5144.3 (8)	17.11 (14)
	5156.59 (14)	70.77 (14)
^{241}Am	5388 (1)	1.66 (2)
	5442.80 (13)	13.1 (3)
	5485.56 (12)	84.8 (5)
^{244}Cm	5762.64 (3)	23.1 (1)
	5804.77 (5)	76.9 (1)

Table 8.2: Energies E_α (in keV) and intensities I_α (in %) of the α-particle emitted by the 3-α source (values are taken from NNDC data base).

The α-source is a combination of ^{241}Am, ^{244}Cm and ^{239}Pu (in the following referred as 3-α source) with a nominal activity $A = 3$ kBq $\pm$ 30 %; the diameter of the active area is 7 mm. The energies and intensities of the emitted α-particle are reported in Table 8.2. This source has a 50 µg/cm^2 gold coating.

The Si detector is a circular PIPS (Passivated Implanted Planar Silicon) detector (25 mm^2 area, 100 µm thickness) with a resolution of ∼12 keV FWHM.

The sample foil is placed in between the source and the detector and can move along the x-axis as shown on the scheme of figure 8.3 in order to have measurements with and without the foil. It can also rotate around the vertical axis to perform measurement with a non-normal incidence. Those measurement with a non-normal incidence were used to test that the SiN foil internal structure was not allowing for channelling effects (see section 8.4.1). Data are accumulated for a given position of the sample foil (usually for 30 min) and then a motor moves the sample foil to the next position where data are accumulated again. In a typical measurement, a few points are first taken without the foil (usually 2 or 3), then a few points are taken with the sample foil (usually between 3 and 6) and at the end again a few points whitout the foil (usually 2 or 3).

8.2.2 . Analysis

E_α (keV)	S (keV/(µg/cm^2))	
	Carbon	SiN
5105.5 (8)	0.7981	0.6579
5144.3 (8)	0.7940	0.6549
5156.59 (14)	0.7927	0.6538
5388 (1)	0.7683	0.6355
5442.80 (13)	0.7625	0.6312
5485.56 (12)	0.7579	0.6277
5762.64 (3)	0.7322	0.6083
5804.77 (5)	0.7284	0.6054

Table 8.3: Stopping power S (in keV/(µg/cm^2)) given by SRIM for α-particles at a given energy E_α (in keV) and for a given material.

The analysis starts with a check that all spectra taken without the sample foil are properly aligned together in order to sum them. The same process is applied to the spectra taken with the sample foil. With that, one obtains two un-calibrated spectra, one taken without the sample foil and one taken with the sample foil. The spectra are then fitted with the skewed gaussians presented in section 4.1.2. For each emitter in the source, a set of skewed gaussians (with the same shape parameters for a given emitter and with relative intensities forced to the literature relative intensities) is used to fit the proper energy range of the spectrum in order to extract the centroids and the width of the peaks.

Then the centroids extracted from the spectrum taken without the sample foil are used to make an energy calibration using the literature values given in table 8.2. With this energy calibration, one can extract the energy for each peak with and without the foil and compute the energy loss in the sample foil $\Delta E = E_{nofoil} - E_{foil}$ for each α-peak.

Once the energy loss ΔE is extracted, one can use it, combined with SRIM simulations, to extract the thickness of the sample foil with the formula $S = \frac{\Delta E}{\Delta x}$ where S is the stopping power in keV/(µg/cm^2), ΔE is the energy loss in the sample foil in keV and Δx is the thickness of the foil in µg/cm^2. Using SRIM to compute the stopping power for α-particles at a given energy in a given material (see table 8.3), one can compute the thickness of the sample foil from the energy loss in the sample foil. An uncertainty of 5% is assumed on the SRIM stopping powers (matching the average observed discrepancies between SRIM results and experimental measurement).

In principle, the gold coating should to be taken into account as the α-particles have already lost some energy before exiting the source. However, for a 6 MeV α-particle, this represent ∼10 keV of energy loss, and thus a change in stopping power of ∼0.2 %, which is negligeable with respect to the 5 % uncertainty assumed for the stopping power.

At this point the thickness is expressed in µg/cm^2 and one needs to divide it by the density of the sample foil to obtain a thickness in distance units. For GANIL carbon foils the density is assumed to be the density of graphene: $\rho = 2.26 \pm 0.15$ g/cm^3. For ACF carbon foils, ACF estimates the density at 2.01 ± 0.02 g/cm^3 for 20 µg/cm^2 thickness. For SiN foils it is estimated at $\rho = 3.0 \pm 0.3$ g/cm^3. This uncertainty on the density is the main contribution on the uncertainty on the thicknesses of the foils when expressed in nm.

In addition, the degradation of the energy resolution due to the presence of the sample foil is also measured. The quantity used to measure this is the "straggling" and is computed with the formula $\Delta_{stragg} = \sqrt{\Delta_{foil}^2 - \Delta_{out}^2}$ with Δ_{foil} (resp. Δ_{out}) the Full Width at Half Maximum (FWHM) of the peaks with (resp. without) the sample foil.

8.3 . GANIL's carbon foils

A set of carbon foils were produced at GANIL with the help of G. Frémont and were studied using the test bench. It was expected that these foils would be of similar or slightly greater thickness than the target thickness (20 µg/cm^2). Measurements made with the test bench indicate that the thicknesses are indeed of the right order of magnitude. However, there are quite large variations from one batch of foils to another.

8.3.1 . Production

The foils were produced by evaporating a carbon rod in a vacuum chamber. The carbon rod was placed in the centre of the chamber and heated by the passage of a current. The carbon evaporates

and is deposited on glass supports placed around it and previously coated with a product that dissolves in water. Thanks to this product, once the foils are deposited on their glass supports, it is possible to detach them and place them on another support by immersing the glass support in water. The product covering the glass support will then dissolve and the foil (previously cut to a proper size) will float on the surface of the water. The foil can then be gently retrieved with the final support.

8.3.2 . Test bench study

Foil	t		Δ_{stragg} (keV)
	µg/cm^2	nm	
C1	36.0 (18)	159 (13)	13.6 (5)
C2	23.0 (12)	102 (8)	8.8 (7)
C3	22.2 (12)	98 (8)	9.8 (6)
C4	25.9 (14)	115 (10)	12.1 (11)
C7	34.9 (18)	154 (13)	13.4 (8)
C10	26.9 (15)	119 (10)	10.0 (19)
C11	20.2 (11)	90 (8)	10.3 (8)
C15	20.5 (11)	91 (8)	9.5 (18)
C17	24.8 (15)	110 (10)	11.4 (19)

Table 8.4: Measured thicknesses t (in µg/cm^2 and in nm) and straggling Δ_{stragg} (in keV) for each measured GANIL carbon foil. Thicknesses in nm are computed assuming a density $\rho = 2.26 \pm 0.15$ g/cm^3.

The foils were then studied following the procedure described in section 8.2.2. The thicknesses and straggling measured for each foil are reported in Table 8.4. Significant variations in thickness and straggling can be observed from one foil to another. This is due to the lack of reproducibility of the foil deposition method. From batch to batch, as the thickness of the foil cannot be controlled during deposition, large variations can be observed. Within a given batch, the thicknesses are closer from one foil to another, however there is some variability remaining due to an non-homogenous deposition on the support. Indeed, as the glass support is large, the deposit is thicker in the middle than on the edges.

In summary, it is observed that 20 µg/cm^2 carbon foils yield about 10 keV of straggling. The foils produced at GANIL are often thicker than 20 µg/cm^2 and their production lacks reliability. To obtain foils with a reliable thickness, all foils thicknesses should be measured and only those with the correct thickness should be kept.

8.4 . SiN foils

The second type of foil studied was SiN foils supplied by Silson. Four foils were ordered, two of nominal thickness 50 nm (15 µg/cm^2) and two of nominal thickness 30 nm (9 µg/cm^2), with a 10% tolerance announced by the supplier. The advantage of these SiN foils is that they are more robust and therefore thinner foils can be used. On the other hand, they also present additional constraints, as their integration into SEASON is more complex: the foils are delivered already deposited on a support that cannot be changed and the support in question must be integrated into the SEASON

wheel. Moreover, they represent a significant additional cost compared to carbon foils (∼10 times more per foil).

8.4.1 . Test bench study

Foils	θ °	t		Δ_{stragg} keV
		µg/cm^2	nm	
30nm 1	0	7.1 (6)	23.6 (32)	6.9 (12)
30nm 2	0	9.7 (7)	32.3 (40)	8.2 (9)
50nm	0	11.5 (7)	38.3 (45)	7.0 (8)
50nm	0	12.6 (7)	41.9 (49)	6.3 (11)
50nm long	0	11.8 (6)	39.3 (44)	5.9 (2)
50nm weighted	0	11.5 (6)	38.2 (39)	7.0 (2)
50nm	7	10.9 (7)	36.4 (43)	5.8 (16)
50nm	-7	11.8 (8)	39.5 (47)	6.4 (13)

Table 8.5: Measured thicknesses t (in µg/cm^2 and in nm) and straggling Δ_{stragg} (in keV) for each measured SIN foil. Measurement angle θ are also reported here. See text for details. Thicknesses in nm are computed assuming a density $\rho = 3.0 \pm 0.3$ g/cm^3.

An extensive study of SiN foils was carried out using the DEDIP test bench. Indeed, the first measurements were not fully understood due to uncertainties on some parameters. This led to the TEM study described below and to the addition of the ability to rotate the sample by a specific angle to the test bench.

The measurements of the SiN foils are summarised in Table 8.5. The foils are indexed by their thickness. For the 30 nm thick foils the foils are additionally indexed (30 nm 1 and 30 nm 2) to differentiate the two foils. This is not necessary for the 50 nm foils as one of the foils was broken by a mechanical contact before it could be measured.

For the remaining 50 nm foil, in addition to two regular measurements, a long measurement was made. This measurement consisted of a series of 24 round trips with 3 points taken without the foil, 5 with, 3 without, 5 with and so on for a total of 195 points with 30 min acquisition time per point, thus reaching a total acquisition duration of 97.5 h. This measurement was analysed in two different ways:

- as if it were a single measurement, by summing all the points taken without the foil on the one hand and all the points taken with the foil on the other. This measurement is referred to as "50 nm long". This measurement is slightly distorted. Indeed the vacuum reached at the beginning of the measurement was not perfect and it has improved significantly (from 10^{-6} mbar to 10^{-7} mbar) during the measurement, causing a visible energy shift as the measurement proceeds.

- As if it were 24 successive and independent measurements by taking groups of 11 points (3 without the foil, 5 with the foil and again 3 without the foil). A weighted average of all the measurements is then taken (using each measurement uncertainty to weight it). This measurement is referred to as the "50 nm weighted" and is the most trusted one.

In summary, it can be seen that the SiN foils announced as 50 nm thick by the manufacturer are measured at 38 ± 4 nm with the test bench. This large deviation with respect to the tolerance announced by the supplier (± 10 %) could be explained by a crystal structure for the SiN. Indeed a crystal structure could lead to "tunnels" in the foil that could channel the α-particles, causing a lower energy loss than expected within the foil.

The measurements made with a tilted angle reported in table 8.5 were made to check this point. Indeed, by tilting the foil, one could expect the alignment of the crystal structure with respect to the source and to the detector to change and thus to see a modification of the channelling effect. No significant difference are seen with this measurement, which seems to disprove the channeling hypothesis. In principle this also increases the foil thickness, however a 7° tilt will increase it by $\sim$0.7 % ($\frac{1}{\cos(7)}$), a value comparable to the experimental uncertainties.

To try to understand what was measured and to verify the validity of our thickness measurement, another measurement by reflectometry was carried out by CEA's Service de Physique de l'Etat Condensé (SPEC) on the broken foil leading to a thickness of 39 nm (no error bars were extracted from the measurement). However, the person who made the measurement was not very confident about the result. This led to a TEM (Transmission Electron Microscopy) study to have a better characterisation of the foil.

8.4.2 . TEM study

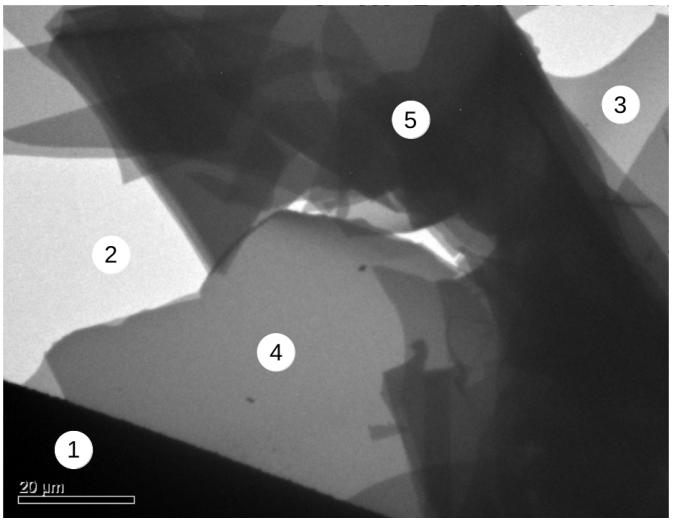

Figure 8.4: TEM view of the sample. Several kind of areas can be observed. 1 : Part of the grid supporting the sample. 2 : Nothing. 3 : One layer of SiN foil. 4 : Two layers of SiN foil. 5 : Multiple layers of SiN foil. (see section 8.4.2.1 for details)

Transmission Electron Microscopy (TEM) technique involves sending an accelerated beam of electrons (In this case with a nominal energy of 200 keV) onto a sample to image it. This allows one to obtain images such as the one shown in figure 8.4. In addition to this imaging capability, various options are available :

1. an X-ray detector is used to identify the elements present in the sample and to measure their respective proportions;

2. a spectroscope is used to measure the electron energy losses in the foil (with a resolution of 1.1 eV) to determine the thickness of the foil;

3. the beam can be concentrated at a point in order to make a diffraction measurement and reveal a possible crystal structure.

Other options exist (irradiation with ions etc.) but are not detailed here as they were not used in our measurement.

I applied for a measurement with the JANNuS plateform and it was accepted. Thus our measurement was made within the JANNuS platform thanks to C. Baumier.

8.4.2.1 . Sample preparation

(a) Photo of the sample wedged between two grids and placed on a sample holder. The grids are 3 mm in diameter and are rotated with respect to each other. The sample is visible in between the grids.

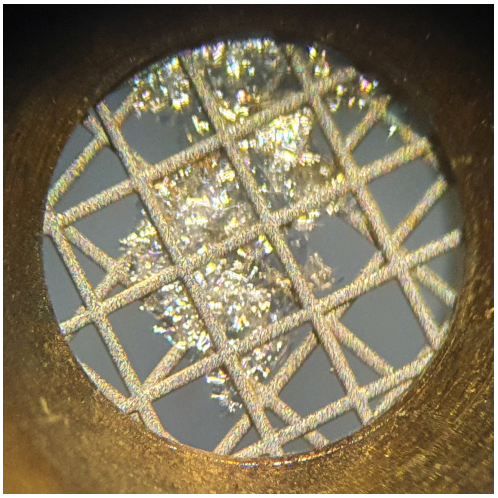

(b) Photo of the sample taken through an optical microscope. The SiN sheet is clearly visible between the two copper grids. One can also see that the foil is folded on itself.

Figure 8.5: Photos of the sample foil.

The sample was taken from the 50 nm thick SiN foil (announced by the supplier, measured at 39 nm by the SPEC using reflectometry, not measured with the test bench) which had broken before any measurement on the test bench. A piece of the broken foil was placed between two 3 mm diameter copper grids (see fig. 8.5a), themselves placed on a sample holder. A first quick visualisation by optical microscopy allows to notice immediately that the foil has folded on itself (see figure 8.5b). Indeed, once the foil is broken, effects like surface tension are likely to fold the foil over itself and the manipulations to prepare the sample and trap it between the grids made it worse. However, C. Baumier's expert eye ensured that we could already see areas with a single foil layer (grey/more transparent areas).

8.4.2.2 . Imaging and the appearance of bubbles

TEM imaging is very powerful and can image the foil at different scales. Theoretical spatial resolution is 0.23 nm, however here we were limited by the fragility of the sample which twisted

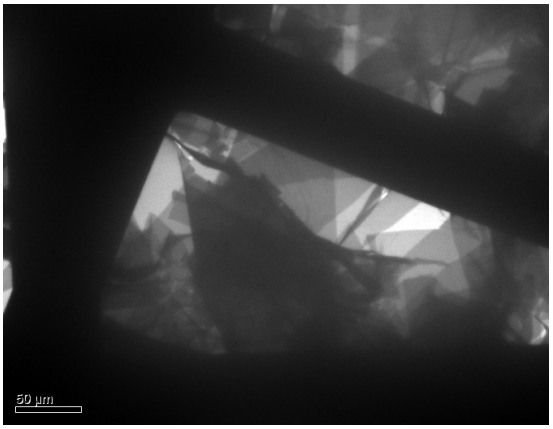

(a) TEM view of the SiN foil (Scale is 50 µm). One can see the support grid of the sample as well as the foil folded on itself. Depending on the area, there are more or less SiN layers overlapping each other.

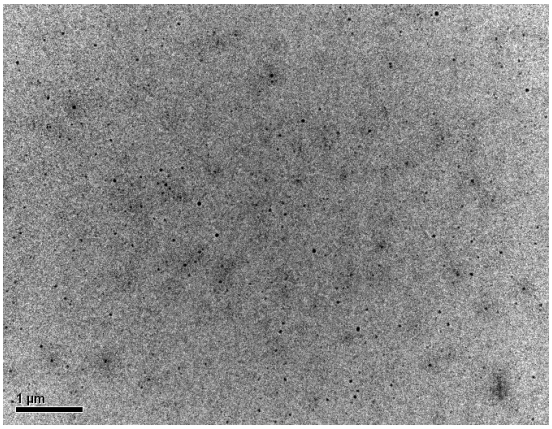

(b) TEM view of the SiN foil (Scale is 1 µm). A large number of small black spots (bubbles) appear.

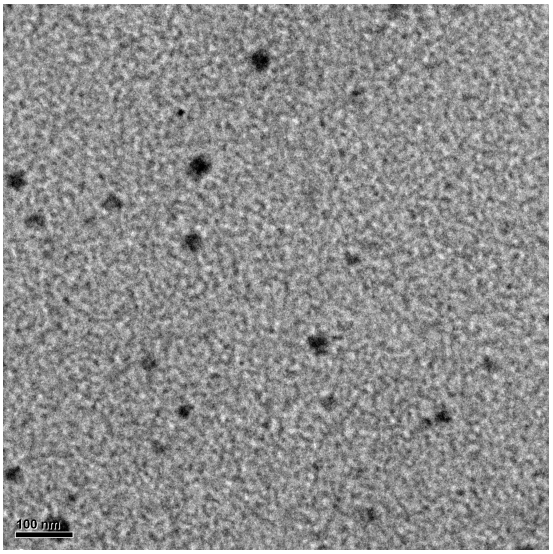

(c) TEM view of the SiN foil (Scale is 100 nm). The black spots (bubbles) can be seen more clearly.

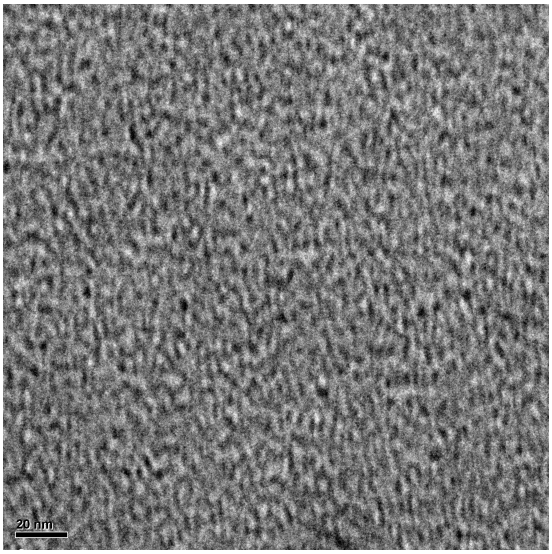

(d) TEM view of the SiN foil (Scale is 100 nm). No crystal structure appears to be present on the sample.

Figure 8.6: TEM views with different magnifications.

under the electron beam when it was too focused so it was difficult to make images at very high magnification.

On the large-scale images (see fig. 8.4 and fig. 8.6a) we can see the foil and the places where it folds over itself. It is then possible to look for areas with a single layer in order to make the various measurements. With a higher magnification, we can see black spots appearing (see figure 8.6b). Those spots can be a few tens of nm diameter (see fig. 8.6b and fig. 8.6c) and, according to C. Baumier, these are bubbles that have formed in the foil at the time of production. These bubbles are probably composed of nitrogen gas at atmospheric pressure.

When the magnification is further increased, no crystal structure seems to appear (see fig. 8.6d), the foil would thus be amorphous. However, a diffraction measurement is needed to confirm this.

8.4.2.3 . Diffraction measurement

The diffraction measurement was carried out last because it is necessary to focus the beam at a single point, which is likely to damage the sample. If the sample is amorphous, diffraction circles appear. If the sample has a crystal structure, intense diffraction spots appear and their arrangement tells us about the structure of the sample. If the sample is partially crystalline and partially amorphous, the two should mix.

During the measurement, a diffraction pattern is seen that clearly corresponds to an amorphous sample (see fig. 8.7), which confirms the previous observations: there are no crystal structure and thus no channeling effect.

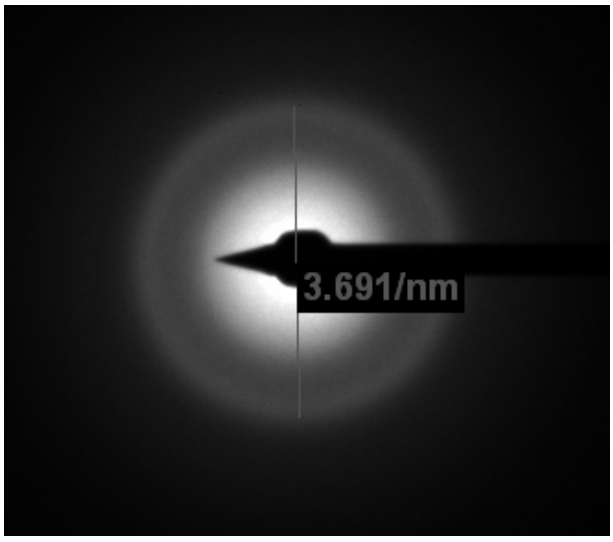

Figure 8.7: Diffraction measurement on the SiN foil.

8.4.2.4 . X-rays study

A silicon detector is placed in the device in order to measure the X-rays emitted during the de-excitation of the atoms excited by the electron beam. This detector is sensitive to energies of the order of a hundred eV to a few tens of keV with a very good resolution (<100 eV). It can be seen that silicon and nitrogen are the two major components with a stoichiometry close to the expected 1/1 ratio (see fig. 8.8 and tab. 8.6).

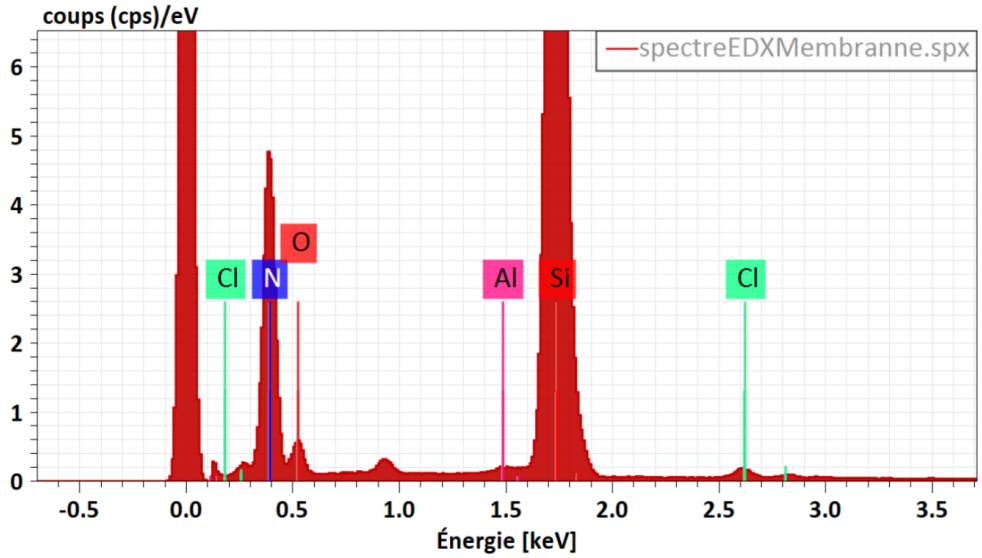

Figure 8.8: X-ray energy spectrum of the sample. The elements indicated on the spectrum are those coming a priori from the sample, other elements are present (in particular the copper of the grid around 1 keV) but are not highlighted here.

We also note the presence of contamination. Excluding contamination coming from the microscope (for example the presence of copper around 1 keV on the figure 8.8), there are three elements that are probably contaminants of the sample itself:

1. oxygen, probably due to a slight oxidation of the foil;
2. chlorine, probably originating, according to C. Baumier, from the cleaning of SiN foils (usually cleaned with hydrochloric acid after production);
3. aluminium, possibly from the substrate of the foil.

Element	Z	$p_m(\%)$	$p_A(\%)$
Nitrogen	7	34.08	50.40
Silicon	14	63.12	46.56
Oxygen	8	1.87	2.42
Aluminium	13	0.44	0.34
Chlorine	17	0.49	0.29

Table 8.6: Mass (p_m) and atomic (p_A) proportion of the different elements present in the foil

8.4.2.5 . Electron Energy Loss Spectroscopy (EELS)

A spectroscope is used to measure the electron energy losses in the foil (see fig. 8.9). An analysis software (DigitalMicrograph, available for free on Gatan's website) allows to reconstruct the thickness of the foil from these energy losses.

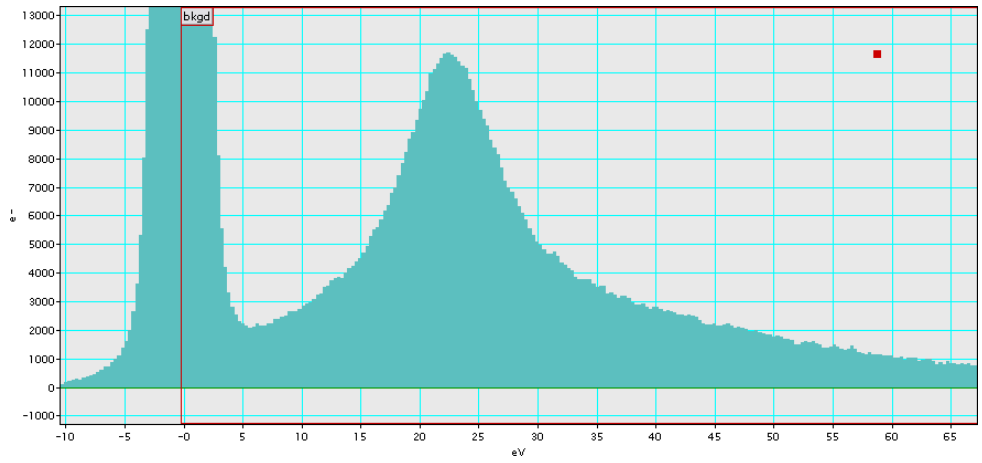

Figure 8.9: Electron energy loss spectrum. The 0 eV peak is called the zero-loss peak and correspond to transmitted electrons/elastic scattering.

More precisely, assuming the independent nature of scattering events, the thickness of the foil t and the mean free path of inelastic electron scattering in the foil λ are related through the formula:

$$\frac{t}{\lambda} = \ln(\frac{I}{I_0}) \tag{8.1}$$

with I the integral of the whole EEL spectrum and I_0 the intensity of the zero-loss peak. If one know the mean free path of inelastic electron scattering in the material λ, one can obtain the thickness of the foil. However measuring λ is not an easy task. Some empirical laws are able to link λ with different parameters of the foil such as the average Z or the density of the foil. The most common one uses the following formula [125, 126]:

$$\lambda \approx \frac{106 F E_0}{E_m \ln(2E_0\beta/E_m)} \tag{8.2}$$

with :

- E_0 the energy of the incident electron (in keV, $E_0 = 200$ keV in our case);
- $F = \frac{(1+E_0/1022)}{(1+E_0/511)^2}$ a relativistic factor;
- $E_m \approx 7.6 Z_{ef}^{0.36}$ the average energy loss (with Z_{ef} the average Z of the material);
- β the collection semi-angle in mrad ($\beta = 11.81$ mrad in our case).

Z_{ef} can be obtained using the X-rays study ($Z_{ef} = 10.33$). Using this value for Z_{ef}, we obtain $\lambda \approx 133$ nm.

This empirical law is sometimes questioned in the literature, however C. Baumier affirms that in our case it should be valid within $\pm 10\%$.

On the EEL spectrum, one can obtain $t = 0.32 \times \lambda = 42.5 \pm 4.3$ nm, which is consistent with our α-particles energy loss measurement, with the reflectometry measurement made by the SPEC (39 nm) and, on the limit, with what was announced by the supplier (50 ± 5 nm).

8.5 . ACF Metal carbon foils

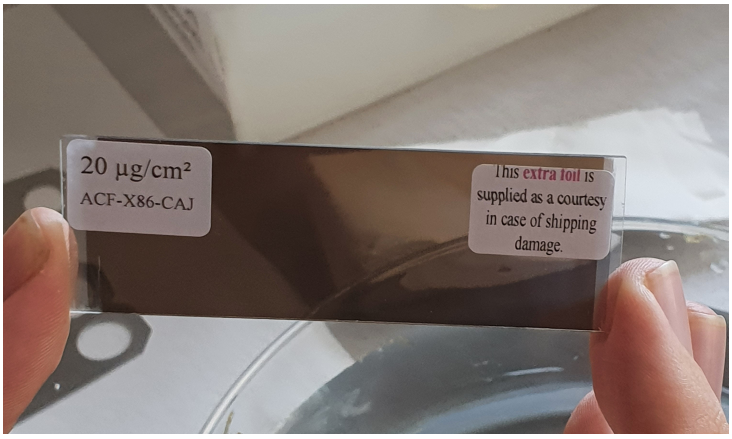

Figure 8.10: Photo of an ACF Metal carbon foil on its glass support.

ACF Metal is an American supplier of carbon foils of varying thicknesses (between 0.1 µg/cm^2 and 2000 µg/cm^2), notably for accelerator physics. Their thin foils (<100 µg/cm^2) are supplied on glass supports (see fig. 8.10) coated with a parting agent that allows them to be removed by immersing them in water. While the foil remains on its glass support, it can be stored for a long time (years) without any problem, as long as it is not exposed to excessive humidity. Once the foil is removed from the glass support and is deposited on its final support, its storage becomes harder as it is very sensitive to pressure changes.

ACF Metal offers two basic formats for their foils: ACF and XCF. ACF foils are 25×70 mm and XCF foils are 50×70 mm. Seven foils were ordered in ACF format, four in 20 µg/cm^2 thickness and three in 15 µg/cm^2 thickness. Nine foils were delivered as ACF offered an extra foil of each type in case of shipping damage.

The thickness of each foil provided by ACF Metal has been individually measured by them through optical measurement before shipping and is given with a tolerance of $\pm 10\% \pm 0.5$ µg/cm^2. In addition, the macroscopic non-uniformity of the foils have been studied by ACF Metal, and has been found to be always better than 10% and typically better than 5% for the whole foil.

The foils provided by ACF are well documented and a technical document [123] is available on their website (https://www.acf-metals.com/)

8.5.1 . Foil preparation

Before they can be used, the foils must be separated from their glass support and placed on their final support. To do this, they must first be cut out (see fig. 8.11a) as a 25×22 mm format is sufficient for our final supports. Three foils can be cut for each glass support supplied by ACF. Once the foil is cut, it must be removed by immersing it in distilled water. Ideally, a 45° angle should be maintained between the plane of the water surface and the plane of the glass support (see fig. 8.11b) and the foil should be immersed very slowly to allow time for the water to dissolve the parting agent.

Once the foil is separated from its support, it will float on the surface of the water. It can then be picked up with the final support (see fig. 8.11c) and will attach itself to the support. Once the foil has dried completely, it is ready to be used (see fig. 8.11d).

(a) Photo of an ACF Metal carbon foil being cut.

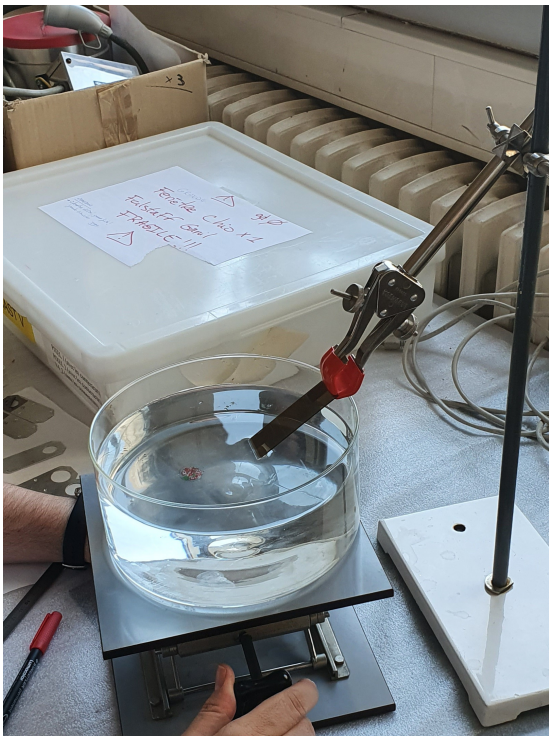

(b) Photo of the immersion of an ACF Metal carbon foil in distilled water.

(c) Photo of an ACF Metal carbon foil being picked up with the final support.

(d) Photo of an ACF Metal carbon foil deposited on the final support.

Figure 8.11: Photos taken during the preparation of ACF Metal carbon foils.

In principle, ACF Metal indicates that a N µg/cm^2 foil should be able to be deposited on a support with a N mm diameter hole. After some difficulties during the first attemps, where we have only been able to deposit 20 µg/cm^2 foils on 15 mm diameter holes, the proper technique was found and we were able to deposit 20 µg/cm^2 foils on 20 mm diameter holes, 15 µg/cm^2 foils on 15 mm diameter holes and we even successfully deposited a 15 µg/cm^2 foil on 20 mm diameter hole.

8.5.2 . Test bench study

Foil	t (µg/cm^2)	t (nm)	Δ_{stragg} (keV)
ACF 2	20.3 (11)	101 (6)	9.2 (7)
ACF 3 long	19.9 (10)	99 (5)	6.1 (2)
ACF 3 weighted	19.3 (10)	96 (5)	6.3 (2)

Table 8.7: Measured thicknesses t (in µg/cm^2 and in nm) and straggling Δ_{stragg} (in keV) for each measured ACF carbon foil. Thicknesses in nm are computed assuming a density $\rho = 2.01 \pm 0.02$ g/cm^3.

The 20 µg/cm^2 carbon foils provided by ACF Metal were also studied with the test bench. The goal was to ensure that their properties were matching the expectations. The results are summarised in Table 8.7.

As for the SiN foil, a long measurement was made for one of the ACF Metal foils. This measurement consisted of a series of 22 round trips with 3 points taken without the foil, 5 with, 3 without, 5 with and so on for a total of 179 points with 30 min acquisition time per point, thus reaching a total acquisition duration of 89.5 h. As for the SiN foil, this measurement was analysed in two different ways:

- as if it were a single measurement, by summing all the points taken without the foil on the one hand and all the points taken with the foil on the other. This measurement is referred to as "ACF 3 long". This time the measurement is not distorted as special care was put to ensure the quality of the vacuum at the beginning of the measurement.
- As if it were 22 successive and independent measurements by taking groups of 11 points (3 without the foil, 5 with the foil and again 3 without the foil). A weighted average of all the measurements is then taken (using each measurement uncertainty to weight it). This measurement is referred to as the "ACF 3 weighted".

The foils are measured with a thickness matching the one indicated by ACF Metal within error bars. For the long measurement, the straggling seems to be lower than for the other measurements. While the other measurements had a straggling slightly larger than what would be expected from the simulations, this measurement has a straggling slightly lower than the simulations. This variation is not fully understood.

In addition, it was noted during the measurements that the foils are very fragile and that extreme care should be taken when handling them.

8.6 . Summary

Foils	Nominal thickness		Measured thickness		Straggling (keV)	Cost (€)	Advantages	Drawbacks
	(µg/cm^2)	(nm)	(µg/cm^2)	(nm)				
Carbon Ganil	$\sim$ 20	$\sim$ 90	20-36	90-160	9-14	/	On site	reliability
SiN	$\sim$ 15	50	$\sim$ 11.5	$\sim$ 38	$\sim$ 7	$\sim$ 220	Robust	bubbles, support, expensive
	$\sim$ 9	30	$\sim$ 7-10	$\sim$ 24-32	$\sim$ 7-8	$\sim$ 300		
Carbon ACF	20	100	20	100	$\sim$ 9	$\sim$ 15	reliability cheap	fragile
	15	75						

Table 8.8: Summary of the main points for each type of foil : thickness, straggling, estimated cost for a foil, advantages and drawbacks. For the GANIL carbon foils, the cost was not estimated as it was made on site.

A summary of relevant informations for each type of foil is given in table 8.8. For each foil type, the nominal and measured thicknesses are listed, as well as the straggling caused by the foil, an estimate of the cost of a foil and the main advantages and drawbacks.

The SiN foils appear to be fairly robust in use as long as there is no physical contact with the foil. They also have very low straggling. On the other hand, they are very expensive and their integration into the SEASON wheel would not be easy. Moreover, they have bubbles/holes whose impact on ion implantation is unknown. Finally, the dialogue with the supplier is not always easy and there seems to be a large discrepancy between the nominal and measured thickness of the foils.

The ACF foils correspond to what is advertised by the supplier, with very good reproducibility at a very low cost (75 foils cost just over 1000 €). The supplier is used to supply foils for accelerator physics and thus seems to understand well the problems we may encounter and answers questions clearly and precisely. However, straggling is slightly more important in these foils than in SiN foils. In addition, more care is needed during handling. Despite those last drawbacks, the choice was made to use the ACF Metal carbon foils for the first version of the SEASON detector. SiN could be an option for a future upgrade of the detector.

9 - Conclusion and perspectives

In this work, the ^{225}Pa $\rightarrow$ ^{221}Ac $\rightarrow$ ^{217}Fr decay chain was studied. ^{225}Pa was produced at IGISOL, University of Jyväskylä, using the ^{232}Th(p,8n)^{225}Pa reaction using a 65 MeV proton beam. The reaction products were then mass selected, implanted in a carbon foil and studied through α, γ and conversion electron decay spectrocopy. Several new α-transitions and γ-transitions have been observed and conversion electrons were measured for the first time in ^{221}Ac following the α-decay of ^{225}Pa. This study enabled the reconstruction of the low-lying level schemes of ^{221}Ac and ^{217}Fr and, for ^{221}Ac, the reconstrution of the spin and parity of the levels thanks to the measured α-decay hindrance factors and γ-transition multipolarities.

This analysis showed a strong similarity between ^{221}Ac and ^{223}Ac level schemes. Notably the lowest hindrance factor is in both cases for the decay towards the ground state, a property somewhat unusual for odd-mass nuclei. This, combined with the low hindrance factors towards both positive and negative parity states, lead to the interpretation of ^{221}Ac as an octupole deformed nucleus, as its neighbour ^{223}Ac. However a high splitting between parity doublets, as well as a comparison with theoretical calculations, indicate that ^{221}Ac is probably at the limit of the static octupole deformation region in the actinides, and the lower N actinium isotopes would present octupole vibrations instead of static deformation. A study of ^{219}Ac through the decay spectrocopy of ^{223}Pa would provide more informations on the subject.

In addition, NPTool (GEANT4) simulations have been performed for the SEASON detector, as well as a study of its implantation foils. This detector is designed to perform α, γ and conversion electron spectroscopy with a high detection efficiency and a good energy resolution. It will also be part of the S^3-LEB setup, for which it will act as a counting station. This will enable the comparison of the results obtained through decay spectroscopy with SEASON and through laser spectrocopy with S^3-LEB. To characterise this, simulations of the detector have been performed using NPTool. The simulations showed an expected detection efficiency, in the most compact configuration, of $\sim$80 % for the α-particles and of $\sim$50 % for the electrons. Furthermore, the simulations helped characterised the impact of the detectors dead layer on the resolution, which lead to the choice of the thinnest possible dead layer for the detector: 50 nm.

The detector implantation foils were also studied. Two materials were considered for those implantation foils: i) carbon foils, cheap and known to work in similar setups, and ii) SiN foils, more expensive and not as well characterised in the context of nuclear physics, but also less fragile, which made thinner foils accessible with SiN. The use of thin foils is crucial as the α-particles will loose energy and see their energy distribution widen while passing through the foil. The study, using simulations, a test bench located at CEA and a TEM located at IJCLab, enabled the characterisation of both type of foils in term of energy loss, energy straggling and properties of the material. Notably it was found that the thickness of the SiN foils did not seem to be reliable and that SiN is a porous material. This study lead to the decision to use carbon foils produced by ACF Metal for the SEASON detector, with a potential future upgrade of the detector with SiN foils.

In the future, the commissioning of SEASON is planned first at IGISOL using the same reaction as the one used in this thesis: proton-induced fusion evaporation on a ^{232}Th target. The large improvement in α-particle detection efficiency (from $\sim$30 % to $\sim$80 %), α-particle energy resolution

(from 25 keV for the best detector to less than 20 keV) and most importantly for conversion electrons detection efficiency (from $\sim$1 % to $\sim$50 %) should enable a considerable improvement of the measurements (for example towards the $I^{\pi} = 3/2^{+}$ state mentionned in section 5.3). Notably some weaker α-decay branches are expected in the ^{225}Pa α-energy spectrum. In addition other experiments should take place, using other beam-target combinations such as proton beam on ^{233}U target or α-beam on ^{232}Th target. Notably the ^{233}U(p,7n)^{227}Np channel should be accessible and thus the ^{227}Np $\rightarrow$ ^{223}Pa $\rightarrow$ ^{219}Ac chain could be studied. This could help confirm the position of the transition between the static octupole deformation and octupole vibrations for the actinium isotopes. After this campaign at Jyväskylä, SEASON should be installed at S^3-LEB where the heavy and super-heavy nuclei will be studied. In the neutron-deficient actinides there are already plans to study the uranium isotopes, more specifically $^{225-228}$U, combining decay spectroscopy with laser spectrocopy.

In this work, the interest of hindrance factors, for the characterisation of the extent of the octupole deformation region in the actinides, appeared. This was already studied in the 80s and 90s, notably by R. K. Sheline, but the new facilities offer new opportunities to complete this kind of study, both at IGISOL and at S^3. The evolution of the hindrance factors through the region should be studied, as well as its correlation with octupole deformation, as this seems to be a strong indicator of static octupole deformation. However decay spectroscopy alone will not be enough to perform quantitative measurements of octupole deformations. With the perspective of NEWGAIN at GANIL-SPIRAL2 and inverse kinematic reactions, the study of the neutron-deficient actinides through Coulomb excitation, at the intermediate focal plane of S^3, might become possible. This could provide a direct access to the octupole deformation of those nuclei. Laser spectroscopy could also provide considerable information. Indeed, even if octupole deformation cannot be measured directy through those techniques, it provides considerable insight in the ground-state properties of the nucleus and signs of octupole deformation have been found indirectly through other observables and experiment-theory comparisons.

The development of new production techniques at IGISOL, the near arrival of S^3 and S^3-LEB and the development of new detectors like SEASON open up many opportunities for further studies in the heavy and super-heavy nuclei. In particular new opportunities arise to study the neutron-deficient actinides and their octupole deformation.

And who knows what new questions it will open ?

A - X-Ray table

The following table give the energy (in keV) of the K and L x-rays for elements between lead (Pb) and protactinium (Pa).

Element	$K\alpha_1$	$K\alpha_2$	$K\beta_1$	$L\alpha_1$	$L\alpha_2$	$L\beta_1$	$L\beta_2$	$L\gamma_1$
82 Pb	74.9694	72.8042	84.936	10.5515	10.4495	12.6137	12.6226	14.7644
83 Bi	77.1079	74.8148	87.343	10.8388	10.73091	13.0235	12.9799	15.2477
84 Po	79.290	76.862	89.800	11.1308	11.0158	13.447	13.3404	15.744
85 At	81.520	78.950	92.300	11.4268	11.3048	13.876	—	16.251
86 Rn	83.780	81.070	94.870	11.7270	11.5979	14.316	—	16.770
87 Fr	86.100	83.230	97.470	12.0313	11.8950	14.770	14.450	17.303
88 Ra	88.470	85.430	100.130	12.3397	12.1962	15.2358	14.8414	17.849
89 Ac	90.884	87.670	102.850	12.6520	12.5008	15.713	—	18.408
90 Th	93.350	89.953	105.609	12.9687	12.8096	16.2022	15.6237	18.9825
91 Pa	95.868	92.287	108.427	13.2907	13.1222	16.702	16.024	19.568

B - α and γ energy spectra

This appendix shows for each α-transition in ^{225}Pa decay scheme, the energy spectrum for the γ-rays detected in coincidence and for each γ-ray the energy spectrum for the α-particles detected in coincidence. The spectra are grouped by states in ^{221}Ac level scheme: for each state, the γ-ray energy spectrum detected in coincidence with the α-particles feeding this state is shown (the α-particle energy range for the coincidence is adapted for each state). Then, for each γ-ray emitted from this state, the α-particle energy spectrum detected in coincidence in shown (the γ-ray energy range for the coincidence is always ± 1 keV around the peak centroid).

B.1 . Spectra for the $I^{\pi} = 7/2^{+}$ state at 223.7 keV

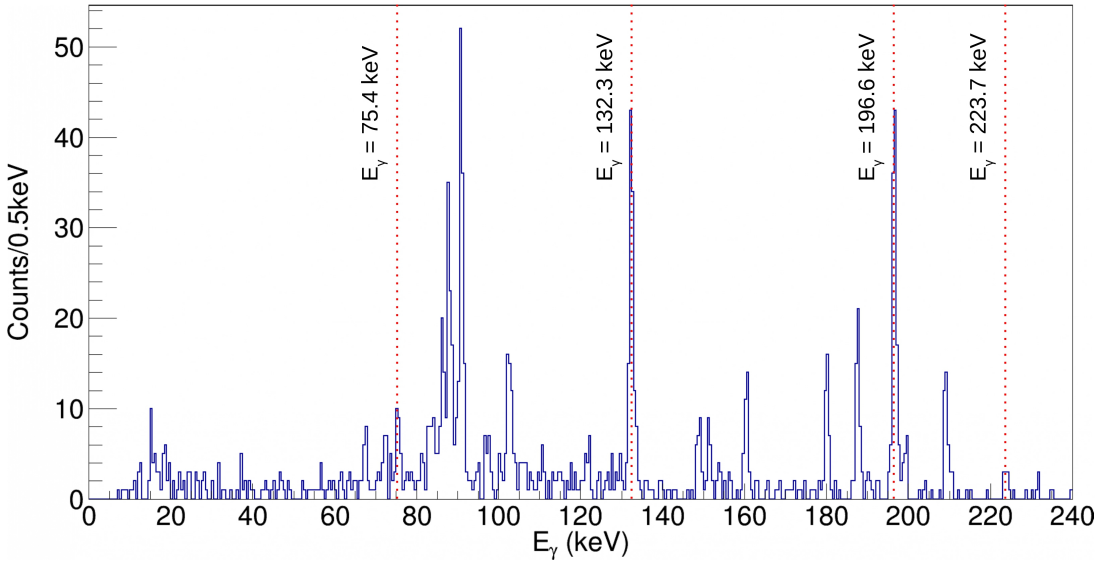

Figure B.1: γ-ray energy spectrum for γ-rays detected in coincidence with an α-particle with $7000\,\text{keV} < E_{\alpha} < 7050\,\text{keV}$.

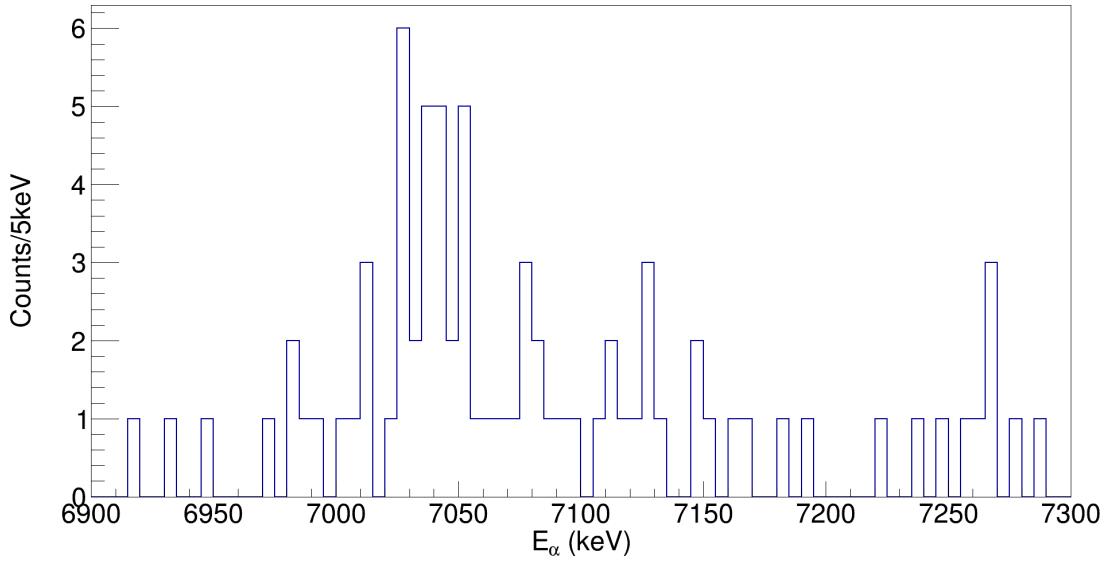

Figure B.2: α-energy spectrum for α-particles detected in coincidence with a γ-ray with $74.4\,\text{keV} < E_\gamma < 76.4\,\text{keV}$.

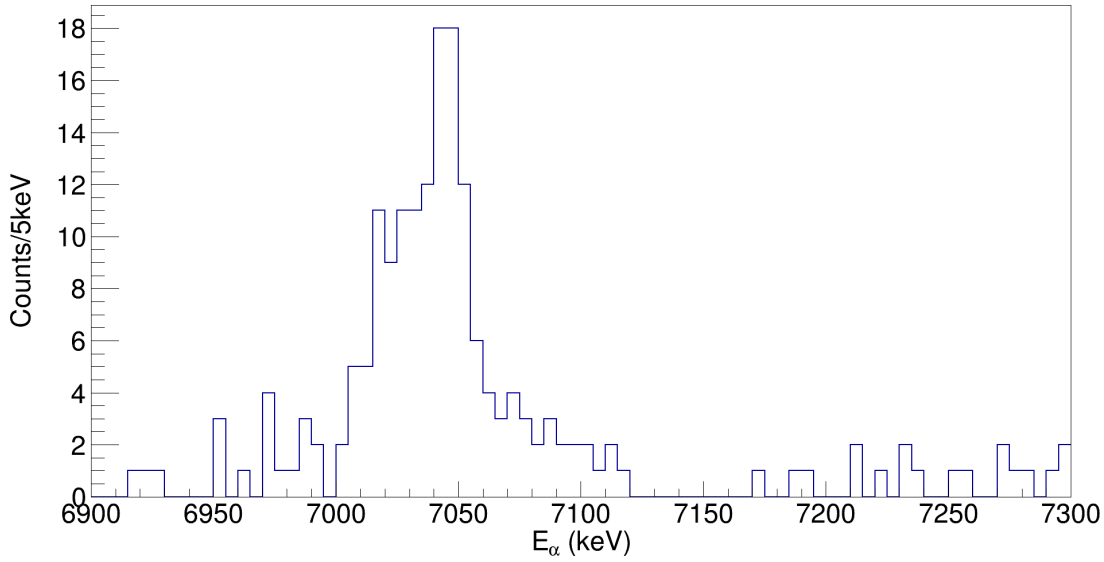

Figure B.3: α-energy spectrum for α-particles detected in coincidence with a γ-ray with $131.3\,\text{keV} < E_\gamma < 133.3\,\text{keV}$.

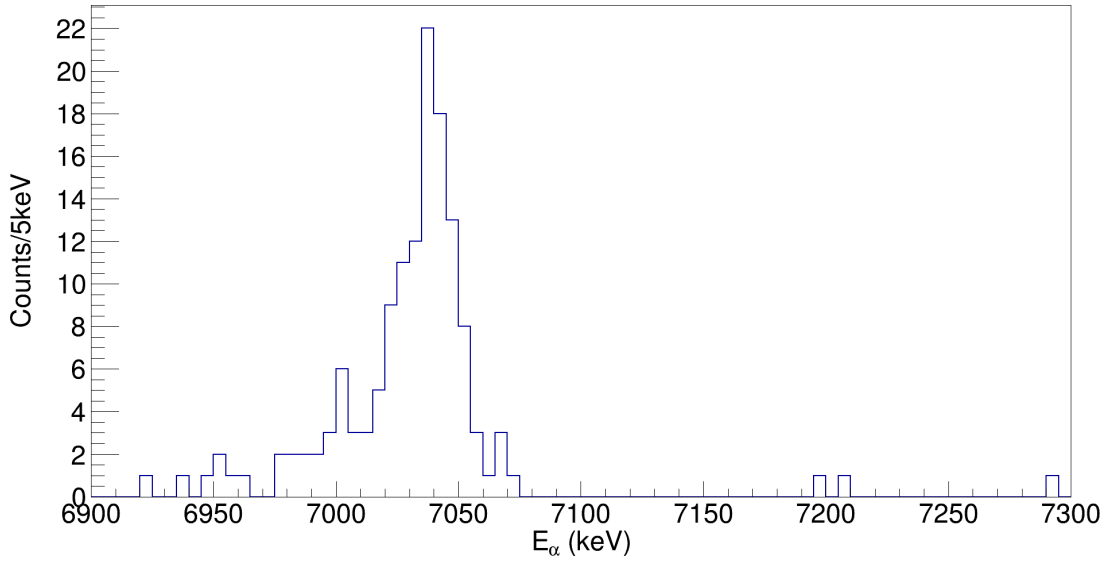

Figure B.4: α-energy spectrum for α-particles detected in coincidence with a γ-ray with 195.6 keV $< E_\gamma <$ 197.6 keV.

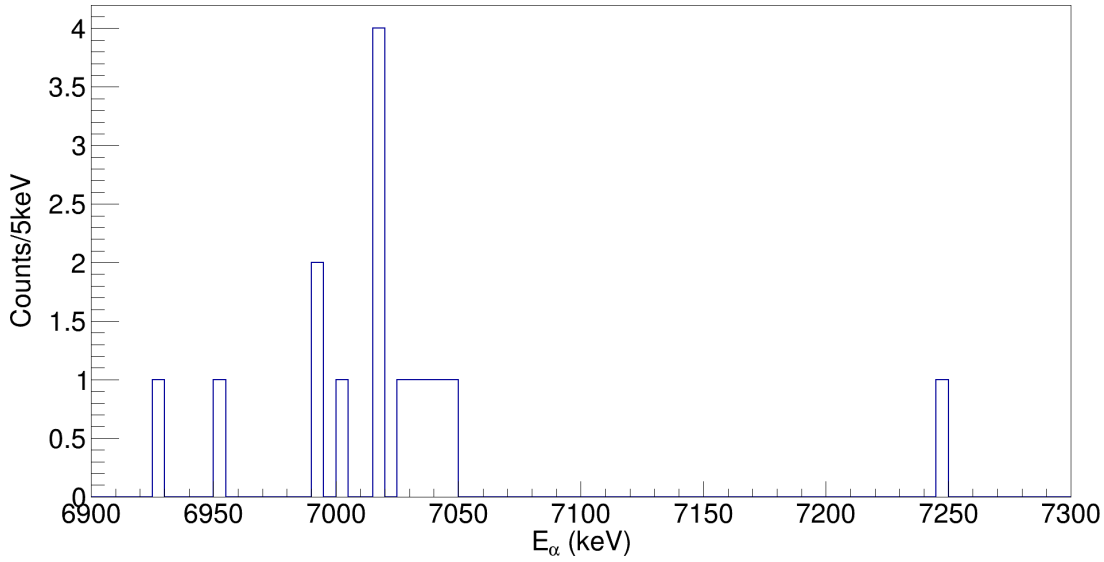

Figure B.5: α-energy spectrum for α-particles detected in coincidence with a γ-ray with 222.7 keV $< E_\gamma <$ 224.7 keV.

B.2 . Spectra for the $I^{\pi} = 7/2^{+}$ state at 180.0 keV

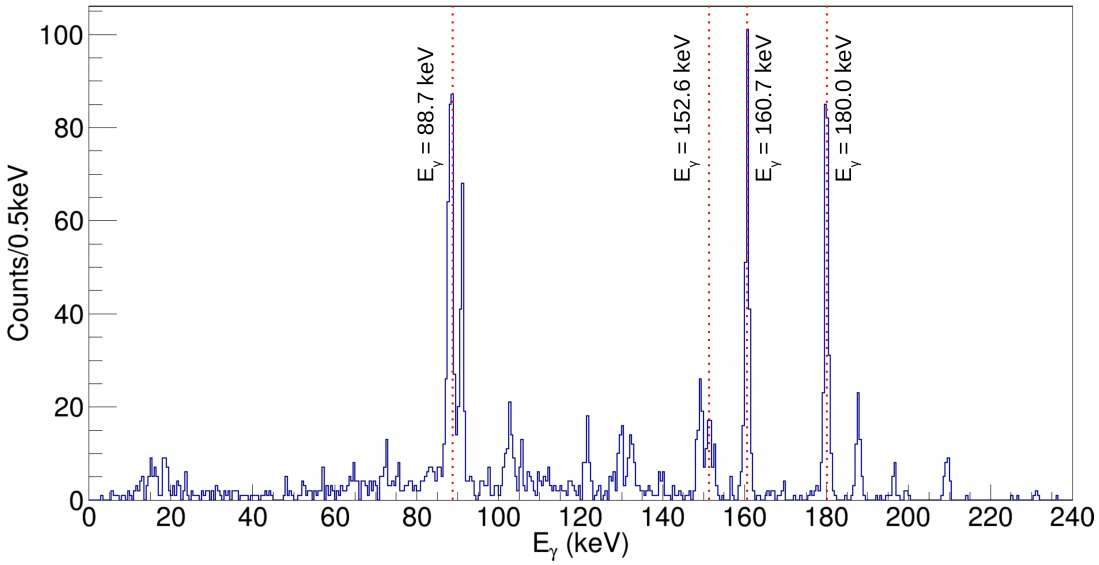

Figure B.6: γ-ray energy spectrum for γ-rays detected in coincidence with an α-particle with 7050 keV $< E_{\alpha} <$ 7100 keV.

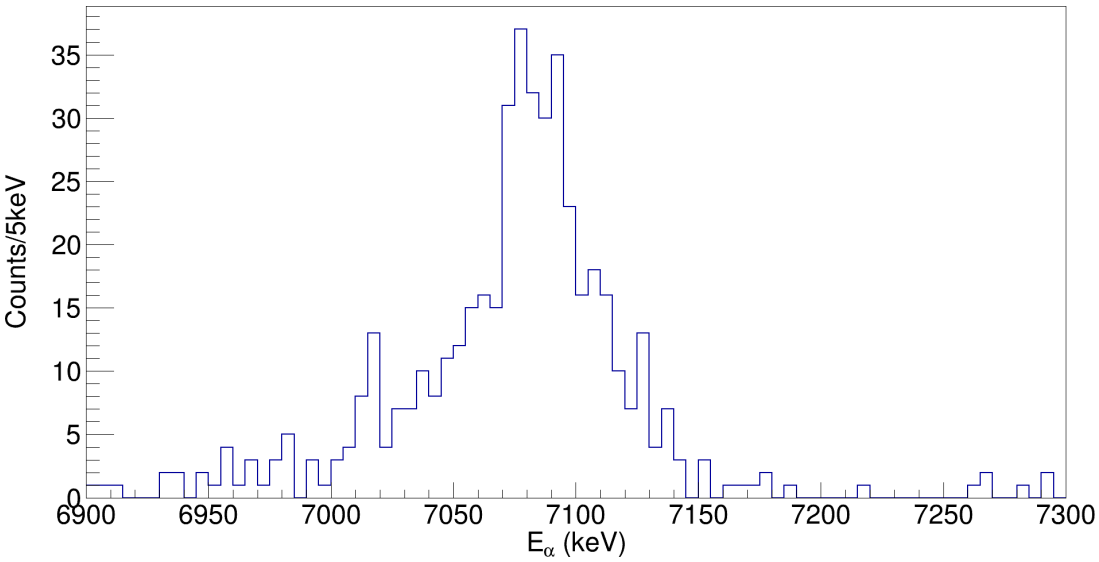

Figure B.7: α-energy spectrum for α-particles detected in coincidence with a γ-ray with 87.7 keV $< E_{\gamma} <$ 89.7 keV.

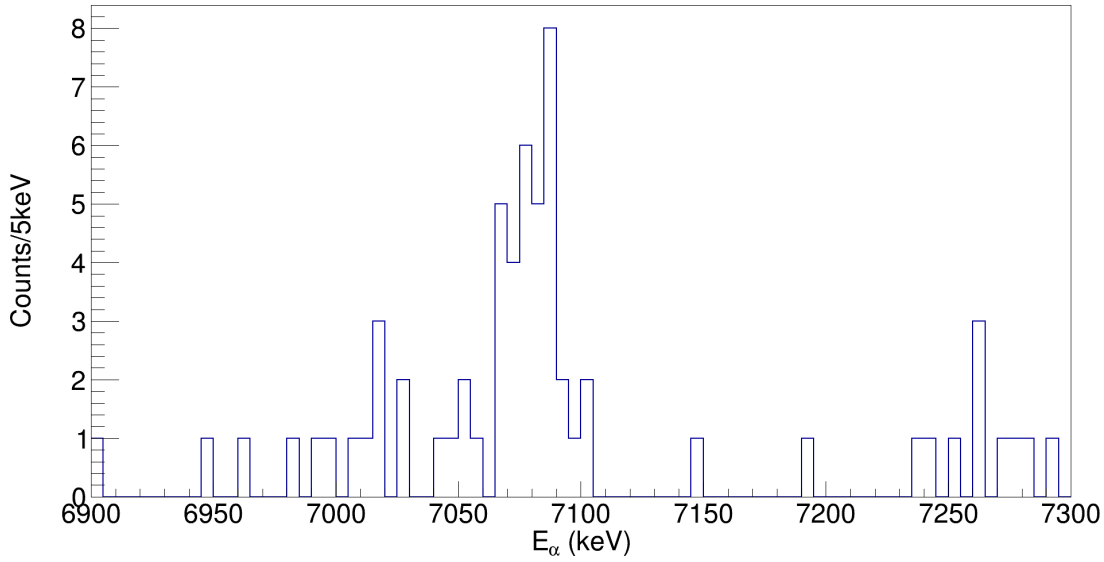

Figure B.8: α-energy spectrum for α-particles detected in coincidence with a γ-ray with 151.6 keV $< E_\gamma <$ 153.6 keV.

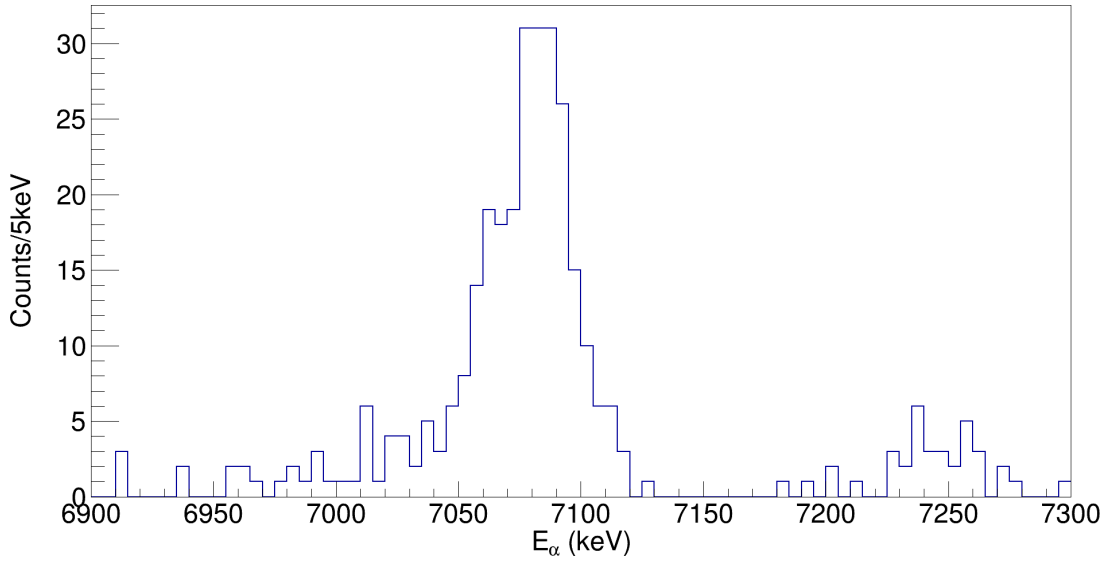

Figure B.9: α-energy spectrum for α-particles detected in coincidence with a γ-ray with 159.7 keV $< E_\gamma <$ 161.7 keV.

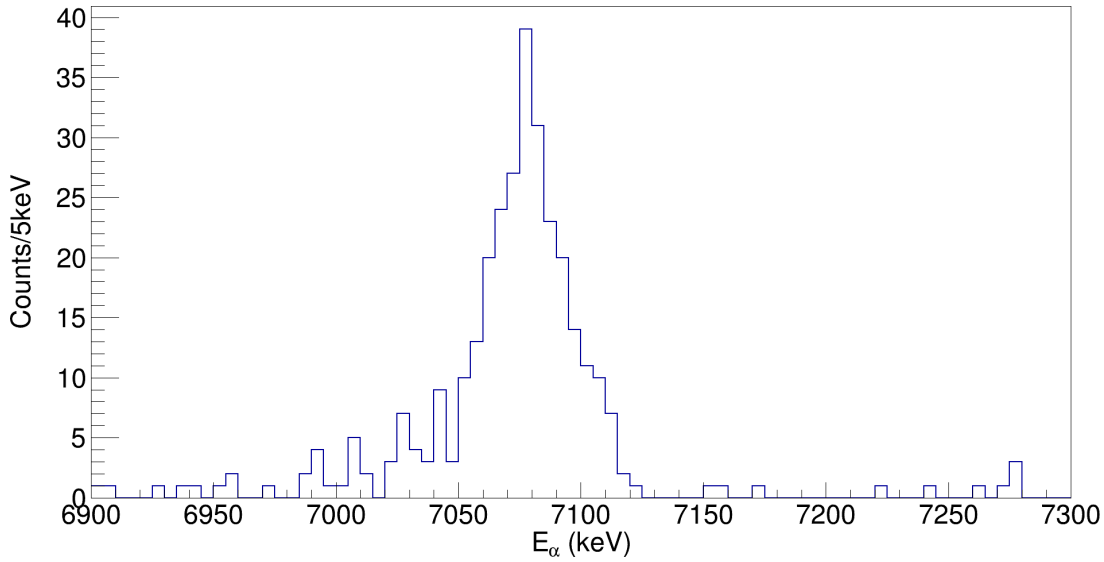

Figure B.10: α-energy spectrum for α-particles detected in coincidence with a γ-ray with $179.0\,\mathrm{keV} < E_\gamma < 181.0\,\mathrm{keV}$.

B.3 . Spectra for the $I^{\pi} = 7/2^{+}$ state at 149.7 keV

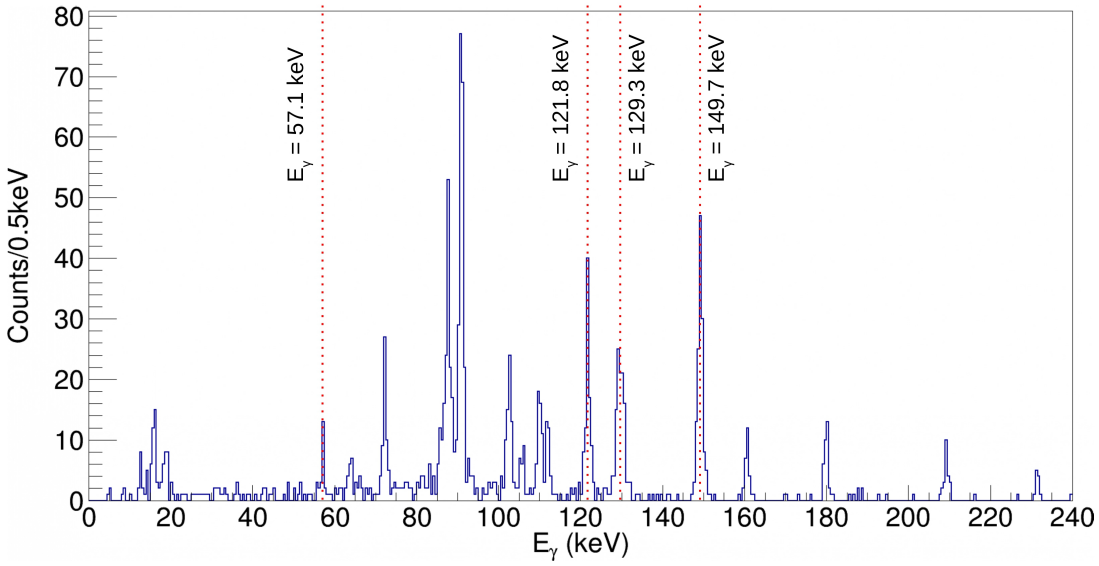

Figure B.11: γ-ray energy spectrum for γ-rays detected in coincidence with an α-particle with 7100 keV $< E_{\alpha} <$ 7140 keV.

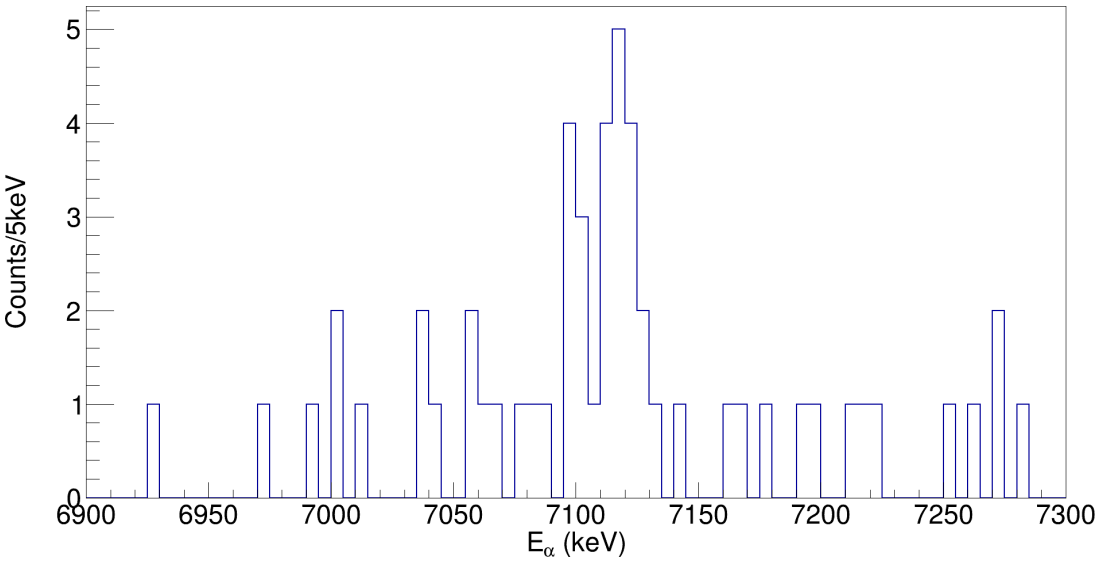

Figure B.12: α-energy spectrum for α-particles detected in coincidence with a γ-ray with 56.1 keV $< E_{\gamma} <$ 58.1 keV.

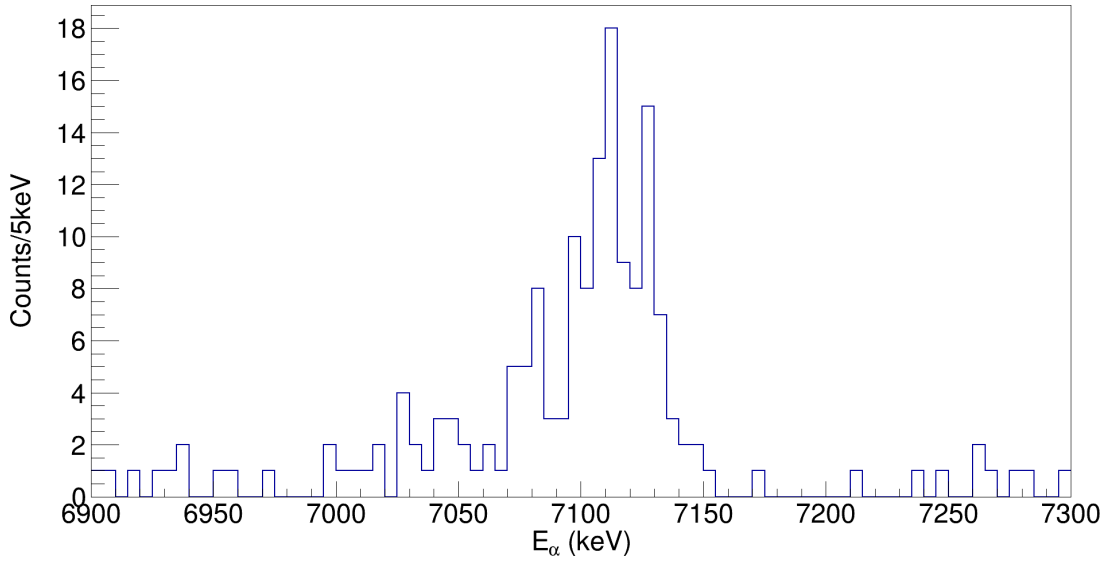

Figure B.13: α-energy spectrum for α-particles detected in coincidence with a γ-ray with 120.8 keV $< E_\gamma <$ 122.8 keV.

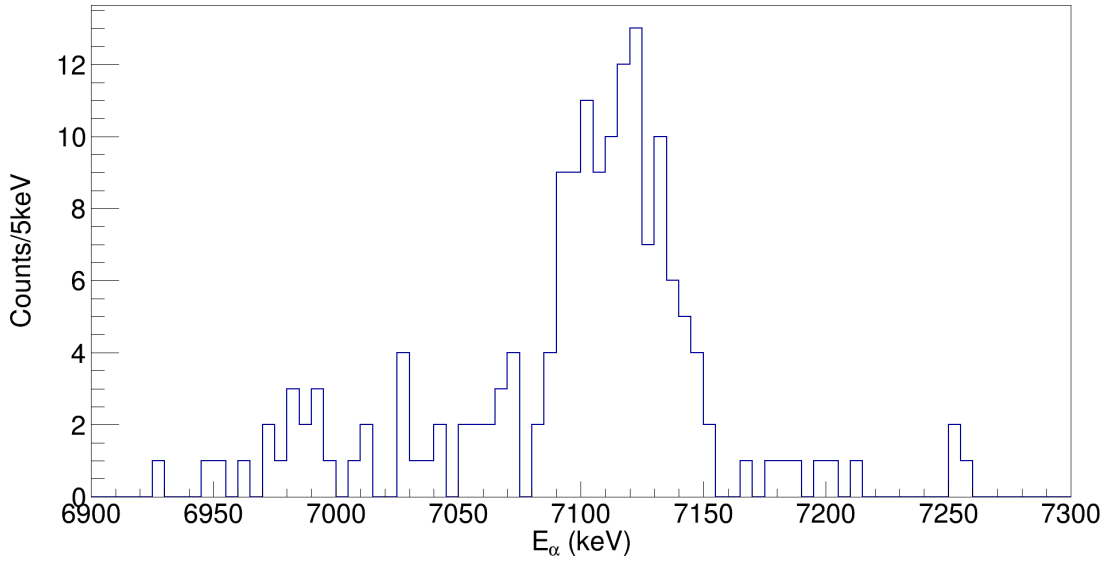

Figure B.14: α-energy spectrum for α-particles detected in coincidence with a γ-ray with 128.3 keV $< E_\gamma <$ 130.3 keV.

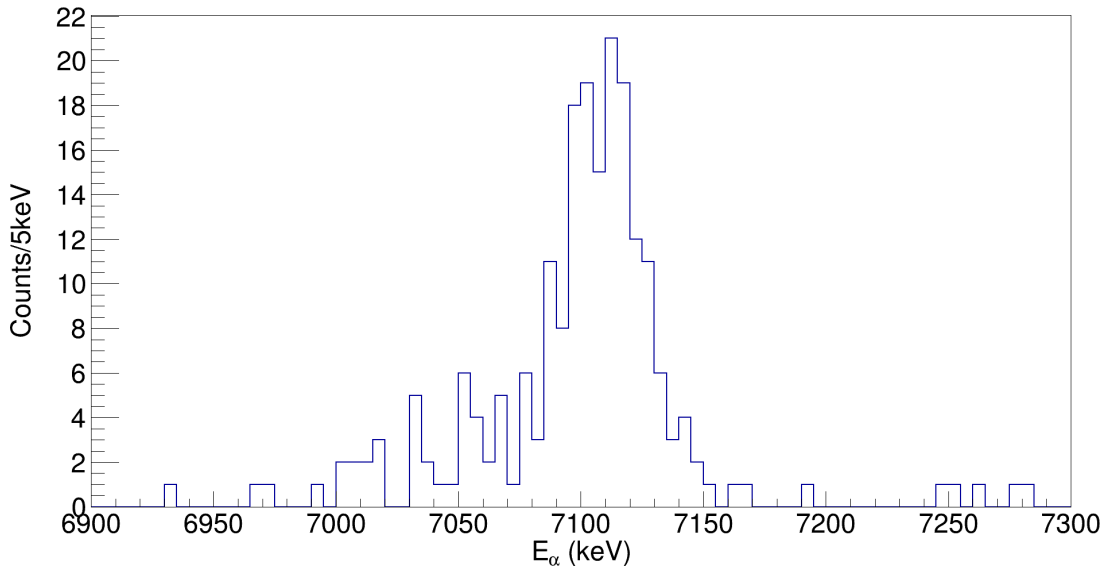

Figure B.15: α-energy spectrum for α-particles detected in coincidence with a γ-ray with $148.7\,\text{keV} < E_\gamma < 150.7\,\text{keV}$.

B.4 . Spectra for the $I^{\pi} = 7/2^{+}$ state at 91.5 keV

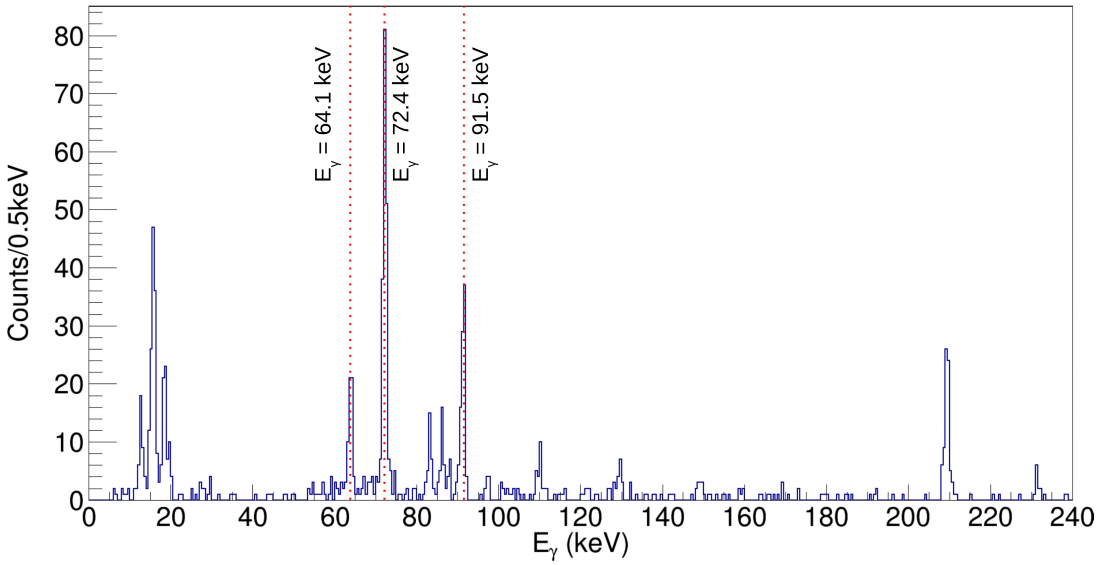

Figure B.16: γ-ray energy spectrum for γ-rays detected in coincidence with an α-particle with 7140 keV $< E_{\alpha} <$ 7200 keV.

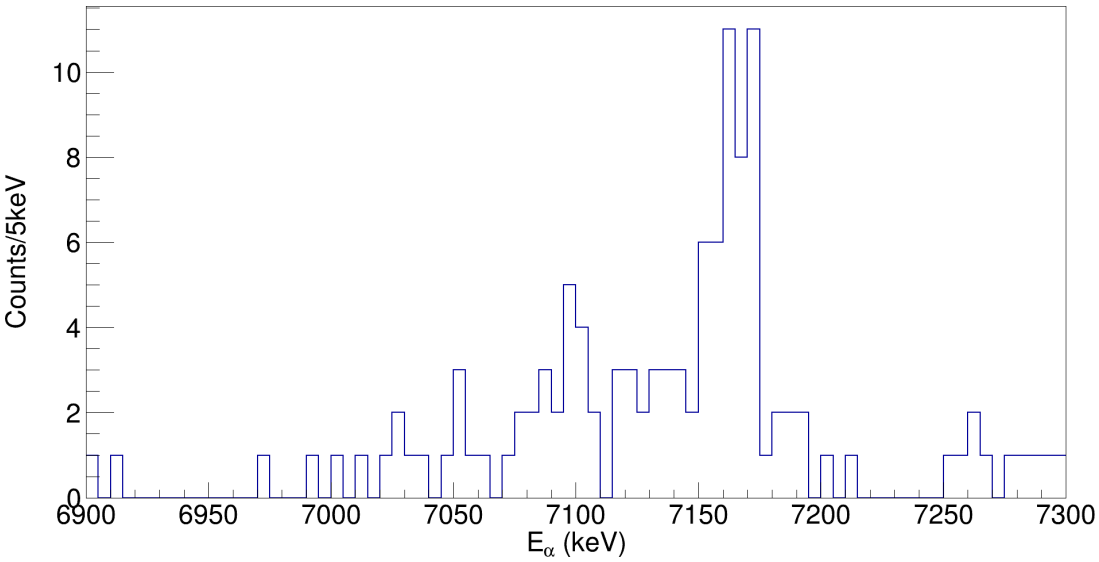

Figure B.17: α-energy spectrum for α-particles detected in coincidence with a γ-ray with 63.1 keV $< E_{\gamma} <$ 65.1 keV.

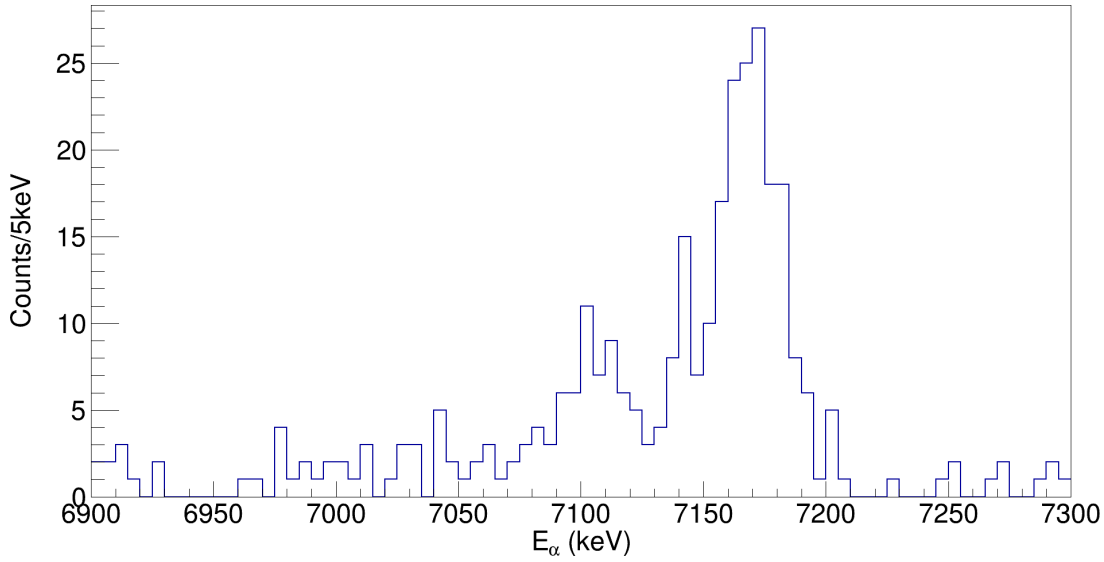

Figure B.18: α-energy spectrum for α-particles detected in coincidence with a γ-ray with $71.4\,\text{keV} < E_\gamma < 73.4\,\text{keV}$.

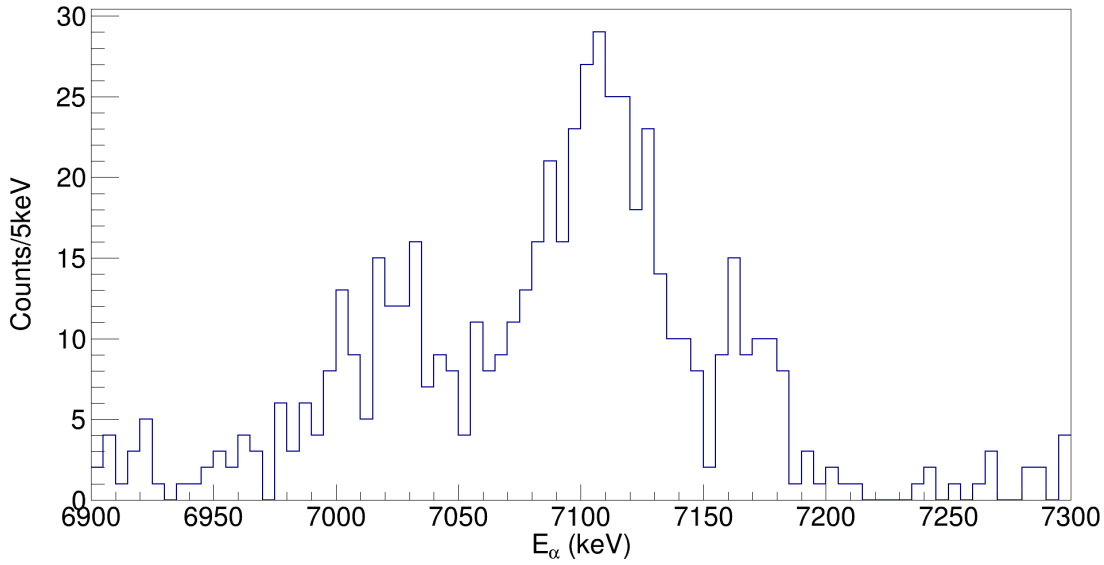

Figure B.19: α-energy spectrum for α-particles detected in coincidence with a γ-ray with $90.5\,\text{keV} < E_\gamma < 92.5\,\text{keV}$.

B.5 . Spectra for the $I^{\pi} = 7/2^{+}$ state at 27.4 keV

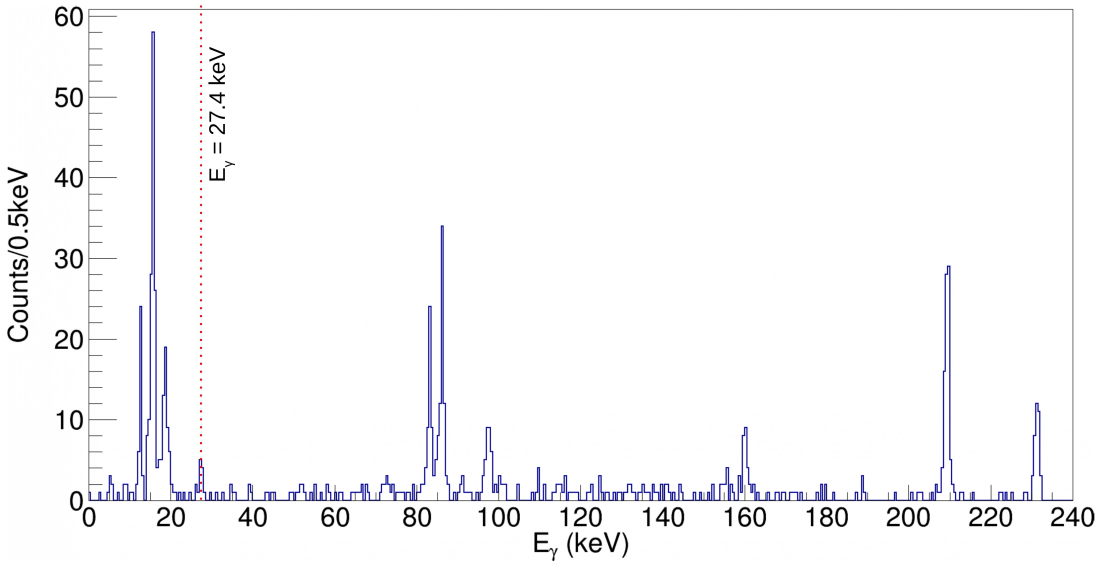

Figure B.20: γ-ray energy spectrum for γ-rays detected in coincidence with an α-particle with 7200 keV $< E_\alpha <$ 7250 keV.

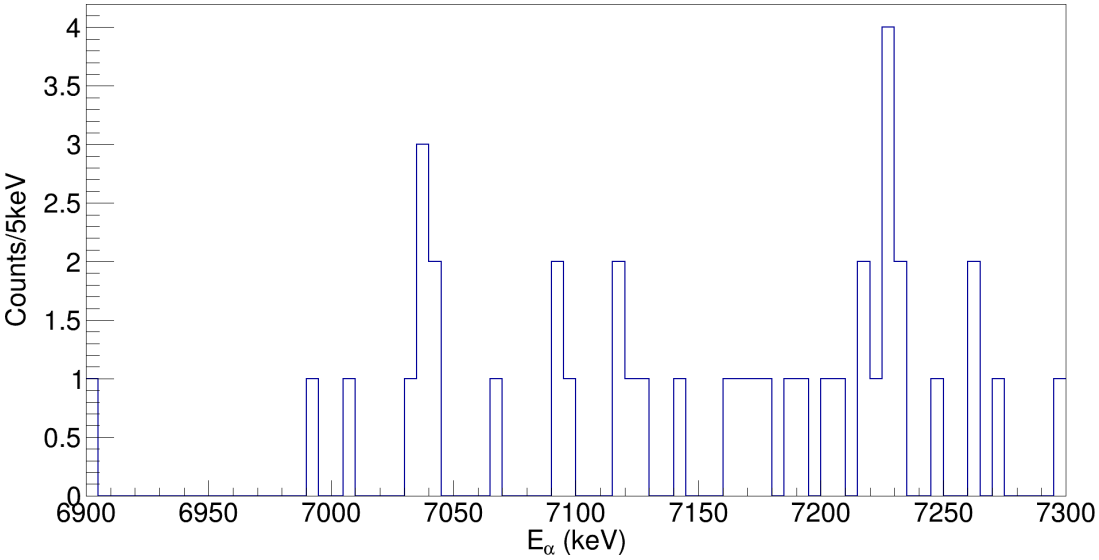

Figure B.21: α-energy spectrum for α-particles detected in coincidence with a γ-ray with 26.4 keV $< E_\gamma <$ 27.4 keV.

Bibliography

[1] L. Meitner and O. R. Frisch. "Disintegration of Uranium by Neutrons: A New Type of Nuclear Reaction". In: *Nature* 143.3615 (Feb. 11, 1939), pp. 239–240. ISSN: 0028-0836, 1476-4687. DOI: 10.1038/143239a0.

[2] *Quadrupole Deformation Chart*. URL: https://www-phynu.cea.fr/science_en_ligne/carte_potentiels_microscopiques/carte_potentiel_nucleaire.htm.

[3] P. Campbell, I. D. Moore, and M. R. Pearson. "Laser Spectroscopy for Nuclear Structure Physics". In: *Progress in Particle and Nuclear Physics* 86 (Jan. 1, 2016), pp. 127–180. ISSN: 0146-6410. DOI: 10.1016/j.ppnp.2015.09.003.

[4] S. G. Nilsson. "Binding States of Individual Nucleons in Strongly Deformed Nuclei". In: (1955).

[5] P. Möller et al. "Axial and Reflection Asymmetry of the Nuclear Ground State". In: *Atomic Data and Nuclear Data Tables* 94.5 (Sept. 1, 2008), pp. 758–780. ISSN: 0092-640X. DOI: 10.1016/j.adt.2008.05.002.

[6] S. E. Agbemava, A. V. Afanasjev, and P. Ring. "Octupole Deformation in the Ground States of Even-Even Nuclei: A Global Analysis within the Covariant Density Functional Theory". In: *Phys. Rev. C* 93.4 (Apr. 4, 2016), p. 044304. DOI: 10.1103/PhysRevC.93.044304.

[7] S. E. Agbemava and A. V. Afanasjev. "Octupole Deformation in the Ground States of Even-Even Z∼96, N∼196 Actinides and Superheavy Nuclei". In: *Phys. Rev. C* 96.2 (Aug. 3, 2017), p. 024301. DOI: 10.1103/PhysRevC.96.024301.

[8] L. M. Robledo and R. R. Rodríguez-Guzmán. "Octupole Deformation Properties of Actinide Isotopes within a Mean-Field Approach". In: *J. Phys. G: Nucl. Part. Phys.* 39.10 (Aug. 2012), p. 105103. ISSN: 0954-3899. DOI: 10.1088/0954-3899/39/10/105103.

[9] R. K. Sheline. "Definition of the Actinide Region of Static Quadrupole-Octupole Deformation". In: *Physics Letters B* 197.4 (Nov. 1987), pp. 500–504. ISSN: 03702693. DOI: 10.1016/0370-2693(87)91042-2.

[10] L. P. Gaffney et al. "Studies of Pear-Shaped Nuclei Using Accelerated Radioactive Beams". In: *Nature* 497.7448 (7448 May 2013), pp. 199–204. ISSN: 1476-4687. DOI: 10.1038/nature12073.

[11] E. Verstraelen et al. "Search for Octupole-Deformed Actinium Isotopes Using Resonance Ionization Spectroscopy". In: *Phys. Rev. C* 100.4 (Oct. 28, 2019), p. 044321. ISSN: 2469-9985, 2469-9993. DOI: 10.1103/PhysRevC.100.044321.

[12] J. Giovinazzo et al. "Two-Proton Radioactivity of ^{45}Fe". In: *Phys. Rev. Lett.* 89.10 (Aug. 19, 2002), p. 102501. ISSN: 0031-9007, 1079-7114. DOI: 10.1103/PhysRevLett.89.102501.

[13] F. Mercier et al. "Microscopic Description of 2 α Decay in ^{212}Po and ^{224}Ra Isotopes". In: *Phys. Rev. Lett.* 127.1 (July 2, 2021), p. 012501. ISSN: 0031-9007, 1079-7114. DOI: 10.1103/PhysRevLett.127.012501.

[14] M. J. Dolinski, A. W. Poon, and W. Rodejohann. "Neutrinoless Double-Beta Decay: Status and Prospects". In: *Annu. Rev. Nucl. Part. Sci.* 69.1 (Oct. 19, 2019), pp. 219–251. ISSN: 0163-8998, 1545-4134. DOI: 10.1146/annurev-nucl-101918-023407.

[15] H. Geiger and J. Nuttall. "LVII. *The Ranges of the a Particles from Various Radioactive Substances and a Relation between Range and Period of Transformation*". In: *The London, Edinburgh, and Dublin Philosophical Magazine and Journal of Science* 22.130 (Oct. 1911), pp. 613–621. ISSN: 1941-5982, 1941-5990. DOI: 10.1080/14786441008637156.

[16] W. D. Loveland, D. J. Morrissey, and G. T. Seaborg. *Modern Nuclear Chemistry*. Second edition. Hoboken, NJ, USA: Wiley, 2017. 744 pp. ISBN: 978-0-470-90673-6.

[17] G. Gamow. "Zur Quantentheorie des Atomkernes". In: *Z. Physik* 51.3-4 (Mar. 1928), pp. 204–212. ISSN: 1434-6001, 1434-601X. DOI: 10.1007/BF01343196.

[18] T. W. Burrow. *ALPHAD Code: A Program to Calculate Alpha Hindrance Factors and Theoretical Half-Lives, Version V2d*. 2018. URL: www-nds.iaea.org/public/ensdf_pgm/.

[19] M. A. Preston. "The Theory of Alpha-Radioactivity". In: *Phys. Rev.* 71.12 (June 15, 1947), pp. 865–877. ISSN: 0031-899X. DOI: 10.1103/PhysRev.71.865.

[20] S. Singh et al. "Nuclear Radius Parameters (R0) for Even-Even Nuclei from Alpha Decay". In: *Nuclear Data Sheets* 167 (July 2020), pp. 1–35. ISSN: 00903752. DOI: 10.1016/j.nds.2020.07.001.

[21] S. Singh, S. Kumar, and B. Singh. *ALP HAD RadD Code : A Program to Calculate Radius Parameter(R0) and Hindrance Factors of Even-Even, Odd-A and Odd-Odd Alpha Emitters*. 2018. URL: www-nds.iaea.org/public/ensdf_pgm/.

[22] T. Kibédi et al. "Evaluation of Theoretical Conversion Coefficients Using BrIcc". In: *Nuclear Instruments and Methods in Physics Research Section A* 589.2 (May 2008), pp. 202–229. ISSN: 01689002. DOI: 10.1016/j.nima.2008.02.051.

[23] K. Rezynkina, A. Lopez-Martens, and K. Hauschild. "On the Graphical Extraction of Multipole Mixing Ratios of Nuclear Transitions". In: *Nuclear Instruments and Methods in Physics Research Section A: Accelerators, Spectrometers, Detectors and Associated Equipment* 844 (Feb. 2017), pp. 96–98. ISSN: 01689002. DOI: 10.1016/j.nima.2016.11.029.

[24] P. A. Butler. "Octupole Collectivity in Nuclei". In: *J. Phys. G: Nucl. Part. Phys.* 43.7 (June 2016), p. 073002. ISSN: 0954-3899. DOI: 10.1088/0954-3899/43/7/073002.

[25] H. Abusara, A. V. Afanasjev, and P. Ring. "Fission Barriers in Covariant Density Functional Theory: Extrapolation to Superheavy Nuclei". In: *Phys. Rev. C* 85.2 (Feb. 22, 2012), p. 024314. DOI: 10.1103/PhysRevC.85.024314.

[26] J.-F. Lemaître et al. "Microscopic Description of the Fission Path with the Gogny Interaction". In: *Phys. Rev. C* 98.2 (Aug. 27, 2018), p. 024623. DOI: 10.1103/PhysRevC.98.024623.

[27] M. Warda and L. M. Robledo. "Microscopic Description of Cluster Radioactivity in Actinide Nuclei". In: *Phys. Rev. C* 84.4 (Oct. 13, 2011), p. 044608. DOI: 10.1103/PhysRevC.84.044608.

[28] M. Warda, A. Zdeb, and L. M. Robledo. "Cluster Radioactivity in Superheavy Nuclei". In: *Phys. Rev. C* 98.4 (Oct. 24, 2018), p. 041602. DOI: 10.1103/PhysRevC.98.041602.

[29] J. Engel et al. "Time-Reversal Violating Schiff Moment of ^{225}Ra". In: *Phys. Rev. C* 68.2 (Aug. 28, 2003), p. 025501. ISSN: 0556-2813, 1089-490X. DOI: 10.1103/PhysRevC.68.025501.

[30] V. V. Flambaum. "Enhanced Nuclear Schiff Moment and Time-Reversal Violation in ^{229}Th-containing Molecules". In: *Phys. Rev. C* 99.3 (Mar. 15, 2019), p. 035501. ISSN: 2469-9985, 2469-9993. DOI: 10.1103/PhysRevC.99.035501.

[31] G. Arrowsmith-Kron et al. *Opportunities for Fundamental Physics Research with Radioactive Molecules*. Feb. 4, 2023. arXiv: 2302.02165 [nucl-ex, physics:nucl-th, physics:physics]. URL: http://arxiv.org/abs/2302.02165. preprint.

[32] P. A. Butler and W. Nazarewicz. "Intrinsic Reflection Asymmetry in Atomic Nuclei". In: *Rev. Mod. Phys.* 68.2 (Apr. 1, 1996), pp. 349–421. DOI: 10.1103/RevModPhys.68.349.

[33] I. Ahmad and P. A. Butler. "Octupole Shapes in Nuclei". In: *Annual Review of Nuclear and Particle Science* 43 (Dec. 1993), pp. 71–116.

[34] P. A. Butler. "Pear-Shaped Atomic Nuclei". In: *Proc. R. Soc. A.* 476.2239 (July 2020), p. 20200202. ISSN: 1364-5021, 1471-2946. DOI: 10.1098/rspa.2020.0202.

[35] L. Gaffney. "Octupole Collectivity in ^{220}Rn and ^{224}Ra". University of Liverpool, 2012. 122 pp. URL: https://livrepository.liverpool.ac.uk/9255/1/GaffneyLia_Sep2012_9255.pdf.

[36] P. Möller and J. Nix. "Nuclear Mass Formula with a Yukawa-plus-exponential Macroscopic Model and a Folded-Yukawa Single-Particle Potential". In: *Nuclear Physics A* 361.1 (May 1981), pp. 117–146. ISSN: 03759474. DOI: 10.1016/0375-9474(81)90473-5.

[37] G. A. Leander et al. "The Breaking of Intrinsic Reflection Symmetry in Nuclear Ground States". In: *Nuclear Physics A* 388 (Apr. 13, 1982), pp. 452–476.

[38] W. Nazarewicz et al. "Analysis of Octupole Instability in Medium-Mass and Heavy Nuclei". In: *Nuclear Physics A* 429.2 (Nov. 1984), pp. 269–295. ISSN: 03759474. DOI: 10.1016/0375-9474(84)90208-2.

[39] P. Möller. "The Most Important Theoretical Developments Leading to the Current Understanding of Heavy-Element Stability: With Some Personal Recollections from the Past 55 Years (1965–2020)". In: *Eur. Phys. J. A* 59.4 (Apr. 13, 2023), p. 77. ISSN: 1434-601X. DOI: 10.1140/epja/s10050-023-00913-z.

[40] V. M. Strutinski. "Remarks on Nuclei of Reflectional Asymmetry". In: *Journal of Nuclear Energy* 4.4 (Apr. 1957), pp. 523–529.

[41] A. Bohr and B. R. Mottelson. "Electric Dipole Moment Associated with Octupole Vibrations of a Spheroïdal Nucleus". In: *Nuclear Physics* 4 (1957), pp. 529–531.

[42] B. Bucher et al. "Direct Evidence of Octupole Deformation in Neutron-Rich ^{144}Ba". In: *Phys. Rev. Lett.* 116.11 (Mar. 17, 2016), p. 112503. ISSN: 0031-9007, 1079-7114. DOI: 10.1103/PhysRevLett.116.112503.

[43] B. Bucher et al. "Direct Evidence for Octupole Deformation in ^{146}Ba and the Origin of Large E1 Moment Variations in Reflection-Asymmetric Nuclei". In: *Phys. Rev. Lett.* 118.15 (Apr. 12, 2017), p. 152504. ISSN: 0031-9007, 1079-7114. DOI: 10.1103/PhysRevLett.118.152504.

[44] R. K. Sheline, A. K. Jain, and K. Jain. "Possible Octupole Deformation in Cs and Ba Nuclei from Their Differential Radii". In: *Phys. Rev. C* 38.6 (Dec. 1, 1988), pp. 2952–2954. ISSN: 0556-2813. DOI: 10.1103/PhysRevC.38.2952.

[45] I. Ragnarsson. "Further Evidence for Reflection Asymmetry in the Ra Region — The Decoupling Parameter and the Magnetic Moment". In: *Physics Letters B* 130.6 (Nov. 1983), pp. 353–358. ISSN: 03702693. DOI: 10.1016/0370-2693(83)91520-4.

[46] R. K. Sheline and G. A. Leander. "Strong and Weak Coupling to the Octupole-Deformed Mode in ^{227}Ac". In: *Phys. Rev. Lett.* 51.5 (Aug. 1, 1983), pp. 359–362. ISSN: 0031-9007. DOI: 10.1103/PhysRevLett.51.359.

[47] G. A. Leander and R. K. Sheline. "Intrinsic Reflection Asymmetry in Odd-A Nuclei". In: *Nuclear Physics A* 413.3 (Feb. 1984), pp. 375–415. ISSN: 03759474. DOI: 10.1016/0375-9474(84)90417-2.

[48] A. Jokinen. "The Jyväskylä Accelerator Laboratory". In: *Nuclear Physics News* 24.4 (Oct. 2, 2014), pp. 4–10. ISSN: 1061-9127, 1931-7336. DOI: 10.1080/10619127.2014.972165.

[49] M. Leino et al. "Gas-Filled Recoil Separator for Studies of Heavy Elements". In: *Nuclear Instruments and Methods in Physics Research Section B: Beam Interactions with Materials and Atoms* 99.1-4 (May 1995), pp. 653–656. ISSN: 0168583X. DOI: 10.1016/0168-583X(94)00573-7.

[50] J. Sarén et al. "The New Vacuum-Mode Recoil Separator MARA at JYFL". In: *Nuclear Instruments and Methods in Physics Research Section B: Beam Interactions with Materials and Atoms* 266.19-20 (Oct. 2008), pp. 4196–4200. ISSN: 0168583X. DOI: 10.1016/j.nimb.2008.05.027.

[51] P. Papadakis et al. "Development of a Low-Energy Radioactive Ion Beam Facility for the MARA Separator". In: *Hyperfine Interact* 237.1 (Dec. 2016), p. 152. ISSN: 0304-3843, 1572-9540. DOI: 10.1007/s10751-016-1364-8.

[52] J. Pakarinen et al. "The Jurogam 3 Spectrometer". In: *Eur. Phys. J. A* 56.5 (May 2020), p. 149. ISSN: 1434-6001, 1434-601X. DOI: 10.1140/epja/s10050-020-00144-6.

[53] J. Pakarinen et al. "The SAGE Spectrometer". In: *Eur. Phys. J. A* 50.3 (Mar. 2014), p. 53. ISSN: 1434-6001, 1434-601X. DOI: 10.1140/epja/i2014-14053-6.

[54] R. Page et al. "The GREAT Spectrometer". In: *Nuclear Instruments and Methods in Physics Research Section B: Beam Interactions with Materials and Atoms* 204 (May 2003), pp. 634–637. ISSN: 0168583X. DOI: 10.1016/S0168-583X(02)02143-2.

[55] J. Äystö et al., eds. *Three Decades of Research Using IGISOL Technique at the University of Jyväskylä: A Portrait of the Ion Guide Isotope Separator On-Line Facility in Jyväskylä*. Dordrecht: Springer Netherlands, 2014. ISBN: 978-94-007-5554-3 978-94-007-5555-0. DOI: 10.1007/978-94-007-5555-0.

[56] I. Moore et al. "Towards Commissioning the New IGISOL-4 Facility". In: *Nuclear Instruments and Methods in Physics Research Section B: Beam Interactions with Materials and Atoms* 317 (Dec. 2013), pp. 208–213. ISSN: 0168583X. DOI: 10.1016/j.nimb.2013.06.036.

[57] jyu. *Ion Guide Isotope Separator On-Line (IGISOL)*. URL: https://www.jyu.fi/science/en/physics/research/infrastructures/accelerator-laboratory/nuclear-physics-facilities/the-exotic-nuclei-and-beams/ion-guide-isotope-separator-on-line-igisol.

[58] P. Karvonen et al. "A Sextupole Ion Beam Guide to Improve the Efficiency and Beam Quality at IGISOL". In: *Nuclear Instruments and Methods in Physics Research Section B: Beam Interactions with Materials and Atoms* 266.21 (Nov. 2008), pp. 4794–4807. ISSN: 0168583X. DOI: 10.1016/j.nimb.2008.07.022.

[59] A. Giatzoglou et al. "A Facility for Production and Laser Cooling of Cesium Isotopes and Isomers". In: *Nuclear Instruments and Methods in Physics Research Section A: Accelerators, Spectrometers, Detectors and Associated Equipment* 908 (Nov. 2018), pp. 367–375. ISSN: 01689002. DOI: 10.1016/j.nima.2018.08.095.

[60] A. Giatzoglou. "Towards Laser Cooling and Trapping of Unstable Caesium Atoms". 2019.

[61] K. M. Jadeja. "Development and Testing of a Facility for the Trapping and Cooling of Isomers". 2023.

[62] B. Cheal and D. H. Forest. "Collinear Laser Spectroscopy Techniques at JYFL". In: *Hyperfine Interact* 223.1-3 (Mar. 2012), pp. 63–71. DOI: DOI10.1007/s10751-012-0608-5.

[63] B. Cheal and D. H. Forest. "Collinear Laser Spectroscopy at the New IGISOL 4 Facility". In: *Hyperfine Interact* 223.1-3 (Jan. 2014), pp. 223–230. ISSN: 0304-3843, 1572-9540. DOI: 10.1007/s10751-012-0621-8.

[64] R. De Groote et al. "Upgrades to the Collinear Laser Spectroscopy Experiment at the IGISOL". In: *Nuclear Instruments and Methods in Physics Research Section B: Beam Interactions with Materials and Atoms* 463 (Jan. 2020), pp. 437–440. ISSN: 0168583X. DOI: 10.1016/j.nimb.2019.04.028.

[65] T. Eronen et al. "JYFLTRAP: A Penning Trap for Precision Mass Spectroscopy and Isobaric Purification". In: *Eur. Phys. J. A* (2012), p. 21.

[66] P. Delahaye et al. "The MORA Project". In: *Hyperfine Interact* 240.1 (Dec. 2019), p. 63. ISSN: 0304-3843, 1572-9540. DOI: 10.1007/s10751-019-1611-x.

[67] Canberra. *Canberra BEGe Technical Sheet*. URL: https://www.gammadata.se/assets/Uploads/BEGe-SS-C49318.pdf.

[68] A. Raggio. "VADER: A Novel Decay Station for Actinide Spectroscopy". In: *Nuclear Instruments and Methods in Physics Research Section B: Beam Interactions with Materials and Atoms* 540 (2023), pp. 148–150. DOI: 10.1016/j.nimb.2023.04.021.

[69] E. Parr et al. "Single-Particle States and Parity Doublets in Odd- Z ^{221}Ac and ^{225}Pa from α -Decay Spectroscopy". In: *Phys. Rev. C* 105.3 (Mar. 2, 2022), p. 034303. ISSN: 2469-9985, 2469-9993. DOI: 10.1103/PhysRevC.105.034303.

[70] A. K. Mistry et al. "Decay Spectroscopy of Heavy Isotopes at SHIP Using the COMPASS Focal Plane Detection Set-up". In: *Acta Phys. Pol. B* 49.3 (2018), p. 613. ISSN: 0587-4254, 1509-5770. DOI: 10.5506/APhysPolB.49.613.

[71] M. Sakama et al. "New Isotope ^{233}Am". In: *Eur Phys J A* 9.3 (Dec. 1, 2000), pp. 303–305. ISSN: 1434-601X. DOI: 10.1007/s100500070013.

[72] R. L. Hahn, M. F. Roche, and K. S. Toth. "New Neptunium Isotopes, ^{230}Np and ^{229}Np". In: *Nuclear Physics A* 113.1 (May 24, 1968), pp. 206–214.

[73] J. Borggreen, K. Valli, and E. K. Hyde. "Production and Decay Properties of Protactinium Isotopes of Mass 222 to 225 Formed in Heavy-Ion Reactions". In: *Phys. Rev. C* 2.5 (Nov. 1, 1970), pp. 1841–1862. DOI: 10.1103/PhysRevC.2.1841.

[74] M. Huyse, P. Dendooven, and K. Deneffe. "Production and Mass Separation of Short-Living Neutron-Deficient Actinides". In: *Nuclear Instruments and Methods in Physics Research Section B: Beam Interactions with Materials and Atoms* 31.3 (May 1, 1988), p. 483486. ISSN: 0168-583X. DOI: 10.1016/0168-583X(88)90350-3.

[75] M. Aïche et al. "High-Spin Spectroscopy of the Reflection-Asymmetric Nucleus ^{221}Ac". In: *Nuclear Physics A* 567.3 (Jan. 1994), pp. 685–700. ISSN: 03759474. DOI: 10.1016/0375-9474(94)90032-9.

[76] D. Radford. *Radware - Gf3*. URL: https://radware.phy.ornl.gov/gf3/gf3.html.

[77] M. Defurne. "Photon and π Electroproduction at Jefferson Laboratory-Hall A". Université Paris-Sud, June 25, 2015. URL: https://theses.hal.science/tel-01281332v1/.

[78] M.-M. Bé and B. international des poids et mesures, eds. *Table of Radionuclides. Vol. 2*. Vol. 2. Monographie BIPM 5. Sèvres: BIPM, 2004. 282 pp. ISBN: 978-92-822-2207-2.

[79] M.-M. Bé and B. international des poids et mesures, eds. *Table of Radionuclides. Vol. 5*. Vol. 5. Monographie BIPM. Sèvres: BIPM, 2010.

[80] M.-M. Bé and B. international des poids et mesures, eds. *Table of Radionuclides. Vol. 6*. Vol. 6. Monographie BIPM. Sèvres: BIPM, 2011.

[81] M.-M. Bé and B. international des poids et mesures, eds. *Table of Radionuclides. Vol. 8*. Vol. 8. Monographie BIPM. Sèvres: BIPM, 2016.

[82] A. Matta et al. "NPTool: A Simulation and Analysis Framework for Low-Energy Nuclear Physics Experiments". In: *J. Phys. G: Nucl. Part. Phys.* 43.4 (Mar. 2016), p. 045113. ISSN: 0954-3899. DOI: 10.1088/0954-3899/43/4/045113.

[83] S. Agostinelli et al. “Geant4—a Simulation Toolkit”. In: *Nuclear Instruments and Methods in Physics Research Section A: Accelerators, Spectrometers, Detectors and Associated Equipment* 506.3 (July 2003), pp. 250–303. ISSN: 01689002. DOI: 10.1016/S0168-9002(03)01368-8.

[84] W. R. Leo. *Techniques for Nuclear and Particle Physics Experiments*. Berlin, Heidelberg: Springer Berlin Heidelberg, 1994. ISBN: 978-3-540-57280-0 978-3-642-57920-2. DOI: 10.1007/978-3-642-57920-2.

[85] J. Kalef-Erza, Y. S. Horowitz, and J. M. Mack. “Electron Backscattering from Low Z Thick Absorbers”. In: *Nuclear Instruments and Methods in Physics Research* 195.3 (Apr. 15, 1982), pp. 587–595. ISSN: 0167-5087. DOI: 10.1016/0029-554X(82)90023-4.

[86] S. Pommé and B. Caro Marroyo. “Improved Peak Shape Fitting in Alpha Spectra”. In: *Applied Radiation and Isotopes* 96 (Feb. 2015), pp. 148–153. ISSN: 09698043. DOI: 10.1016/j.apradiso.2014.11.023.

[87] Y. A. Akovali. “Nuclear Data Sheets for A = 225”. In: *Nuclear Data Sheets* 60.2 (June 1990), pp. 617–653. ISSN: 00903752. DOI: 10.1016/S0090-3752(05)80148-6.

[88] R. R. Chasman et al. “Survey of Single-Particle States in the Mass Region A > 228”. In: *Rev. Mod. Phys.* 49.4 (Oct. 1, 1977), pp. 833–891. ISSN: 0034-6861. DOI: 10.1103/RevModPhys.49.833.

[89] Y. A. Akovali. “Nuclear Data Sheets for A=221”. In: *Nuclear Data Sheets* 61.4 (Dec. 1, 1990), pp. 623–653. ISSN: 0090-3752. DOI: 10.1016/S0090-3752(05)80140-1.

[90] M. Aiche et al. “Yrast States of ^{217} Fr and the Onset of Static Intrinsic Reflection Asymmetric Shapes in the Light Actinide Region”. In: *J. Phys. G: Nucl. Phys.* 14.9 (Sept. 1988), pp. 1191–1200. ISSN: 0305-4616. DOI: 10.1088/0305-4616/14/9/007.

[91] R. K. Sheline, C. F. Liang, and P. Paris. “Level Structure and Reflection Asymmetric Shape in ^{223} Ac”. In: *Int. J. Mod. Phys. A* 05.14 (July 20, 1990), pp. 2821–2831. ISSN: 0217-751X, 1793-656X. DOI: 10.1142/S0217751X90001318.

[92] G. A. Leander and Y. S. Chen. “Reflection-Asymmetric Rotor Model of Odd A ∼ 219-229 Nuclei”. In: *Phys. Rev. C* 37.6 (June 1, 1988), pp. 2744–2778. DOI: 10.1103/PhysRevC.37.2744.

[93] S. Ćwiok and W. Nazarewicz. “Reflection-Asymmetric Shapes in Odd-A Actinide Nuclei”. In: *Nuclear Physics A* 529.1 (July 1, 1991), pp. 95–114. ISSN: 0375-9474. DOI: 10.1016/0375-9474(91)90787-7.

[94] R. K. Sheline and B. B.-M. Bossinga. “Alpha Decay Hindrance Factors and Reflection Asymmetry in Nuclei”. In: *Phys. Rev. C* 44.1 (July 1, 1991), pp. 218–222. ISSN: 0556-2813, 1089-490X. DOI: 10.1103/PhysRevC.44.218.

[95] R. K. Sheline. “Comment on the Question of Reflection Asymmetry in ^{229}Pa”. In: *Phys. Rev. C* 48.3 (Sept. 1, 1993), pp. 1003–1004. DOI: 10.1103/PhysRevC.48.1003.

[96] R. K. Sheline et al. “Experimental and Theoretical Study of the Nuclear Structure of ^{223}Fr”. In: *Phys. Rev. C* 51.4 (Apr. 1, 1995), pp. 1708–1719. DOI: 10.1103/PhysRevC.51.1708.

[97] I. Ahmad et al. “Octupole Deformation in ^{223}Ac”. In: *Nuclear Physics A* 505.2 (Dec. 11, 1989), pp. 257–266. ISSN: 0375-9474. DOI: 10.1016/0375-9474(89)90373-4.

[98] I. Ahmad et al. “Possible Ground-State Octupole Deformation in ^{229}Pa”. In: *Phys. Rev. Lett.* 49.24 (Dec. 13, 1982), pp. 1758–1761. DOI: 10.1103/PhysRevLett.49.1758.

[99] G. Ardisson et al. “Levels in ^{221}Fr Fed by the α Decay of ^{225}Ac”. In: *Phys. Rev. C* 62.6 (Nov. 9, 2000), p. 064306. DOI: 10.1103/PhysRevC.62.064306.

[100] I. Ahmad et al. “Level Structure of ^{225}Ac”. In: *Nuclear Physics A* 472.2 (Sept. 28, 1987), pp. 285–294. ISSN: 0375-9474. DOI: 10.1016/0375-9474(87)90211-9.

[101] C. F. Liang et al. “^{219}Fr, a Transitional Reflection Asymmetric Nucleus”. In: *Phys. Rev. C* 44.2 (Aug. 1, 1991), pp. 676–688. DOI: 10.1103/PhysRevC.44.676.

[102] E. Rey-herme et al. “Level Structure of ^{221}Ac and ^{217}Fr from Decay Spectroscopy, and Reflection Asymmetry in ^{221}Ac”. In: *Phys. Rev. C* 108.1 (July 5, 2023), p. 014304. ISSN: 2469-9985, 2469-9993. DOI: 10.1103/PhysRevC.108.014304.

[103] S. Gales. “SPIRAL2 at GANIL: Next Generation of ISOL Facility for Intense Secondary Radioactive Ion Beams”. In: *Nuclear Physics A* 834.1-4 (Mar. 2010), pp. 717c–723c. ISSN: 03759474. DOI: 10.1016/j.nuclphysa.2010.01.130.

[104] X. Ledoux et al. “First Beams at Neutrons for Science”. In: *Eur. Phys. J. A* 57.8 (Aug. 2021), p. 257. ISSN: 1434-6001, 1434-601X. DOI: 10.1140/epja/s10050-021-00565-x.

[105] A. Drouart et al. “The Super Separator Spectrometer (S3) for SPIRAL2 Stable Beams”. In: *Nuclear Physics A* 834.1-4 (Mar. 2010), pp. 747c–750c. ISSN: 03759474. DOI: 10.1016/j.nuclphysa.2010.01.135.

[106] F. Déchery et al. “The Super Separator Spectrometer S3 and the Associated Detection Systems: SIRIUS & LEB-REGLIS3”. In: *Nuclear Instruments and Methods in Physics Research Section B: Beam Interactions with Materials and Atoms* 376 (June 2016), pp. 125–130. ISSN: 0168583X. DOI: 10.1016/j.nimb.2016.02.036.

[107] D. Toprek and T. Kurtukian-Nieto. “DESIR High Resolution Separator at GANIL, France”. In: *Nucl Technol Radiat Prot* 27.4 (2012), pp. 346–350. ISSN: 1451-3994, 1452-8185. DOI: 10.2298/NTRP1204346T.

[108] L. Perrot, P. Blache, and S. Rousselot. “The DESIR Facility at GANIL-SPIRAL2: The Transfer Beam Lines”. In: (2016).

[109] N. Karkour et al. “SIRIUS Project (Spectroscopy & Identification of Rare Isotopes Using S3)”. In: *2016 IEEE Nuclear Science Symposium, Medical Imaging Conference and Room-Temperature Semiconductor Detector Workshop (NSS/MIC/RTSD)*. 2016 IEEE Nuclear Science Symposium, Medical Imaging Conference and Room-Temperature Semiconductor Detector Workshop (NSS/MIC/RTSD). Strasbourg: IEEE, Oct. 2016, pp. 1–6. ISBN: 978-1-5090-1642-6. DOI: 10.1109/NSSMIC.2016.8069937.

[110] P. Brionnet et al. “Characterization of a New Generation of Silicon Detector: The SIRIUS Side “Strippy-Pad” Detector”. In: *Nuclear Instruments and Methods in Physics Research Section A: Accelerators, Spectrometers, Detectors and Associated Equipment* 1015 (Nov. 2021), p. 165770. ISSN: 01689002. DOI: 10.1016/j.nima.2021.165770.

[111] R. Ferrer et al. “In Gas Laser Ionization and Spectroscopy Experiments at the Superconducting Separator Spectrometer (S3): Conceptual Studies and Preliminary Design”. In: *Nuclear Instruments and Methods in Physics Research Section B: Beam Interactions with Materials and Atoms* 317 (Dec. 2013), pp. 570–581. ISSN: 0168583X. DOI: 10.1016/j.nimb.2013.07.028.

[112] P. Chauveau et al. “PILGRIM, a Multi-Reflection Time-of-Flight Mass Spectrometer for Spiral2-S3 at GANIL”. In: *Nuclear Instruments and Methods in Physics Research Section B: Beam Interactions with Materials and Atoms* 376 (June 2016), pp. 211–215. ISSN: 0168583X. DOI: 10.1016/j.nimb.2016.01.025.

[113] R. Ferrer et al. “Towards High-Resolution Laser Ionization Spectroscopy of the Heaviest Elements in Supersonic Gas Jet Expansion”. In: *Nat Commun* 8.1 (Feb. 22, 2017), p. 14520. ISSN: 2041-1723. DOI: 10.1038/ncomms14520.

[114] Yu. Kudryavtsev et al. “The In-Gas-Jet Laser Ion Source: Resonance Ionization Spectroscopy of Radioactive Atoms in Supersonic Gas Jets”. In: *Nuclear Instruments and Methods in Physics Research Section B: Beam Interactions with Materials and Atoms* 297 (Feb. 2013), pp. 7–22. ISSN: 0168583X. DOI: 10.1016/j.nimb.2012.12.008.

[115] R. Ferrer et al. “Hypersonic Nozzle for Laser-Spectroscopy Studies at 17 K Characterized by Resonance-Ionization-Spectroscopy-Based Flow Mapping”. In: *Phys. Rev. Research* 3.4 (Oct. 15, 2021), p. 043041. ISSN: 2643-1564. DOI: 10.1103/PhysRevResearch.3.043041.

[116] J. Romans et al. “First Offline Results from the S3 Low-Energy Branch”. In: *Atoms* 10.1 (Feb. 9, 2022), p. 21. ISSN: 2218-2004. DOI: 10.3390/atoms10010021.

[117] J. Simpson et al. “The EXOGAM Array: A Radioactive Beam Gamma-Ray Spectrometer”. In: *Acta Physica Hungarica New Series-Heavy ion* 11 (2000), pp. 159–188. URL: https://hal.in2p3.fr/in2p3-00438782.

[118] Micron. *BB7 Specification*. URL: http://www.micronsemiconductor.co.uk/product/bb7/.

[119] T. Goigoux. *SEASON, Compte-rendu des simulations*. Jan. 10, 2020.

[120] F. P. Heßberger et al. “Decay Studies of K Isomers in 254No”. In: *Eur. Phys. J. A* 43.1 (Jan. 2010), p. 55. ISSN: 1434-6001, 1434-601X. DOI: 10.1140/epja/i2009-10899-9.

[121] M. D. Seliverstov et al. “Electromagnetic Moments of Odd- A $^{193\text{-}203,211}$Po Isotopes”. In: *Phys. Rev. C* 89.3 (Mar. 31, 2014), p. 034323. ISSN: 0556-2813, 1089-490X. DOI: 10.1103/PhysRevC.89.034323.

[122] SILSON. *SILSON SiN Foils*. URL: https://www.silson.com/product/silicon-nitride/.

[123] A. Metal. *ACF Metal's Product Information*. Jan. 15, 2019. URL: https://www.acf-metals.com/.

[124] L. Thulliez et al. "Impact of Material Thicknesses on Fission Observables Obtained with the FALSTAFF Experimental Setup". In: *EPJ Web Conf.* 146 (2017), p. 04028. ISSN: 2100-014X. DOI: 10.1051/epjconf/201714604028.

[125] K. Iakoubovskii et al. "Thickness Measurements with Electron Energy Loss Spectroscopy". In: *Microsc. Res. Tech.* 71.8 (Aug. 2008), pp. 626–631. ISSN: 1059910X, 10970029. DOI: 10.1002/jemt.20597.

[126] J. Thomas, J. Ramm, and T. Gemming. "Density Measurement of Thin Layers by Electron Energy Loss Spectroscopy (EELS)". In: *Micron* 50 (July 2013), pp. 57–61. ISSN: 09684328. DOI: 10.1016/j.micron.2013.05.001.